Technical Report Documentation Page

1. Report No.	2. Government Accession No.	3. Recipient's Catalog No.
FHWA/TX-15/0-5997-2		

4. Title and Subtitle	5. Report Date
STRUCTURAL ASSESSMENT OF "D" REGIONS AFFECTED BY PREMATURE CONCRETE DETERIORATION: TECHNICAL REPORT	Published: March 2015
	6. Performing Organization Code
7. Author(s)	8. Performing Organization Report No.
John B. Mander, Madhu M. Karthik, and Stefan Hurlebaus	Report 0-5997-2
9. Performing Organization Name and Address	10. Work Unit No. (TRAIS)
Texas A&M Transportation Institute College Station, Texas 77843-3135	
	11. Contract or Grant No. Project 0-5997
12. Sponsoring Agency Name and Address	13. Type of Report and Period Covered
Texas Department of Transportation Research and Technology Implementation Office 125 E. 11th Street Austin, Texas 78701-2483	Technical Report: September 2007–August 2014
	14. Sponsoring Agency Code

15. Supplementary Notes

Project performed in cooperation with the Texas Department of Transportation and the Federal Highway Administration.
Project Title: Structural Assessment of "D" Regions Affected by Premature Concrete Deterioration
URL: http://tti.tamu.edu/documents/0-5997-2.pdf

16. Abstract

The current study is a continuation of the earlier study that investigated the effects of Alkali Silica Reaction (ASR) and Delayed Ettringite Formation (DEF) induced deterioration on the D-Regions of structures. Of the four near full-scale C-Beam specimens that were constructed, and conditioned over time as part of the earlier study, the last specimen (Specimen 3), which was field conditioned through the Texas heat along with supplemental water for a period of five years, is the main focus of this study. With time, additional cracks caused by ASR/DEF swelling were observed in addition to the load induced cracks. Based on the deterioration data collected and observations made on Specimen 3, it was classified to show *heavy* damage due to ASR/DEF deterioration. The experimental test of Specimen 3 which resulted in a brittle shear failure through the beam-column joint, showed a similar failure mechanism to the other three C-Beam specimens. The heavy deterioration caused by ASR/DEF deterioration also did not seem to have any effect on the load carrying capacity of the specimen. However, the response of the specimen was considerably stiffer and less ductile than the earlier tested C-Beam specimens with no, *slight,* and *moderate* amounts of deterioration. This is due to the restraint offered to ASR/DEF swelling strain by the reinforcement, which causes tensile strains in the reinforcement. This effectively put the concrete under a state of active prestress. Although no signs of corrosion are observed in the specimen during the deterioration phase, in terms of concrete cover spalling or rust stains in concrete, a considerable amount of corrosion was observed on the reinforcement bars once the cover concrete was removed.

A minimalist semi-empirical analysis technique is developed to model the expansion strains caused by ASR/DEF expansion in reinforced concrete. The proposed model takes into account the effects of compressive and tensile prestrains on the expansion strains caused by ASR/DEF, in addition to the daily variations in temperature and humidity. This enables the model to capture the expansion strains in reinforced concrete structures that are exposed to environmental conditions. The model is validated and applied to simulate the expansion strains observed for the C-Beam specimens. Considering the complex nature of the ASR/DEF phenomena, the nature of the structure considered, and the variability in the field recorded data, the model simulates the expansion strains quite well.

The Compatibility Strut-and-Tie Modeling (C-STM) technique, which was developed and verified in Phase I of this report, is used to model the force-deformation behavior of C-Beam Specimen 3. The expansion strains that are obtained from the ASR/DEF model is used to compute the prestress loads to be applied in the C-STM technique to account for the effects of ASR/DEF expansion in the model. The C-STM simulates the overall force-deformation and the internal behavior of the structure quite well.

17. Key Words	18. Distribution Statement
Bridge Bent; ASR/DEF Deterioration; Expansion Modeling; Force-Deformation Modeling; Compatibility Strut-and-Tie Modeling	No restrictions. This document is available to the public through NTIS: National Technical Information Service Alexandria, Virginia http://www.ntis.gov

19. Security Classif. (of this report)	20. Security Classif. (of this page)	21. No. of Pages	22. Price
Unclassified	Unclassified	210	

Form DOT F 1700.7 (8-72) Reproduction of completed page authorized

STRUCTURAL ASSESSMENT OF "D" REGIONS AFFECTED BY PREMATURE CONCRETE DETERIORATION: TECHNICAL REPORT

by

John B. Mander
Zachry Professor of Design and Construction Integration
Zachry Department of Civil Engineering

Madhu M. Karthik
Graduate Assistant Researcher
Zachry Department of Civil Engineering

and

Stefan Hurlebaus
Peter C. Forster Career Development Professor
Zachry Department of Civil Engineering

Report 0-5997-2
Project 0-5997
Project Title: Structural Assessment of "D" Regions Affected by Premature Concrete Deterioration

Performed in cooperation with the
Texas Department of Transportation
and the
Federal Highway Administration

Published: March 2015

TEXAS A&M TRANSPORTATION INSTITUTE
College Station, Texas 77843-3135

DISCLAIMER

This research was performed in cooperation with the Texas Department of Transportation (TxDOT) and the Federal Highway Administration (FHWA). The contents of this report reflect the views of the authors, who are responsible for the facts and the accuracy of the data presented herein. The contents do not necessarily reflect the official view or policies of the FHWA or TxDOT. This report does not constitute a standard, specification, or regulation.

The United States Government and the State of Texas do not endorse products or manufacturers. Trade or manufacturers' names appear herein solely because they are considered essential to the object of this report.

ACKNOWLEDGMENTS

This project was conducted at Texas A&M University in conjunction with the Texas A&M Transportation Institute. The experiments were conducted in the High Bay Structures and Material Testing Laboratory. Dr. Peter Keating, Mr. Matthew Potter, and Mr. Ramiro Vanoye are thanked for their assistance.

Funding for this project was provided via a contract with the Texas Department of Transportation (TxDOT) (Project 0-5997) with Mr. Wade Odell serving as Project Director. The guidance of Mr. Odell and the project control group is gratefully acknowledged.

TABLE OF CONTENTS

LIST OF FIGURES

LIST OF TABLES

1 INTRODUCTION

1.1 RESEARCH BACKGROUND AND CONTEXT

This report follows, and should be read in conjunction with, an earlier TxDOT funded companion publication entitled "Structural Assessment of 'D' Region Affected by Premature Concrete Deterioration," Project 0-5997-1 (Mander et al., 2012). In that experimental and analytical study, four large (near full-scale) C-Beam reinforced concrete specimens were constructed to represent key disturbed (D-) region features of hammerhead and straddle bent bridge piers. Many such bridge piers have been constructed over the past two decades and are now showing signs of distress due to Alkali-Silica Reaction (ASR) and/or Delayed Ettringite Formation (DEF) within concrete.

Of the four specimens that were cast, Specimen 1 remained indoors in a controlled environment and constant temperature and then was tested as the benchmark or *control* specimen. The other three specimens were taken to Texas A&M Riverside Campus in Bryan, Texas, and conditioned outdoors under normal environmental conditions with supplemental water for varying lengths of time. The condition of the three specimens was observed over time via surface and subsurface strains. The progression of cracks was periodically mapped for all the specimens.

Specimen 2 was returned to the laboratory for testing after 252 days (8.4 months) of exposure when the condition of the concrete was *slightly* deteriorated from the effects of ASR/DEF. Specimen 3, which showed slightly more deterioration than Specimen 4, was reserved for future testing outside the initial research contract period. Specimen 4 was returned to the laboratory for load testing after 748 days (2 years) of exposure when the condition of the specimen was judged to be *moderate* damage due to the effects of ASR/DEF deterioration.

In spite of the deterioration, load testing demonstrated that neither the strength nor stiffness of the structure were impaired due to *slight* or *moderate* levels of ASR/DEF deterioration. In fact both the strength and stiffness increased slightly and this improvement was attributed to the ASR/DEF swelling (volumetric expansion) of the concrete, which in turn caused a passive post tensioning of the reinforcing steel to develop over time.

Results from strain gages showed that most hoops would have exceeded their yield strain thereby applying a confining action in strengthening the concrete. Similarly, strains induced in the

longitudinal rebars provide an axial prestress effect, thereby delaying the decompression of the concrete under flexural bending action.

In spite of the apparent poor appearance of the specimens it was concluded that, provided the ASR/DEF deterioration was not excessive, a structure was able to continue to perform its purpose of resisting loads without penalty.

However, one caution was noted in particular. During the testing of the moderately deteriorated Specimen 4, it was noticed that when the outer cover concrete of the knee-joint spalled and the reinforcing steel was exposed, the onset of corrosion in the rebars was observed. It was apparent that the ASR/DEF induced cracking formed a pathway for moisture ingress and served as a trigger for corrosion deterioration. Such deterioration over a longer term may impair the performance of the structure, especially in the knee-joint region as that reinforcing steel is often a vital part of the load resisting mechanism for joint shear.

This report investigates the continued deterioration and load resistance of the final specimen in the series, Specimen 3. Specimen 3 was returned to the laboratory after 1829 days (5 years) of field exposure for testing and analysis. The deteriorated condition of the specimen at this age is judged as being *heavy*.

1.2 SCOPE

The report is divided into nine chapters. Following the introductory chapter, Chapter 2 presents the literature review. As a major part of the literature review on truss modeling was extensively presented in Mander et al. (2012), Chapter 2 mainly focuses on an expanded literature relevant to the ASR/DEF phenomena and on modeling ASR/DEF in concrete.

Chapter 3 presents the development of a minimalist semi-empirical model to simulate the expansion strains caused by ASR/DEF expansion in reinforced concrete. First, the model is formulated to simulate expansion strains in reinforced concrete members that are cured under standard conditions of temperature and humidity, and validated against experimentally observed data. Following this, modifications are introduced into the model, to take into account the variation in temperature and humidity. This enables the model to be applied to reinforced concrete structures that are exposed to environmental conditions. The model is validated by simulating the field

recorded expansions in a reinforced concrete column splice specimens from a TxDOT funded companion project "Performance of Lap Splices in Large-Scale Column Specimens Affected by ASR and/or DEF," Project 0-5772-1 (Bracci et al., 2012).

Chapter 4 presents the visual observations from the *heavily* deteriorated C-Beam specimen. Visual observations, the surface strain measurements from DEMEC points on the concrete specimen, and concrete and steel strains obtained from the embedded instrumentation are also presented. Also presented in this chapter are the progression of cracks at various ages of the specimen and the final crack widths that were measured on the specimen. Discussions are made based on the observations.

Chapter 5 presents the application of the expansion model developed in Chapter 3 to the field observations made on Specimen 3 presented in Chapter 4. Comparisons are made between the field observations and the expansions obtained from the model. To demonstrate the repeatability of the model, the model is also applied to the previously examined Specimens 2 and 4 observed expansion strains (Mander et al., 2012).

Chapter 6 presents the experimental test setup and the instrumentation details. The experimental testing procedure and the load history are also presented in this chapter. The performance, force-deformation behavior, and various other important observations made during the destructive testing of the *heavily* deteriorated specimen are discussed in detail.

Chapter 7 presents the application of the Compatibility Strut-and-Tie Method (C-STM) analysis methodology that was developed in Mander et al. (2012) to the specimen tested in Chapter 6. In light of the new methodology to predict the expansion strains in the specimen (presented in Chapter 3), the C-STM analysis is re-run for all four C-Beam specimens and the results are presented in Chapter 7. Chapter 7 also studies the internal strains obtained from the C-STM model and the corresponding failure analysis results, in addition to modeling the overall force-deformation behavior of the specimen. All C-STM results are compared with the experimental results.

Finally, Chapter 8 presents a summary of the dual experimental and analytical modeling program and the key findings from this study. Major conclusions from each of the chapters are presented, and recommendations for future work are made.

1.3 WHAT IS PARTICULARLY NEW IN THIS WORK?

The major contributions from this current work toward the existing pool of knowledge can be summarized as:

- A minimalist semi-empirical model with very limited input parameters that can be used to estimate the progression of expansion strains caused by ASR/DEF in reinforced concrete is developed. The application of this model is also successfully demonstrated.
- Observations and measurements made on a large-scale reinforced concrete specimen conditioned under alternate wet-dry cycles over time, allows for examining ASR/DEF evolution, and how heavy ASR/DEF deterioration progresses with time.
- Large-scale experimental tests on reinforced concrete members with D-regions experiencing *heavy* ASR/DEF deterioration were conducted through failure. The comparison of these results with the control specimen and with specimens with slight and moderate amounts of ASR/DEF induced deterioration will give an idea of the structural performance of the structure.
- Ways to include the expansion strains obtained from the model into the C-STM analysis will be demonstrated. Additionally, the C-STM results will be compared with the experimental force-deformation and internal behavior of the structure. Finally, an in-depth analysis will reveal the internal mechanisms that eventually lead to the failure of the specimen.

2 LITERATURE REVIEW

2.1 SCOPE OF CHAPTER

A very brief review on the phenomenon of ASR/DEF related deterioration in concrete was presented in Mander et al. (2012). In this chapter a more comprehensive review of ASR/DEF related mechanism, laboratory studies on the effects of ASR/DEF on reinforced concrete, and a review of modeling deterioration in concrete are presented. Finally a review of a few recent studies on the effects of ASR/DEF in large-scale reinforced concrete structural members is presented. A review on the historic developments on truss modeling is presented in Mander et al. (2012) and will not be covered in this chapter.

2.2 ALKALI-SILICA REACTION

2.2.1 The ASR Chemical Process

The expansion of concrete caused by the reaction between cement and aggregate was first reported by Stanton (1940). It is now well known that the reaction between alkalis in Portland cement and certain reactive silica in the aggregates can lead to what is called the Alkali Silica Reaction (Hobbs, 1988; Swamy and Al-Asali, 1988; Poole, 1992; among others). This can cause excessive cracking and deterioration of concrete structures (Multon et al., 2006; Deschenes et al., 2009; Bracci et al., 2012; Mander et al., 2012).

The overall process of ASR is still not fully understood. However, based on the present state of knowledge, ASR can be considered to be a multistage process, described as follows (Pesavento et al., 2012):

a. The hydroxyl ions (OH^-) in the pore solution react with silanol groups $(Si-OH)$, which cause the breakage of the siloxane bonds and the creation of additional silanol bonds (Bažant and Steffens, 2000; Kurtis, 2003).

$$Si-O-Si+OH^- \rightarrow Si-OH+Si-OH$$

b. Silanol groups react with hydroxyl ions on the aggregate particle surfaces (Glasser and Kataoka, 1981; Bažant and Steffens, 2000), liberating more water.

$$Si-OH+OH^- \rightarrow SiO^- + H_2O$$

Cations of the pore solution are attracted to the negatively charged group (SiO^-). Na^+ and K^+ diffuse into the gel in sufficient numbers to balance the negatively charged group.

c. After reaching the saturation point, a gel consisting of silica, alkalis, water, and other ions is created. The alkali-silicate gel has a higher specific volume than the reactants. The gel is hydrophilic, hence in the presence of water it expands causing a swelling process. The composition of the gel can vary a lot, thus making the prediction of its behavior quite difficult.

The extent of the damage induced by ASR depends on the magnitude and time-evolution of ASR induced strains. These in turn depend on several factors (Multon et al., 2006) such as the content of the reactive materials (alkali and reactive silica), environmental factors like temperature and humidity (Olafsson, 1986), water supply (Larive, 1998; Larive et al., 2000), stress conditions due to either mechanical loading (Larive et al., 1996; Gravel et al., 2000; Multon, 2004; Multon et al., 2004) or restraint provided to ASR expansion by steel reinforcement (Swamy and Al-Asali, 1989; Fan and Hanson, 1998; Monette et al., 2002; Multon et al., 2005).

2.2.2 Review of Laboratory Experiments on ASR Deteriorated Reinforced Concrete

In this sub-section some of the relevant experimental studies that were conducted to study the performance of reinforced concrete affected by expansion due to ASR are reviewed.

Hobbs (1988) carried out tests on plain and reinforced concrete specimens and focused on axial strains measurements caused by ASR expansion. The concrete specimens were moist cured at a constant temperature of 68°F. Two series of tests were conducted, for Series I of the test the reactive particle size varied from 300–1200 μm whereas for Series II the particle size varied from 150–300 μm. The evolution of expansion strain was recorded with time. From the strain evolution data, researchers observed that as the reinforcement ratio in the reinforced concrete beam increased, the maximum expansion strain considerably reduced. It was also evident from the experimental results that irrespective of the amount of reinforcement present, the rise time, i.e., the time between the onset of ASR expansion until the final expansion was reached, was approximately the same. Hobbs observed that the reactive particle size had a considerable effect on the free expansion of ASR in plain concrete. Series I with larger reactive aggregate particles showed less expansion in plain concrete compared to Series II with finer reactive aggregates. The

effect of the size of the reactive particle in reinforced concrete was not as significant as observed in plain concrete.

Swamy and Asali (1989) conducted laboratory studies on the effects of ASR on the structural behavior of reinforced concrete beams. The beams (2.95 × 3.94 × 31.50 in.) were singly reinforced with shear reinforcement and two different reactive aggregates were used for the study. The specimens were placed in a fog room at 68°F and a relative humidity of 96 percent. The concrete expansion, cracking, and reinforcing steel strains were monitored. The researchers observed that the presence of tension face reinforcement subjected the beam to differential expansion. Due to the lack of compression face reinforcement the differential expansion caused a camber in the ASR affected beam specimens. Based on pulse velocity measurements, it was hypothesized that the ASR cracking was limited to the surface and did not always extend to the core of the beam. Load tests showed that the effects of ASR substantially reduced the stiffness of the beam, and beams affected by ASR did not appear to lose their ductility or capability to absorb large amounts of energy at failure. However, during the load tests, the ASR affected beams showed little sagging before failure as the loads were insufficient to overcome the camber that was initially caused by the expansion. The irreversible strains caused by ASR accelerated the yield of the reinforcing steel under load tests and caused the beams to fail at lower loads compared to the reference sound beam.

Jones and Clark (1996) experimentally studied the effects of restraints on ASR expansion in reinforced concrete. The experimental program involved testing concrete cylinders (3.94 × 7.87 in.) with a single reinforcing bar running through the center of the cylinder, which were conditioned under different stresses and had various reinforcement ratios. Reinforced concrete beams (3.94 × 7.87 × 78.74 in.) with two different reinforcement ratios, unreinforced prisms (7.87 × 7.87 × 3.94 in.) and a concrete block (17.72 × 11.81 × 23.62 in.) with reinforcement were also cast. After curing, most specimens were stored under water at 100°F. To study the effects of temperature on the expansion rate few specimens were also stored in water at 86°F and 68°F. The researchers observed that the applied stresses reduced ASR expansion, and even at higher applied stresses there was noticeable expansion. The increase in the reinforcement ratio caused a decrease in ASR expansion. However, observations also revealed that increasing the reinforcement ratios beyond 2 percent had minimal effect in decreasing the expansion caused by ASR. As

observed earlier by Hobbs (1988), after the commencement of expansion, the expansion rate for all reinforcement ratios was constant until the final expansion was reached. Additionally, applied compressive stresses further decreased the expansion in reinforced concrete specimens, but beyond an applied stress of 0.29 ksi the reinforcement ratio made little difference in the expansion. Other important observations that were made in the experimental study was that the free expansion was dependent on the casting direction, size of the specimen appeared to have an effect on the expansion, rate of expansion had little effect on the relationship between restraint and expansion, the restraint did not significantly affect the expansion perpendicular to its direction, and with an increase in temperature there was an increase in the rate of expansion.

Fan and Hanson (1998) investigated the effects of ASR expansion on the structural behavior of reinforced concrete beams. The beam test specimens (5.91 × 9.84 × 59.06 in.) were singly reinforced with different reinforcement ratios. Concrete cylinders (3.94 × 7.87 in.) were cast to study the effects of ASR on the mechanical properties of concrete. To simulate service load conditions, two beams (one reactive and one non-reactive) were preloaded until cracks of specific widths were observed on the tension side. The test specimens were placed in 0.5N alkali solution, and the solution in the tank was heated to 100°F. The tank was alternately heated to 100°F and cooled to 75°F for 5–7 days and 2 days, respectively. The expansion of the reactive specimen due to ASR started at about 5 months of immersion of the test specimens. The longitudinal expansion at the level of reinforcement was greatly reduced due to the restraint provided by the reinforcement. The difference in the reinforcement ratio did not cause any difference in the rate of expansion and cracking in the reactive beams. For the pre-cracked reactive beam, cracks were observed in the compression face after one year of conditioning. A substantial reduction in the compressive strength, splitting tensile strength and dynamic modulus were observed with the onset of expansion due to ASR. Results from the load tests on the beam specimens showed that the ASR expansion and cracking did not reduce the flexural load capacity of the reinforced concrete beams. The researchers hypothesized that the effects of ASR were limited to the beam surface or that since the beams were under-reinforced the reduction in concrete compressive strength made little difference to the beam flexural strength.

Ahmed et al. (1998) conducted experimental studies to investigate the effects of ASR on the static and fatigue strength of reinforced concrete. For the purpose of this study reactive and

non-reactive (control) beams (3.15 × 5.12 × 51.18 in.) were constructed with different reinforcement details, such as, with and without compression and shear reinforcement and with and without proper anchorage for the longitudinal reinforcement bars. The beams were stored for six months in a hot water tank at 104°F to accelerate ASR induced expansion. The expansion data showed that good anchorage of the longitudinal tension reinforcement is necessary for inhibiting the detrimental effects of ASR expansion. Moreover, the addition of some compression reinforcement further reduced ASR induced expansion. The lateral expansion was also reduced with proper anchorage of longitudinal reinforcement and in the presence of shear reinforcement. As expected a rapid increase in the steel strain was observed with the commencement of ASR reaction. Ultrasonic Pulse Velocity tests further affirmed that the deleterious effects of ASR in concrete members can be reduced with good anchorage and with the presence of shear links. From the static test for shear, researchers observed that ASR increased the shear capacity of reinforced concrete beams with and without shear links, and the increase was greater in doubly reinforced beams affected by ASR. Fatigue tests demonstrated that neither the fatigue life nor the shear strength of beams were adversely affected by ASR, because of: (a) the prestress induced by the tensile reinforcement; (b) the beneficial effects of hydration of cement, which were greater than the detrimental effect of cracking; and (c) the ASR gel acting as a strong filler, which reduced the loss of tensile strength due to ASR reaction. The flexural stiffness of both the control and ASR affected specimens decreased significantly with increase in the number of cycles. The ASR affected beams also experienced lower deflections than the control specimens under repeated loading.

Monette et al. (2002) conducted experimental investigation on the effects of ASR expansion on reinforced concrete beams (3.5 × 4.76 × 35.5 in.) conditioned without loads and under sustained and cyclic loads. Concrete cylinders (3.94 × 7.87 in.) were used to monitor the concrete expansion and compressive strength, and concrete prisms (3.94 × 2.95 × 15.75 in.) were used to monitor resonant frequency and concrete flexural strength. The major goals of this research were to examine the relationship between measured ASR expansions and visual observations of ASR on the beams and quantify the damage using Damage Rating Index (DRI), and make observations on the residual strength and stiffness of the beams under different conditioning loads. The reactive and non-reactive beams, respectively, were conditioned under 1N NaOH at 100°F for 147 days and 161 days and were air dried for 150 days and 60 days. The expansion data showed

that the sustained and cyclic flexural conditioning loads and the longitudinal reinforcement had significant restraining effects on ASR expansions. The DRI measurements were unable to differentiate between the mechanical cracks and the cracks caused by ASR expansion, and the expansion measurements better indicated the expansion due to ASR. The beams were load tested to failure under four-point bending. All the beams, both reactive and non-reactive, showed similar load-deformation behavior, even when conditioned under different loads. Tests on the mechanical properties of concrete revealed that ASR did not prevent the increase in concrete compressive strength with time; however, concrete cracking caused by ASR significantly reduced the stiffness of the reactive concrete cylinders. The dynamic modulus of elasticity was found to be less sensitive to ASR effects when compared to the static modulus of elasticity. Researchers also observed that the flexural strength of concrete reduced with ASR expansion and it was more sensitive to ASR expansion than the concrete compressive strength.

Mohammed et al. (2003) conducted an experimental investigation on how various restrained conditions provided by the embedded steel reinforcement in concrete could affect the strains induced on the concrete surface and the steel bars. For this study, plain and reinforced concrete prisms (9.84 × 9.84 × 23.62 in.) and cylinder specimens (3.94 × 7.87 in.) were cast with and without reactive aggregates, and then submerged in seawater at 104°F for a period of 200 days. The study was oriented in determining if the degree of restraint provided by the reinforcement, and location of reinforcement and if the presence of stirrups had any effects on the concrete surface and steel strains. Eight different cases, which included plain concrete and concrete with different restraint conditions and reinforcement ratios, were considered. From the deterioration data, researchers observed that the degree of restraint had significant influence on the concrete surface strain and the strains in the bars. Additionally, the closer the reinforcement was to the concrete surface, less concrete surface strains and higher steel strains were observed. The presence of stirrups did not appear to have any significant effect on the lateral expansion or the longitudinal steel strain. Additionally, the strains in the lateral reinforcement were higher compared to their longitudinal bars. However, the influence of lateral reinforcement was not fully established as only one configuration was tested and investigation of beams with more confinement by stirrups was necessary.

Multon et al. (2005) conducted experiments to study the effects of ASR on the structural behavior of concrete. The major scope was to study how moisture gradients in the structure affected the structure, as this could lead to differential ASR development and expansion. For this study, plain and reinforced concrete beams (9.84 × 19.68 × 118.11 in.) were cast along with concrete cylinders (6.30 × 12.60 in.) and prisms (5.51 × 5.51 × 11.02 in.) to study the evolution of the mechanical properties of concrete. The bottom of the concrete beams was immersed in water and the upper face was exposed to air at 30 percent relative humidity. The side faces were covered with watertight aluminum sheets to ensure a vertical drying process. The beams were stored in an air-conditioned room with 30 percent relative humidity at 100°F. From the deterioration data collected for about 14 months of exposure, the following major conclusions were drawn. The ASR expansion was highly anisotropic and significant expansions occurred even without external water supply. Distribution of water within the reactive specimen induced large expansions in the transverse and vertical directions between depths of 6.70 in. to 19.68 in. from the top of the specimen, and shrinkage on the exposed drying face. As evident in the earlier tests, researchers noticed that the longitudinal reinforcement caused a large decrease in ASR expansion strain. However, the local effects on stirrups were hardly significant on the vertical and transverse deformations.

The experimental studies conducted by the various authors on the effects of ASR expansion on reinforced concrete elements clearly established that the presence of reinforcement significantly decreases the expansion caused by ASR in the direction of the reinforcement. Additionally, there was also a need to model the expansion caused by ASR in concrete structures, to enable prediction of expansion strains in concrete. Various authors proposed models to simulate the expansion caused by ASR in concrete. Models that are relevant to this study are briefly reviewed in the following sub section.

2.2.3 Review of Modeling Concrete Deterioration Caused by ASR

This section concentrates on the relevant developments on how to model the expansion caused by ASR in plain and reinforced concrete.

Hobbs (1981) presented a model to predict ASR induced expansion in mortar. Hobbs assumed that ASR expansion was a two-stage process where, in the first stage the alkalis and

reactive silica react rapidly until one of the reactants is depleted, and in the second phase the reaction product absorbs water and hydroxyl ions to form alkali-silica gel, which expands and causes cracking in the mortar. The author presented expressions that predicted the time to cracking and the expansion caused by ASR. However, the expressions had a few constant terms that were determined numerically from the experimental data. The proposed model was observed to be in general agreement with observed expansion behavior of mortar bars, which were stored under water at 68°F.

Groves and Zhang (1990) presented a dilation model for the expansion of silica glass in ordinary Portland cement mortar. This model was based on the observation that the main reaction product was a layer of C-S-H gel that was formed at the surface of the glass. The mortar expansion was predicted as the increase in the glass volume plus the reaction product layer, and was found to be in the same order of magnitude as the observed results.

Clark (1991) carried out studies in order to identify the main factors to be considered in modeling the effects of ASR on a structure. Clark found it necessary to consider numerous factors to efficiently model the effects of ASR on a structure, including: the proportion of reactive particles; particle size; porosity of the aggregate and concrete; curing conditions; rate of expansion; specimen size; reinforcing steel content; specimen shape; and casting direction, etc. Clark advised caution when extrapolating modeled results to prototype structures, as accelerated laboratory conditions may not be observed in the field. Clark's study provides a glimpse on how complex it is to model each of the interacting factors where ASR may adversely affect reinforced concrete behavior.

Charlwood et al. (1992) presented a phenomenological model in which the expansion was treated as an initial strain induced by temperature increase. The anisotropic expansion was dependent on the stress state and was defined as a function of the stress tensor. Though this model was simple and effective, it did not consider the detailed mechanism of ASR.

Furusawa et al. (1994) dealt with modeling the chemical reaction and the ensuing expansion in the case of ASR. They assumed that the rate of diffusion of hydroxyl and alkali ions into the aggregate determined the overall propagation rate of ASR. The researchers also assumed that there was a porous zone around the aggregate and expansion was initiated only after the

reaction product exceeded the volume of this porous zone. From an analysis of powdered specimens at the end of mortar bar tests, a close agreement was found between the estimated and actual values of total amount of reaction products. The proposed model was able to capture certain characteristic features of ASR related expansion such as the initial incubation period, varying rates of expansion, and the shapes of expansion-time curves. However, the applicability of this model to reinforced concrete needed further investigation.

Pietruszczak (1996) proposed a continuum theory for the description of mechanical effects of Alkali Aggregate Reaction (AAR) in concrete. In the formulation of this phenomenological approach restricted to isothermal conditions, the progressive expansion of concrete due to ASR was coupled with the degradation of mechanical properties, which was described within the framework of elastoplasticity. They assumed a reduction in Young's modulus and the compressive and tensile strength of concrete due to ASR expansion. The rate of expansion however was assumed to depend on the available alkali content in the cement matrix. Other important factors like the variation of temperature and humidity effects on the rate of the reaction were not considered. Huang and Pietruszczak (1996) later made modifications to the model and included a parameter to control the rate of strain softening. The authors developed an implicit integration scheme for the implementation of the continuum model in a finite element analysis. An application of the numerical analysis to a powerhouse was also presented. In a later development Huang and Pietruszczak (1999) assumed that the expansion rate depended on the alkali content, magnitude of confining stress, and the evolution of temperature. The authors discussed a mathematical formulation under nonisothermal conditions, describing the thermomechanical effects of ASR. The temperature of the concrete mass was assumed to affect both the rate of volumetric expansion and the degradation of mechanical properties. A notion of thermal activation time was introduced to formulate the evolution law for ASR induced expansion. The formulation presented focuses on the description of long-term degradation resulting from continuing ASR, and the influence of temperature fluctuations on the instantaneous values of material constants was neglected. A finite element model consisting of about 23,000 four-node tetrahedral elements was used for the analysis of a power plant consisting of gravity dams, powerhouse, and water intake structures. The analysis was carried under nonisothermal and isothermal conditions. The predictions based on the thermomechanical analysis were consistent with the field measurements. However, the continuum approach presented by these researchers is complicated to implement. Additionally, the analysis

involves employing the non-unique complexity of finite element models to determine the effects of ASR on the structure.

Léger et al. (1996) presented a flowchart for the numerical simulation of concrete expansion in dams affected by AAR. The authors note that due to the complexity of ASR expansion, any simulation model has to be calibrated against the displacements recorded from the monitoring system and strains in rebars and concrete when possible. Normalized expansion factors for different zones of the dam considering confinement, temperature, moisture, and material reactivity were introduced into the numerical simulation. A calibration factor was also introduced to adjust the computed displacements to match the field measurements. This model was based on trial-and-error to match observed deformations and did not reflect the physical mechanism.

Bažant and Steffens (2000) proposed a mathematical model for a quantitative prediction of ASR expansion. The two problems to be dealt with were identified as the kinetics of the chemical reaction with the associated diffusion process and the fracture mechanics of the damage process. The authors only address the kinetics of the reaction in this work. The study was done on ground waste glass used as an aggregate in concrete; the authors noted that it could be extended to cases where natural aggregates were used. Their model was developed by analyzing an idealized repetitive cubical cell with one spherical reactive particle. The radial growth of the spherical layer of basic ASR gel was assumed to be controlled by the diffusion of water through the gel layer toward the reaction front. Concrete, however, resists this swelling and a pressure is developed. Parametric studies on the numerical solutions clarified the effects of particle size. However, it is not clear how this model could be applied to concrete with natural aggregates, as waste glass consists entirely of silica and a radial growth can be assumed.

Ulm et al. (2000) proposed a chemoelastic model for ASR swelling in concrete from the level of macroscopic material modeling to the level of analysis for full-size concrete structures. This was a first-order engineering approach to capture the timescale and magnitude of ASR expansion. Two timescales, specifically (a) the latency time associated with the dissolution of reactive silica, and (b) characteristic time scale associated with ASR product formation, were required for a realistic prediction of structural effects caused by ASR. In the model, concrete is considered as a porous medium consisting of a solid matrix skeleton with ASR gel occupying the

voids. In their analogue spring model, one spring modeled the gel (comprising of an expansion cell in series with a linear spring representing ASR gel expansion and gel compressibility, respectively) while the other modeled the concrete solid matrix. The researchers concluded that temperature played a major role in ASR expansion kinetics. However the effects of humidity and stress induced anisotropy of ASR swelling were not considered in this model. Additionally, the equations derived remain complex and not amenable for application by practicing engineers.

Capra and Sellier (2003) noted that due to the random distribution of reactive sites and the lack of complete understanding of the chemical reactions, it becomes difficult to model ASR. The authors presented a new approach, based on the probabilistic description of the main physical parameters of concrete and AAR, that allowed simulation of the orthotropic swelling of concrete subjected to AAR. In order to perform structural computations, reactions were modeled within a phenomenological approach framework by taking into account the reaction kinetics, temperature, moisture, and stress state. Concrete was modeled as a damageable material having elastic and inelastic strains, whereas AAR was modeled by a global kinetics including temperature and humidity effects. Modeling of AAR also took into account the probability of cracking due to AAR and due to tensile and compressive stresses. A coupling between the mechanics and AAR was established by introducing damage coefficients and this made it possible to simulate tests carried out on concrete specimens. The model showed good agreement with the longitudinal and transverse swelling data of concrete specimens subjected to uniaxial loading.

Frange et al. (2004) presented a macroscopic approach where the uncoupling between AAR and stress and the representation of anisotropic characteristic of chemical swelling was considered. In their constitutive model, Ulm et al.'s (2000) analogue model for concrete was modified by adding a cohesive joint element for modeling crack opening in tension, represented by concrete tensile strength. The proposed model was able to simulate laboratory tests concerning reactive concrete samples under constant uniaxial loading. For the case of free expansion, isotropic behavior was assumed, which led to an overestimation. Factors such as random distribution of reactive sites, temperature, and moisture conditions could be incorporated into the model to improve the modeling for free expansion. The model was able to represent adequately the unloading and loading behavior of AAR affected concrete. Further studies were recommended to study the coupling between stresses and AAR to extend the application of the model to structures

under complex loading conditions and boundary conditions. One of the shortcomings of the model is that the gel and concrete properties and the characteristic parameters for gel kinetics are required as an input for the implementation of the model, which could be a difficult task in itself for existing ASR damaged structures. There could also be difficulty in implementation of this finite element approach for complex structures.

Fairbairn et al. (2005) presented a thermo-chemo-mechanical expansion model for ASR. In their model the stress induced anisotropy was represented by a classical smeared cracking model. The influence of temperature and humidity in ASR expansion was considered. Their model was an enhanced version of the model proposed by Ulm et al. (2000), to better capture the cracking of the concrete skeleton. The model was applied to a concrete dam affected by ASR through a finite element code, and a good agreement between the experimental and numerical data was observed.

Saouma and Perotti (2006) proposed a new thermo-chemo-mechanical model that was rooted in the chemistry (kinetics of the ASR reaction), physics (crack gel absorption, effect of compression), and mechanics of concrete. A few considerations that were taken into account in the proposed model were the kinetics and volumetric expansion of the ASR gel, temperature, constraining effects of compression on ASR expansion, effects of triaxial compressive state of stress and high compressive hydrostatic stresses on the ASR expansion, and reduction of tensile strength and elastic modulus due to ASR expansion. Anisotropy of the ASR induced expansion was accounted for by assigning weights to each of the three principal directions. The model was used in the analysis of a dam subjected to ASR deterioration. Extensive preliminary work was conducted to prepare the necessary initial data for the model. The results from this model were compared to the current state of the practice model proposed by Charlwood et al. (1992). The dam structure was subjected to the same final crest displacement using the two models. However, the internal field stresses were drastically different in the two models considered. The lack of stress redistribution in Charlwood's model led to underestimation of the stress field.

Multon et al. (2006) noted that the major parameters to be considered for predicting the mechanical behavior of ASR-damaged structures are the concrete mixture, environmental conditions, water supply, the stresses due to mechanical loading, and the restraint to ASR

expansion caused by the steel reinforcement. The analysis showed that steel reinforcement not only caused direct prestressing effects by restraining ASR expansion, but the compressive stresses due to local restraints by steel caused a reduction in ASR expansion along the compressed direction. The study found that taking into account the elastic effects of reinforcing bars alone could not explain the structural behavior of reinforced beams subjected to ASR. ASR expansion was not only counteracted by compressive stresses, but it appeared to be largely prevented in the compressed direction. A reduction factor in the range of 0.45–0.30 was used to account for this effect. The model could, however, not be used for predictive purposes for the case of reinforced concrete. The authors conclude that the effect of compressive stresses on ASR expansions had still not been solved by predictive models using chemoelastic concepts.

Winnicki and Pietruszczak (2008) proposed a continuum approach for describing chemomechanical interaction in reinforced concrete. Mathematical formulations were derived for the mechanical degradation of reinforced concrete due to ASR. Based on Pietruszczak and Winnicki (2003), the material was treated as a composite medium consisting of the concrete matrix and two orthogonal families of reinforcement. The model was formulated in two stages: Phase I dealt with homogeneous deformation mode prior to cracking of the concrete matrix; and Phase II involved the localized deformation associated with formation of macrocracks. The numerical analysis was restricted to the material point level in order to validate the formulation against experimental data involving homogeneous stress states. The formulation was able to capture the basic trends in mechanical response of reinforced concrete subjected to ASR effects and external loading. However, the mathematical formulations are considered rather difficult for implementation by practicing engineers. The validity of the formulation also needs to be verified for actual reinforced concrete structures, particularly reinforced concrete beams that are not under homogeneous stress states.

Many of the modeling approaches that have been briefly reviewed here are limited to ASR expansion caused in plain concrete, and almost all require a finite element implementation to predict the expansion caused in concrete. Very limited studies have been conducted in studying ASR related expansion in reinforced concrete. The various methodologies presented take into account different factors that affect ASR related expansion, which is important in fully understanding the phenomena. However, this leads to a more complex equation and difficulties

can arise during its implementation on structures. In the present research a general strain-based approach is proposed as a minimalist, easy to implement, semi-empirical model for the analysis of swelling strains in reinforced concrete members where the reinforcement ratios are different in each of the three orthogonal axes.

2.3 DELAYED ETTRINGITE FORMATION

2.3.1 The DEF Chemical Process

Delayed Ettringite Formation is the formation of ettringite and associated expansion when the concrete is subjected to high temperature during its curing period. Experiments have shown that when mortar/concrete is subjected to high temperatures during the curing and hardening process, they tend to expand and crack when subsequently exposed to moisture. The chemistry/phenomenon behind DEF is explained in the following paragraph (Folliard et al. 2006).

Very early in the cement hydration process calcium aluminates (C_3A and C_4AF) react with gypsum ($C\hat{S}H_2$) to produce ettringite ($C_3A.3CaSO_4.32H_2O$). After the completion of this reaction, if additional C_3A is available, calcium monosulphoaluminate ($C_3A.CaSO_4.12H_2O$) or monosulphate forms. There is a general tendency for monosulphate to exist in higher proportions than ettringite, but it is not uncommon to find both hydrates in the hydrated cement paste. After a majority of the ettringite is formed, calcium silicate hydrate (C-S-H) gel fills in the bulk of the concrete matrix and provides much of the concrete strength. At elevated curing temperatures (>158°F) C-S-H gel production is accelerated when compared to ettringite. The accelerated formation rate of C-S-H gel physically traps some of the sulphates and aluminates in its layered structure before they can react to form ettringite (Older, 1980; Fu, 1996; Scrivener et al., 1999). At high curing temperatures, the trapping continues until the C-S-H gel becomes fully saturated with sulphates. Ettringite and then monosulphate are formed with the remaining sulphates as would occur in concrete cured in ambient temperatures. After the concrete has gone through the entire heat curing cycle, and is stored in a moist environment at ambient temperatures, the sulphates diffuse out of the C-S-H gel into the pore solution. This provides an internal source of sulphate and triggers the reformation of ettringite in hardened concrete. This reformation of ettringite causes expansion and cracking of concrete. This delayed or secondary formation of ettringite in hardened concrete is widely known as Delayed Ettringite Formation.

2.3.2 Experimental Investigations on DEF

A brief review of relevant past work with regard to DEF in concrete is presented in what follows.

Heinz and Ludwig (1987) investigated the causes of loss in strength and damages to structures that were precast units made of high strength concrete and heat treated during production. In particular, these damages occurred in structural components that were exposed to frequent moisture saturation for several years. The authors carried out an experimental investigation on mortar prisms, concentrating on the threshold temperature of damage, SO_3 content in cement, storage humidity, and the water-cement ratio. Heat treatment at temperatures above 167°F led to expansion linked with a decrease in strength. Temperatures below 167°F did not bring any damaging reaction in the specimen. The researchers suggested keeping the SO_3/Al_2O_3 molar ratio in cement to below 0.55 to minimize the contribution of SO_3 toward the deterioration of concrete. The samples that were stored under water showed early signs of the damage reaction and different water-cement ratios did not cause any variation in the swelling reaction.

Scrivener and Taylor (1993) tested cement paste samples that were cured at 176°F and examined them by scanning electron microscopy, X-ray microanalysis, and X-ray diffraction immediately or after storage in water for various periods at 68°F. The experiments showed that ettringite present in the cement paste was destroyed during curing in water for 16 hours at 176°F. After the heat treatment, aluminate and sulphate were largely present in the C-S-H gel. Ettringite formation, in the form of very small crystals thinly distributed in the C-S-H gel, started within a few days after the heat cured specimen was stored in water at 68°F. The ettringite recrystallized in cavities 5–10 μm in size, and there was no indication that this process disrupted the surrounding material in any way different from the surrounding empty but otherwise similar cavities. The ettringite seen at aggregate interfaces in mortars and concretes expanded following recrystallization. From these observations the authors were of the view that the paste expanded, thereby creating spaces around the aggregate particles. The ettringite seen at the interfaces was a result of these expansions and was not what caused the expansion.

Based on field reports of damage associated with DEF in non-steam cured concrete (Pettifer and Nixon, 1980; Jones and Poole, 1986; Larive and Louarn, 1992), Diamond (1996) refuted the claim that DEF is confined to steam cured concrete that had been subjected to excessive

temperatures during curing. The crack pattern observed were a network, with cracks running partly along the aggregate peripheries (rim cracks), generally connecting cracks running through the cement paste (paste cracks). This pattern reflected local and inhomogeneous crack propagation. In concrete affected by DEF, the crack network resulted in a severe loss of dynamic elastic modulus. Filling up of fine air voids by ettringite may also interfere with frost resistance.

Kelham (1996) studied the effects of cement composition and fineness on expansion associated with DEF. Kelham concluded that curing temperature was a dominant factor in determining the extent of expansion, while the expansion also increased with the cement fineness, alkali, C_3A, C_3S, and MgO contents.

Hobbs (1999) conducted laboratory studies to study the factors that caused DEF in precast concrete and cast in-situ concrete structures that saw high temperatures during curing and were subsequently subjected to wetting and drying cycles. Hobbs observed that laboratory studies on mortar and concrete showed that DEF related expansion was not possible when the early temperatures were below 160°F. Based on the laboratory and field observations it was estimated that for DEF to occur in cast in-situ concrete, the initial curing temperature had to exceed 185°F. Hobbs also observed that the laboratory specimen showed a reduction in water/cement ratio greatly prolonged the time to expansion and resulted in a higher final expansion. Based on the study on the composition of cement, Hobbs concluded that no single product was responsible for the expansion, and that it was a combination of parameters like MgO, SO_3, equivalent Na_20 content, and the fineness of cement contributed to the final expansion. Hobbs established that not all cements having low contents of the above constituents were immune to DEF or vice-versa, and it was not possible to predict the susceptibility to expansion based on the cement composition alone.

Lawrence et al. (1999) presented case studies on concrete structures that showed signs of excessive cracking as early as one year after construction. Two types of noticeable cracks were noticed on the precast prestressed concrete box beams that were investigated. The first type was hairline map cracking as was observed in structures affected by ASR, while the second type of cracking, though it had a map type pattern, had cracks that were as wide as ¼ in. and were predominantly confined to the end block region of the girder. Based on a review of fabrication and material documentation, chemical analysis, petrographic examination, and scanning electron

microscopy, they concluded that the cracking was associated with DEF expansion while ASR was ruled out. During the investigation it was revealed that all other materials and storage conditions remaining the same, the box beams that were cast using ASTM Type III (high-alkali) cement showed signs of deterioration whereas those cast using ASTM Type III (low-alkali) cement did not show DEF deterioration and were declared to be sound beams.

Taylor et al. (2001) offers a good review of the developments that have been made in understanding the DEF phenomenon. The authors briefly review various topics pertaining to DEF such as temperature range, expansion, chemistry, microstructural changes, mechanism of expansion, physical chemistry of crystal growth, factors governing expansion, effect of concrete, or mortar micro structure expansion, among other relevant topics. From a review of previous work, the authors conclude that temperature was a critical factor for the formation of DEF, disputing the claim by some authors (Mielenz et al., 1995; Diamond 1996; Collepardi, 1999) that DEF can cause damage in concrete that had not experienced elevated temperatures. The authors also suggested exercising caution while extrapolating laboratory test results to field conditions. They also proposed that the traditional practice of studying expansion in mortar/concrete bars with different kinds of cement, by placing them in the same water tank was unsound. The authors noted that though a lot of studies have been conducted on DEF, it was still not properly understood (in 2001) and that the effect of the various variables that affect DEF should be studied by varying one parameter at a time.

Collepardi (2003) in his review of the stare-of-the-art of DEF attack on concrete classifies ettringite formation in concrete as Early Ettringite Formation (EEF) and DEF. EEF or primary ettringite occurs homogenously and immediately (within hours or days of a concrete pour). The related expansion does not cause localized and disruptive action as the concrete is still deformable. However, DEF occurs heterogeneously and at a later time (after months or years). The related expansion causes cracking and spalling of concrete as DEF occurs in rigid, stiff, and hardened concrete. The author further classifies DEF as External Sulphate Attack (ESA) where the environmental sulphate from water or soil penetrates the concrete structure, and Internal Sulphate Attack (ISA) where the sulphate attack occurs from the late sulphate release from gypsum-contaminated aggregates or thermal decomposition of ettringite. High permeability of concrete, sulphate-rich environment, and presence of water were identified as the necessary conditions for

ESA related DEF. For ISA related DEF, micro-cracking in concrete, late sulphate release and exposure to water were considered three essential factors.

Barbarulo et al. (2005) conducted laboratory tests on mortar bars to study if a cementitious material could develop DEF under its own heat of hydration as was reported in various field observations (e.g., Hobbs, 1999; Lawrence et al., 1999). From the experimental work the researchers observed that the heat of hydration did indeed cause the formation of DEF. This was the first time that this was confirmed in a laboratory setting, though it was widely accepted from field observations. They also conducted studies to determine if concrete steam-cured long after its hydration process would present DEF symptoms in the long term. In this regard, one-year old mortar bars were subjected to one month of steam curing at 185°F. The test samples that did and did not expand from DEF previously, expanded further when subjected to reheating. This was the first time this observation was made, and the authors concluded that the DEF phenomenon was not solely related to the high temperature during the hydration process.

Ekolu et al. (2007) experimentally studied concrete mortar specimens with microcracks induced by ASR expansion and freeze-thaw cycles; the influence of the microcracks on DEF expansion was then investigated. The presence of the microcracks resulted in an early onset of DEF and also greater expansion strains in the mortar specimens. Maximum DEF related expansions were recorded for a critical range of ASR expansion, beyond which any further increase in microcracking reduced the extent of DEF expansion.

DEF due to high heat of hydration has been reported in structures with mass pour of concrete, like various parts of bridge structures (abutments, piers, wing walls and piles as reported in Wimpenny et al., 2007), concrete blockwork walls (Eriksen et al., 2006; Baldwin and Knights, 2010), and concrete armor units (Fozein Kwanke et al., 2009) in maritime works. DEF has also been increasingly detected in combination with ASR (Ingham, 2012), which has a similar expansion and cracking pattern.

Brunetaud et al. (2008) studied the effects of DEF related expansion on the dynamic modulus. The researchers concluded that for negligible swelling (expansion < 0.04 percent) the dynamic modulus slightly improved with time and reached a plateau within 1 to 2 years. For weak swelling that resulted in linear expansion (final expansion amplitude between 0.04–0.2 percent),

the expansion rate was limited by the stiffness of the material by a linear relationship between the rate of expansion and the dynamic modulus. This behavior did not result in any notable modification of the concrete mechanical properties, at least until an expansion of 0.1 percent. Large swelling that resulted in sigmoidal expansion (final amplitude >0.4 percent), caused a decrease in the dynamic modulus. After the swelling reached its plateau, the dynamic modulus improved gradually due to filling of the previously open cracks by ettringite. The researchers observed that the compressive strength could decrease as much as 63 percent for an expansion of 1.2 percent. Pavoine et al. (2012) observed that the dynamic elastic modulus can drop (by 37 percent) in the course of inner sulphate attack. This, however, is compensated in the long term, where the formation of ettringite in the voids helps to a gradual increase in the dynamic elastic modulus.

Bouzabata et al. (2012) investigated the mechanical conditions acting on DEF expansion, including the analysis and quantification of the mechanical effects of restraint on DEF expansion. In this regard the following points on the mechanical behavior of concrete undergoing DEF expansion were analyzed: isotropy of stress-free expansion, anisotropy of expansion under restraint, and consequences of DEF expansion on compressive strength. From the experimental observation for a period of about 600 days the following conclusions were made: (a) under stress free conditions DEF expansion was isotropic; (b) compressive stresses decreased expansion due to DEF and caused cracks parallel to the restraint; (c) larger the restraint smaller was the DEF expansion observed; (d) DEF expansion in the stress-free direction of the restrained specimens remained unchanged to those of free expansion, which implied that the DEF expansion under restrained conditions was anisotropic; (e) the concrete compressive strength decreased significantly within 70 to 100 days (corresponding to significant expansion); (f) and a slight increase in compressive strength was observed after the expansion stabilized at about 180 days. The authors also noted that DEF is a more localized phenomena because once they crystalize, they cannot move easily in the cracks unlike ASR gel that can migrate in the porosity and cracks after their formation. Therefore the structural models have to take into account this localized effect to assess DEF damaged structures.

Limited literature is available on modeling the effects of DEF on reinforced concrete structures, a few of which are reviewed next.

Seignol et al. (2009) developed a new model to assess concrete structures subjected to the effects of DEF expansion. In their constitutive model, chemical degradation was represented by a prescribed expansive strain and a damage law. The variables representing the mechanical effects of DEF were explicitly dependent on the material moisture and the stress tensor. A model was also proposed to take into account the strong relationship between early-age temperature history and DEF development. Using a finite element program, the authors illustrated the application of the model on a prototype structure affected by DEF.

Martin et al. (2010) conducted an experimental investigation on concrete cylinders to compare the effects of DEF-only expansion with combined effects of DEF and ASR expansion. Higher expansion strains were recorded in specimens that were subjected only to DEF when they were immersed in water, than when they were stored in 100 percent relative humidity (RH) atmosphere. The specimens subjected to DEF-only and DEF and ASR expansion showed similar maximum expansion strains when they were immersed in water. However, the specimens with combined DEF and ASR showed slightly early onset of expansion strains compared to the DEF-only specimens. When immersed in water, the ASR contribution to the overall expansion strain of the specimens was minimal, whereas when exposed to 100 percent RH atmosphere, ASR contributed to about one-third of the overall expansion strains. This was associated with the leaching of alkalis that could occur when the specimen was immersed in water. Martin et al. (2010) hypothesized that DEF mechanism occurred prior to ASR. Based on the expansion strains that were recorded from the concrete cylinders, they proposed a model for the expansion strains due to the combined effects of DEF and ASR. Their proposed model demonstrated the respective contributions of DEF and ASR. However, all parameters in the empirical model were inferred from a least-squares fit with the experimental results.

Martin et al. (2013) presented a chemo-mechanical model to reassess structures affected by ASR/DEF expansion. Their model took into effect the coupling between the expansion and the moisture content by introducing coupling functions, thereby enabling the behavior of ASR to be simulated, as long as alkali leaching was not a factor. However, the model did not simulate the behavior of DEF affected structures. This was attributed to the inability of the model to account for the intense water uptake due to crack development in the structure.

Salgues et al. (2014) proposed a physio-chemical model to predict the kinetics and the amount of DEF in concrete subjected to curing at high temperatures. Several phenomena like the thermodynamic equilibrium of hydrate crystallization, binding of ions to hydrated calcium silicates and the mass balance equation were considered. Their model was used to simulate the free expansion test of concrete cylinders subjected to DEF using a finite element program. The computed kinetics of ettringite formation were correlated with the measured expansion on the concrete cylinder specimens.

In this work a minimalist, practical, and easy to implement approach to model the effects of DEF in reinforced concrete structures is proposed.

2.4 STRUCTURAL DETERIORATION DUE TO ASR/DEF

Ingham and McKibbins (2013) give a brief review on the causes of cracking in structural concrete. Various factors like under-design, corrosion of reinforcement, thermal contraction of fresh concrete, and ASR and DEF were identified. The authors state that serviceability issues in concrete structures were in one way or the other related to concrete cracking. While concrete cracking may not result in failure of the structure, it is usually indicative of undesirable mechanisms taking place within the concrete structure.

2.4.1 Previous Research Sponsored by TxDOT

This subsection reviews few of the latest studies that were performed to study the effects of ASR/DEF induced deterioration on large-scale reinforced concrete structural members.

TxDOT project # 12-8XXIA006

As part of the experimental study conducted at the University of Texas at Austin, Deschenes et al. (2009) conducted experimental tests on near full-scale bent cap specimen (21 × 42 × 332 in.) to study the effects of ASR/DEF deterioration on the structural capacity of these reinforced concrete members. Shear span-to-depth (a/d) ratio of 1.85 (deep beam) and 3 (sectional) was accommodated at opposite ends of each specimen. This was one of the first studies to conduct such large scale structural testing to study the effects of ASR/DEF deterioration on reinforced concrete beams. The study included two non-reactive and four reactive bent cap specimens. High-alkali Portland cement and reactive fine aggregates were used to promote ASR in the specimen. Hot mixing water and

external heaters were used to promote the formation of DEF in the specimen. The completed concrete beams were moved outdoors under conditions favorable for the development of realistic ASR and DEF damage. A sustained load was applied to replicate the impact of externally applied stresses on the propagation of ASR/DEF. The load conditioning on the specimens was maintained close to field representation. After a year of field exposure three (one non-reactive and two reactive) of the six specimens were tested in the laboratory. The results suggested that the ultimate shear strength was not diminished by ASR/DEF deterioration as long as the deteriorated concrete was actively confined by reinforcement. The longitudinal reinforcement minimized the expansion of the beam in the longitudinal direction. As a consequence, damage accumulated in the transverse direction and significant tensile strains were generated in the transverse reinforcement. After yielding the confinement potential of the reinforcement was lost leading to accelerated expansion. The minimum shear reinforcement recommended by AASHTO (2007) failed to effectively restrain the long-term expansion due to ASR/DEF. Samples extracted out of the specimen core lacked any visible signs of deterioration. Within the structural core, the confining stresses introduced by the reinforcement prevented the development of severe cracking. Tests on deteriorated concrete cylinders indicated a reduction in elastic stiffness. However, the structural test of the specimen revealed that the load response of the deteriorated specimen was equivalent to the undamaged specimen, and the loss of elastic stiffness as indicated in the material testing was not representative of the deteriorated specimen. Deschenes et al. (2009) also observed that the deflection of the deteriorated specimen at any given service load was less than the undamaged beam. ASR/DEF deterioration did not have any effect on the failure mode of the sectional or deep beam shear spans. However, the authors note that the structural safety of structures subjected to long-term exposure and related deterioration need to be further investigated.

TxDOT project #0-6491

A part of the study by Gianni et al. (2013) at the University of Texas at Austin was to determine the effects of severe deterioration caused by ASR/DEF reaction. The test specimens were similar to those by Deschenes et al. (2009); however, the reinforcement details were altered to ensure flexure failure rather than shear failure. Of the total of three specimens, one was the non-reactive specimen, and the *First* and *Second* reactive specimens, respectively, were subjected to deterioration due to ASR only and due to the combined effects of both ASR and DEF. The

deterioration data also clearly suggested that the *Second* reactive specimen, which was subjected to combined deterioration from ASR and DEF showed significantly higher expansion strains (1.25–1.95 percent at the end of 600 days) compared to the *First* reactive specimen, which was subjected to ASR only deterioration (0.65–0.84 percent at about 700 days). However, the experimental testing of the specimen demonstrated that ASR/DEF deterioration effects did not have any adverse consequences on the ultimate flexural capacity of the specimen. In fact, both the deteriorated specimens showed higher ultimate load carrying capacity and ductility compared to the non-reactive specimen. However, the yielding of the tension reinforcement in the reactive specimen occurred prior to that on the non-reactive specimen. Gianni et al. (2013) concluded that though the effects of ASR and/or DEF did not negatively impact the load carrying capacity of the structure, the deterioration caused by this mechanism could be the cause of initiation of other deterioration mechanism (like steel corrosion/rebar fracture), which could affect the load carrying capacity of the structure.

TxDOT project #0-5772

At Texas A&M University, College Station, Bracci et al. (2012) conducted experimental studies on large-scale specimens (24 × 48 × 300 in.) to evaluate the experimental behavior of critical column lap splice regions under varying levels of premature concrete deterioration due to ASR/DEF. For this study 16 large-scale column specimens with critical lap splice region were designed, constructed, subjected to deterioration (14 specimens were subjected to deterioration and 2 remained in a climate controlled laboratory and served as the control specimen), and later load tested in the laboratory. To simulate in-service gravity loading on the bridge column, unbounded post-tensioning strands were jacked to apply a total compression load of 580 kip. The specimens were instrumented internally and external strain measurements were made to monitor the concrete and reinforcing strains especially during the deterioration and load testing phases. Reactive aggregates and cement high in alkali content were used in the construction of the specimens to promote ASR in the specimen. Sodium Hydroxide (NaOH) was also used to increase the alkali content in the concrete mixture. The area of interest of the specimens was 54 in. in length on either side of the centerline, which represented the splice region. The end regions were heavily reinforced with hoops to prevent failure in this region during load testing. Electrical heating wires were used to attain the 160°F threshold temperature to promote DEF in the specimens. The

specimens were exposed to the environmental weather conditions, and supplemental water was sprinkled to accelerate ASR/DEF deterioration. Field deterioration data showed that direct sunlight had a large impact on the expansion due to ASR and minimal DEF related expansion. Due to the longitudinal restraint provided by the longitudinal reinforcement and the post-tensioning steel, the observed transverse surface strains were about 10 times larger than the longitudinal surface strains. The petrographic analysis showed that after a field exposure period of about two to three years, there was significant premature concrete deterioration due to ASR and minimal DEF was observed.

The specimens were structurally tested in two different test setups to evaluate the performance of the lap splice region. The four-point flexural load setup applied a constant moment demand and no shear demand across the entire splice region. The specimens were then subjected to a three-point flexural load test. The objective of the test was to evaluate the column splice performance by introducing large flexural moment demands that were not constant throughout the splice region, but were more critical at the middle section of the splice. Constant shear forces were also present in the splice region. The force-deformation results of the four-point flexure test showed that all the specimens had the same stiffness until first cracking. Between the first cracking and first yielding of the reinforcing steel, the deteriorated specimens were some 25–35 percent stiffer and had a slight increase in the yield strength when compared to the undamaged control specimen. Similarly, for the three-point flexural test the deteriorated specimen compared to the control specimen showed higher yield strengths and about 25–35 percent higher stiffness from post-cracking until first yield. The deterioration of the specimen due to varying levels of ASR and minimal DEF did not have any overall detrimental effects on the structural response. The increase in stiffness and strength of deteriorated specimens was attributed to the volumetric expansion of concrete due to ASR/DEF that engaged the longitudinal and transverse reinforcement for a better confinement of the core concrete. The expansion also engaged the post-tensioning reinforcement and the longitudinal reinforcement to generate additional axial compression load. However, the detrimental effects of DEF could not be studied as very minor to no DEF had formed in the specimen.

TxDOT project #0-5997

A companion study to the current research was conducted at Texas A&M University, College Station, by Mander et al. (2012) to study the effects of deterioration caused by ASR/DEF on bridge bent caps. Four large-scale specimens (one non-reactive and three reactive) were designed, constructed, and tested as part of this study. The specimen was designed as 'C' shaped beams such that one end of the specimen represented a straddle bent and the other end represented a cantilever bent. The current study being a direct extension of the work presented in Mander et al. (2012), relevant information and appropriate references are made in the chapters as and when required.

3 MODELING ASR/DEF EXPANSION IN REINFORCED CONCRETE STRUCTURES

3.1 INTRODUCTION

Alkali-Silica Reaction can be described as a chemical reaction between the alkalis in the cement and the reactive silica in the aggregates, which react to form alkali-silica gel. This gel absorbs moisture and expands causing the concrete to crack. Delayed Ettringite Formation is the formation of ettringite in hardened concrete when the concrete is subjected to high temperatures, generally greater than 160°F, during curing and is exposed to moisture later in its life. This, like ASR, causes the hardened concrete to expand and thereby induces tensile cracking.

The effects of ASR and DEF on long term concrete behavior have been studied extensively over the past few years. Studies have shown that several factors affect ASR expansion in concrete, such as alkali content of the cement, reactivity of aggregates, temperature, and humidity, among others. The majority of previous studies, however, have concentrated on the effects of ASR on plain concrete; only a few are related to reinforced concrete. It has been established that external restraint (compressive) stresses and passive restraint stresses induced by reinforcement (confinement) can significantly influence the expansion caused by ASR on reinforced concrete (Hobbs, 1988; Jones and Clark, 1996; Multon et al., 2006). The effect of DEF induced expansion on reinforced concrete also has gained significant attention in recent times. Again, there is sufficient evidence to show that externally applied stresses and/or internal restraint stresses induced by confining or longitudinal reinforcement can significantly reduce the expansion caused by DEF in reinforced concrete (Bouzabata et al., 2012).

Although extensive research has been conducted to model the expansion caused by ASR in concrete, a review of past investigations show that a majority of the work has been limited to plain concrete. The effects of compressive stresses on ASR expansion have not been solved by predictive models using the concepts of chemoelasticity (Multon et al., 2006). Additionally, most of the research combines the finite element method with the chemical mechanism to come up with a model for expansion in concrete due to ASR (Ulm et al., 2000; Li and Coussy, 2002; Capra and Sellier, 2003; to name a few). These methods are complex and difficult to effectively implement in a regular design office engineering practice.

The present study presents a minimalist semi-empirical strain-based model for the analysis of swelling strains in reinforced concrete members due to ASR/DEF expansion. The proposed model is then validated against small-scale experimental observations made on specimens cast and cured in saturated conditions in a laboratory test setting. Later, modifications are proposed to the model to account for realistic field temperature and moisture content (partial saturation) variations. Finally, the proposed model is used to simulate the expansion strains observed in field-cured large scale specimens showing signs of ASR and DEF. Considering the wide variability in the experimental data, one can observe that the proposed minimalist model is able to satisfactorily capture the expansion strains in reinforced concrete.

3.2 MODELING ASR/DEF EXPANSION IN SATURATED PRISMS

Based on an examination of experimental results, expansion over time follows the general form presented in Figure 3-1 for plain and reinforced concrete. Therefore, a semi-empirical model to estimate the expansion strains caused by the evolving ASR/DEF expansion in reinforced concrete is developed herein. A hyperbolic tangent function is proposed for the backbone equation which has the general form:

$$\varepsilon(t) = \varepsilon_{\rho}^{\max} \tanh\left\langle \frac{t - t_o}{t_r} \right\rangle \tag{3-1}$$

in which $\varepsilon(t) =$ the expansion strain in reinforced concrete due to the combined effects of ASR and DEF expansion at time t; $\varepsilon_{\rho}^{\max} =$ the maximum expansion in concrete, which is a function of reinforcement ratio ρ; $t_o =$ the initiation time when expansion due to ASR/DEF commences; $t_r =$ the "rise time" of the hyperbolic tangent line, which is the time from the beginning of ASR/DEF induced expansion to when the maximum expansion is reached along the tangent line; and $\langle \bullet \rangle$ are the Macaulay brackets, which represent a common engineering notation used to describe if $t - t_o < 0$, then $(t - t_o) = 0$. The parameters t_o and t_r are empirically determined from the experimental expansion observations.

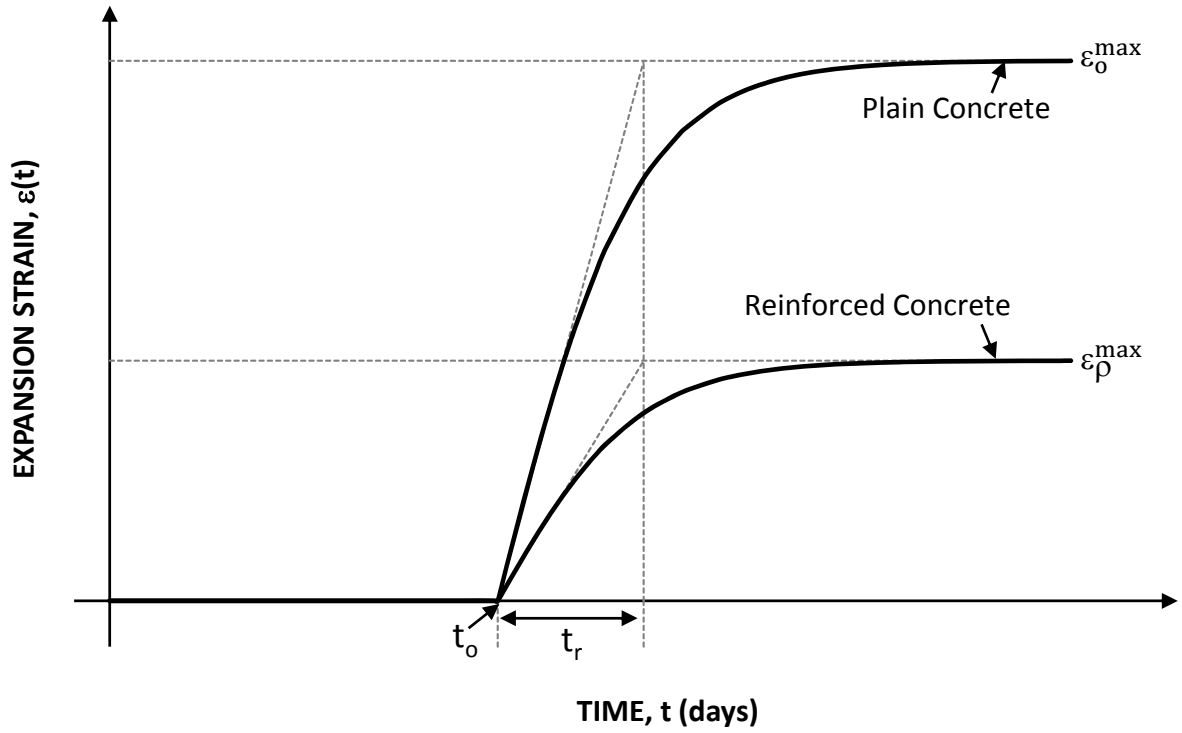

Figure 3-1: Expansion Model for ASR/DEF Induced Expansion in Concrete.

The other unknown parameter in (3-1), the maximum expansion in concrete $\varepsilon_{\rho}^{\max}$, is determined based on a strain energy approach. The strain energy density (u) of the concrete prism of area A, length L as shown in Figure 3-2a, and subjected to an axial stress, σ, is given by:

$$u = \int_0^{\varepsilon} \sigma d\varepsilon \tag{3-2}$$

where ε and σ, respectively, are the strain and stress. In the simple case, to compute the strain energy in reinforced concrete, the strain energy in concrete (U_c) and steel (U_s) needs to be calculated.

Figure 3-2b shows an equivalent elasto-plastic stress-strain relation of concrete in tension that is adopted for this study. This can be explained as follows. Consider the rectangular concrete specimen in Figure 3-2a with a single reinforcing bar running through the center of the specimen. The longitudinal free expansion of the concrete specimen is restrained by the reinforcing bar. As the ASR/DEF induced expansion within the concrete proceeds over time, the concrete reaches its maximum tensile strength and a crack forms about the mid-length of the specimen. This results in the concrete tensile strength at the crack to be zero. As further expansion occurs, the maximum concrete tensile strength is reached mid-way on either side of the cracked specimen, resulting in cracks at every quarter-point of the specimen; the next cracks form at the $1/8^{th}$ points of the concrete specimen. This phenomenon may be considered as a *divide and conquer mechanism*; accordingly the process continues until the cracks are spaced about the maximum aggregate size. At its final cracked state, as shown in Figure 3-2b, the tensile strength of concrete at the cracks will be zero, but the concrete will possess some tensile strength between the cracks. The effective saw tooth model of the tensile stress-strain relation averaged over the length of the prism of concrete can be represented by the equivalent elasto-plastic model shown in Figure 3-2b. The concrete strain energy density, which is the shaded area beneath the stress-strain curve shown in Figure 3-2b, is given as:

$$u_c = \frac{E_c}{2}\left[\varepsilon_c^{\,2} - \left\langle \varepsilon_c - \frac{\varepsilon_t}{2} \right\rangle^2\right] \tag{3-3}$$

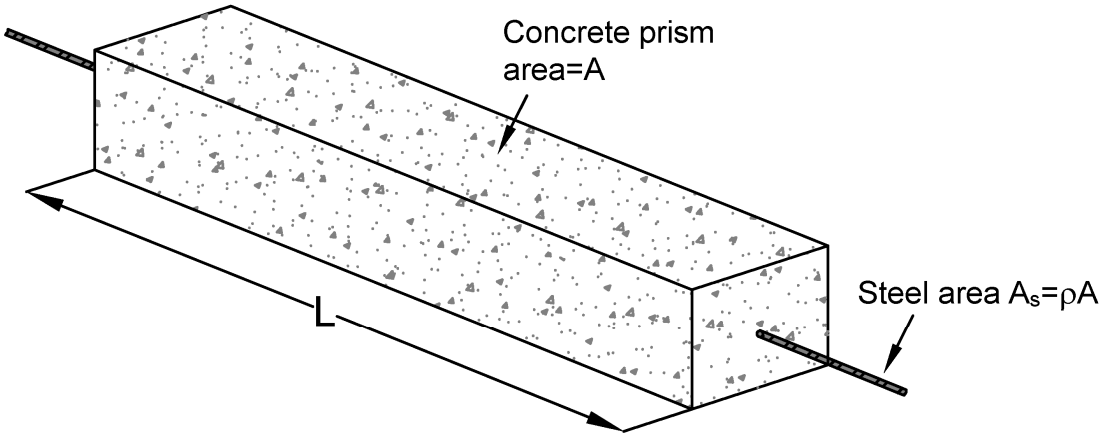

(a) Idealized Reinforced Concrete Prism Subjected to the Expansion Effects of ASR/DEF

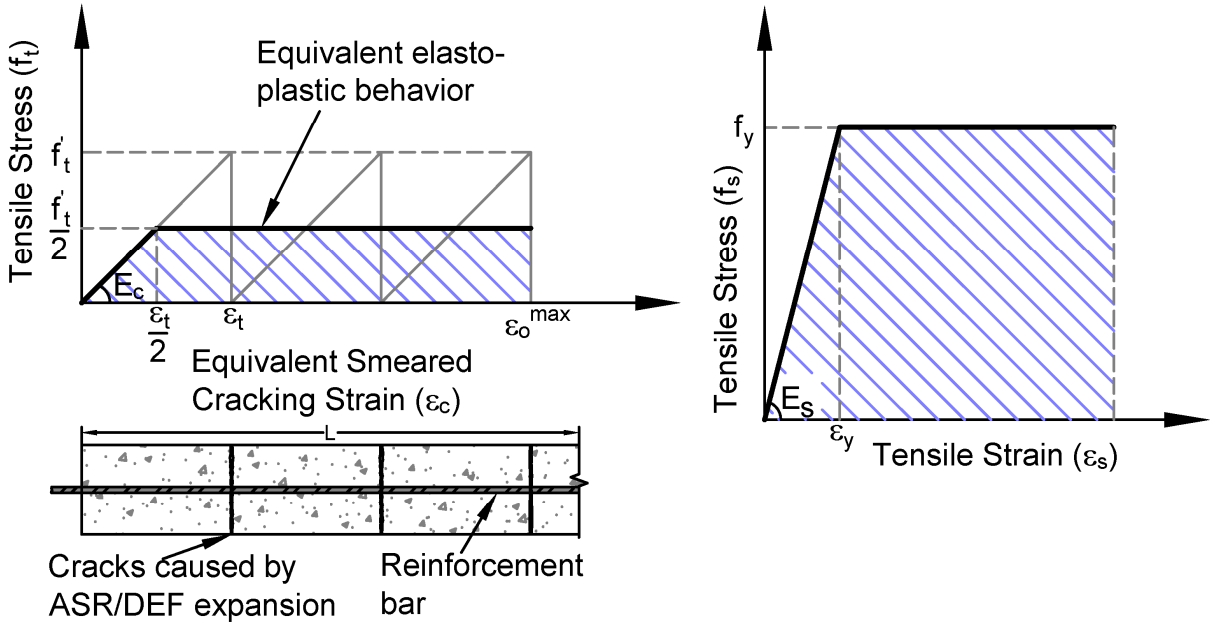

(b) Elasto-Plastic Model of Concrete in Tension

(c) Elasto-Plastic Model of Reinforcing Steel

Figure 3-2: Stress-Strain Models for Components of Reinforced Concrete.

in which E_c = Young's modulus of concrete; ε_c = tensile strain in concrete; ε_t = strain corresponding to tensile strength of concrete ($f_t^{'}$); and $\langle \bullet \rangle$ are the Macauly brackets.

Figure 3-2c shows the elasto-plastic stress-strain relation of reinforcing steel. Depending on the reinforcement ratio of the reinforced concrete structure, two cases require consideration. First, when the expansion strains caused by the combined ASR/DEF expansion are greater than the yield strain of the reinforcing steel, and second when the strains are below the yield strain. The strain energy density of steel, which is the area under the curve in Figure 3-2c, is given by:

$$u_s = \frac{E_s}{2}\left[\varepsilon_s{}^2 - \left\langle \varepsilon_s - \varepsilon_y \right\rangle^2\right] \tag{3-4}$$

in which E_s = Young's modulus of steel; ε_s = tensile strain in steel; ε_y = yield strain of reinforcing steel. When the strain is below the yield strain, the term in the Macaulay brackets $\langle \bullet \rangle$ in (3-4) vanishes.

Multiplying (3-3) and (3-4) with their respective concrete and steel volume gives the total strain energy of concrete (U_c) and steel (U_s), respectively. Using the principle of conservation of energy, the work done by ASR/DEF related expansion in plain concrete (U_{PC}) is equal to the work done by ASR/DEF related expansion in reinforced concrete (U_{RC}), that is:

$$U_{PC} = U_{RC} = U_c + U_s \tag{3-5}$$

The maximum strain in plain concrete is represented by $\varepsilon_o^{\max}$ as shown in Figure 3-2b. Assuming strain compatibility in reinforced concrete results in the same strain in concrete and steel ($\varepsilon_c = \varepsilon_s$). Making necessary substitutions in (3-5) and rearranging the terms gives the following conditional quadratic equation:

$$\frac{1}{2}\rho n \varepsilon_s^2 \left(1 - \left\langle 1 - \frac{\varepsilon_y}{\varepsilon_s}\right\rangle^2\right) + \frac{\varepsilon_t}{2}\varepsilon_s - \frac{\varepsilon_t}{2}\varepsilon_o^{\max} = 0 \tag{3-6}$$

Solving (3-6) for the two cases, Case I when the expansion strains are beyond the yield strain of the reinforcement and Case II where the expansion strains are lesser than the yield strain, respectively, gives rise to the following two equations:

For $\varepsilon_s > \varepsilon_y$:

$$\varepsilon_\rho^{\max} = \frac{\varepsilon_o^{\max}\left[1+\left(\rho n\frac{\varepsilon_y}{\varepsilon_t}\right)\left(\frac{\varepsilon_y}{\varepsilon_o^{\max}}\right)\right]}{1+\left(2\rho n\frac{\varepsilon_y}{\varepsilon_t}\right)} \tag{3-7a}$$

For $\varepsilon_s < \varepsilon_y$:

$$\varepsilon_\rho^{\max} = \frac{\varepsilon_t}{2\rho n}\left[\sqrt{1+4\rho n\frac{\varepsilon_o^{\max}}{\varepsilon_t}}-1\right] \tag{3-7b}$$

in which $\varepsilon_\rho^{\max}$ = the maximum expansion strain possible for a particular reinforcement ratio ρ. Substituting (3-7) into (3-1) gives the expression for ASR/DEF induced expansion strain with time. It is evident from the (3-1) and (3-7) that the proposed minimalist semi-empirical formulation requires only a few physical parameters, specifically $\varepsilon_o^{\max}$, t_0, and t_r. The reinforcement ratio (ρ) can be determined from the cross-section properties while the remaining parameters ε_y and ε_t can be determined knowing the reinforcing steel and concrete material properties.

However, in the presence of post-tensioning (PT) compressive loads or cracks induced by tensile loads as shown in Figure 3-3, contributions from the compressive/tensile loads toward ASR/DEF induced expansion need to be accounted for. The derivation of the related equations is shown below.

Figure 3-4a shows an equivalent elasto-plastic stress-strain relation of concrete in tension as explained earlier. In the presence of a constant compressive force (P) applied across the section, by means of a constant axial load or post-tensioned prestress, the concrete experiences a compressive strain (ε_{pc}) as shown in Figure 3-4a. This compressive effect essentially further increases resistance to the expansion caused by ASR/DEF in reinforced concrete. The concrete strain energy density, which is the shaded area beneath the stress-strain curve shown in Figure 3-4a, is given as:

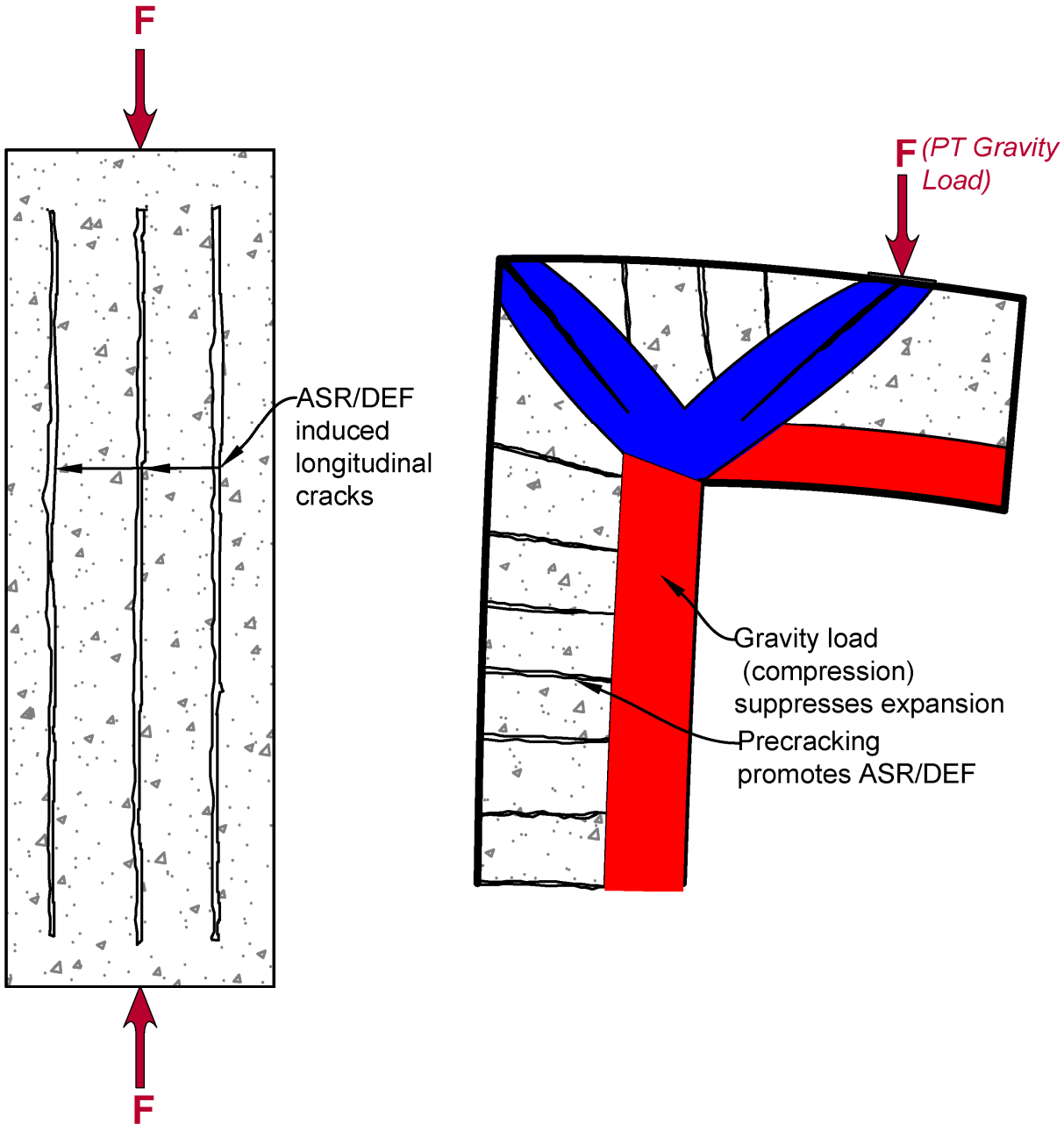

(a) Constant Axial Load due to PT Suppresses Expansion

(b) PT Gravity Load Suppresses Expansion on the Compression Side and Precracks Promotes Expansion along the Tension Side

Figure 3-3: Effects of Compressive and Tensile Loads on ASR/DEF Induced Expansion.

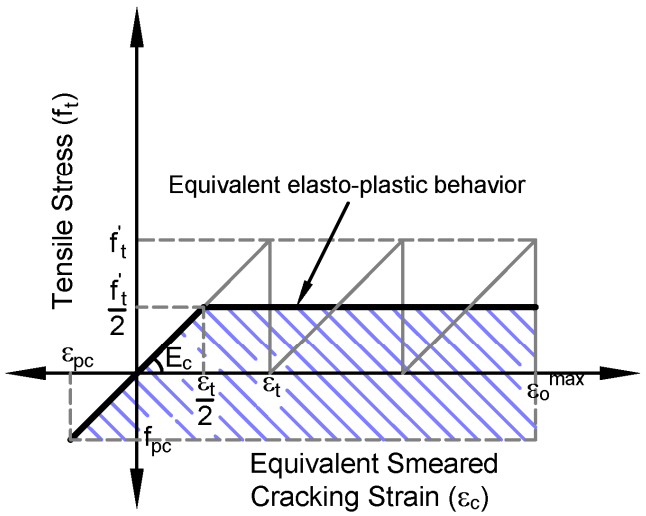

(a) Elasto-Plastic Model of Concrete in Tension Subjected to Compressive Forces

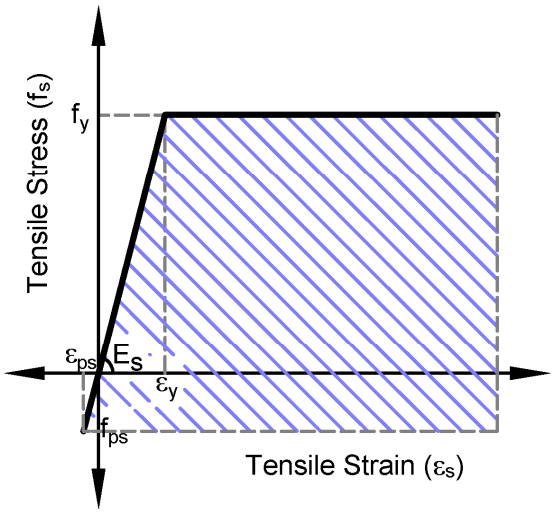

(b) Elasto-Plastic Model of Reinforcing Steel Subjected to Compressive Forces

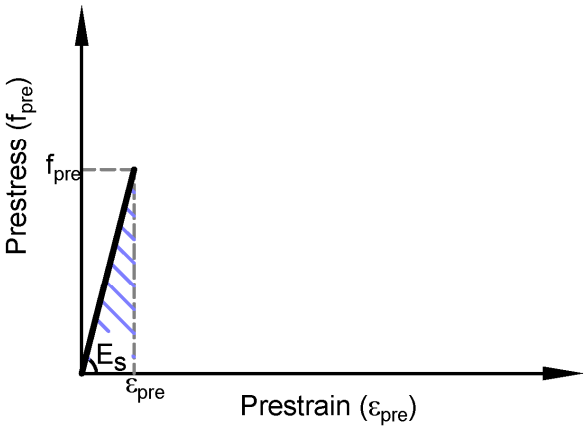

(c) Elasto-Plastic Model of Prestressing Steel

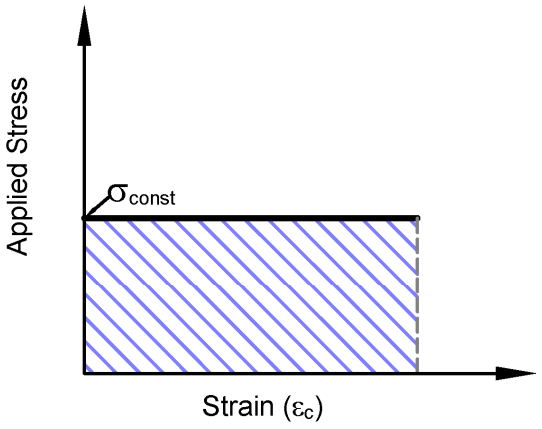

(d) Constant Applied Stress

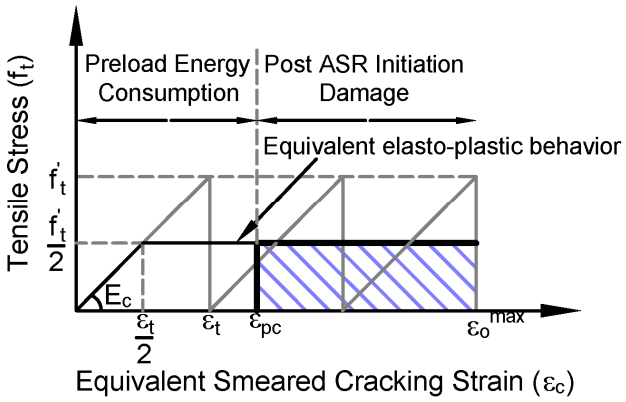

(e) Elasto-Plastic Model of Precracked Concrete in Tension

Figure 3-4: Stress-Strain Models for Various Components.

$$u_c = \frac{E_c}{2}\left[(\varepsilon_{pc} + \varepsilon_c)^2 - \left\langle \varepsilon_c - \frac{\varepsilon_t}{2} \right\rangle^2\right] \tag{3-8}$$

in which $E_c =$ Young's modulus of concrete; $\varepsilon_c =$ tensile strain in concrete; $\varepsilon_t =$ strain corresponding to tensile strength of concrete ($f_t^{'}$); and $\varepsilon_{pc} =$ compressive strain corresponding to the compressive stress in concrete $f_{pc} = P/A_c$ where $A_c =$ cross-sectional area of concrete.

Figure 3-4b shows the elasto-plastic stress-strain relation of reinforcing steel. Here again, in the presence of applied compressive force, the reinforcement experiences a compressive strain (ε_{ps}). Depending on the reinforcement ratio and the compressive load applied on the reinforced concrete structure, two cases have to be considered. First, when the expansion strains caused by ASR/DEF expansion are greater than the yield strain of the reinforcing steel, and second when the strains are below the yield strain. The strain energy density of steel, which is the shaded area in Figure 3-4b, is given by:

$$u_s = \frac{E_s}{2}\left[(\varepsilon_{ps} + \varepsilon_s)^2 - \left\langle \varepsilon_s - \varepsilon_y \right\rangle^2\right] \tag{3-9}$$

in which $E_s =$ Young's modulus of steel; $\varepsilon_s =$ tensile strain in steel; $\varepsilon_y =$ yield strain of reinforcing steel; and $\varepsilon_{ps} =$ compressive strain corresponding to the compressive stress in steel $f_{ps} = P/A_s$ where $A_s =$ total cross-sectional area of reinforcing steel.

In the presence of prestressing strands, their contribution to the strain energy density of the structure also needs to be accounted for. The strands are tensioned well below their yield strength, and the area of the shaded region under the stress-strain curve in Figure 3-4c is given as:

$$u_{pre} = \frac{E_s}{2}\varepsilon_{pre}^2 \tag{3-10}$$

in which $\varepsilon_{pre} = P/\left(E_s A_{pre}\right) =$ prestrain in the strands where $A_{pre} =$ area of prestressing strands.

Finally, the constant applied compressive force results in a constant compressive stress (σ_{const}) across the concrete structure as shown in Figure 3-4d. The strain energy density due to the constant applied stress is given as:

$$u_{const} = \sigma_{const}\varepsilon_c \tag{3-11}$$

Multiplying (3-8)–(3-11) with their respective concrete and steel volume gives the total strain energy of concrete (U_c), reinforcing steel (U_s), prestressing strands (U_{pre}), and constant stress (U_{const}). Using the principle of conservation of energy, the work done by ASR/DEF related expansion in plain concrete (U_{PC}) is equal to the work done by ASR/DEF related expansion in reinforced concrete (U_{RC}), which may or may not be subjected to a constant applied load, that is:

$$U_{PC} = U_{RC} = U_c + U_s + U_{pre} + U_{const} \tag{3-12}$$

The maximum strain in plain concrete is represented by $\varepsilon_o^{\max}$ as shown in Figure 3-4a. Assuming strain compatibility in reinforced concrete results in the same strain in concrete and steel ($\varepsilon_c = \varepsilon_s$). Making necessary substitutions in (3-12) and rearranging the terms gives the following conditional quadratic equation:

$$\frac{1}{2}\rho n\varepsilon_s^2\left(1-\left\langle 1-\frac{\varepsilon_y}{\varepsilon_s}\right\rangle^2\right)+\varepsilon_s\left(\frac{\varepsilon_t}{2}-\varepsilon_{pc}-\rho n\varepsilon_{ps}-\frac{\sigma_{const}}{E_c}\right)-\frac{\varepsilon_t}{2}\varepsilon_o^{\max}+\frac{\varepsilon_{pc}^2}{2}+\frac{\rho n}{2}\varepsilon_{ps}^2+\frac{\rho_{pre}n}{2}\varepsilon_{pre}^2=0 \tag{3-13}$$

in which $\rho = A_s/A_c =$ reinforcement ratio; $\rho_{pre} = A_{pre}/A_c =$ prestressing strand ratio; and $n = E_s/E_c =$ modular ratio. Solving (3-13) for the two cases, Case I when the expansion strains are beyond the yield strain of the reinforcement and Case II where the expansion strains are lesser than the yield strain (then $\varepsilon_y = \varepsilon_s$ in Eq. 3-13), respectively, gives rise to the following two equations:

For $\varepsilon_s > \varepsilon_y$:

$$\varepsilon_\rho^{\max} = \frac{\varepsilon_o^{\max}\varepsilon_t + \rho n\left(\varepsilon_y^2 - \varepsilon_{ps}^2\right) - \varepsilon_{pc}^2 - \rho_{pre} n \varepsilon_{pre}^2}{2\left(\frac{\varepsilon_t}{2} - \varepsilon_{pc} + \rho n\left(\varepsilon_y - \varepsilon_{ps}\right) - \frac{\sigma_{const}}{E_c}\right)} \tag{3-14a}$$

For $\varepsilon_s < \varepsilon_y$:

$$\varepsilon_\rho^{\max} = \frac{\frac{\varepsilon_t}{2} - \varepsilon_{pc} - \rho n \varepsilon_{ps} - \frac{\sigma_{const}}{E_c}}{\rho n}\left(\pm\sqrt{1 - \frac{\rho n\left(\varepsilon_{pc}^2 + \rho n \varepsilon_{ps}^2 + \rho_{pre} n \varepsilon_{pre}^2 - \varepsilon_t \varepsilon_o^{\max}\right)}{\left(\frac{\varepsilon_t}{2} - \varepsilon_{pc} - \rho n \varepsilon_{ps} - \frac{\sigma_{const}}{E_c}\right)^2}} - 1\right) \tag{3-14b}$$

In (3-13) and (3-14) ε_{pc}, ε_{ps} and σ_{const} are positive for tensile strains induced by tensile loads and negative for compressive strains induced by compressive loads. In the case where no prestressing strands are present, $\rho_{pre} = 0$. The parameters $\varepsilon_{pc}, \varepsilon_{ps}, \varepsilon_{pre}$ and σ_{const} can be determined from the applied axial load P, and corresponding cross-sectional areas. In the case of a reinforced concrete member without constant applied loads or prestress the terms $\varepsilon_{pc}, \varepsilon_{ps}, \varepsilon_{pre}$ and σ_{const} are zero.

The work done by ASR/DEF expansion on concrete is further reduced if the concrete is pre-cracked due to tensile prestrains, that is, $\varepsilon_{pc} > \varepsilon_t$. In this case the concrete strain energy density, which is the shaded area beneath the stress-strain curve shown in Figure 3-4e, is given by:

$$u_c = \frac{E_c}{2}\left[\varepsilon_t\left(\varepsilon_c - \varepsilon_{pc}\right)\right] \tag{3-15}$$

Equating the work done by ASR/DEF related expansion in plain concrete and reinforced concrete as before, the maximum expansion can be computed using the following equations:

For $\varepsilon_s > \varepsilon_y$:

$$\varepsilon_\rho^{\max} = \frac{\varepsilon_o^{\max}\varepsilon_t + \rho n\left(\varepsilon_y^2 - \varepsilon_{ps}^2\right) + \varepsilon_t\varepsilon_{pc} - \left(\frac{\varepsilon_t}{2}\right)^2}{2\left(\frac{\varepsilon_t}{2} + \rho n\left(\varepsilon_y - \varepsilon_{ps}\right) - \frac{\sigma_{const}}{E_c}\right)} \tag{3-16a}$$

For $\varepsilon_s < \varepsilon_y$:

$$\varepsilon_\rho^{\max} = \frac{\frac{\varepsilon_t}{2} - \rho n\varepsilon_{ps} - \frac{\sigma_{const}}{E_c}}{\rho n}\left(\pm\sqrt{1 - \frac{\rho n\left(\rho n\varepsilon_{ps}^2 + \rho_{pre}n\varepsilon_{pre}^2 - \varepsilon_t\varepsilon_o^{\max} - \varepsilon_t\varepsilon_{pc} + \left(\frac{\varepsilon_t}{2}\right)^2\right)}{\left(\frac{\varepsilon_t}{2} - \rho n\varepsilon_{ps} - \frac{\sigma_{const}}{E_c}\right)^2}} - 1\right) \tag{3-16b}$$

In (3-14b) and (3-16b) it is important to consider only the positive value of $\varepsilon_\rho^{\max}$ as it is an expansive strain and cannot be negative. Substituting the relevant expression for $\varepsilon_\rho^{\max}$ into (3-1) gives the expression for ASR/DEF induced expansion strain with time.

The following section investigates the influence of variation in temperature, and also the degree of saturation on the expansion caused by the ASR/DEF mechanisms in reinforced concrete.

3.3 Modifications to Account for Temperature and Moisture Variations

It is well known that the reactive material content and environmental factors such as temperature and humidity, stress conditions, boundary restraint, and moisture supply, all affect the extent of expansion rate caused by the ASR/DEF in concrete. Of these the reactive material content is implicitly taken into account when estimating the parameters $\varepsilon_o^{\max}$, t_o, and t_r. The effects of the restraints are also taken into account in the expression proposed for maximum expansion $\varepsilon_\rho^{\max}$.

To account for the effects of the other two important factors, temperature and moisture content (degree of saturation), necessary modifications to the proposed expansion equation are considered here. Implicit in the earlier development of the proposed equations were: (i) constant temperature of 100°F; and (ii) saturated conditions (water bath) were used for curing. However, the temperature and moisture content conditions of an actual structure subjected to ASR/DEF expansion may vary on a daily basis. To account for these real field temperature and moisture variations, modifications are proposed to (3-1) to include their effects.

Eq. (3-1) can be slightly modified to include the effects of temperature (T):

$$\varepsilon_{t,T} = \varepsilon_{\rho}^{\max} \tanh\left\langle \frac{t - t_o}{t_{r,T}} \right\rangle \tag{3-17}$$

where the parameters are defined as before and $\varepsilon_{\max}(\rho)$ is given by (3-7), (3-14) or (3-16).

Ulm et al. (2000) defined the characteristic time (τ_c) associated with ASR product formation as:

$$\tau_c(\theta) = \tau_c(\theta_o)\exp\left[\frac{U_c}{\theta\theta_o}(\theta_o - \theta)\right] \tag{3-18}$$

in which $\tau_c(\theta_o) =$ characteristic time at standard temperature of $\theta_o = 311°\text{K} = T_o = 38°\text{C}$ (100°F) and $U_c = 5400 \pm 500°\text{K}$ = activation energy constant of the characteristic time τ_c. $(\theta_o - \theta)$ °K can be re-written as $(T_o - T) = -\Delta T$ °C (say). By the definition of the two terms τ_c and t_r, $t_r \approx 2\tau_c$. Therefore, the rise time of the tangent line (t_r) is assumed to follow the same relation as (3-18) proposed by Ulm et al. and is given by:

$$t_r(\theta) = t_r(\theta_o)\exp\left[\frac{U_c}{\theta\theta_o}(\theta_o - \theta)\right] \tag{3-19}$$

Substituting for $\theta = \theta_o + \Delta T$, $U_c = 5400°\text{K}$ and as $\Delta T \ll \theta_0$ (=311°K) then $\Delta T/\theta_o \to 0$, thus (3-19) may be simplified to give:

$$t_{r,T} = t_{r,T_o} \exp\left(\frac{T_o - T}{18}\right) \tag{3-20}$$

Finally substituting $T_o = 38°C$ in (3-20) leads to:

$$t_{r,T} = t_{r,T_o} \exp\left(\frac{38 - T}{18}\right) \tag{3-21}$$

which may now be substituted into (3-17) to give:

$$\varepsilon_{t,T} = \varepsilon_{\rho}^{\max} \tanh\left[\exp\left(\frac{T - 38}{18}\right)\left\langle\frac{t - t_o}{t_{r,T_o}}\right\rangle\right] \tag{3-22}$$

Eq. (3-22) gives the modified expression for the expansion caused by ASR/DEF in reinforced concrete taking into consideration the temperature variations.

To account for the variations in moisture content, necessary modifications to (3-22) need to be made. Figure 3-5 shows the variation of characteristic time (τ_c) at 311°K with the degree of saturation (S), where the data points are adopted from Ulm et al. (2000). The experimental data can be reasonably well represented by the exponential function e^{1-S}. Incorporating this into the modified equation (3-22) leads to the following overall time-dependent expansion strain model:

$$\varepsilon_{t,T,S} = \varepsilon_{\rho}^{\max} \tanh\left[\exp\left(\frac{T}{18} + S - 3.11\right)\left\langle\frac{t - t_o}{t_{r,T_o}}\right\rangle\right] \tag{3-23}$$

Eq. (3-23) represents the proposed model modified for temperature and moisture content variations, for expansion strains in reinforced concrete caused by ASR/DEF expansion. Note that at standard temperature of 38°C (100°F) and degree of saturation of $S = 1$, (3-23) reverts back to (3-1).

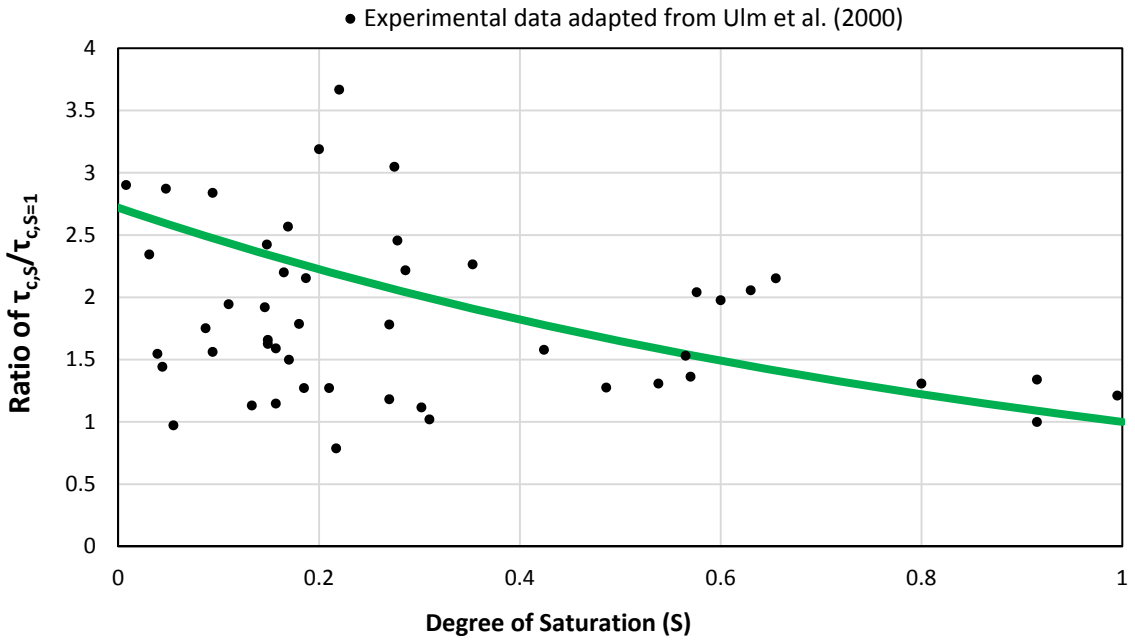

Figure 3-5: Variation of Characteristic Time with Relative Weight Increase.

Differentiating (3-23) with respect to time gives the expansion strain rate as follows:

$$\frac{d\varepsilon_{t,T,S}}{dt} = \dot{\varepsilon}_{t,T,S} = \frac{\varepsilon_{\rho}^{\max}}{t_{r,\mathrm{T}_o}} \exp\left(\frac{\mathrm{T}}{18} + S - 3.11\right)\left[1 - \left(\frac{\varepsilon_{t,T,\mathrm{S}}}{\varepsilon_{\rho}^{\max}}\right)^2\right] \tag{3-24}$$

which is an ordinary differential equation with variable coefficients dependent on temperature and degree of saturation, T and S. Because in field conditions T and S vary constantly, (3-24) requires a numerical solution as follows:

$$\varepsilon_{i+1} = \varepsilon_i + \left(\dot{\varepsilon}_{t,T,S}\right)_i \Delta t \tag{3-25}$$

in which $\Delta t =$ time increment and the parameters with subscript i denote their value at the i^{th} time interval; and $\left(\dot{\varepsilon}_{t,T,S}\right)$ is the temperature and saturation dependent strain rate given by (3-24). Eq. (3-25) can be easily solved computationally in an incremental time-stepping fashion. Daily temperatures and degree of saturation (assessed from rainfall records) are used directly in (3-24).

3.4 Validation of Proposed Model for ASR Related Expansion

The proposed expansion equation is validated against the experimental observations from Hobbs (1988) and Jones and Clark (1996), in which, expansion was caused by ASR in saturated reinforced concrete specimens. In the laboratory tests conducted by Hobbs, and Jones and Clark, the specimens were moist cured at a constant temperature of 68°F and 100°F, respectively. The literature does not provide all the information required as input for the proposed model. Therefore, typical values for the unknown parameters are assumed in the following. In Figure 3-6 the experimental data are plotted as data points, and the solid lines represent the results from the proposed model.

Figure 3-6a and b show a comparison of the experimental data with the results from the proposed semi-empirical model for Series I and II respectively, of Hobbs (1988). For Series I $\varepsilon_o^{\max} = 0.005$ and $t_r =$ 5 days were adopted based on the experimental observations, and a modular ratio of $n = 20$, about three times the typical values of modular ratio, was assumed to account for creep effects in the reinforced concrete specimen. The value of reinforcement yield strain

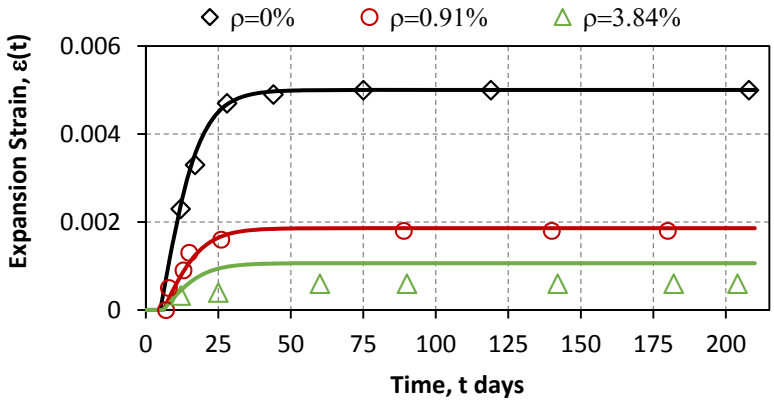

(a) Hobbs (1988)-Series I

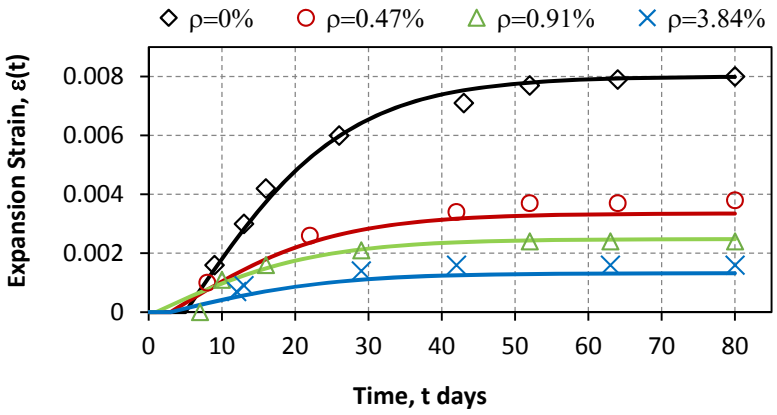

(b) Hobbs (1988)-Series II

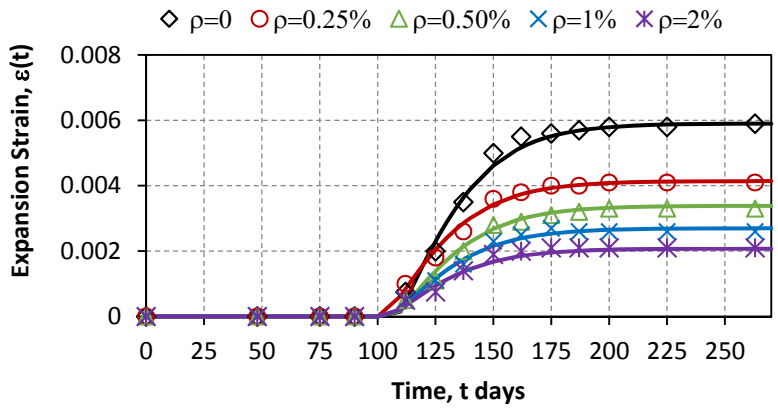

(c) Jones and Clark (1996)

Note: Experimental data points are shown as symbols, and solid lines are derived using the proposed model.

Figure 3-6: Model Validation for ASR Expansion with Experimental Data in Reinforced Concrete.

ε_y = 0.0022, and concrete tensile strain corresponding to f_t', $\varepsilon_t' = 0.1\varepsilon_{co}$ = 0.0002 (Karthik and Mander, 2011) were assumed. For Series II, values of $\varepsilon_o^{\max} = 0.008$, $t_r = 8$ days and the modular ratio $n = 20$ (that includes creep effects) were adopted. Similar to Series I, values of $\varepsilon_y = 0.0022$ and $\varepsilon_t' = 0.0002$ were assumed.

Figure 3-6c shows a comparison of the experimental and analytical results that were obtained for the experimental tests conducted by Jones and Clark (1996). In this case $\varepsilon_o^{\max}$ = 0.0059, $t_r = 39$ days and the modular ratio $n = 20$ (that includes creep effects) were adopted. The value of yield strain $\varepsilon_y = 0.0022$ is assumed, and the tensile fracture strain is estimated from $\varepsilon_t' = f_t'(1 + c_f)/E_c = 0.0004$, were $f_t' = 7.5\sqrt{f_c'(\text{psi})}$; $E_c = 57000\sqrt{f_c'(\text{psi})}$; and c_f = 2 is the creep coefficient.

The results presented in Figure 3-6 suggest that if reasonable values are adopted for the few parameters that are required for the proposed model, an adequate prediction can be made for the expansion caused by ASR reaction in reinforced concrete.

3.5 Validation of Proposed Model for DEF Related Expansion

Limited relevant data are available for studying DEF related expansion in reinforced concrete. Bouzabata et al. (2012) studied the effects of restraints on DEF induced expansion in concrete. In their experimental study, 1.6 × 1.6 × 6.3 in. ($b \times d \times l$) concrete prism specimens were subjected to expansion caused by DEF, and restrained by a setup that was composed of two stainless steel plates connected by four threaded stainless steel bars. To obtain different restraint levels, threaded bars consisting of either 0.08 or 0.20 in. diameter were used. Although the restraints in this study were provided externally, their effect in restraining the expansion caused by DEF in concrete can be considered similar to that of the reinforcement in concrete. The expansion strains obtained over time from this study, plotted as data points in Figure 3-7, show similar expansion characteristics as shown by ASR induced strains in reinforced concrete, so the same equation is used to model the expansion strains caused by DEF in concrete.

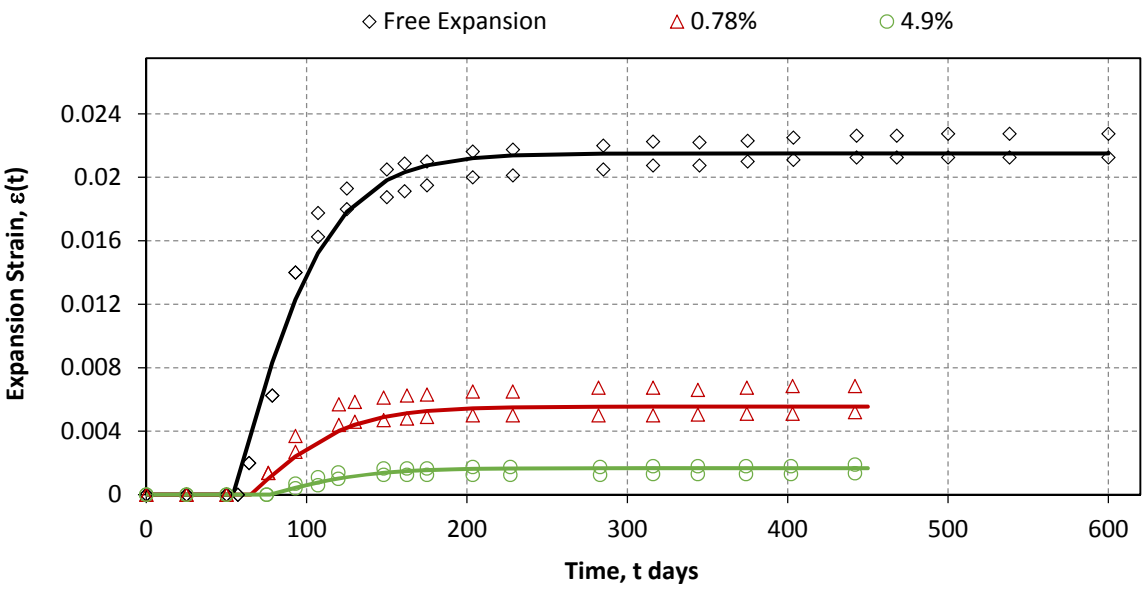

Note: Experimental data points are shown as symbols, and solid lines are derived using the proposed model.

Figure 3-7: Model Validation for DEF Expansion with Experimental Data (Bouzabata et al., 2012) in Reinforced Concrete.

The following parameters were identified from the experimental observations to model the expansion strains: $\varepsilon_o^{\max} = 0.0215$ and $t_r =$ 60 days. In this study concrete with compressive and tensile strength of $f_c' = 6.7$ ksi and $f_t' =$ 0.35 ksi, respectively, and 304 stainless steel with yield strength of $f_y =$ 40.6 ksi were used (Multon, 2013). The properties required for the model were calculated to be $\varepsilon_y = 0.00145$ based on $E_s = 28000$ ksi, $n = 17$ (that includes creep effects), and $\varepsilon_t' = 0.00013$. Figure 3-7 shows a comparison of the experimental data with the proposed model results. It is evident that the proposed model simulates well the DEF induced expansion in concrete.

From Figure 3-6 and 3-7 it is clear that the proposed minimalist semi-empirical model can be used efficiently to simulate the expansion strains caused by ASR/DEF in reinforced concrete members. Additionally, the model requires very limited input data.

In each of the above laboratory studies, the specimens were cured at a constant temperature and saturated conditions to accelerate the ASR and DEF reactions. The following section demonstrates how the developed theory can be used to obtain a reasonable prediction of the expansion strain in post-tensioned reinforced concrete members, which are exposed to environmental conditions, and as a result subjected to the daily variations in temperature and moisture content.

3.6 Application of Proposed Model to Post-Tensioned Reinforced Concrete Column Specimen

The proposed model for ASR/DEF related expansion in reinforced concrete members subjected to field conditions under varying temperature and moisture content is validated against the expansion results recorded by the experimental program conducted by TxDOT sponsored research in project 0-5772 (Bracci et al., 2012). The purpose of that experimental study was to investigate the impact of ASR/DEF related expansion in columns within lap splice regions. As part of the study, large-scale column specimens were designed, constructed, subjected to ASR/DEF related deterioration, and tested to failure under a 4-point bending setup. High alkali content cement and aggregates with reactive silica along with sodium hydroxide in the mix water were used to incorporate the necessary ingredients to promote ASR expansion in a laboratory setting. To promote DEF related

expansion in the specimen, each specimen was subjected to curing temperatures in excess of 160°F by means of an electrical resistive wiring setup. After curing, each specimen was conditioned in an outdoor environment subject to the daily variation of temperature and humidity for varying periods of up to 5 years. To further accelerate the ASR/DEF related expansion in the specimen, all specimens were wetted for 15 minutes, four times per day by a sprinkler system that was installed.

The cross-section and the reinforcement details of the column specimens are shown in Figure 3-8. The column specimens were prestressed using unbonded post-tensioned strands to simulate in-service gravity load effects. The expansion data in the column specimen, primarily from the splice region, were collected on a regular basis from the strain and concrete gages embedded in the specimen and DEMEC points on the surface of the specimen. In the following, the expansion results obtained from the proposed model are compared to the measured expansion data.

The data collected from the specimen DEMEC points were categorized into two sets as shown in Figure 3-9a. One set of data was collected in the longitudinal and transverse direction on the specimen large face (48 in. wide), and the second set was collected in the transverse direction on the specimen small face (24 in. wide). The reinforcement ratio in the small and large face has to be computed to model the expansion results. The variation of maximum expansion $(\varepsilon_{\rho}^{\max})$ with the reinforcement ration (ρ) is shown in Figure 3-9b. It is clear from Figure 3-9b that the expansion strains decrease with an increase in the reinforcement ratio. It is also evident from Figure 3-9b that the presence of the compressive loads significantly reduces the maximum expansion. Figure 3-9c shows the variation of observed daily average temperature for the period the specimen was exposed to the field conditions.

All of the data required to model ASR/DEF related expansion results are not available from the literature. Therefore, certain assumptions are made based on the experimental observations that were made on the C-Beam specimen from a study by Mander et al. (2012), where the same materials were used in the specimen construction. From the experimental results reported by Mander et al. (2012), the rise time of the tangent line at standard temperature $t_r(\theta_0)$ was assumed as 120 days. Since no data were available on the expansion caused in plain concrete ($\varepsilon_o^{\max}$), this

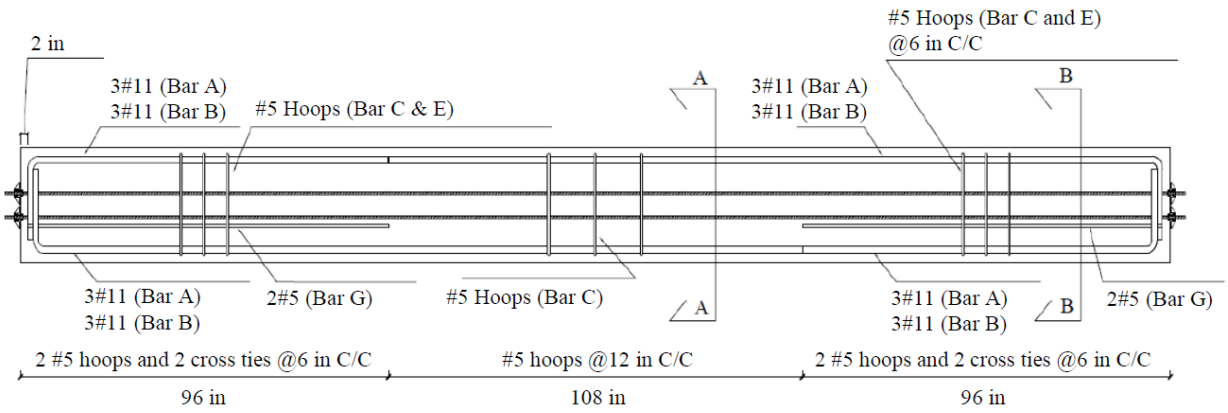

(a) Reinforcement Layout

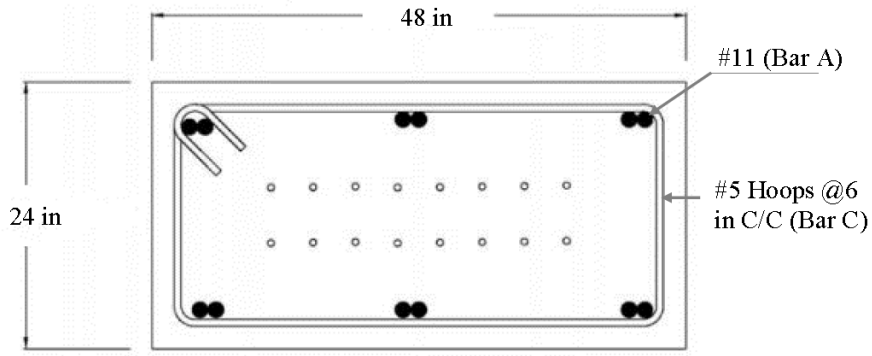

(b) Section A—A: Splice Region

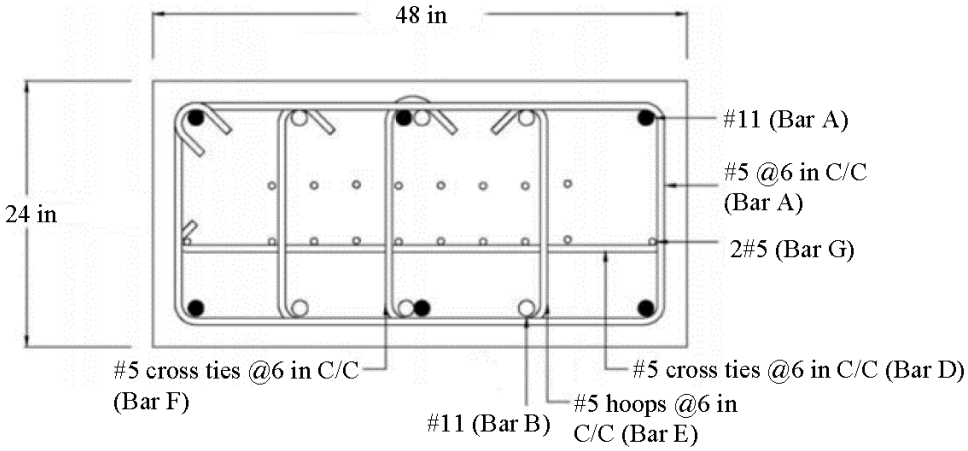

(c) Section B—B: End Region

Figure 3-8: Reinforcement Details of Splice Column Specimen.

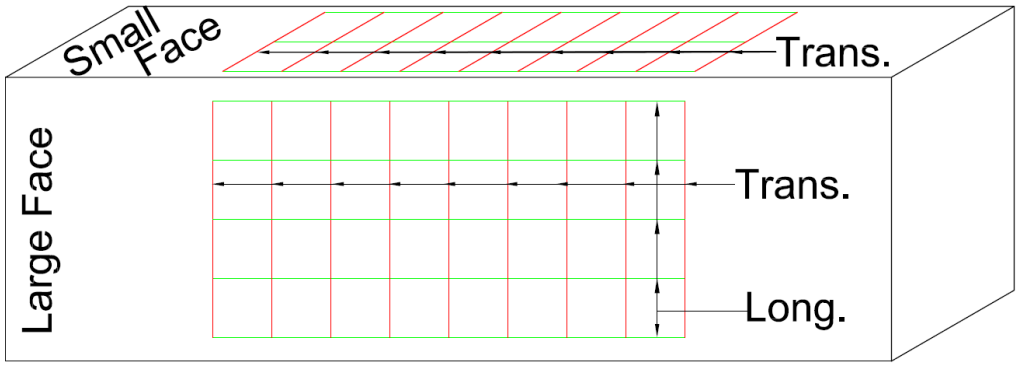

(a) DEMEC Layout on Splice Column Specimen

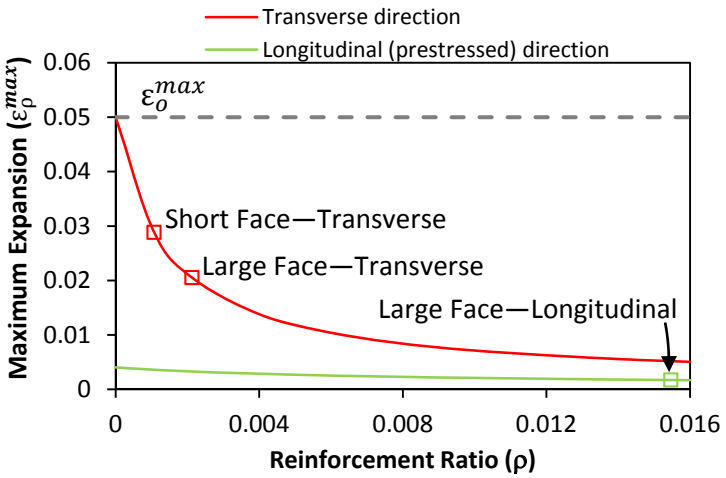

(b) Variation of Maximum Expansion with Reinforcement Ratio

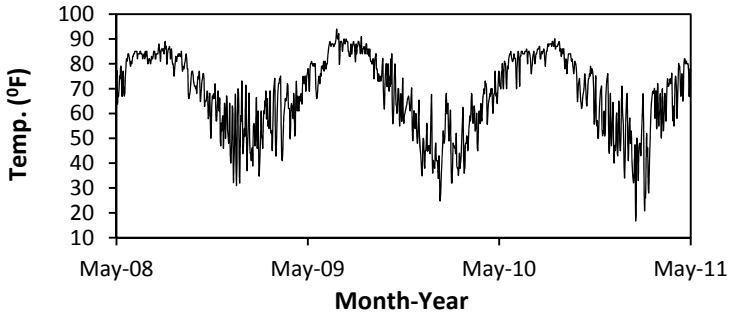

(c) Observed Average Daily Temperature

Figure 3-9: Information Pertinent to Model Expansion Strains in Splice Column Specimens.

parameter is deduced from the largest crack observed on the C-Beam specimen from an unreinforced part of the specimen. The largest crack that was observed at the knee-joint of the C-Beam specimen was about 1.18 in. wide, where the top face of the column in the joint region was essentially unreinforced. A crack width of 1.18 in. across a section with a total width of 24 in. results in an expansion strain of approximately 0.05. Hence a value of $\varepsilon_o^{\max} = 0.05$ is adopted in this study to model the ASR/DEF related expansion. Based on the experimental results reported by Bracci et al. (2012) the time t_o when expansion strains initiate was deduced to be 130 days.

Figures 3-10 to 3-12 present a comparison of the model results with the experimental data obtained from the column specimen. Of the 14 total specimens that were exposed to the accelerated environmental deterioration program, three specimens (Specimens 4, 8, and 12) are used herein to compare the model expansion results with the experimental results as these specimens were exposed to the field conditions for lengthy time periods. Of the three specimens, the concrete compressive strength at the time of testing of the specimen was reported for only Specimen 8, as the other two specimens were still being subjected to the deterioration program. An average compressive strength of $f_c^{'} = 5.3$ ksi that was reported for Specimen 8 was adopted for this study. Based on this the concrete parameters were computed as $E_c^{actual} = 4368$ ksi, $f_t^{'} = 0.55$ ksi, and $\varepsilon_t = 0.000125$. The reinforcing steel that was used in the study was reported to have a yield strength of 65 ksi, which resulted in a yield strain of $\varepsilon_y = 0.0022$. Taking into account the creep effects of concrete, $E_c = 1456$ ksi, which results in a modular ratio of $n = 19.9$ being adopted. The degree of saturation assumed was S=0.2.

Figure 3-10 shows the growth of the expansion strain with time in the longitudinal direction of the specimen large face and a comparison of the model with the field observations. In the longitudinal direction of the specimen large face, the reinforcement ratio of reinforcing steel and the post-tensioning strands is computed as $\rho = 0.0155$ and $\rho_{pre} = 0.003$, respectively. In addition to the material properties presented earlier, additional parameters are computed to determine the maximum expansion possible due to the application of the post-tensioning force in the longitudinal direction. The total post-tensioned prestress force applied to the beam was 580.5 kip, which results in a constant stress of $\sigma_{const} = 0.504$ ksi. The prestressing strands were stressed to $0.7 f_{pu} = 168$ ksi,

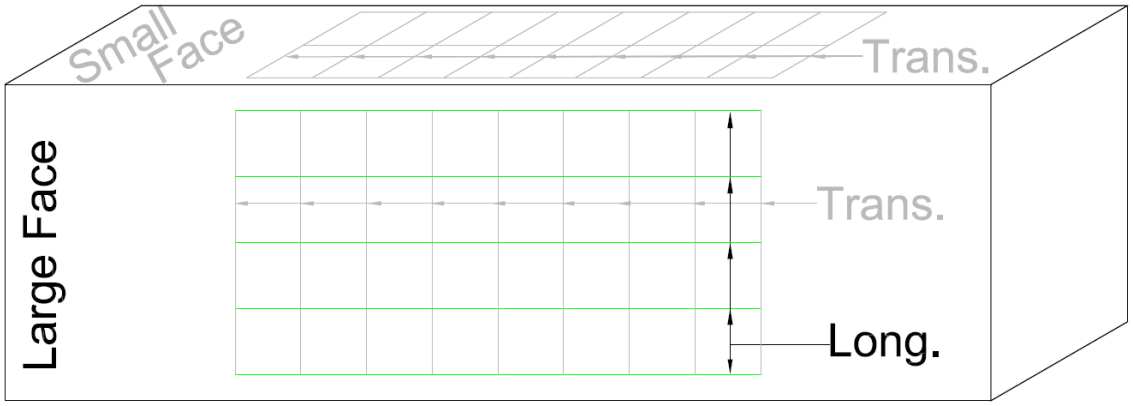

(a) DEMEC Layout on Splice Column Specimen

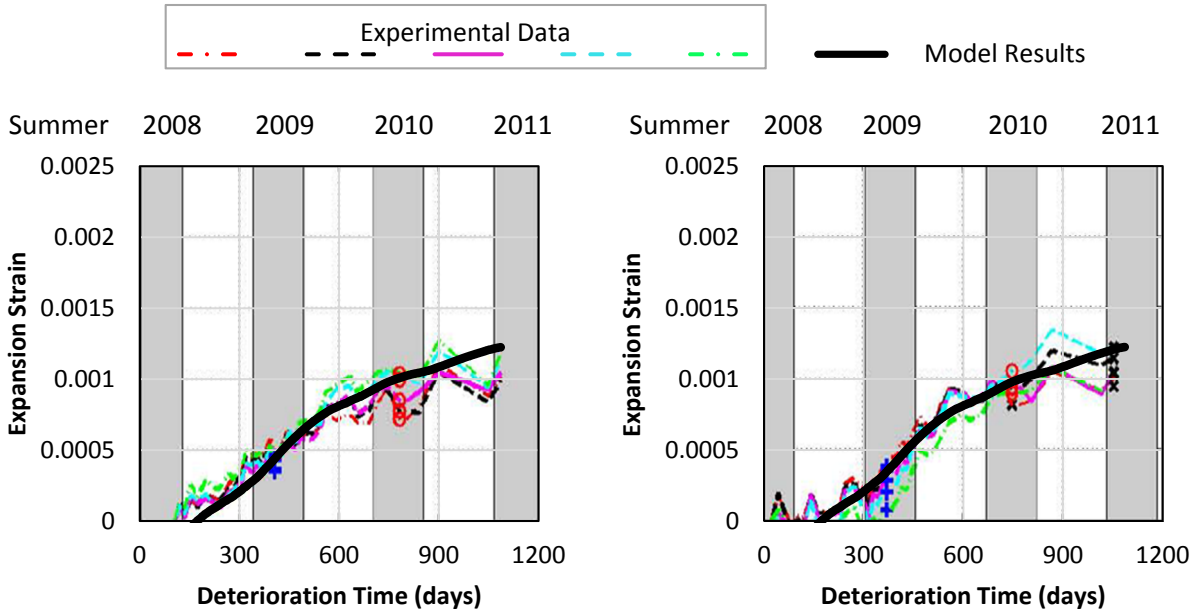

(b) Specimen 4

(c) Specimen 8

Figure 3-10: Comparison of Experimental and Model Strain Propagation Results on Specimen Large Face—Longitudinal Direction.

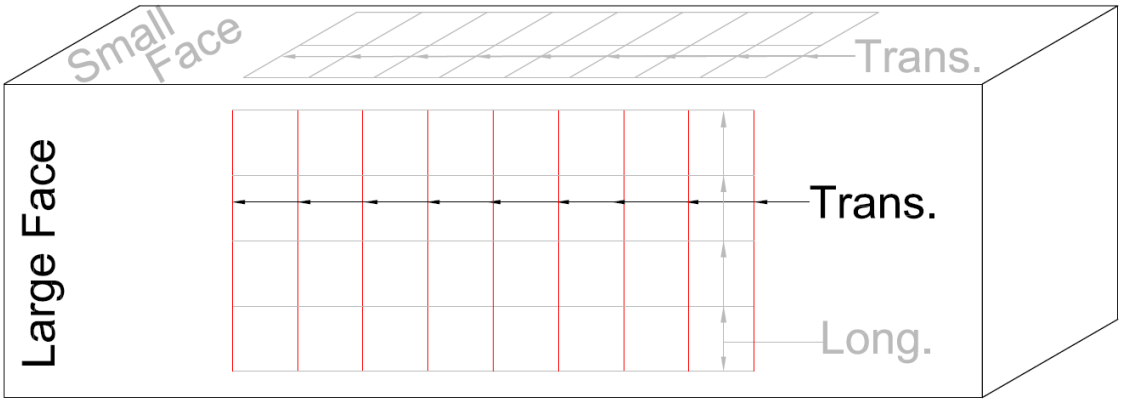

(a) DEMEC Layout on Splice Column Specimen

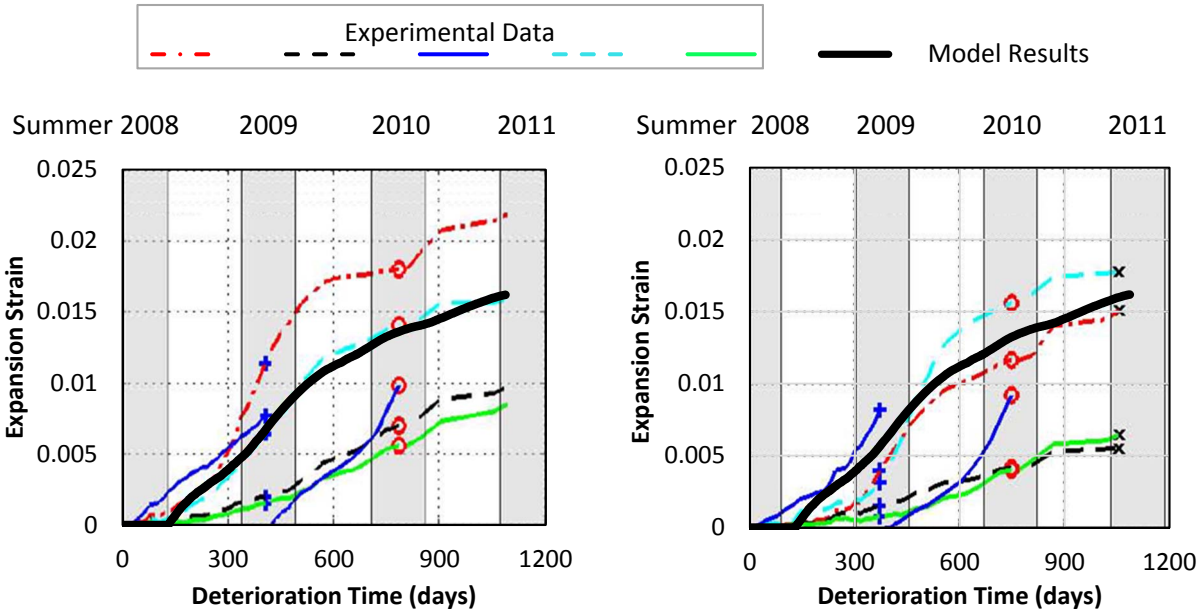

(b) Specimen 4

(c) Specimen 8

Figure 3-11: Comparison of Experimental and Model Strain Propagation Results on Specimen Large Face—Transverse Direction.

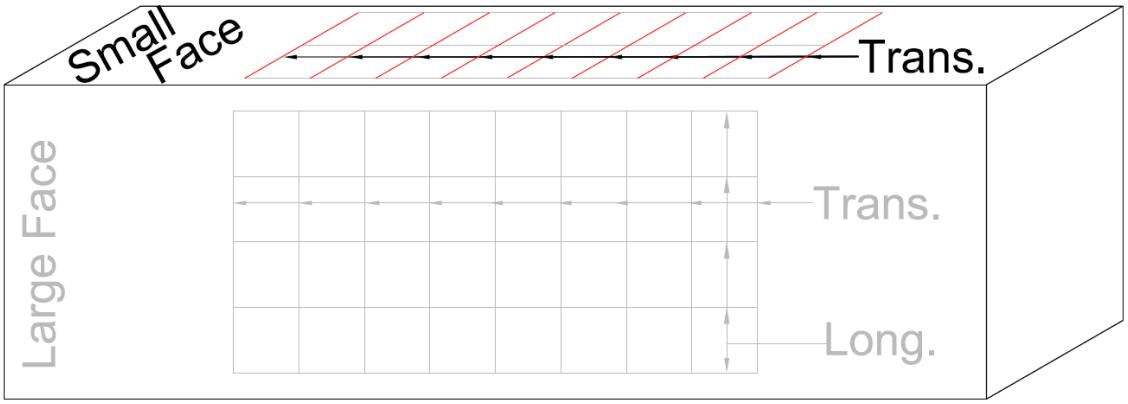

(a) DEMEC Layout on Splice Column Specimen

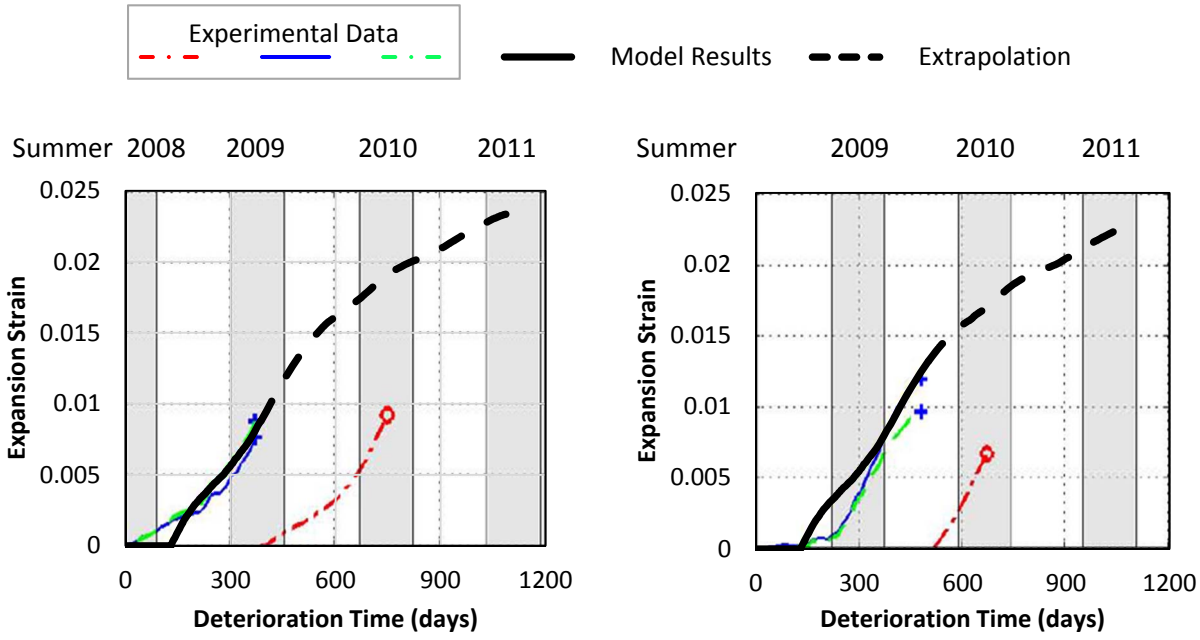

(b) Specimen 8

(c) Specimen 12

Figure 3-12: Comparison of Experimental and Model Strain Propagation Results on Specimen Small Face—Transverse Direction.

which resulted in $\varepsilon_{pre} = 0.0058$. Based on the axial load P, and the cross-section area of concrete and steel the compressive strains in concrete and steel, respectively, were determined as $\varepsilon_{pc} = 0.00012$ and $\varepsilon_{ps} = 0.00112$. Because the applied PT force does not lead to yielding of the longitudinal reinforcing steel, Eq. (3-14b) is used to determine the maximum expansion, which was calculated to be $\varepsilon_{\rho}^{\max} = 0.0017$.

Figures 3-11 and 3-12 show the growth of the expansion strain with time in the transverse direction of the specimen large face and small face, respectively. A comparison of the model with the field observations is also shown. The reinforcement ratio in the transverse direction on the large face and short face, respectively, are computed as $\rho = 0.0021$ and 0.0011. The parameters $\varepsilon_{pc} = \varepsilon_{ps} = \varepsilon_{pre} = \sigma_{const} = 0$ as the longitudinal post-tension force does not have any impact on the ASR/DEF related expansion in the transverse direction. Based on these properties, the maximum possible strain due to ASR/DEF related expansion (using 3-14a) is computed to be $\varepsilon_{\rho}^{\max} = 0.0205$ and 0.0288, respectively, for the large face and the short face.

3.7 DISCUSSION

Figures 3-10 to 3-12 present a comparison of the ASR/DEF related expansion simulated by the proposed model with the experimental data on post-tensioned reinforced concrete members. The simulation of expansion strains in the longitudinal direction was more complicated compared to the transverse strains, because of the PT force that further restrains ASR/DEF induced expansion in the longitudinal direction. The expansion strains have to overcome the prestrain in concrete to result in any expansion strains measured at the DEMEC points. Hence, the concrete prestrain ($\varepsilon_{pc} = 0.00012$) was deducted from the final expansion strains obtained. This results in a slightly delayed start to the expansion strains as shown by the field data and the simulation results in Figure 3-10. It is also evident from Figure 3-10 that the expansion results from the model compare well with the field data collected from the column specimen.

The post-tensioning forces do not have any impact on the ASR/DEF induced expansion caused in the transverse direction, and hence the model computations are straight forward. Figure 3-11 shows the transverse expansion strains along the large face of the specimen. The proposed model simulates the expansion caused in the outer two sets of DEMEC points quite well.

Figure 3-12 shows a comparison of the modeled expansion results with the field data for the expansion strains in the transverse direction of the specimen small face. In this case the field data were collected for just under 400 days. The field data for Specimen 8 indicate that expansion strains were observed from day 1 of the deterioration period. However, for the simulation results the expansion initiation time was maintained at $t_o = 130$ days to be consistent. Again reasonable agreement is evident between the simulated results and the observed field data.

Considering the complex nature of ASR/DEF related expansion in reinforced concrete and the vagaries associated with the expansion data gathered from the field, Figures 3-10 to 3-12 show that the proposed model can be used to simulate the expansion strains in reinforced concrete with or without PT forces with reasonable accuracy.

3.8 CLOSURE AND KEY FINDINGS

The existing models on predicting the expansion caused by ASR/DEF are limited mainly to plain concrete. Additionally, they are complex and typically require a finite element model to implement their effects on structures. In this chapter a semi-empirical minimalist model was proposed that is capable of estimating the expansion in reinforced concrete structures caused by ASR/DEF. The model requires only a limited number of input factors that are related to the expansion characteristics and the material properties. The key findings from this study are summarized below:

- The proposed model can simulate the expansion caused by ASR and/or DEF in laboratory specimens cured under standard laboratory conditions to accelerate ASR/DEF expansion.

- It is necessary to extend the basic laboratory based model to take into account the widely varying field conditions in temperature and moisture (degree of saturation).

- The effects of compressive and tensile pre-strains are included in the model. This is an important aspect as compressive forces suppress the expansion caused by the ASR/DEF mechanisms, whereas tensile forces and initial cracking further promote and accelerate the ASR/DEF induced expansion.

- By taking into account the appropriate reinforcement ratios, the proposed model is able to simulate the expansion strains in both the longitudinal and transverse directions.

- Considering the spread of surface expansion strains observed, the model provides a very satisfactory estimate of the expansion strain in the reinforced concrete specimens exposed to field conditions with varying temperature and humidity conditions.

4 DETERIORATION DATA OF LARGE-SCALE SPECIMEN WITH HEAVY ASR/DEF DETERIORATION

4.1 INTRODUCTION AND SCOPE

As part of the present investigation reported earlier by Mander et al. (2012), four C-Beam specimens each based on the same design were constructed, of which one (Specimen 1) was the control specimen and three others (Specimens 2, 3, and 4) were conditioned outdoors in a natural (but accelerated moisture) Texas environment. Specimens 2 and 4 were conditioned outdoors for a period of nine months and two years, respectively. The level of deterioration observed in Specimens 2 and 4 were classified as *slight* and *moderate.* The field observations from Specimens 2 and 4 have been reported in part in Mander et al. (2012) and Liu (2012). Specimen 3 was further subjected to outdoor conditioning for a total of five years. During this period the deterioration data from Specimen 3 were routinely collected from the concrete gages (KM), strain gages (SG), and DEMEC points on the specimen surface. This chapter presents the deterioration data that were collected from Specimen 3 for a period of just over five years. The deterioration data from Specimen 4 are presented in Mander et al. (2012), and for the sake of completeness, the deterioration data from Specimen 2 will also be presented herein.

4.2 VISUAL INSPECTIONS AND OBSERVATIONS OVER TIME

The condition of Specimen 3 at the end of the five-year exposure period is shown in Figure 4-1. It is evident from the figure that the specimen is excessively cracked, and the damage by ASR/DEF deterioration can be categorized as being *heavy.* The width of the widest crack observed on the north face of the specimen was measured to be 1.18 in. A similar crack was observed on the south side of the specimen and was measured to be 0.43 in. wide. The difference in the extent of damage due to ASR/DEF on the north and south face is attributed to the variation in the amount of moisture that was available from the sprinkler system to promote ASR/DEF expansion.

Figure 4-2 presents the crack pattern that was recorded for Specimen 3 at different time periods of its exposure. The cracks that were observed at Day 0 (first day of exposure) were imposed load-induced cracks caused by the tie-bar loads that were applied to simulate gravity loads. With field conditioning the map cracking that was induced by the ASR expansion in the

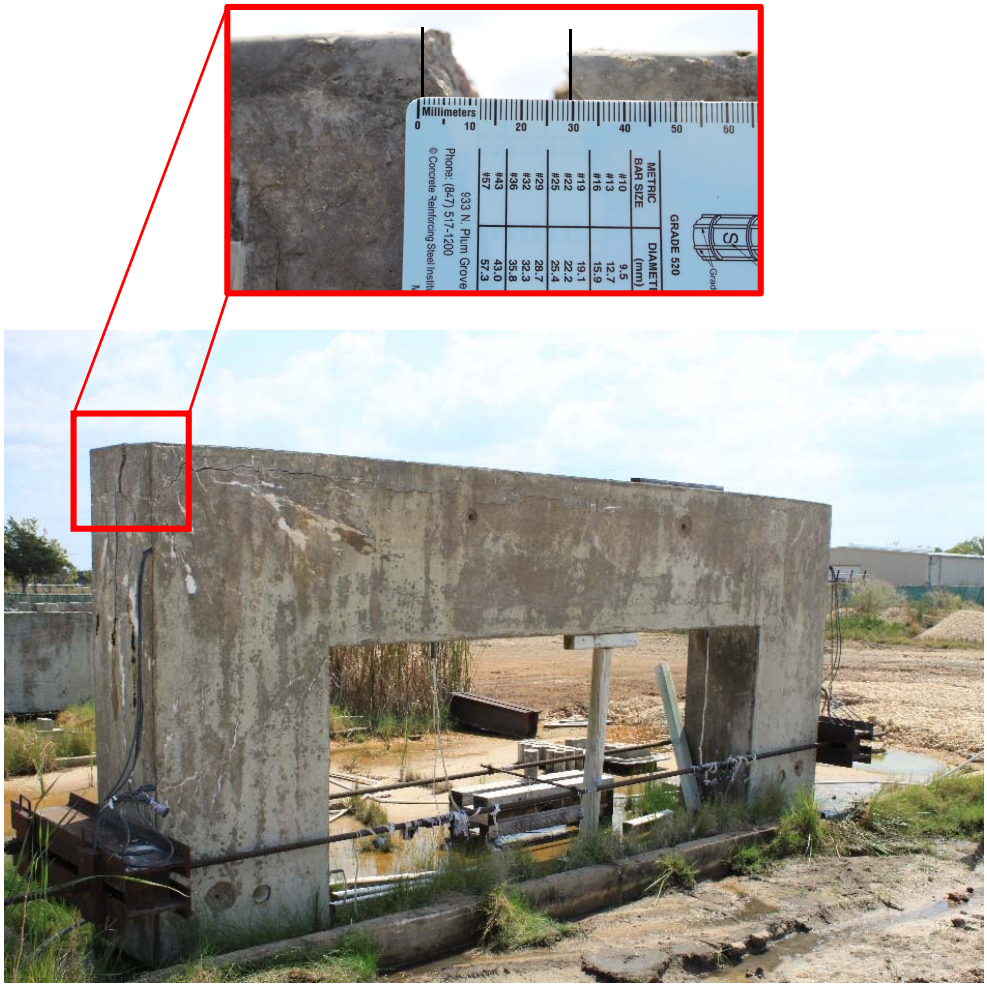

(a) West Face

(b) North Face

(c) South Face

Figure 4-1: Deteriorated State of Specimen 3 at Texas A&M Riverside Campus.

specimen grew with time and eventually merged with the load-induced cracks. It is evident from Figure 4-2 that by 13 months (day 406) of exposure the specimen was excessively cracked on the north, south, and top faces of the specimen. As these faces of the specimen were excessively cracked, more emphasis was placed on mapping the cracks on the west face of the specimen at the time when the final mapping of cracks was performed at the end of the five-year conditioning period prior to the specimen being transported to the laboratory for testing. Over time, the formation of new cracks was also accompanied by the widening of existing cracks.

Figure 4-3 shows the crack widths that were measured on Specimen 3 at the end of its exposure period. Because of the large number of cracks on the specimen, the cracks are classified into different ranges of crack widths. It is evident from Figure 4-3 that the widest cracks are observed on the top edge of the north and south faces and on the edges of the specimen on the top face. This is attributed to the lack of confining transverse reinforcement across the column top face. It can also be seen in Figure 4-3 that the largest crack on the specimen west and top faces was aligned along the longitudinal column reinforcement and the skin reinforcement, respectively. It is also evident from Figure 4-3 that the cracks follow the compression stress trajectories, and the widest cracks are observed where the restraint (reinforcement) is least, and natural tension cracking from load effects is greatest.

Figure 4-4 shows the progression of cracks in Specimen 3 at 48, 76, 129, 176, 406, and 1829 days of exposure. At 48 days of exposure (Figure 4-4a), very few new cracks developed in addition to the load induced cracks. However, by 76 days of exposure (Figure 4-4b) the existing load induced cracks grew in length and map cracking caused by ASR expansion were also observed. Commencement of longitudinal cracks that aligned with the reinforcement layout of the specimen was also observed. This indicated that the expansion due to ASR occurred between 48 and 76 days of exposure. These cracks further provided a path for moisture ingress into the specimen, which resulted in the accelerated formation of cracks caused by ASR expansion. This is evident from the state of the specimen observed at 129 (Figure 4-4c) and 176 (Figure 4-4d) days. At this stage many of the load-induced cracks had grown further and the map cracks caused by ASR/DEF merged with these cracks. By 406 days of exposure (Figure 4-4e), numerous cracks were observed on the specimen, especially the top and north face of the specimen, in addition to the longitudinal cracks that developed along the specimen reinforcement. The final state of the specimen at the end of its exposure period (1829 days = 5 years and 4 days) is shown in

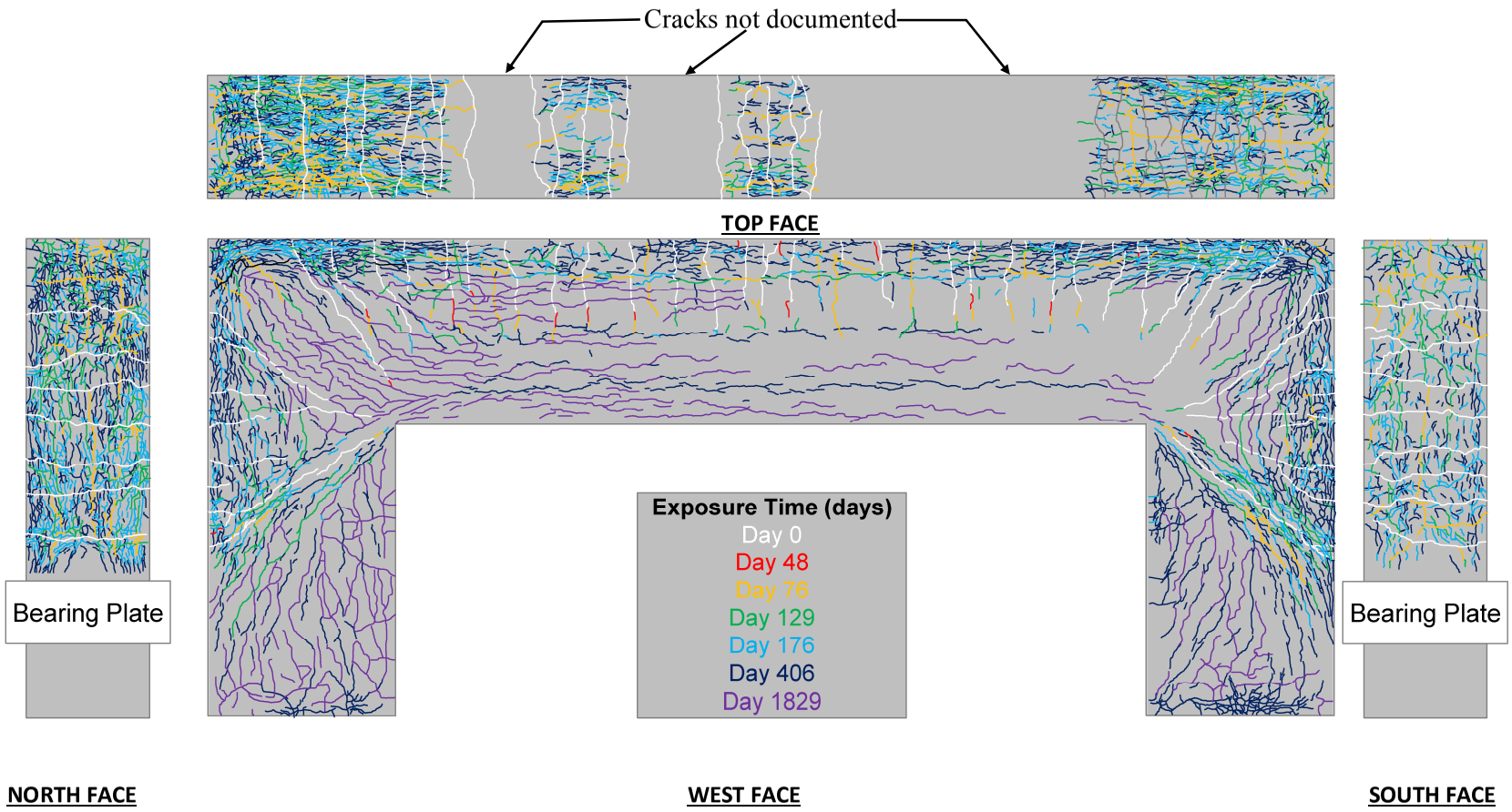

Figure 4-2: Crack Pattern over Time in Specimen 3.

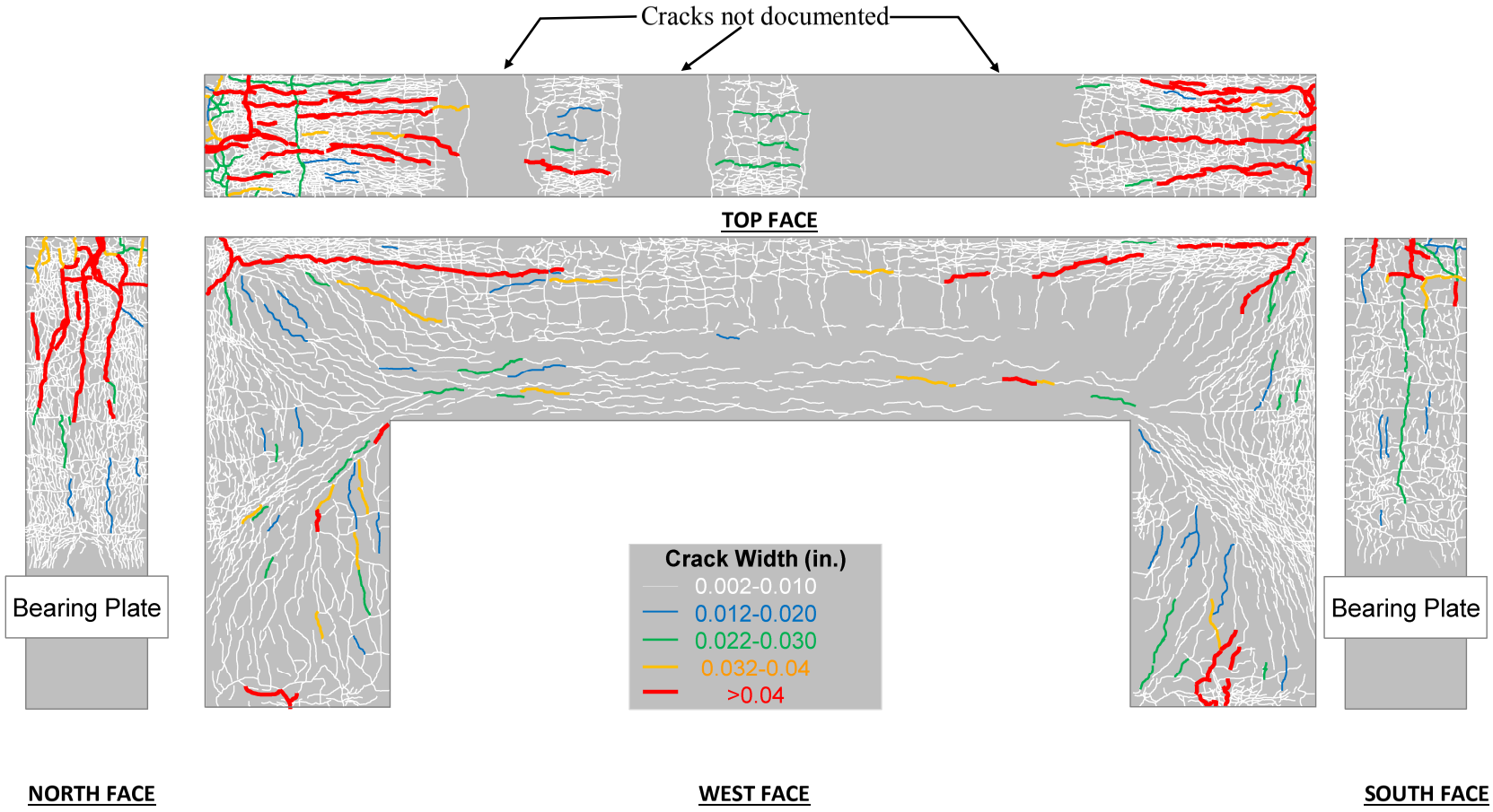

Figure 4-3: Final Crack Widths on Specimen 3.

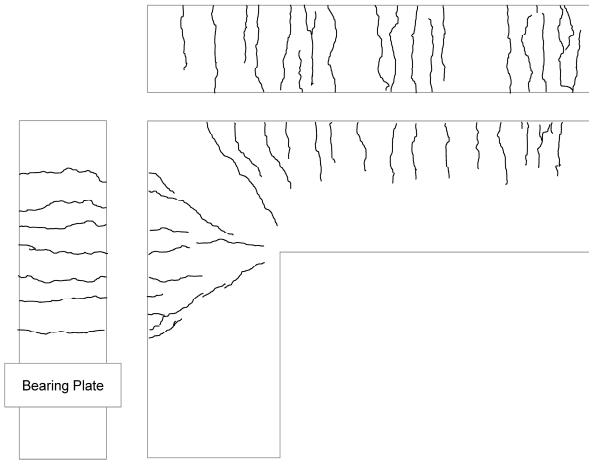

(a) Exposure Time – Day 48

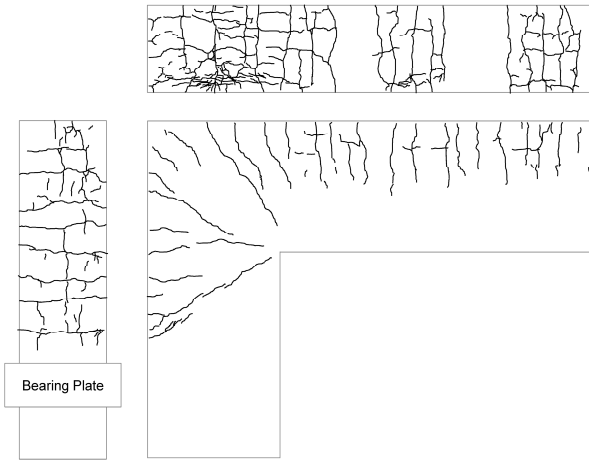

(b) Exposure Time – Day 76

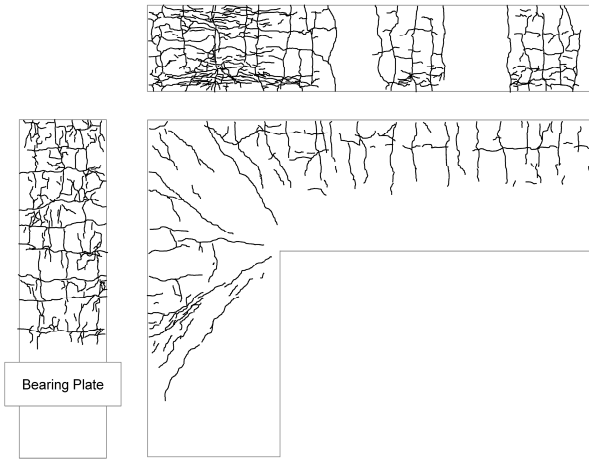

(c) Exposure Time – Day 129

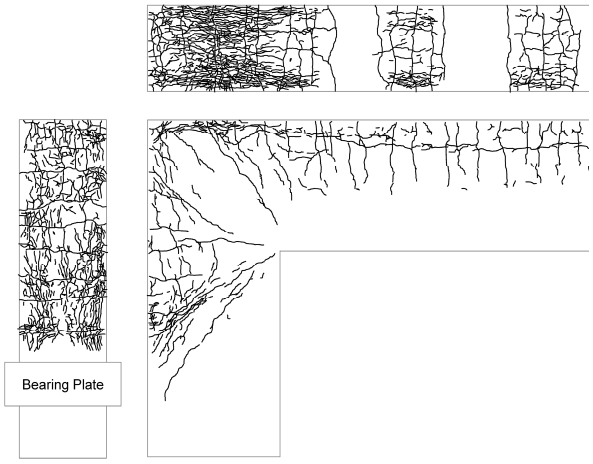

(d) Exposure Time – Day 176

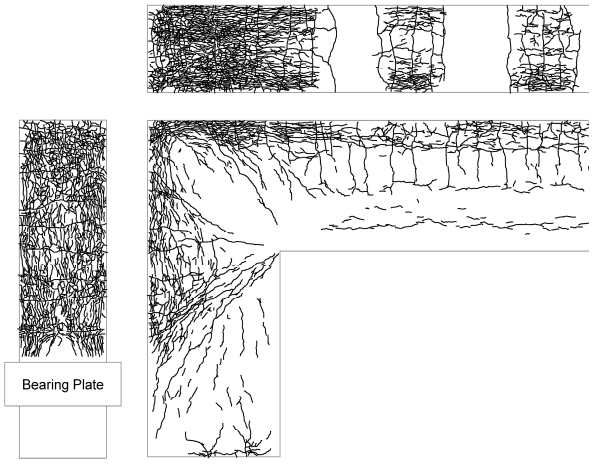

(e) Exposure Time – Day 406

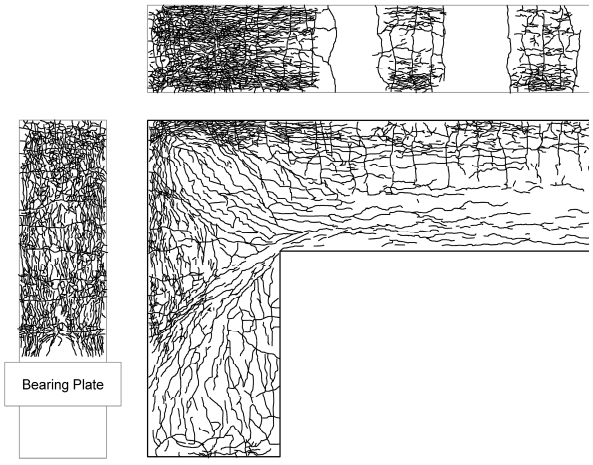

(f) Exposure Time – Day 1829

Figure 4-4: Progression of Cracks on Specimen 3 with Time.

Figure 4-4f and it is evident that the specimen is in a state of severe cracking. While the existing cracks grew considerably, the addition of many new cracks was also observed.

Based on the visual observations presented in Figure 4-1 through 4-4, it is quite evident that Specimen 3 is subjected to excessive cracking due to ASR/DEF induced expansion. The damage caused by ASR/DEF induced deterioration to Specimen 3 can be classified to be *heavy*.

4.3 SURFACE CONCRETE STRAINS

The progression of ASR/DEF induced expansion strains with time was recorded from a system of DEMEC points that were installed at the time of construction on the surface of the specimen. Longitudinal and transverse DEMEC measurements were made in the beam, column, and the beam-column joint. Additionally, the expansion strains transverse to the compressive diagonal strut in the beam and beam-column joint were also recorded. Most of the DEMEC gage lengths were 10.5 in. However, the DEMEC gage lengths along the transverse direction of the beam and column short-widths were 9.8 in.

Although Specimens 2 and 4 were discussed in detail in Mander et al. (2012), the deterioration data for Specimen 2, which exhibited only *slight* damage due to ASR/DEF effects, were not reported. Nevertheless the DEMEC readings for Specimen 2 are also presented herein for sake of completeness.

The surface expansion strains that were recorded from the DEMEC points on Specimen 2 and 3 are presented in Figure 4-5 to 4-12. In most cases it can be seen that measurable expansion strains are recorded at about 60 days of exposure. While the initial rate of expansion is high, the rate of strain reduced over a period of some two years. It appears that most of the ASR/DEF expansion was complete by the end of the 5-year field observation period. DEMEC data presented in each figure are grouped based on the region of the specimen and the direction in which the measurements are made.

Figure 4-5a and b present the layout of the DEMEC points on the top face of the C-Beam specimen in the member and joint regions, respectively. The expansion strains in both the longitudinal and transverse directions are measured. Figure 4-5c shows the longitudinal and transverse expansion strains in the member region of the specimen top face. It is evident from the

figure that the expansion strains in the transverse direction are about three times the expansion strains in the longitudinal direction. This is primarily attributed to the fact that there is more longitudinal reinforcing steel restraining the expansion $(\rho = 0.0308)$ compared to the hoops in the transverse direction $(\rho = 0.0019)$. Figure 4-5d shows the expansion strains in both the longitudinal and transverse direction in the joint region of the specimen top face. As in the earlier case, the expansion strains in the transverse direction are much higher than the expansion strains in the longitudinal direction. Additionally, it should be noted that there are no transverse U-bars $(\rho \simeq 0)$ on the top face of the C-Beam specimen leaving transverse expansion of concrete essentially unconstrained. This explains why the transverse expansion strains in the joint region (Figure 4-5d) are on an average 1.5–2 times the transverse expansion strains in the member region (Figure 4-5c). The expansion strain recorded at DEMEC 204 is over 12 percent. This strain was measured over a gage length of about 9.8 in. However, the cracks on the knee-joint of the specimen were concentrated at about the middle of the specimen close to the center DEMEC stud. Therefore, a more realistic strain at DEMEC 204 would be about 6 percent considering the entire width of the specimen (24 in.), instead of a gage length of 9.8 in. Given that $\rho \to 0$, an unconfined maximum expansion strain can thereby be assigned as $\varepsilon_o^{\max} = 0.05$. This result is subsequently used in the transient expansion modeling analysis in the next chapters. Figure 4-6c and d show the longitudinal and transverse expansion strains in the member and joint regions, respectively, of Specimen 2 top face. The expansion strains recorded in Specimen 2 during its 9 months exposure period are comparable to the strains recorded in Specimen 3 for the same time period.

Figure 4-7a and b, respectively, show the layout of the vertical and horizontal DEMEC points in the joint region of the C-Beam specimen. The vertical and horizontal longitudinal expansion strains are shown in Figure 4-7c and d, respectively. In both the cases the strains are broadly classified into two categories: expansion strains close to the edge of the specimen and expansion strains away from the edge of the specimen. It was previously shown (Mander et al., 2011) that the reinforcement did not reach its yield capacity within the development length zone. Therefore, the restraint provided by the longitudinal reinforcement against the expansion strains in the longitudinal direction varies with the distance from the specimen edge. Hence, the expansion strains recorded closer to the edge of the specimen are greater than the expansion strains that are

recorded farther away from the edge where the bar strains are greater. This is evident from Figure 4-7c and d. In Figure 4-7c and d the strains measured away from the edge in the joint region are comparable whereas the expansion strains measured closer to the edge in the vertical direction (Figure 4-7c) are about 2 times the expansion strains measured close to the edge in the horizontal direction. This is likely because the longitudinal side reinforcement in the beam consisted of only 3 sets of #4 bars, whereas 5 sets of #8 bars were used as the longitudinal side reinforcement in the column. In other words, the beam was lightly reinforced in the longitudinal direction compared to the column, and hence provided less restraint to ASR/DEF induced expansion, which results in greater measured surface strains. Figure 4-8c and d, respectively, show the vertical and horizontal longitudinal expansion strains for Specimen 2 in the joint region. These expansion strains are comparable to the expansion strains observed in Specimen 3 during the same time frame.

Figure 4-9a shows the DEMEC points in the in-plane longitudinal direction in the column, and longitudinal and transverse direction in the beam. Figure 4-9b shows the DEMEC points in the longitudinal and transverse direction along the short-width of the beam. Figure 4-9c shows the strains in the longitudinal and transverse direction in the in-plane direction. As in the earlier cases, it is evident that the expansion strains in the transverse direction were about twice the expansion strains in the longitudinal direction. This is due to the greater amount of longitudinal reinforcing steel $(\rho = 0.0210)$ compared to the transverse hoops $(\rho = 0.0035)$. Similar observations are made in Figure 4-9d, where the transverse expansion strains on an average are about three times the longitudinal expansion strains. Larger strains are observed close to the top edge of the knee-joint because of the influence of the very wide crack that is formed in this region. This crack also influenced the longitudinal strains observed at DEMEC points DM113 and DM114 close to the specimen top edge. Figure 4-10c and d, respectively, show the in-plane strains in the beam and column regions, and the strains along the beam short-width of Specimen 2, which shows similar strains observed in Specimen 3 during the same time period.

Figure 4-11a shows the diagonal DEMEC layout in the beam and beam-column joint region. These DEMEC measurements were made transverse to the main diagonal compressive strut in the beam and joint region. These transverse strains led to the compression softening of the diagonal concrete struts.

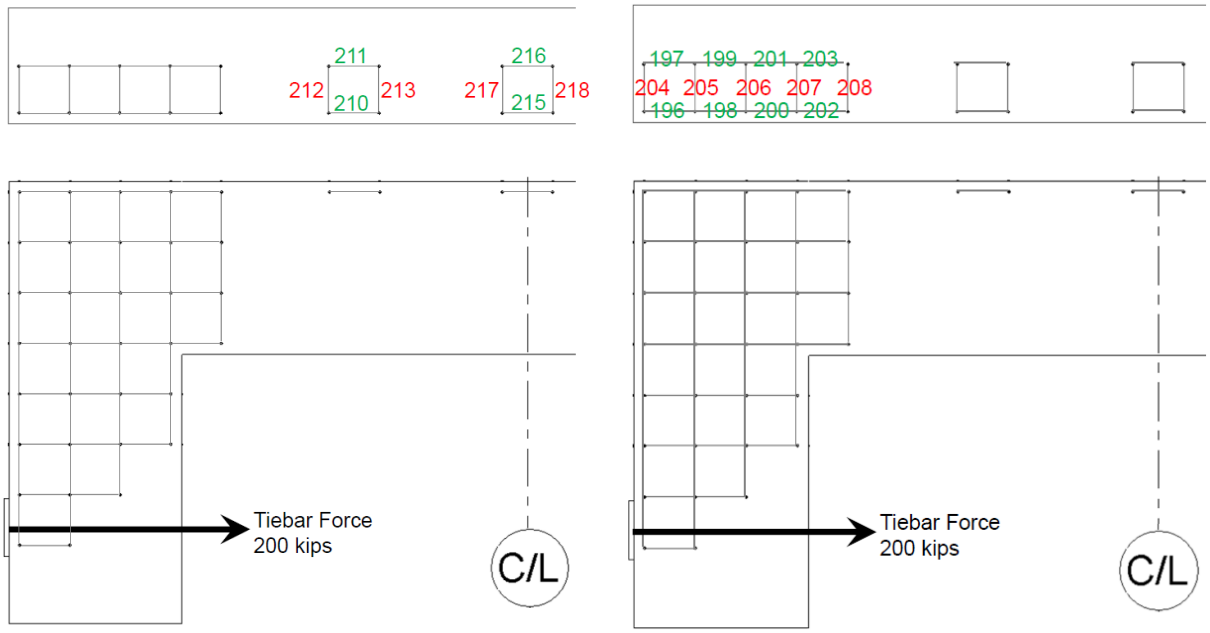

(a) DEMEC Layout on Member Top Face *(b) DEMEC Layout on Joint Top Face*

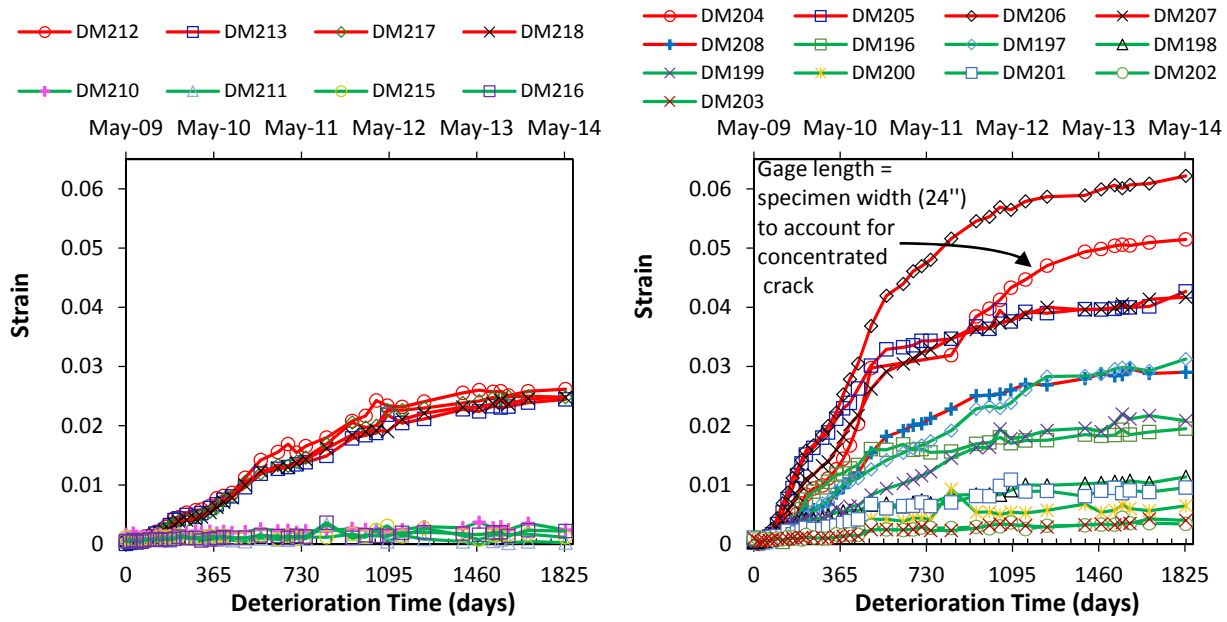

(c) DEMEC Strains in Member *(d) DEMEC Strains in Joint*

Figure 4-5: Horizontal Surface Concrete Strains from DEMEC Points on C-Beam Top Face–Specimen 3.

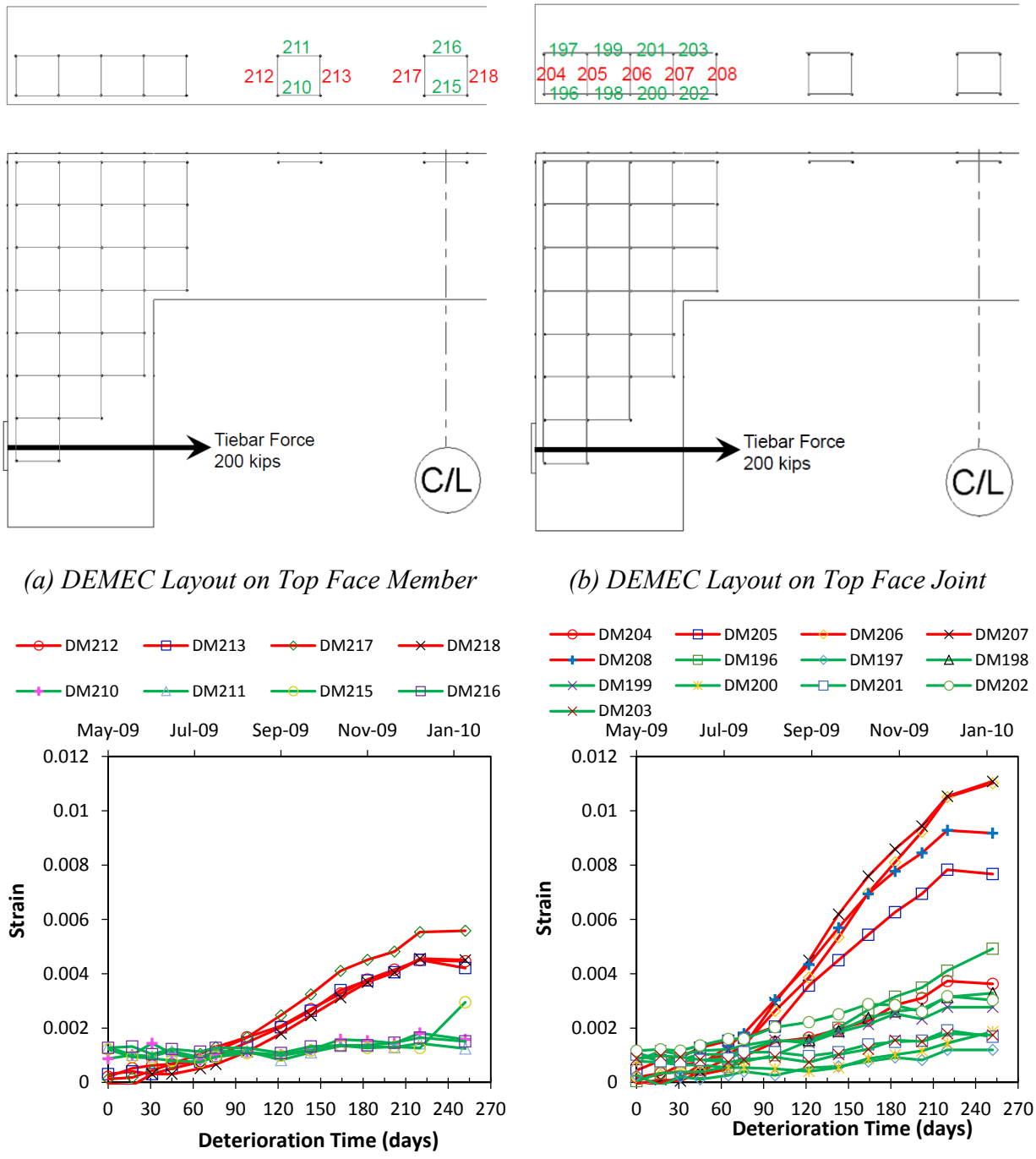

(a) DEMEC Layout on Top Face Member

(b) DEMEC Layout on Top Face Joint

(c) DEMEC Strains in Member

(d) DEMEC Strains in Joint

Figure 4-6: Horizontal Surface Concrete Strains from DEMEC Points on C-Beam Top Face–Specimen 2.

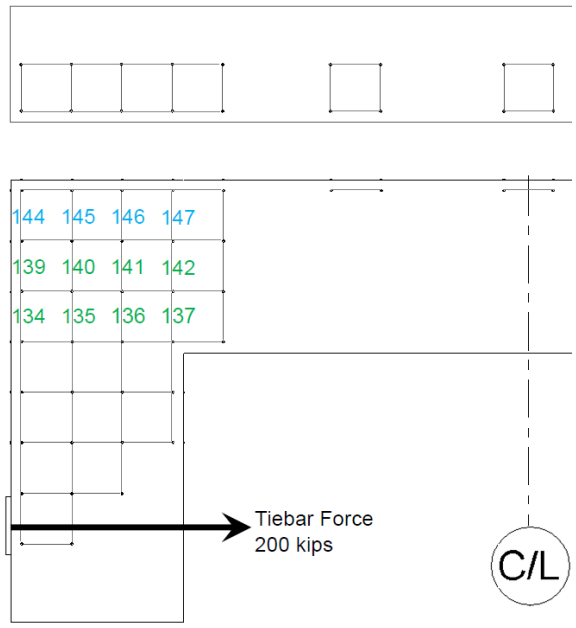

(a) Vertical DEMEC Layout in Joint

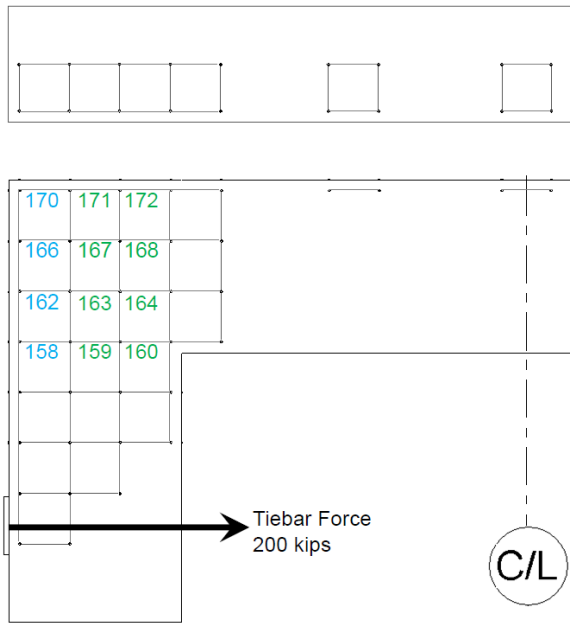

(b) Horizontal DEMEC Layout in Joint

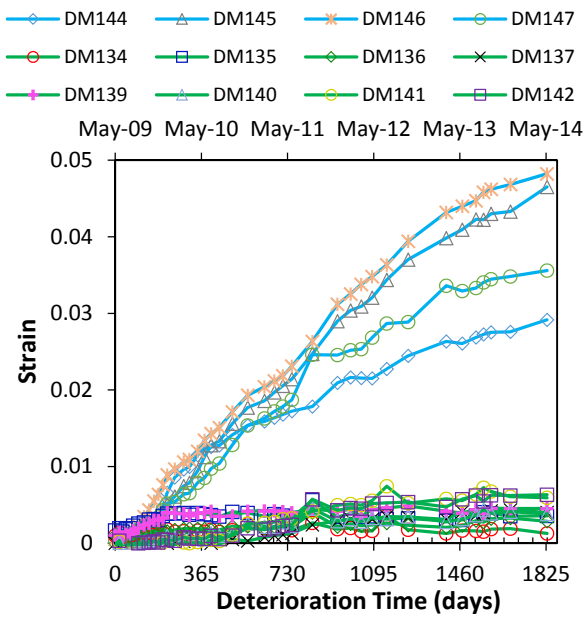

(c) Vertical DEMEC Strains in Joint

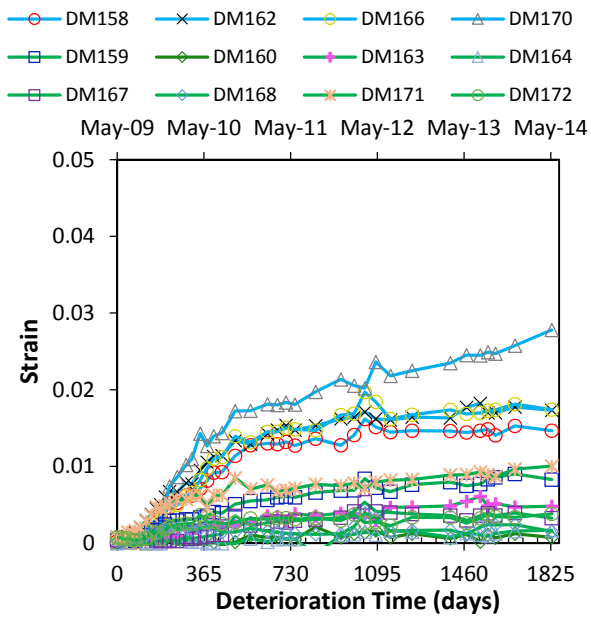

(d) Horizontal DEMEC Strains in Joint

Figure 4-7: Vertical Surface Concrete Strains from DEMEC Points on Joint Region–Specimen 3.

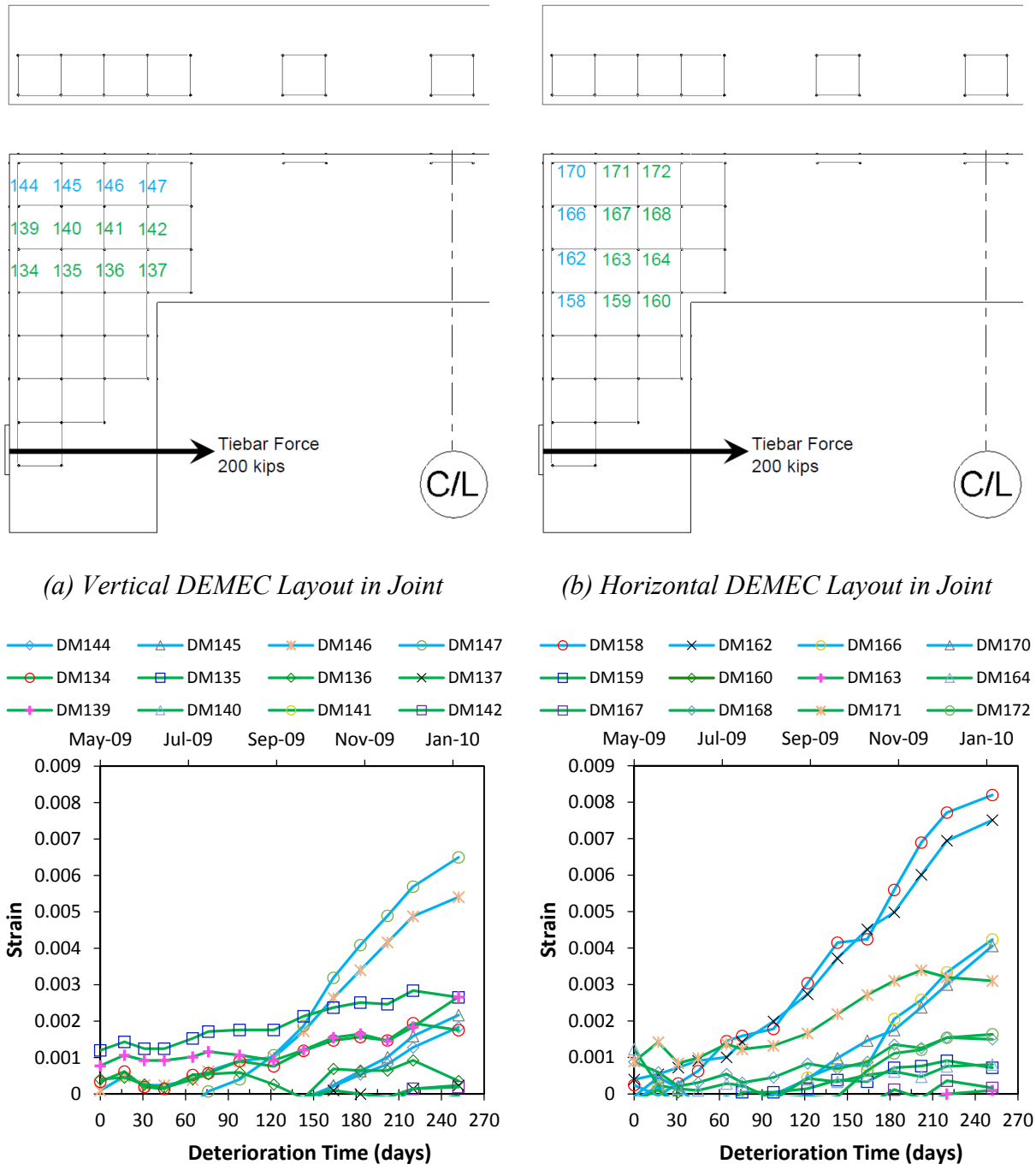

(a) Vertical DEMEC Layout in Joint

(b) Horizontal DEMEC Layout in Joint

(c) Vertical DEMEC Strains in Joint

(d) Horizontal DEMEC Strains in Joint

Figure 4-8: Vertical Surface Concrete Strains from DEMEC Points on Joint Region–Specimen 2.

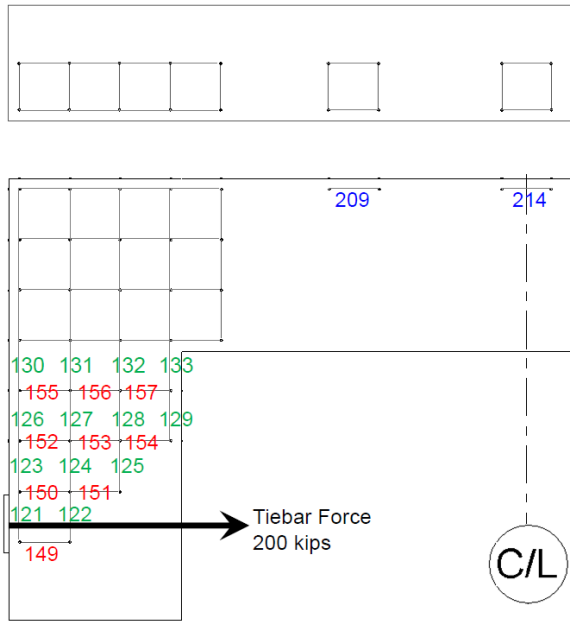

(a) In-Plane DEMEC Layout in Beam and Column

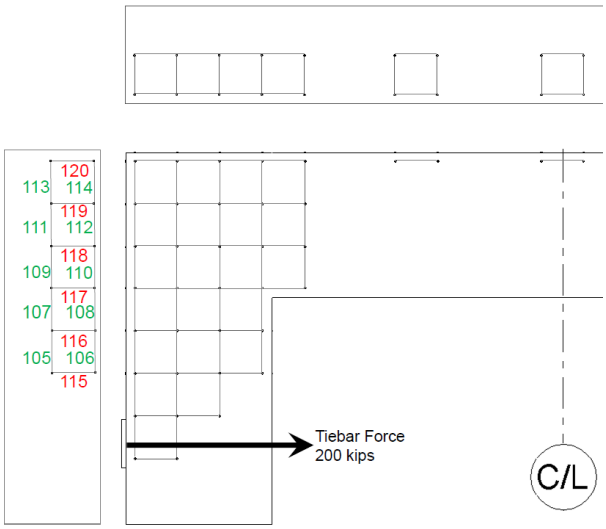

(b) DEMEC Layout along Beam Short-Width

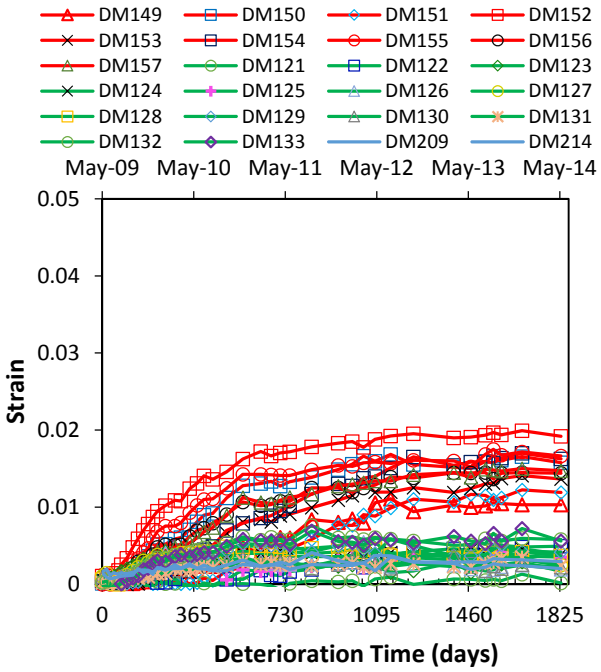

(c) In-Plane Strains in Beam and Column Region

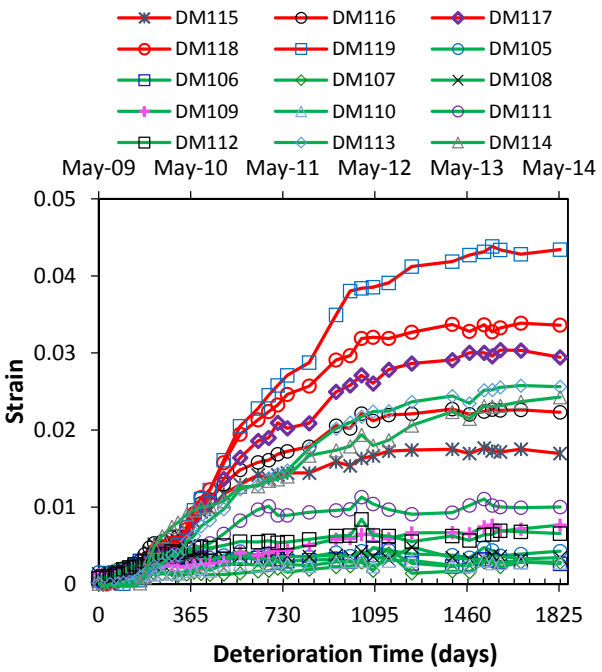

(d) Strains along Beam Short-Width

Figure 4-9: Vertical Surface Concrete Strains from DEMEC Points on Beam and Column Region–Specimen 3.

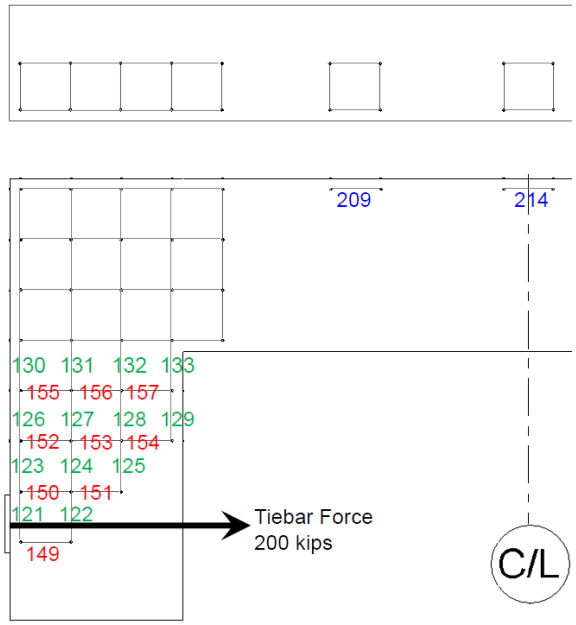

(a) In-Plane DEMEC Layout in Beam and Column

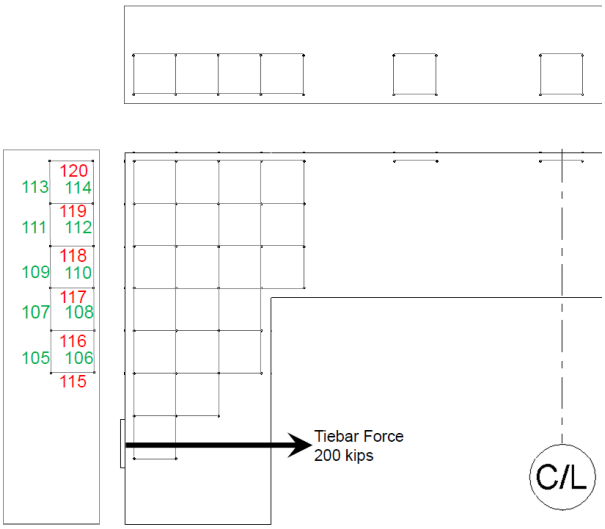

(b) DEMEC Layout along Beam Short-Width

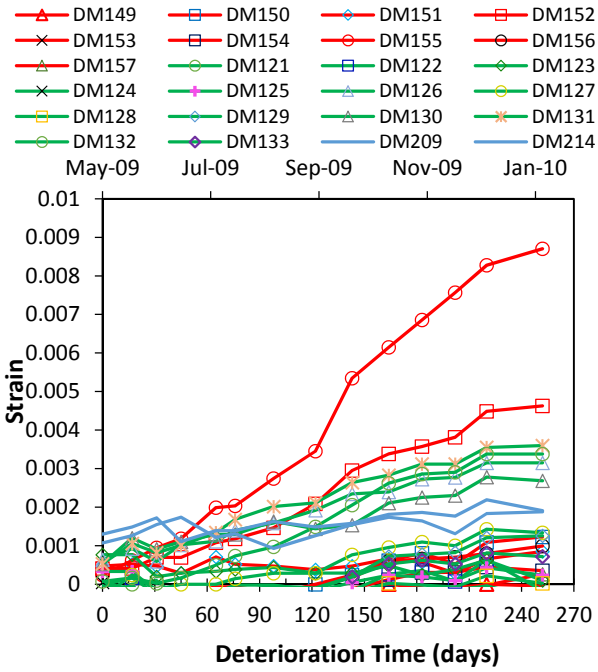

(c) In-Plane Strains in Beam and Column Region

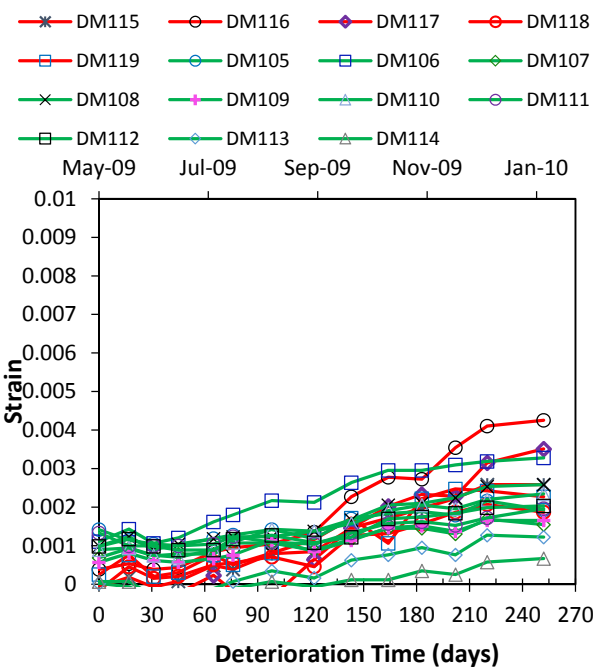

(d) Strains along Beam Short-Width

Figure 4-10: Vertical Surface Concrete Strains from DEMEC Points on Beam and Column Region–Specimen 2.

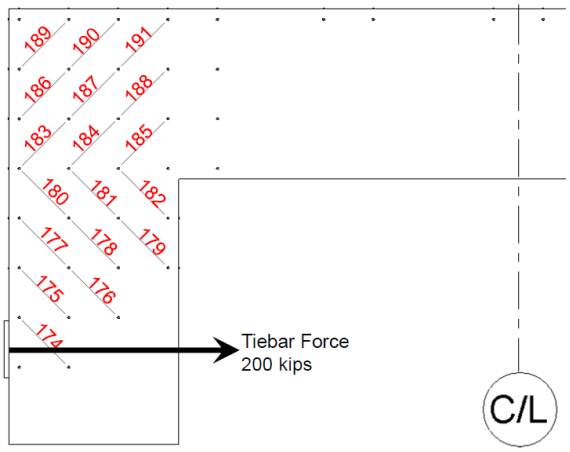

(a) DEMEC Layout Transverse to Diagonal Strut in Beam and Joint Region

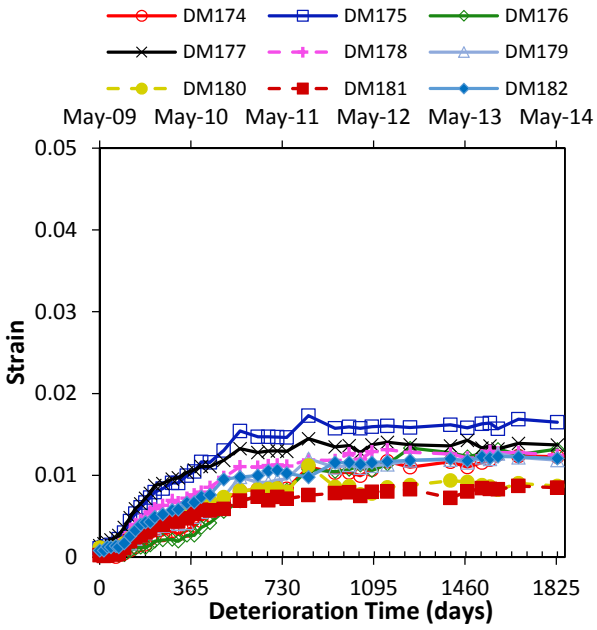

(b) Strains Transverse to Main Diagonal Strut in Beam

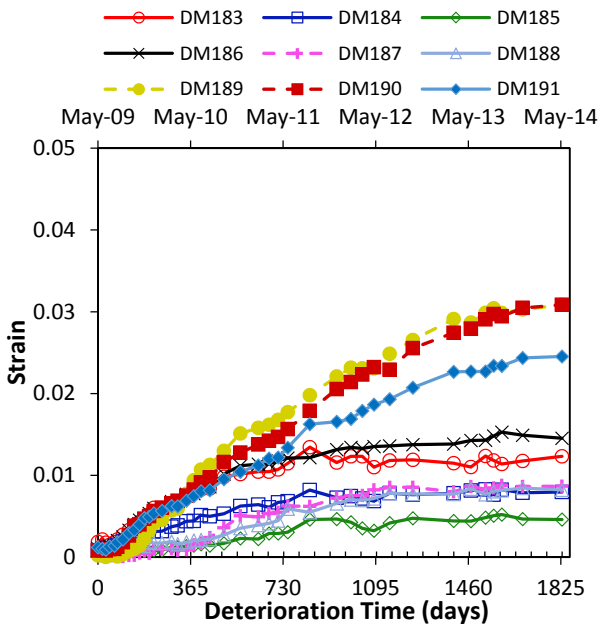

(c) Strains Transverse to Main Diagonal Strut in Joint

Figure 4-11: Diagonal Surface Concrete Strains from DEMEC Points on Beam and Joint Region–Specimen 3.

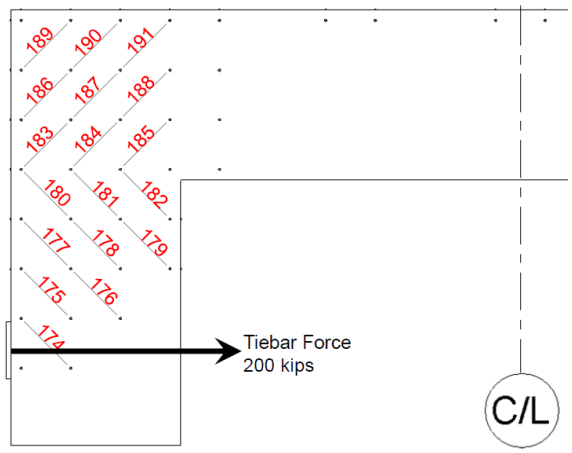

(a) DEMEC Layout Transverse to Diagonal Strut in Beam and Joint Region

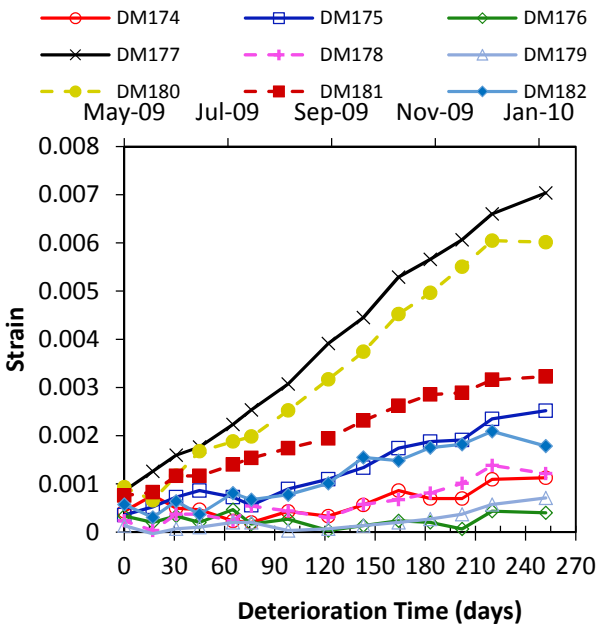

(b) Strains Transverse to Main Diagonal Strut in Beam

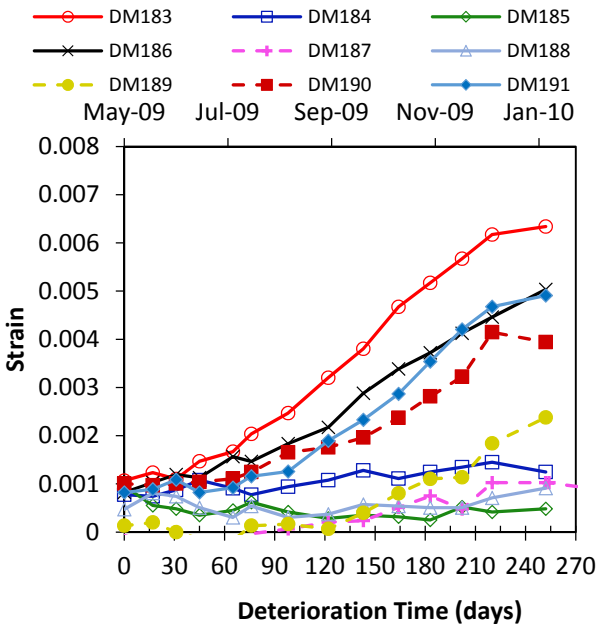

(c) Strains Transverse to Main Diagonal Strut in Joint

Figure 4-12: Diagonal Surface Concrete Strains from DEMEC Points on Beam and Joint Region–Specimen 2.

Figure 4-11b and c show the strains that were measured in the beam and joint regions, respectively. Comparing Figure 4-11b and c it can be seen that the strains measured transverse to the main compressive diagonal strut in the joint region were greater compared to the beam region. This implies that the compressive diagonal strut in the joint region is likely to be subjected to greater compression softening compared to the compressive diagonal strut in the beam. Figure 4-12b and c present the expansion strains transverse to the main diagonal strut in the beam and the joint regions, respectively.

4.4 INTERNAL CONCRETE STRAINS

To monitor the strains in the core concrete, concrete gages (KM) were embedded in each C-Beam specimen core concrete, providing a total of six KM gages embedded on each side of the C-Beam specimens, in which, three gages each were placed within the beam region (KM1–KM3) and beam-column joint (KM4–KM6).

The concrete strain along the main diagonal compression strut formed between the point of loading and the inner knee-joint in the beam was measured using gage KM1, which was aligned along the compression strut. Similarly, KM4 measured the compressive strains along the diagonal compression strut joining the outer and inner knee-joints. Figure 4-13b shows that compressive strains were recorded in gage KM1 (Specimen 3). Although gage KM4 initially measured compressive strains, from about 300 days of exposure it recorded tensile strains. This could likely be because of localized strains caused due to a reactive site that could have existed close to KM4 location.

Gages KM2 and KM5 measured in-plane strains transverse to the diagonal compression strut. While KM2 (Specimen 3) stopped recording data just after 500 days, both KM2 and KM4 measure tensile strains. Tensile strains of 0.008 were measured in KM4 at the end of the exposure period of Specimen 3. Gages KM3 and KM6 measured transverse strains along the short-width perpendicular to the compression strut. Both the gages stopped functioning before two years of exposure, however, it is evident from Figure 4-13b that they too recorded significant tensile strains perpendicular to the diagonal compression struts. It is evident that the core concrete tended to expand across the short-width of the specimen because the transverse hoops, which were restricted to the perimeter of the cross-section provided minimal restraint against ASR/DEF expansion in

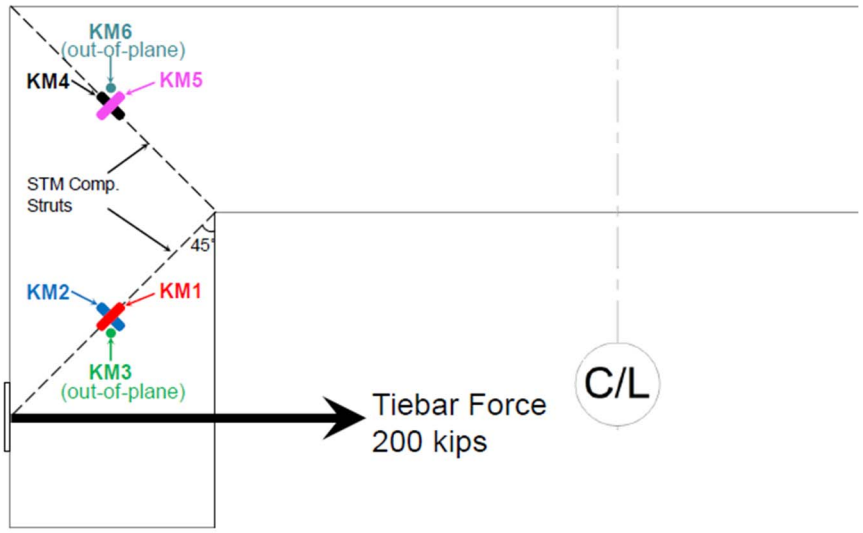

(a) Concrete Gage Layout for C-Beam Specimen

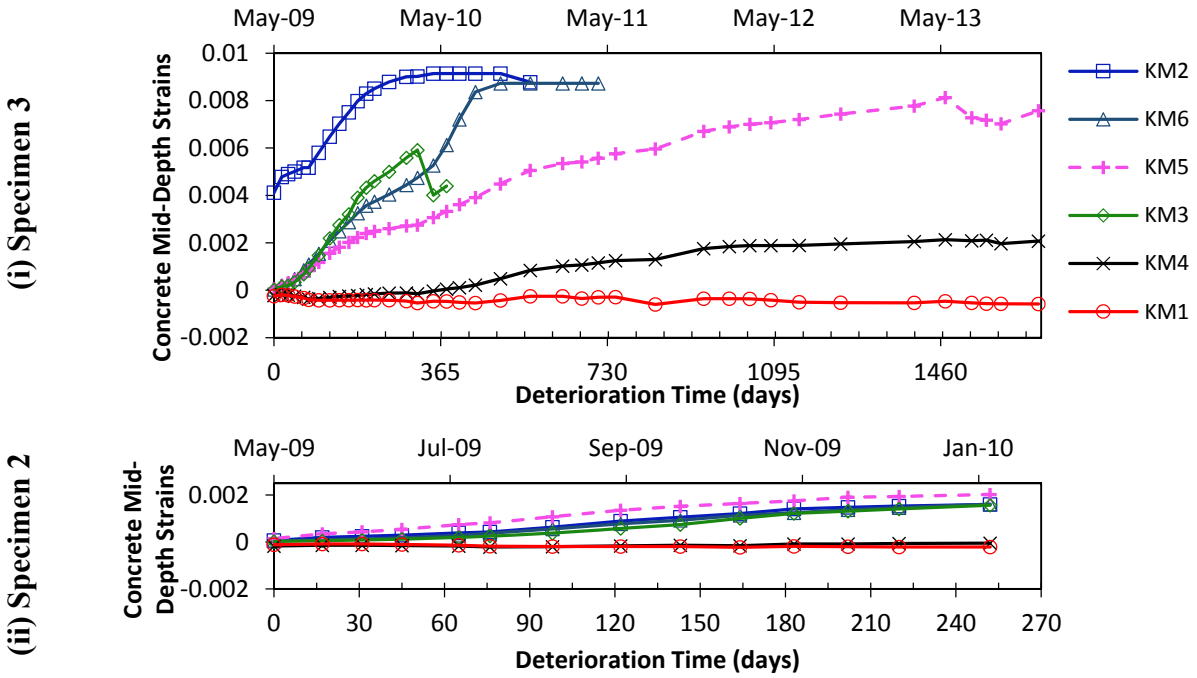

(b) Concrete Strain in Mid-Depth

Figure 4-13: Mid-Depth Concrete Strains Measured from Concrete Gages.

that direction. For completeness the concrete strains in Specimen 2 are also presented in Figure 4-13b. The observations for Specimen 4 were presented previously in Mander et al. (2012).

4.5 Reinforcing Steel Strains

Figure 4-14 to 4-17 present the reinforcing strains in the longitudinal and transverse steel at various regions for C-Beam Specimen 3 and Specimen 2. Each specimen was post-tensioned before it was conditioned in the field to simulate gravity loads. Therefore, prestrains were recorded in the strain gages. Under field exposure conditions, the strains in the steel quickly increased reaching close to or above yield strain of the reinforcement.

Figure 4-14 and 4-15 show the tensile strains that were recorded in the longitudinal reinforcement steel in the beam and column, respectively. For Specimen 3 it can be seen that the tensile strains in the reinforcement reached yield strain (0.0022) at around 300 days of exposure. However, after about one-year of exposure, decreasing tensile strains and eventually compressive strains were recorded in many gages in both the beam and the column. It is to be noted that several longitudinal cracks were formed just over the longitudinal steel. This likely promoted greater ingress of moisture, which in turn promoted the expansion of ASR gel. Therefore, the strains recorded from the strain gage are more likely to be localized strains that are influenced by ASR/DEF reactive sites close to the strain gages and therefore does not give a good idea of the reinforcement strains beyond 360 days of exposure. Figure 4-16 shows the strains that were recorded from the transverse reinforcement and the U-bars in the joint region. For Specimen 3 it can be seen that the tensile strains in the transverse reinforcement reached yield between 180–240 days, much earlier than the longitudinal reinforcement. This can be attributed to the reinforcement ratio in the transverse direction generally being less compared to the longitudinal direction in the various regions of the C-Beam specimen. Hence, less restraint is offered to ASR/DEF induced expansion in the transverse direction, which in turn causes greater expansion strains and yields the transverse steel reinforcement earlier. Again, after a period of 300–360 days scattered strains are observed, which are likely localized strains and therefore unreliable. Figure 4-17b finally shows the reinforcement strains in the compression region. For Specimen 3 the recorded strains tread along the zero strain line with minor variations for about 360 days of exposure. Beyond that period, the strain gage data become unreliable.

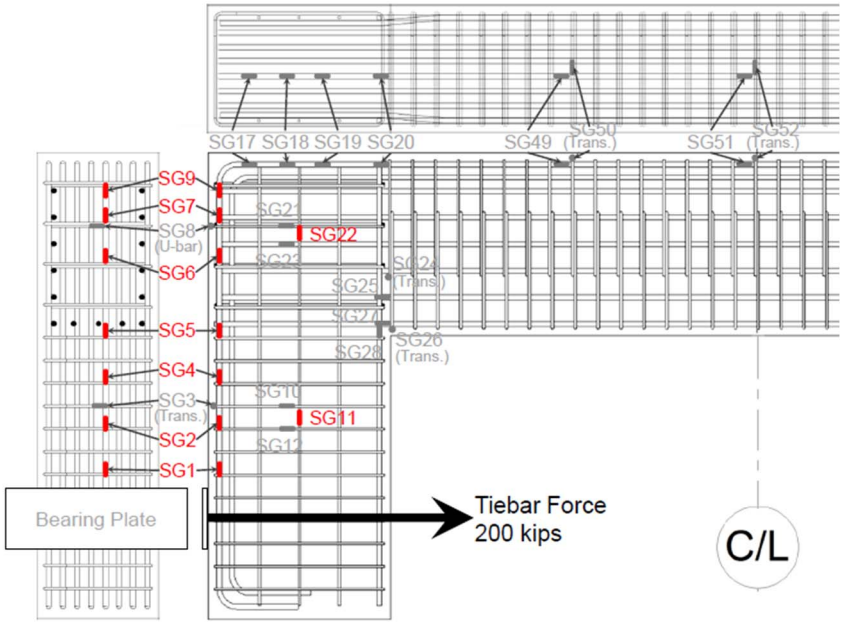

(a) Strain Gage Layout

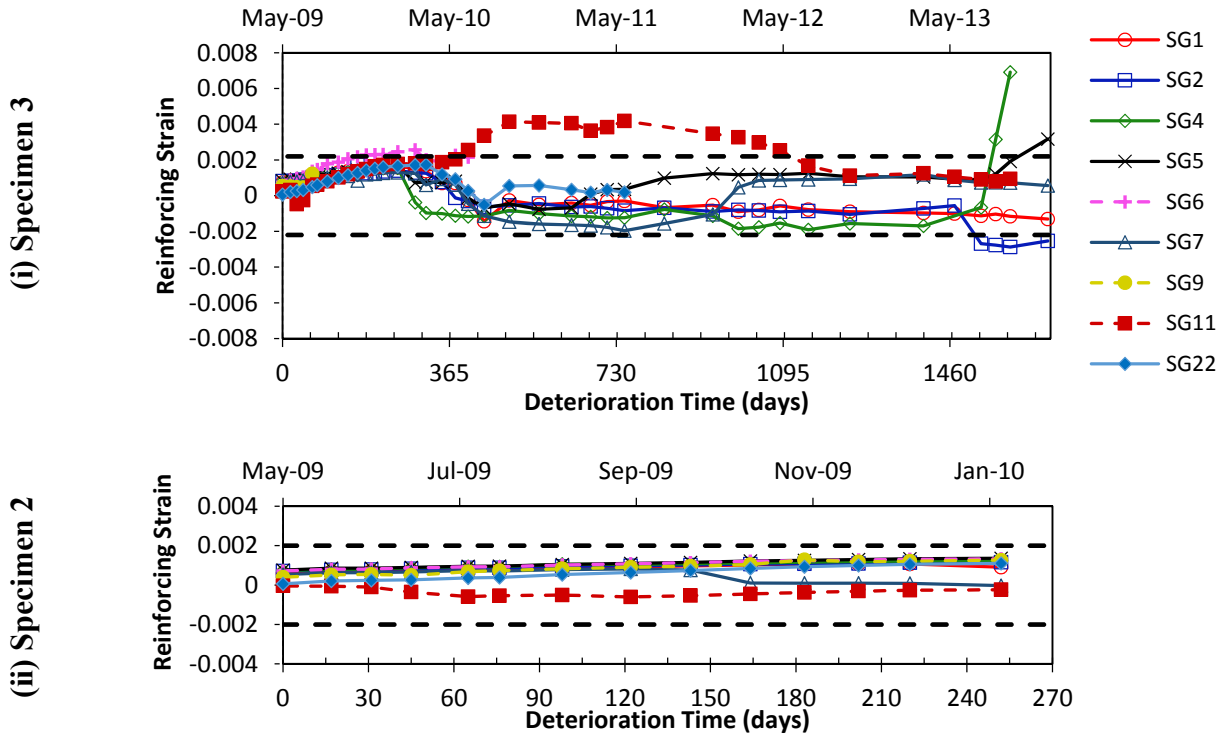

(b) Strain in Longitudinal Reinforcement

Figure 4-14: Longitudinal Reinforcing Steel Strains in Beam.

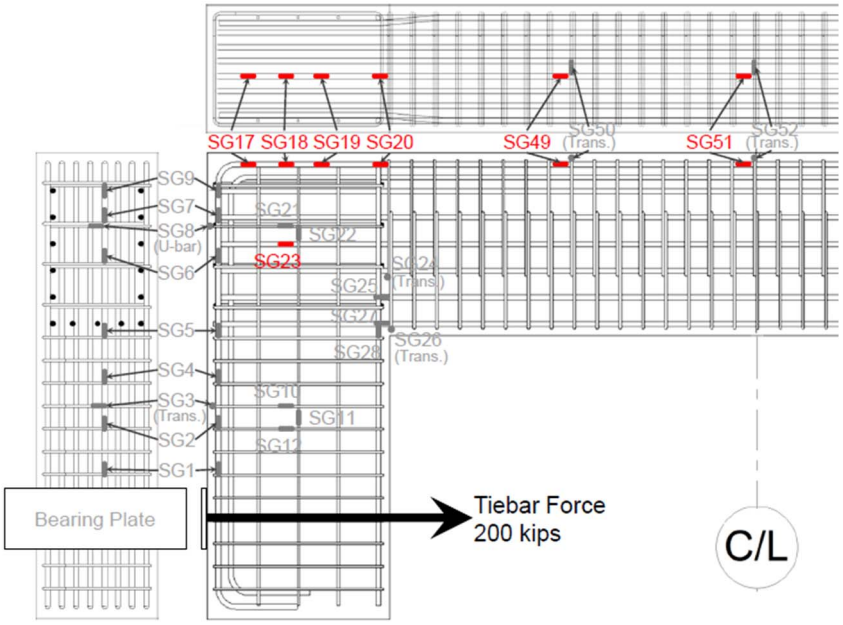

(a) Strain Gage Layout

(i) Specimen 3

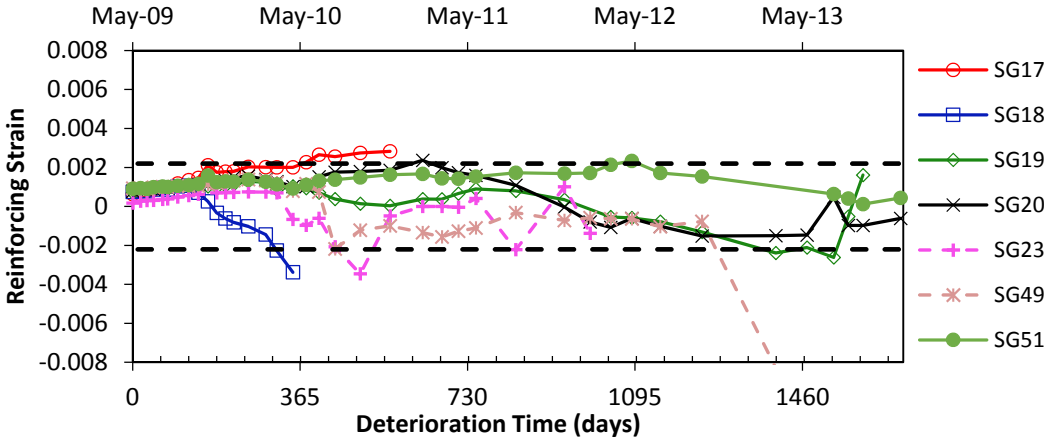

(ii) Specimen 2

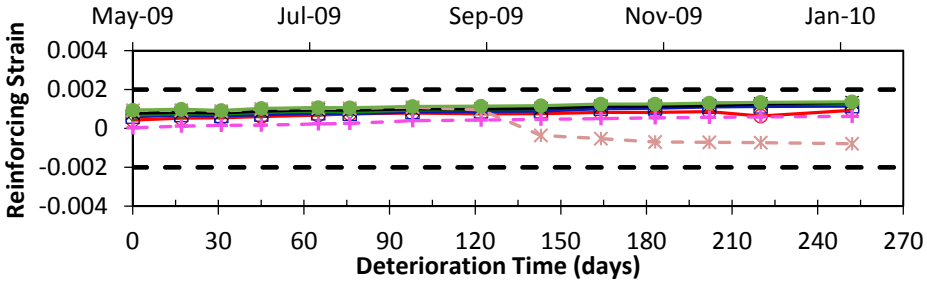

(b) Strain in Longitudinal Reinforcement

Figure 4-15: Longitudinal Reinforcing Steel Strains in Column.

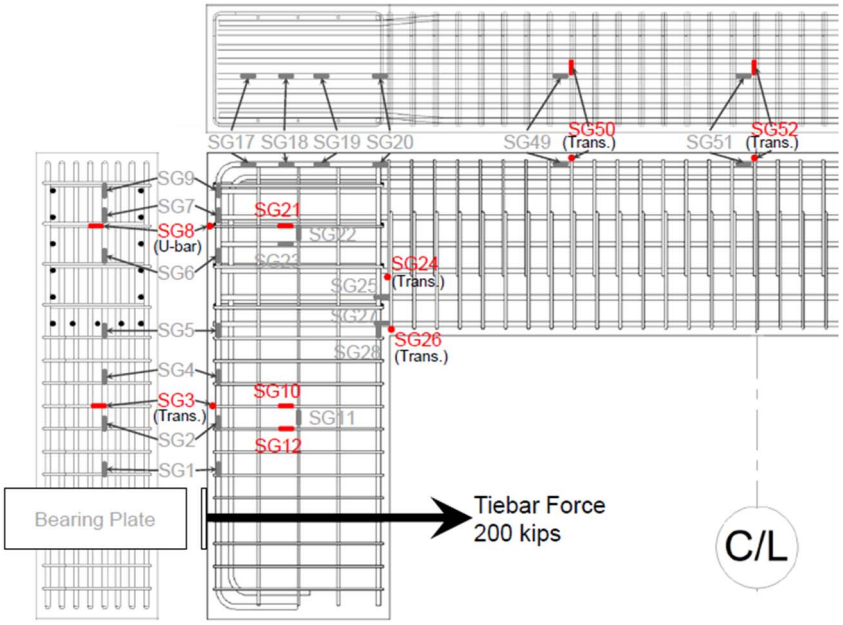

(a) Strain Gage Layout

(i) Specimen 3

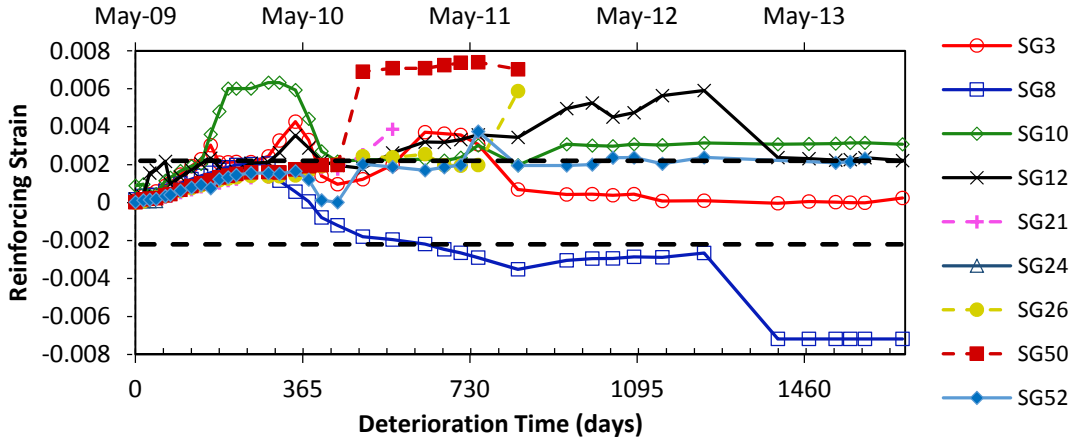

(ii) Specimen 2

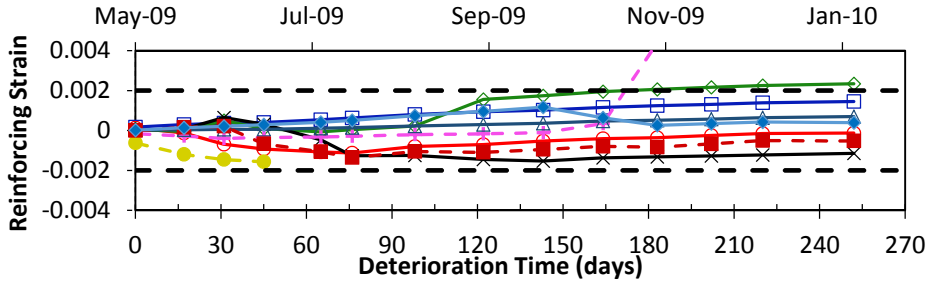

(b) Strain in Transverse Reinforcement

Figure 4-16: Transverse Reinforcing Steel and U-Bar Strains.

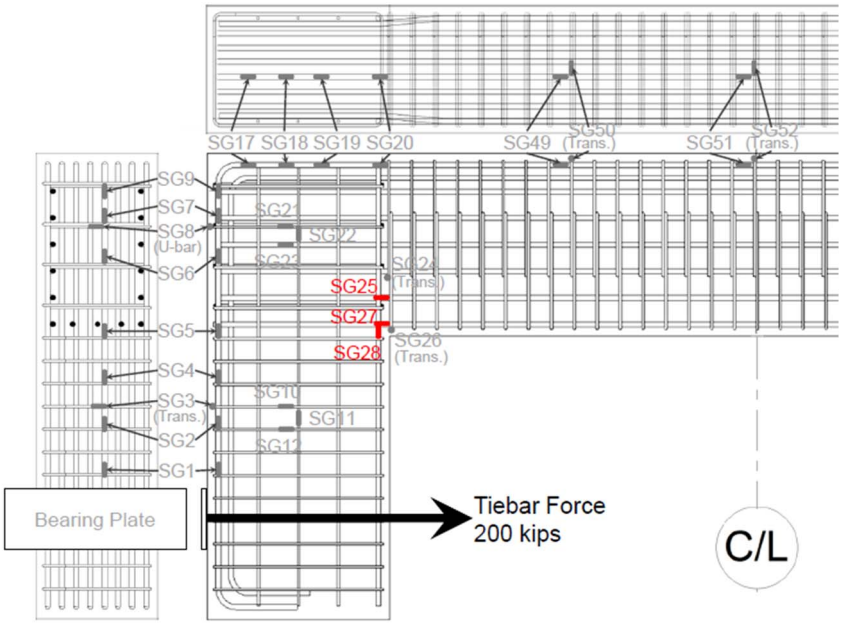

(a) Strain Gage Layout

(i) Specimen 3

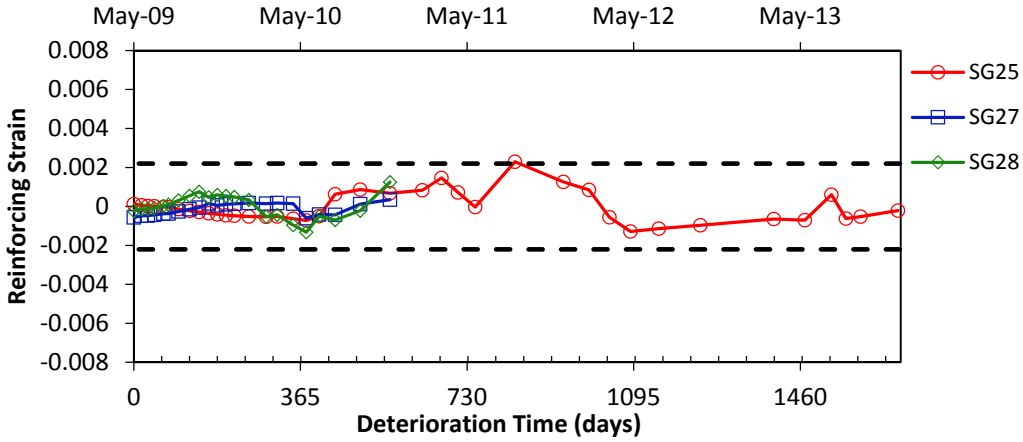

(ii) Specimen 2

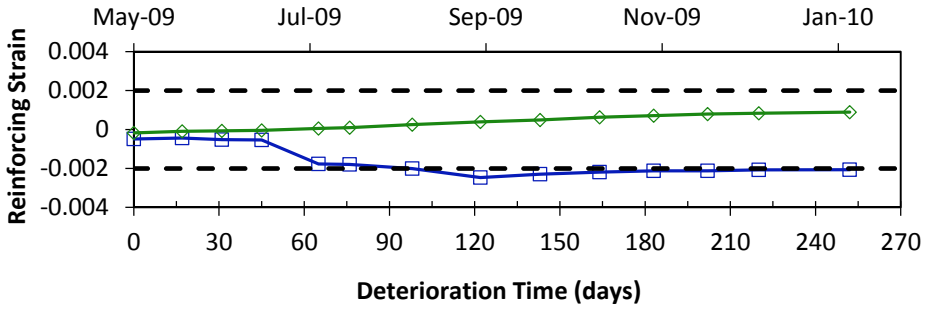

(b) Strain in Longitudinal Reinforcement

Figure 4-17: Reinforcing Steel Strains in Compression Zone.

For the sake of completeness the reinforcement strains in Specimen 2 are also presented in Figure 4-14 to 4-17. The reinforcement strains measured in Specimen 4 are presented in Mander et al. (2012).

4.6 POST-TEST CORES

A post-test petrographic analysis on concrete samples cored from the C-Beam specimen was conducted by TxDOT personnel. The observations from Specimen 2 that had minor damage due to ASR/DEF were presented in Mander et al. (2012). Liu (2012) presents the post-test petrographic analysis for Specimen 4. Figure 4-18a shows the locations where the cores were extracted from Specimen 4. The cores were drilled through the longitudinal and transverse reinforcement, in locations with mild cracking, locations where severe map cracking and large cracks were observed, and on places where white residue was observed on the surface of the specimen. Figure 4-18b–d show ASR gel in the air voids near the reactive aggregates. Some of the aggregates were also cracked as a result of ASR induced expansion. Figure 4-18e shows signs of ASR induced distress in the aggregates. ASR was found to be the primary cause of distress in Specimen 4, and it was reported as high to extensive stages of ASR formation. Debonding of the reinforcing steel with the cement paste was also reported as a result of accumulation of ASR gel around the reinforcing steel bars. Figure 4-18f shows ettringite filled in the cracks. Ettringite was also observed within air voids, cracks, cement paste-aggregate interface, and as a coating around the reinforcing bar. However, it was reported that the distribution of ettringite was not consistent with the formation of DEF.

4.7 DISCUSSION AND COMPARISON

From the field data for the two specimens presented in this study, it is evident that over several years, ASR/DEF reactions continue to increase and cause significant expansion in reinforced concrete. The embedded concrete gages and strain gages attached to the reinforcement give the internal strains in the structure. It is evident from the strain gage measurements, that both the longitudinal and transverse reinforcement started to yield between six months to one year of exposure. Many of the embedded gages either stopped functioning or were influenced by localized effects of ASR/DEF expansion (especially after one year of conditioning) and therefore cannot be relied on completely to obtain general strains in concrete and the reinforcement steel.

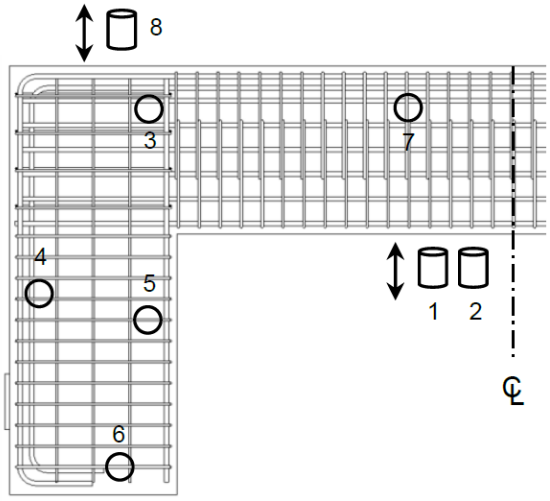

(a) Core Locations

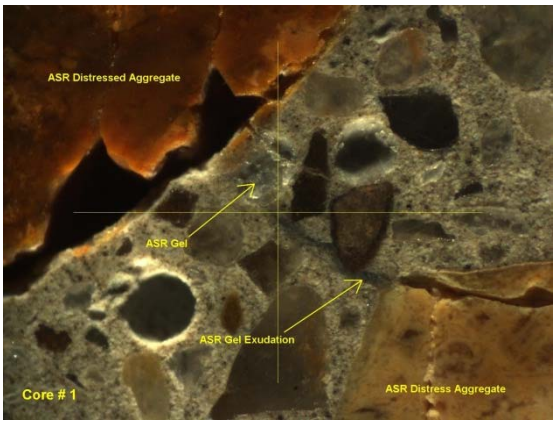

(b) ASR Gel Accumulation in Air Voids and ASR Distressed Coarse Aggregates (Core 1)

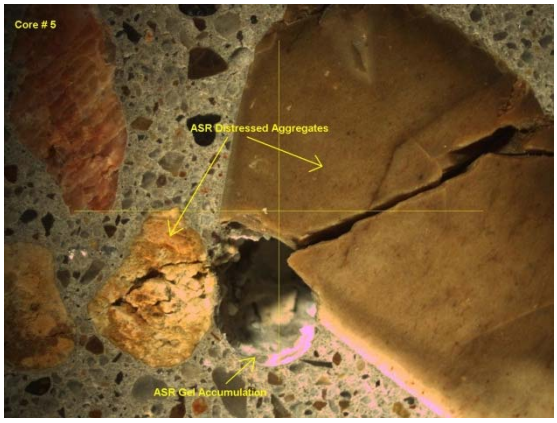

(c) ASR Gel Accumulation in Air Voids and ASR Distressed Coarse Aggregates (Core 5)

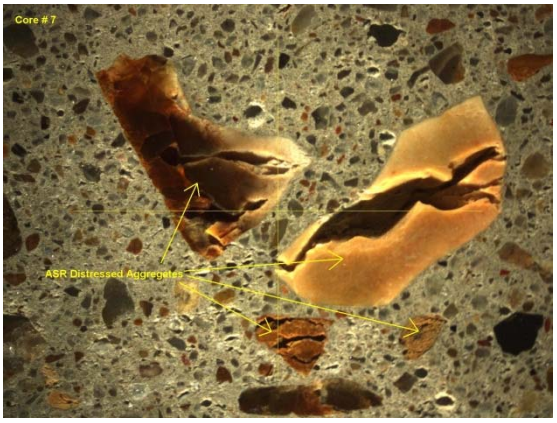

(d) ASR Distressed Coarse Aggregates (Core 7)

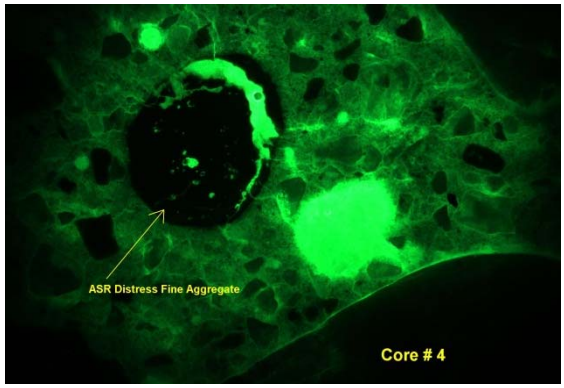

(e) Fine Network of ASR Induced Cracking

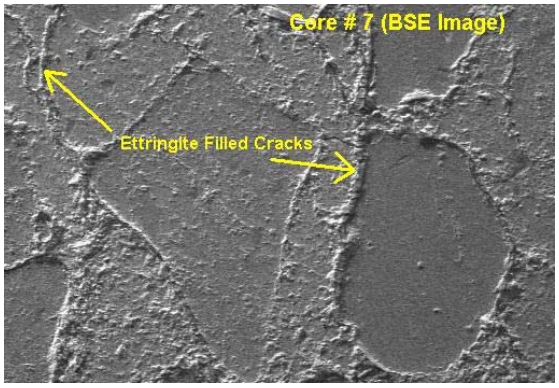

(f) Ettringite Filled in Cracks (Core 7)

Figure 4-18: Results from Petrography Analysis of Specimen 4.

The surface concrete strain measurements obtained from the DEMEC points installed on the specimen surface gave valuable information on the expansion strains in the C-Beam specimen. Figure 4-19 shows a comparison of the external surface strains obtained from the DEMEC points to the corresponding internal strains obtained from strain gages and concrete gages. Figure 4-19a shows the locations of the DEMEC points and the internal strain gage or concrete gage that were closest to the location and orientation of the DEMEC readings. Figure 4-19b shows a comparison of strain measurements from DM187 and KM5 that were made transverse to the concrete diagonal strut in the joint region. Although the strain values do not match exactly, the strain measurements from the DEMEC points and the concrete gages compare very well. Figure 4-19c compares the external surface strains from DM167 with the internal strains obtained from SG21 along the direction of the longitudinal column reinforcement in the C-Beam joint region. The strain gage did not record readings beyond 1.5 years of exposure. However, up to that point, the strains compare well between the DEMEC points and the strain gage. Figure 4-19d compares the longitudinal strains from DM127 and DM128 with SG11 on the beam longitudinal reinforcement. A good comparison between the strain measurements from the DEMEC points and the strain gage is observed until about 2.5 years. Beyond this, the strains recorded by the strain gage decrease. Figure 4-19e compares strains between DM216 and SG51 in the direction of column longitudinal reinforcement on the C-Beam specimen top face. The DEMEC and strain gage expansion strain measurements compare very well with each other for about 3 years, beyond which the internal strains recorded by the strain gage starts falling. The possible reason for decreasing tensile strains recorded by strain gages beyond 2.5 to 3 years in Figure 4-19d and e could be because of the localized formation of ASR gel in the vicinity of the strain gage or due to faulty wiring and the formation of a corrosive layer between the strain gage and rebar. Another possibility could be debonding between the reinforcement bar and the cement paste that was reported in the petrographic analysis of Specimen 4.

Overall it is evident from Figure 4-19 that although the strains measured from the DEMEC points are just surface strains, they are very similar to the internal strains that are measured from the strain gages and concrete gages. However, beyond about 2.5 years, the external strains did not compare well with the internal strains. This is possibly because of the limitations on the range of

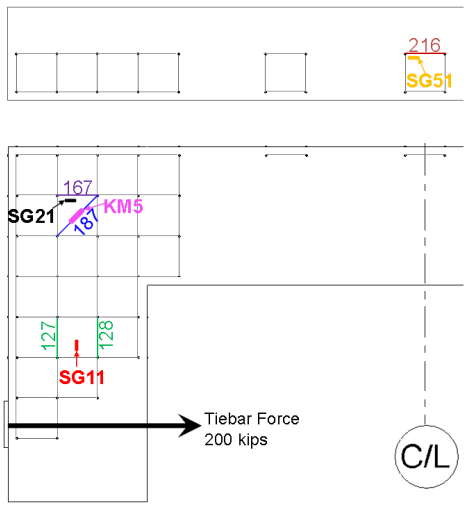

(a) Strain Measurement Locations on the C-Beam Specimen

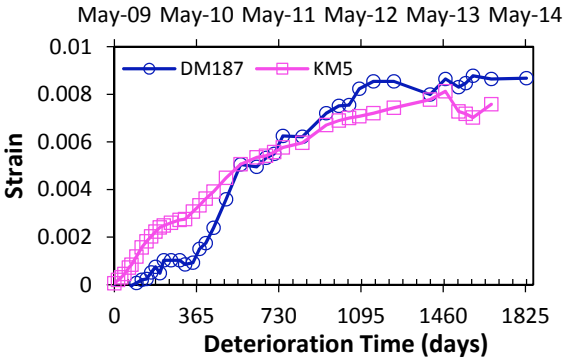

(b) DM187 vs. KM5

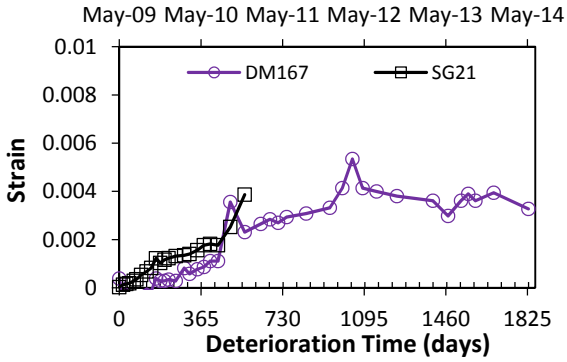

(c) DM167 vs. SG21

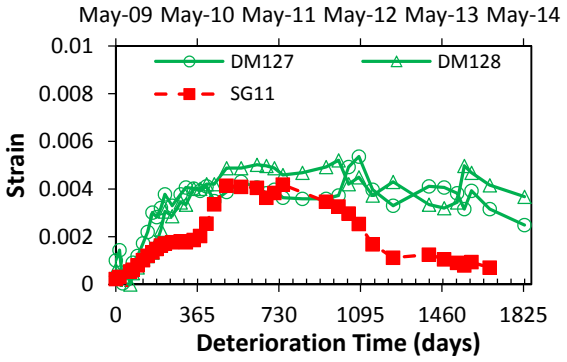

(d) DM127 and DM128 vs. SG11

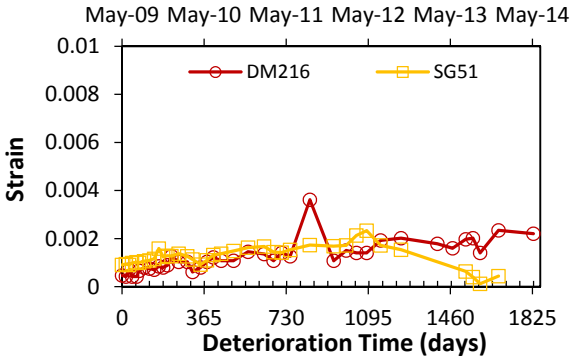

(e) DM216 vs. SG51

Figure 4-19: Comparison of Surface Strains from DEMEC (DM) Points to the Internal Strains from Strain Gages (SG) and Concrete Gages (KM) for Specimen 3.

strains that could be measured by the strain gages and the concrete gages, and the influence of localized effects on the internal strain measurements. The surface strains are also closely related to the reinforcement layout in the region that the expansion strain measurements were made. It is also clear from the data presented in the earlier section that, in general, the expansion strains in the transverse direction were always greater than the strains in the longitudinal direction because of the lower reinforcement ratio in the transverse direction and hence lesser restraint to expansion.

Although the expansion data and the crack widths recorded in this study may seem unlikely in ordinary structures, these observations cannot be completely ruled out in actual structures. For instance, a bridge pier constructed with high alkali content cement and highly reactive aggregates in a coastal region exposed to high moisture and salt water continuously could likely see similar expansion strains and cracks as observed in this study.

4.8 CLOSURE AND KEY FINDINGS

The premature concrete deterioration caused by ASR/DEF induced expansion were monitored by measuring the surface concrete strains through the DEMEC points and from concrete gages embedded within concrete and strain gages attached to the steel reinforcement. The specimen was loaded with post-tensioned tie-bars to simulate gravity loads on the structure. This resulted in load-induced cracks that formed a pathway for moisture ingress into the specimen and evidently helped accelerate the formation of ASR gel in the specimen. The map cracking resulting from ASR/DEF merged with the initial load-induced cracks. Over time, new cracks ceased to form and the existing cracks grew in width. The largest crack width that was observed was 1.18 in. wide. Based on the condition of Specimen 3, the specimen can be categorized as displaying *heavy* deterioration from ASR/DEF expansion.

The transverse and longitudinal steel strains exceeded their yield strain between six months to one year of field conditioning. In general, the expansion strains recorded along the direction of the transverse reinforcement were greater than those along the direction of the longitudinal direction, because of the lower reinforcement ratio in the transverse direction. A comparison of the external expansion strains measured from the DEMEC points with the internal strains from the strain gage and concrete gages showed that the external strains were quite similar to the internal strains recorded.

Although the physical condition of Specimen 3 is concerning, it is not known how the severe nature of ASR/DEF deterioration caused in the specimen affects its structural load carrying capacity. Chapter 6 presents the overall and internal results from the experimental load testing of Specimen 3.

5 APPLICATION OF PROPOSED EXPANSION MODEL TO ESTIMATE EXPANSION STRAINS IN C-BEAM SPECIMEN

5.1 INTRODUCTION

As part of a large scale experimental program described in the Phase I report of this research (Mander et al., 2012), reinforced concrete C-Beam specimens representing cantilever and straddle bent bridge piers were cast and cured to promote ASR/DEF induced expansion in reinforced concrete. Figure 5-1 presents the reinforcement layout and the cross-section details of the C-Beam specimens. To promote ASR in the specimen, high alkali content cement and aggregates with reactive silica along with sodium hydroxide mixed in water were used. The specimens were subjected to curing temperatures in excess of 160°F by means of an electrical resistive wiring setup to promote DEF related expansion in the specimen. The specimens were then transported outdoors and subjected to environmental conditions, as any actual bridge under service would be exposed to. To accelerate the expansion caused by ASR/DEF for purposes of the experimental study, a sprinkler system was installed and the specimens were sprinkled with water at regular intervals. Of the four specimens constructed, Specimen 1 was the control specimen and was stored indoors, while Specimens 2, 3, and 4 were conditioned outdoors and subjected to ASR/DEF deterioration for varying periods of time.

Of the three deteriorated C-Beam specimens, Specimen 3 was conditioned in the field for five years with significant effects of ASR and DEF deterioration observed. The data from the strain and concrete gages embedded in the specimen and DEMEC points on the surface of the specimen were collected on a regular basis. The model proposed for ASR/DEF related expansion in reinforced concrete was applied to the C-Beam specimens, and the results were compared to the field measured DEMEC data obtained for Specimen 3. Later the model was also applied to Specimen 2 and 4 to ensure the repeatability of the proposed expansion model.

5.2 PARAMETERS FOR MODELING EXPANSION IN C-BEAM SPECIMEN

To represent the data collected from the DEMEC points in a meaningful and logical way, the C-Beam specimen was divided into different regions and the DEMEC data categorized accordingly. Figure 5-2a identifies the various regions of the C-Beam specimen used in this

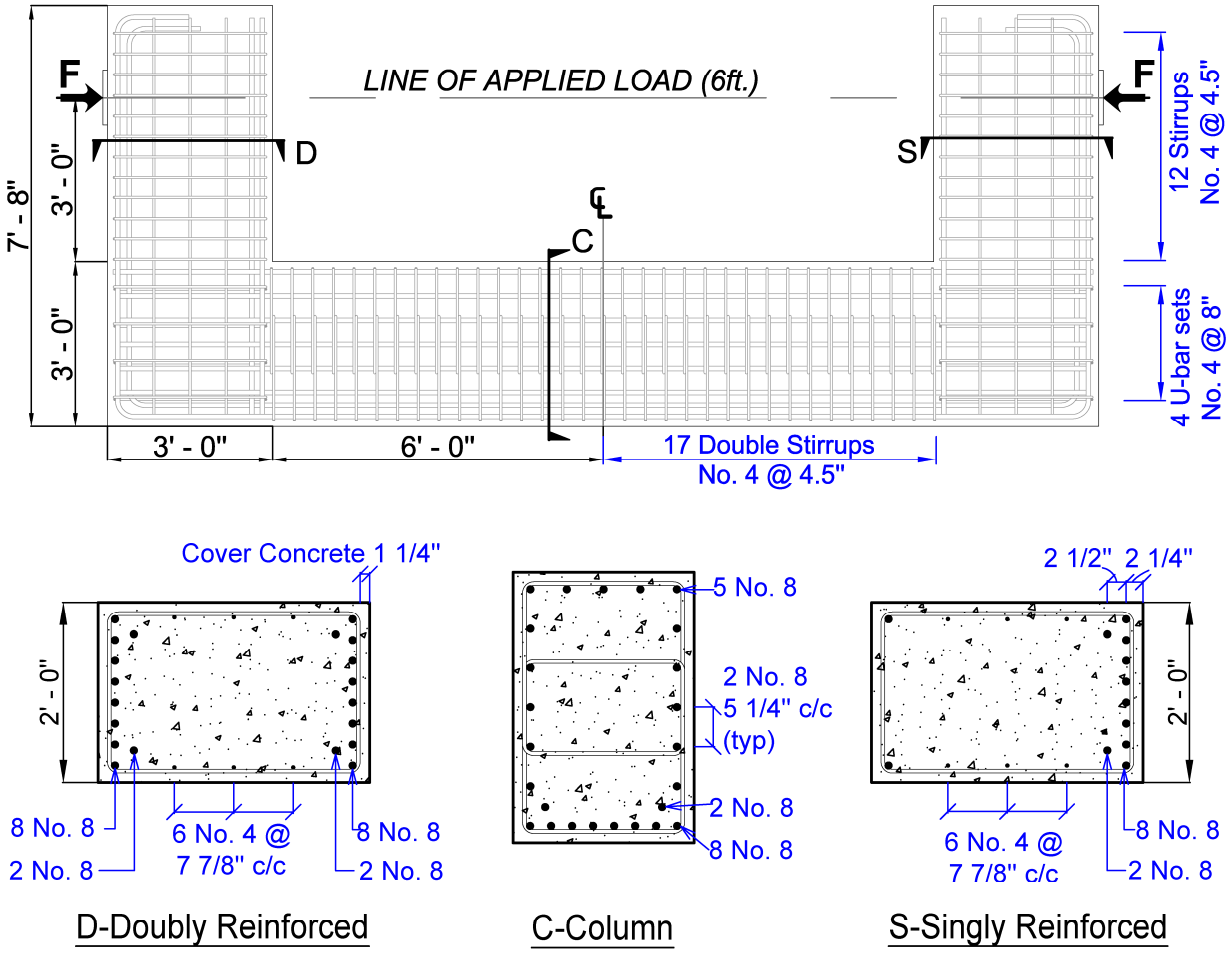

Figure 5-1: Reinforcement Layout of C-Beam Specimen.

study to model expansion strains. The C-Beam specimen is divided into the top face where the exposure face is horizontal, and the west and north side faces where the exposure face is vertical. Figure 5-2a also shows the location and orientation of DEMEC points on the surface of the C-Beam specimen that were used for the purpose of comparison. Longitudinal and transverse strain measurements were made in the different regions of the specimen.

The C-Beam specimens were subjected to both ASR and DEF expansion. Since no clear evidence is available on when and how much each of the two expansion mechanisms contributes toward the total expansion strains in the specimen, the proposed expansion equation is applied once, considering the overall expansion properties. From the experimental results, the time (t_o) when expansion strains initiate was taken as 60 days. The rise time of the tangent line (t_r) was deduced to be 120 days from the expansion data of Specimen 3. Since no data were available on the expansion caused by ASR/DEF expansion in plain concrete ($\varepsilon_o^{\max}$), this parameter was inferred from the largest crack observed from an unreinforced part of the specimen. The largest crack that was observed at the knee-joint of the C-Beam specimen was about 1.18 in. wide. It is to be noted that the top face of the column in the joint region was essentially unreinforced. A crack width of 1.18 in. across a total section width of 24 in., resulted in an expansion strain of approximately 0.05. Therefore, for this study the value of $\varepsilon_o^{\max} = 0.05$ was adopted.

Figure 5-2b shows the relationship between the reinforcement ratio and the maximum expansion strain computed for the various regions of the C-Beam specimen. As expected the maximum expansion strain in the C-Beam specimen decreases with increasing reinforcement ratio. The C-Beam specimen was subjected to tie-bar forces to simulate the effects of gravity loads on the structure. These induce tensile stresses promote cracking. These effects are also taken into account while computing the maximum expansion strain, $\varepsilon_\rho^{\max}$. In Figure 5-2b two curves are presented, one where there are no tensile prestrain effects on the expansion strain and the other with the tensile prestrain effects considered. It is clear that for the same reinforcement ratio, the maximum expansion strain is greater when the tensile prestrain effects are considered. This is complimentary to the case where compressive strains cause lower expansion strains as shown in Figure 3-9b. The computation of the reinforcement ratio is discussed in detail in Appendix I. To account for the variation in expansion due to temperature and moisture content, the average daily

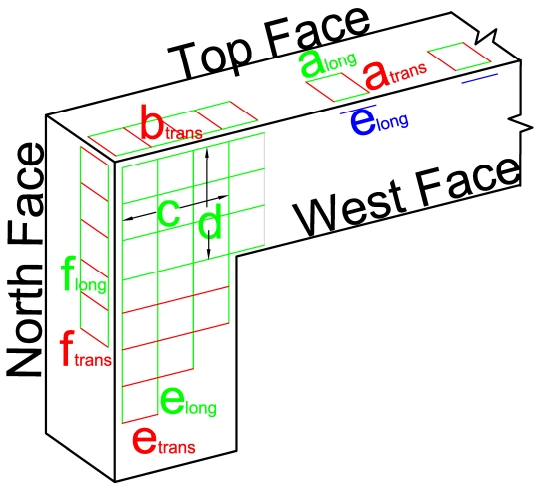

(a) DEMEC Layout of C-Beam Specimen

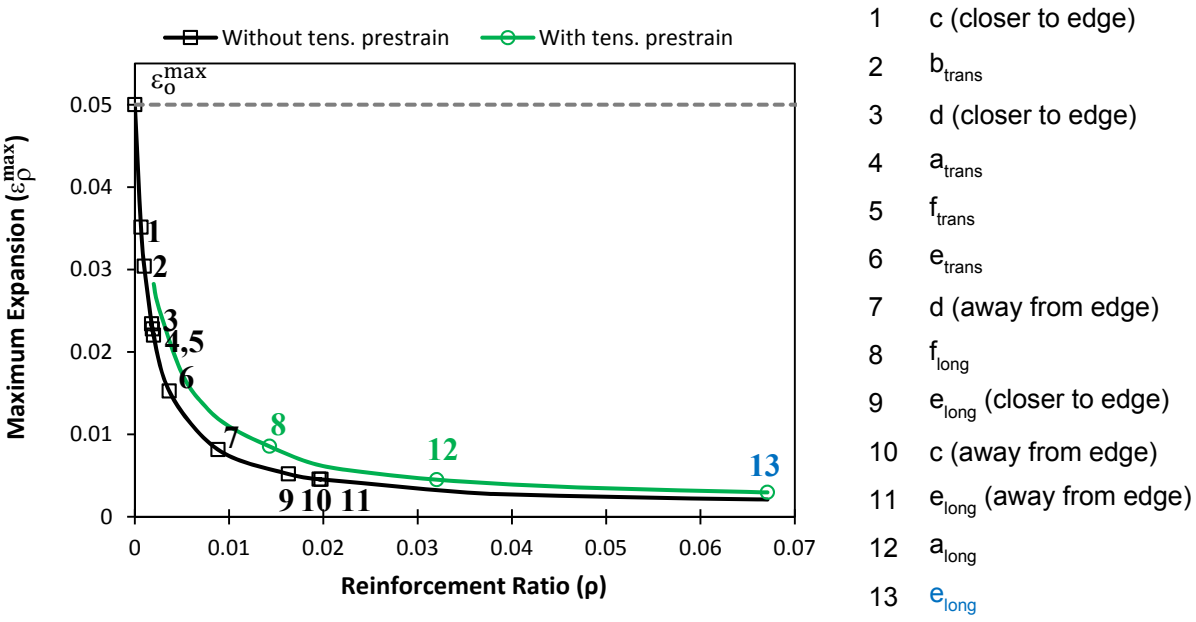

(b) Variation of Maximum Expansion with Reinforcement Ratio

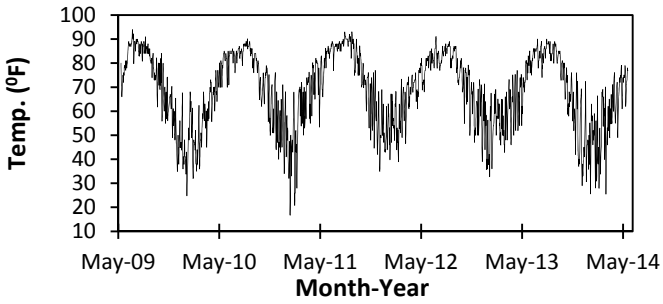

(c) Observed Average Daily Temperature

Figure 5-2: Information Pertinent to Model Expansion Strains in C-Beam Specimen.

temperature and rainfall amounts were obtained from the closest weather station to the site where the specimens were conditioned. Additionally, to obtain a reasonable estimate of the actual amount of moisture that the specimens were subjected to due to supplemental water from the sprinkler system, a series of rain gages were installed at various locations on Specimen 3. For this study a degree of saturation of $S = 0.1$ was assumed for the horizontal exposure surfaces and for strains measured in the horizontal direction caused by cracks in the vertical direction. The vertical cracks allow better ingress of moisture into the specimen, and the related expansion causes horizontal strains. For strains measured in the vertical direction caused by horizontal cracks on the vertical exposure face, a degree of saturation of $S = 0.05$ was adopted as the horizontal cracks do not allow for moisture ingress into the specimen as well as the vertical cracks. The temperature and moisture content data were used in the computation of expansion strains in the reinforced concrete C-Beam specimens. Figure 5-2c shows the variation of the daily average temperature recorded at the closest weather station to the site for the period when Specimen 3 was exposed to field conditions.

Also taken into account in the computation of the maximum expansion strain are the tensile strains induced by the applied tie-bar force used to mimic gravity loads on the specimen. The C-STM model of the C-Beam specimen that was developed by Mander et al. (2012) was used to determine the initial strains. As shown in Figure 5-3, a 200 kip load corresponding to the tie-bar force was applied and the corresponding tensile strains were obtained from the model. The values of the tensile strains in concrete and steel are shown in Figure 5-3. The applied tie-bar force caused tensile stresses in the longitudinal direction along the outer edges of the specimen, which resulted in a tensile prestrain. However, there were no stresses applied in the out-of-plane direction of the specimen, hence there are no prestrains that contribute to the expansion in the out-of-plane direction. However, the presence of transverse reinforcement restrains the expansion in the out-of-plane direction.

Another important parameter that is required for the implementation of the proposed expansion model is the reinforcement ratio of the specimen. As the DEMEC points were located on the surface of the specimen, the influence of reinforcing steel are different at the various DEMEC locations. Hence, it is essential to carefully compute the reinforcement ratio for the different regions of the specimen. In this study, various reinforcement ratios were computed based on the location and direction of the DEMEC strain measurements, and is explained in detail in Appendix I.

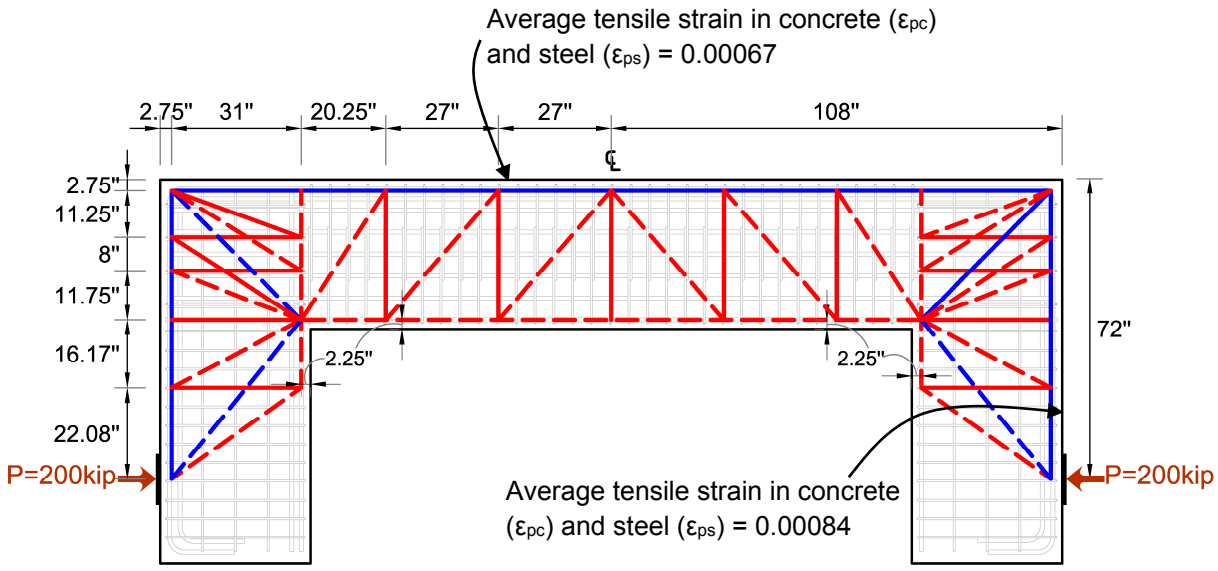

Figure 5-3: Computation of Average Tensile Loads from C-STM in the C-Beam Specimen due to Post-Tension Load.

Table 5-1: Properties for C-Beam Specimen.

	Specimen 3	Specimen 2	Specimen 4
$f_c^{'}(ksi)$	5.93	5.6	4
$kd_{col}(in.)$	13.98	13.89	15.22
$kd_{beam}(in.)$	11.31	10.31	11.31
$l_d(in.)$ for #8 bars	42.20	43.40	51.40
$l_d(in.)$ for #4 bars	16.88	17.40	20.10

5.3 MODELING ASR/DEF EXPANSION IN C-BEAM SPECIMEN

Table 5-1 presents the properties of C-Beam specimen that were used in calculating the reinforcement ratios, where kd_{col} and kd_{beam} are the depth of the neutral axis from the extreme compression fiber for the column and the beam, respectively, and l_d is the development length of the reinforcement. Table 5-2 presents the reinforcement ratio and the maximum expansion strains for the various regions of C-Beam Specimen 3 (see Appendix I for details).

For the purpose of comparing the modeled expansion results with the field data, the averages of the DEMEC data from Specimen 3 were computed and presented as data points in Figure 5-4. The upper and lower extremities of the observed field data are also presented. The surface strains in both the longitudinal and transverse directions are considered for the different regions described in Figure 5-2a. Figure 5-4 also shows a comparison of the proposed model results represented by solid lines with the field data.

Figure 5-4a and b, respectively, consider the member region and the joint region of the C-Beam specimen top face. In the top face member region, the expansion strains in the transverse and longitudinal directions were considered. The concrete and steel volume from the extreme tension fiber to the neutral axis was used in the computation of the reinforcement ratio. In the longitudinal direction, DEMEC measurements were made along two lines, one close to the edge of the column, and the other closer to the middle of the column cross-section as shown in the legend of Figure 5-4. As the DEMEC readings were limited to two lines, the measured strains could be more localized and the reinforcement ratios were computed accordingly as shown in Appendix I. The tensile strains due to the tie-bar force computed from the C-STM analysis as shown in Figure 5-3 resulted in a tensile concrete and steel strain of 0.00067 and were appropriately incorporated into computing the maximum expansion strain, $\varepsilon_{\rho}^{\max}$. Figure 5-4a shows the expansion results obtained in the transverse and longitudinal direction on the column top face member region of the C-Beam specimen.

Figure 5-4b considers the transverse expansion strains in the joint region of the C-Beam specimen top face. As there were no transverse U-bars in the joint region, this region is essentially unreinforced in the transverse direction. Therefore a reinforcement ratio of $\rho = 0$ was considered

Table 5-2: Computation of Reinforcement Ratio and Maximum Expansion Strain for C-Beam Specimen 3.

Region	Dir.	Section Depth (in.)	Concrete Width (in.)	Rebar Considered		ρ	Max. Expansion Strain	Eq. No.	Comments
				No.	Bar (#)				f_c'=5.93 ksi; kd_{col}=13.98"; kd_{beam}=11.31"
(a) Column Top-Member	Long.	22.02	2.785			0.03202	0.0045	3-16a	Average ρ of edge (4-#8, ρ=0.05122) and interior (1-#8, ρ=0.01281) strips. ε_{pc}= ε_{ps}=0.00067.
	Trans.	22.02	---	---	4	0.00198	0.02202	3-16a	
(b) Column Top-Joint	Trans.					0.00099	0.03040	3-16a	ρ=0 close to edge and ρ=half of (a) Column Top-Member Trans. (0.00191) away from edge.
(c) West Face Joint Vertical	Long.	12	6.1875	5	8	0.01974	0.004532	3-16a	Considering edge and scaled for 2nd level of DEMEC points. l_d=42.20", x=15.75", ρ=0.0529.
	Long.	12	23.625	3	4	0.00065	0.03514	3-16a	Considering interior and scaled for 1st level of DEMEC points. l_d=16.88", x=5.25", ρ=0.00208.
(d) West Face Joint Horizontal	Long.	12	36	12	8	0.00881	0.00816	3-16a	Scaled for 2nd level of DEMECs. l_d=42.20", x=15.75", ρ=0.0236.
				4	4				
	Long.	12	36	5	8	0.00186	0.02278	3-16a	Considering interior region and scaled for 1st level of DEMEC points. l_d=42.20", x=5.25", ρ=0.01496.
				4	4				
(e) West Face-Beam	Long.	12	36	10	8	0.01954	0.00456	3-16a	Considering steel and concrete in 12" depth.
				3	4				
						0.01628	0.00519		Scaled for 2nd level of DEMECs. l_d=42.20", x=35.15", ρ=0.01954
	Trans.	12	---	---	4	0.00364	0.01526	3-16a	
(e) West Face-Column	Long.	12	4.875	5	8	0.0671	0.00296	3-16a	
(f) North Face-Beam	Long.	24.69	2.785			0.01428	0.00855	3-16a	Average ρ of edge (1-#8 and 2-#4, ρ=0.01713) and interior (1-#8, ρ=0.01142) strips. ε_{pc}= ε_{ps}=0.00084.
	Trans.	24.69	---	---	4	0.00177	0.02341	3-16a	

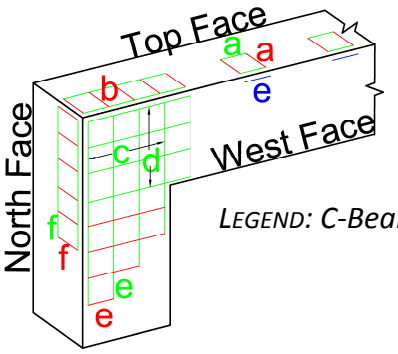

LEGEND: C-Beam Specimen DEMEC Locations

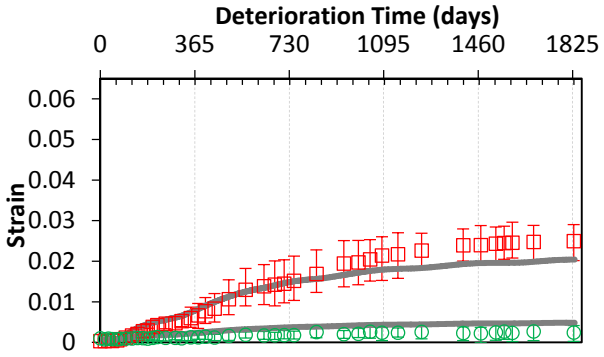

(a) Member

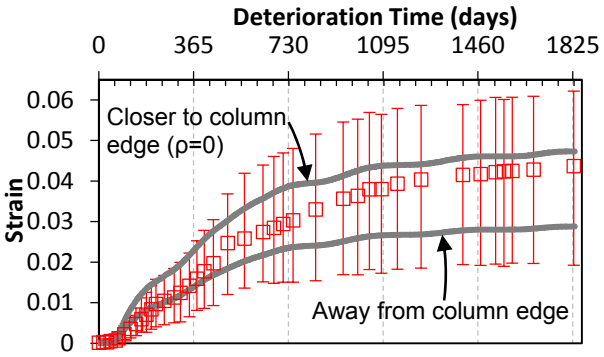

(b) Joint

Top Face (Horizontal Exposure Face)

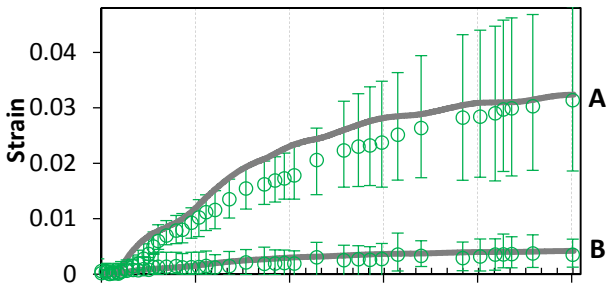

(c) Joint Vertical Direction

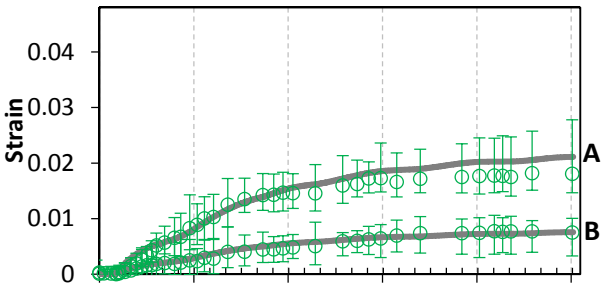

(d) Joint Horizontal Direction

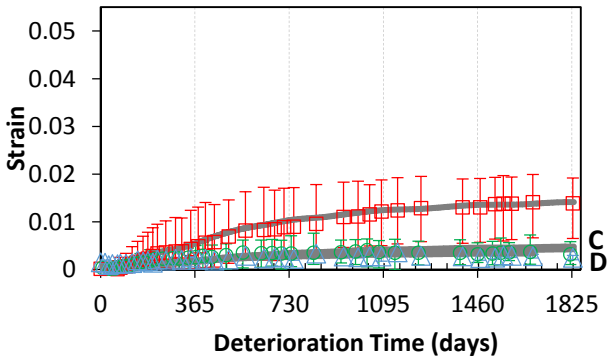

(e) West Face

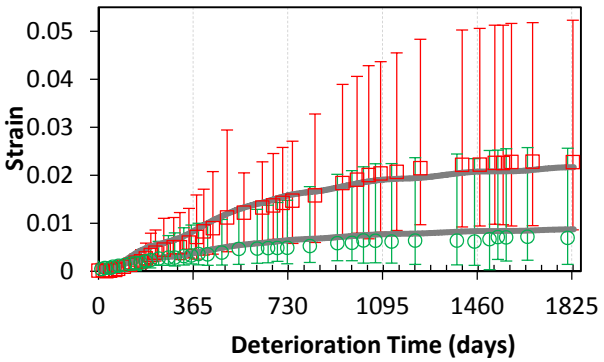

(f) North Face

Side Faces (Vertical Surface Exposed)

Note: A/B: Within Dev. Length Zone Closer/Away from Edge; C/D: Inside/Outside Dev. Length Zone

Figure 5-4: Observed and Computed Expansion Strain–Specimen 3.

for this case. However, the transverse reinforcement in the column region can likely influence the expansion strains caused in the joint region away from the edge of the joint. Therefore, a case with half the transverse reinforcement ratio in the column region is also presented in Figure 5-4b.

Figure 5-4c and d, respectively, consider the expansion strain in the vertical and horizontal directions in the beam-column joint region of the C-Beam specimen's west face. Concrete and steel volume in half the section-depth (12 in.) was considered for calculating the reinforcement ratio.

Depending on the location of the DEMEC points in the vertical direction of the beam-column joint, separate reinforcement ratios were computed as shown in Appendix I. Additionally, Mander et al. (2011) showed that to develop the full yield strength of the reinforcement, the reinforcing bars transverse to the member edge should be longer than the bar development length (l_d). Therefore, scaled reinforcement ratios were considered for DEMEC points within the development length zone. Figure 5-4c shows two curves for the expansion results from the model. Curve A corresponds to the case where the expansion strains were computed closer to the top edge of the specimen (within development length zone close to top edge) and Curve B for expansion strains computed away from the top edge (within development length zone away from top edge).

Figure 5-4d shows a comparison of the model with the field data for the horizontal expansion strains from DEMEC points in the direction of the column longitudinal reinforcement in the joint region. As in the earlier case, half section-depth of 12 in. was used for the computation of reinforcement ratio, and the reinforcement ratio was scaled down accordingly within the development length zone. In Figure 5-4d, Curves A and B, respectively, correspond to the case where the expansion strains were computed closer to the top edge and away from the top edge of the specimen, both still within the development length zone.

Figure 5-4e shows the longitudinal expansion strains in the column and the longitudinal and transverse expansion strains in the beam of the C-Beam specimen's west face. The reinforcement ratios were computed considering half-depth (12 in.) of the cross-section. The DEMEC points in the column of the specimen west face were located close to the specimen top edge, and the reinforcement ratio was computed accordingly to account for the localized nature of the DEMEC readings. The tensile concrete and steel strains due to the applied tie-bar force were

computed to be 0.00067 from the C-STM model shown in Figure 5-3, and they were incorporated into computing the maximum expansion strains. For the longitudinal expansion strains in the beam of the C-Beam specimen west face, scaled reinforcement ratios were considered for DEMEC points within the development length zone. Figure 5-4e shows the expansion results from the model, where Curves C and D, respectively, represent the expansion strains inside and outside the development length zone. In this case it is observed that there is not much difference between the two cases, as the DEMEC measurements were made relatively away from the specimen edges.

Figure 5-4f shows the expansion strains in the longitudinal and transverse direction of the C-Beam specimen's north face. The depth of the beam cross-section from the extreme tension fiber to the neutral axis was considered for the computation of the reinforcement ratios. As in the case of the column top face, the longitudinal DEMEC measurements in the beam were made along two lines, one close to the edge of the beam, and the other closer to the middle of the beam cross-section, as shown in the legend of Figure 5-4. The strains measured could be more localized as the DEMEC readings were limited to two lines, and the reinforcement ratios were computed accordingly as shown in Appendix I. The tensile strains due to the tie-bar force computed from the C-STM analysis as shown in Figure 5-3, resulted in a tensile concrete and steel strain of 0.00084 and were appropriately incorporated in computing the maximum expansion strain. Figure 5-4f shows the simulated transverse and longitudinal expansion strains on C-Beam specimen north face.

To ensure the repeatability of the proposed model, the model was also applied to two other deteriorated C-Beam specimens (Specimens 2 and 4) that were part of the study by Mander et al. (2012). Specimens 2 and 4 were subjected to the outdoor deterioration program for nine months and two years, respectively, and were classified as slightly and moderately deteriorated specimens. In a manner similar to that of Specimen 3, the reinforcement ratios and the corresponding maximum expansion strain were calculated for Specimens 2 and 4. Table 5-1 shows the properties of Specimens 2 and 4 that were necessary for the computation of the reinforcement ratios for the different regions of the C-Beam specimens. Table 5-3 and Table 5-4, respectively, show the computation of the reinforcement ratio and the maximum expansion strains for Specimens 2 and 4. Figure 5-5 shows a comparison of the expansion strains obtained from the model with the field data for the different regions of the C-Beam Specimen 2. Similarly, Figure 5-6 compares the expansion from the model with the field data for Specimen 4.

Table 5-3: Computation of Reinforcement Ratio and Maximum Expansion Strain for C-Beam Specimen 2.

Region	Dir.	Section Depth (in.)	Concrete Width (in.)	Rebar Considered		ρ	Max. Expansion Strain	Eq. No.	Comments
				No.	Bar (#)				f_c'=5.6 ksi; kd_{col}=13.44"; kd_{beam}=10.63"
(a) Column Top-Member	Long.	22.56	2.785			0.03125	0.00378	3-16b	Average ρ of edge (4-#8, ρ=0.050) and interior (1-#8, ρ=0.01250) strips. ε_{pc}= ε_{ps}=0.00067.
	Trans.	22.56	---	---	4	0.00193	0.01135	3-16b	
(b) Column Top-Joint	Trans.					0.00097	0.03036	3-16a	ρ=0 close to edge and ρ=half of (a) Column Top-Member Trans. (0.00193) away from edge.
(c) West Face Joint Vertical	Long.	12	6.1875	5	8	0.01919	0.00394	3-16b	Considering edge and scaled for 2nd level of DEMEC points. l_d=43.4", x=15.75", ρ=0.0529.
	Long.	12	23.625	3	4	0.00063	0.0181	3-16b	Considering interior and scaled for 1st level of DEMEC points. l_d=17.4", x=5.25", ρ=0.00208.
(d) West Face Joint Horizontal	Long.	12	36	12	8	0.00857	0.00577	3-16b	Scaled for 2nd level of DEMECs. l_d=43.4", x=15.75", ρ=0.0236.
				4	4				
	Long.	12	36	5	8	0.00181	0.01169	3-16b	Considering interior region and scaled for 1st level of DEMEC points. l_d=43.4", x=5.25", ρ=0.01496.
				4	4				
(e) West Face-Beam	Long.	12	36	10	8	0.01954	0.0039	3-16b	
				3	4				
						0.01583	0.00431		Scaled for 2nd level of DEMECs. l_d=43.4", x=35.15", ρ=0.01954
	Trans.	12	---	---	4	0.00364	0.00857	3-16b	
(e) West Face-Column	Long.	12	4.875	5	8	0.0671	0.00281	3-16b	$\varepsilon_{pc} = \varepsilon_{ps} = 0.00067$.
(f) North Face-Beam	Long.	25.375	2.785			0.01389	0.00543	3-16b	Average ρ of edge (1-#8 and 2-#4, ρ=0.01667) and interior (1-#8, ρ=0.0111) strips. $\varepsilon_{pc} = \varepsilon_{ps} =$ 0.00084.
	Trans.	25. 375	---	---	4	0.00172	0.01195	3-16b	

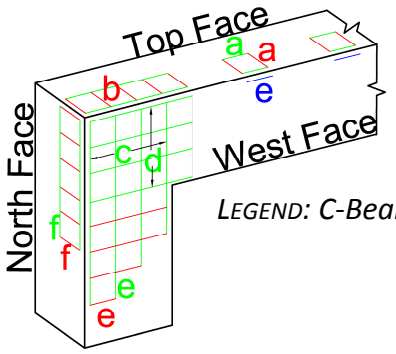

LEGEND: C-Beam Specimen DEMEC Locations

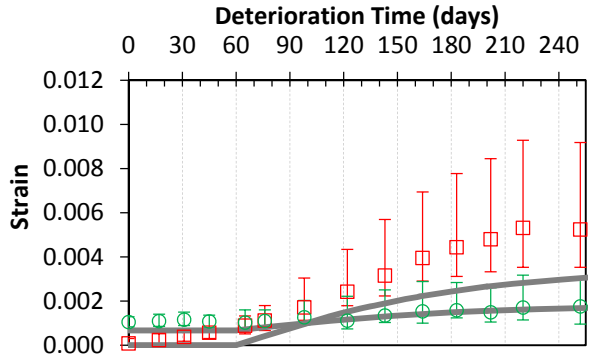

(a) Member

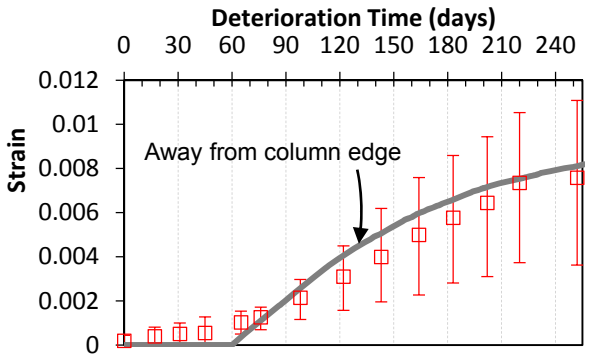

(b) Joint

Top Face (Horizontal Exposure Face)

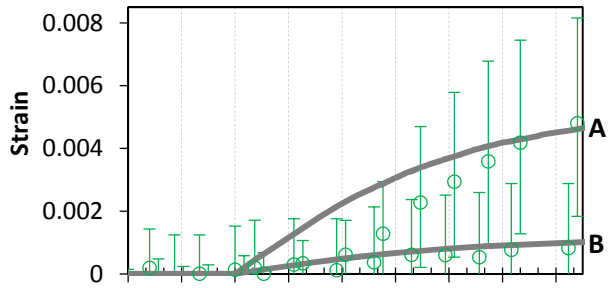

(c) Joint Vertical Direction

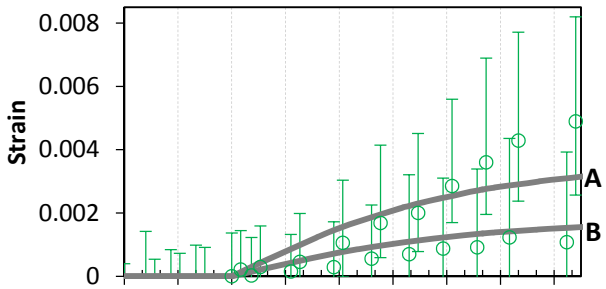

(d) Joint Horizontal Direction

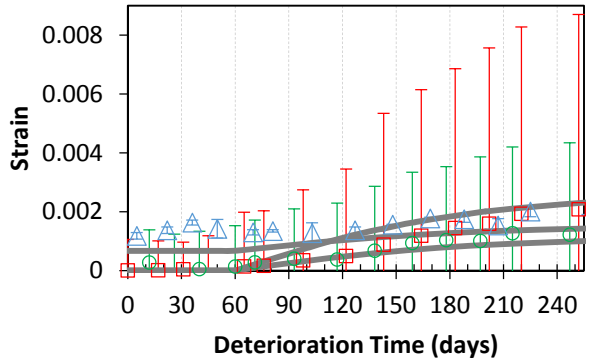

(e) West Face

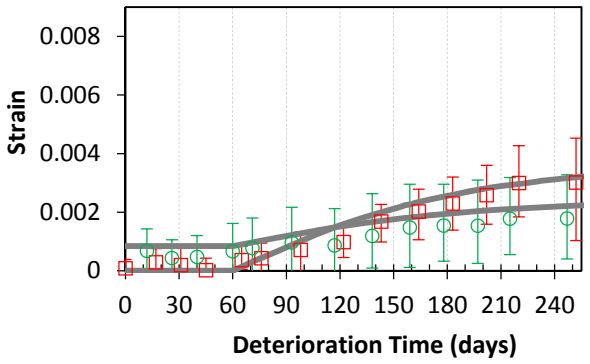

(f) North Face

Side Faces (Vertical Surface Exposed)

Note: A/B: Within Dev. Length Zone Closer/Away from Edge

Figure 5-5: Observed and Computed Expansion Strain–Specimen 2.

Table 5-4: Computation of Reinforcement Ratio and Maximum Expansion Strain for C-Beam Specimen 4.

Region	Dir.	Section Depth (in.)	Concrete Width (in.)	Rebar Considered		ρ	Max. Expansion Strain	Eq. No.	Comments
				No.	Bar (#)				f_c'=4 ksi; kd_{col}=14.90"; kd_{beam}=12.10"
(a) Column Top-Member	Long.	21.11	2.785			0.03339	0.00389	3-16b	Average ρ of edge (4-#8, ρ=0.05343) and interior (1-#8, ρ=0.01334) strips. $\varepsilon_{pc} = \varepsilon_{ps} = 0.00067$.
	Trans.	21.11	---	---	4	0.00207	0.01921	3-16b	
(b) Column Top-Joint	Trans.					0.00104	0.02753	3-16a	ρ=*0* close to edge and ρ=half of (a) Column Top-Member Trans. (0.00207) away from edge.
(c) West Face Joint Vertical	Long.	12	6.1875	5	8	0.01621	0.00394	3-16b	Considering edge and scaled for 2nd level of DEMEC points. l_d=51.4", x=15.75", ρ=0.0529.
	Long.	12	23.625	3	4	0.00054	0.01794	3-16b	Considering interior and scaled for 1st level of DEMEC points. l_d=20.1", x=5.25", ρ=0.00208.
(d) West Face Joint Horizontal	Long.	12	36	12	8	0.00723	0.00577	3-16b	Scaled for 2nd level of DEMECs. l_d=51.4", x=15.75", ρ=0.0236.
				4	4				
	Long.	12	36	5	8	0.00153	0.01168	3-16b	Considering interior region and scaled for 1st level of DEMEC points. l_d=51.4", x=5.25", ρ=0.01496.
				4	4				
(e) West Face-Beam	Long.	12	36	10	8	0.01954	0.00398	3-16a	
				3	4				
						0.01336	0.0052		Scaled for 2nd level of DEMECs. l_d=51.4", x=35.15", ρ=0.01954.
	Trans.	12	---	---	4	0.00364	0.01336	3-16a	
(e) West Face-Column	Long.	12	4.875	5	8	0.06714	0.00269	3-16b	$\varepsilon_{pc} = \varepsilon_{ps} = 0.00067$.
(f) North Face-Beam	Long.	23. 91	2.785			0.01474	0.00496	3-16b	Average ρ of edge (1-#8 and 2-#4, ρ=0.01769) and interior (1-#8, ρ=0.01180) strips. $\varepsilon_{pc} = \varepsilon_{ps} = 0.00084$.
	Trans.	23.91	---	---	4	0.00182	0.01083	3-16b	

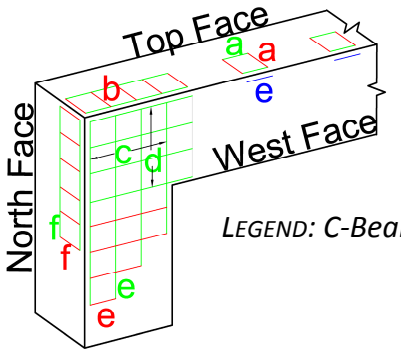

LEGEND: C-Beam Specimen DEMEC Locations

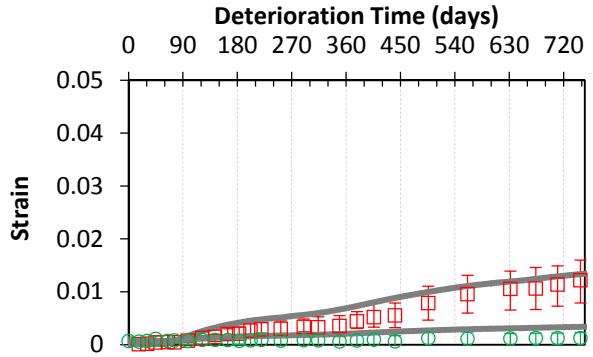

(a) Member

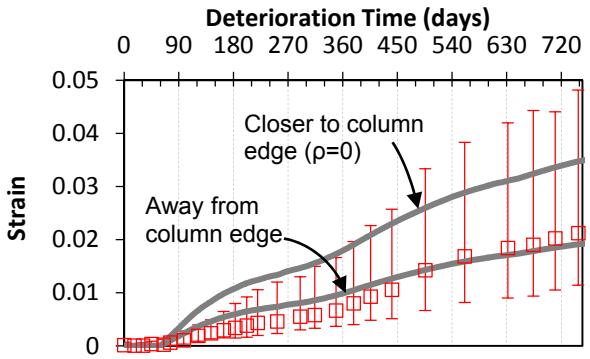

(b) Joint

Top Face (Horizontal Exposure Face)

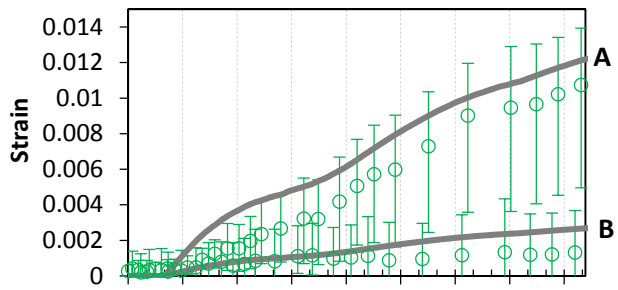

(c) Joint Vertical Direction

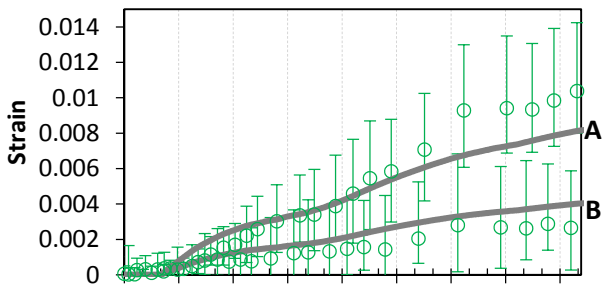

(d) Joint Horizontal Direction

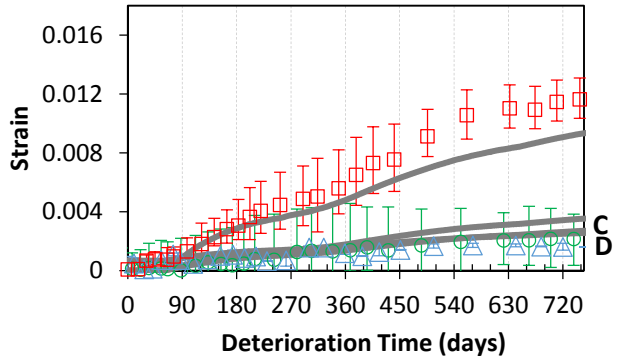

(e) West Face

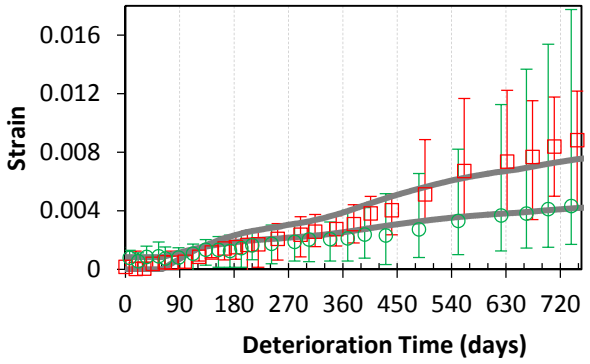

(f) North Face

Side Faces (Vertical Surface Exposed)

Note: A/B: Within Dev. Length Zone Closer/Away from Edge; C/D: Inside/Outside Dev. Length Zone

Figure 5-6: Observed and Computed Expansion Strain–Specimen 4.

5.4 DISCUSSION

Considering the complex nature of ASR/DEF related expansion in reinforced concrete and the vagaries associated with the expansion data gathered from the field, a comparison of the simulated expansion results and the field observations shows that the proposed model can be used to simulate the expansion strains in reinforced concrete reasonably well. In most cases the simulated results were within the range of measured field expansion data for the specimens.

The effects of tensile strains caused by gravity loads on ASR/DEF expansion were also taken into account in the model to simulate the expansion results with good accuracy. The tie-bar force that was applied to simulate gravity loads in the C-Beam specimens caused tensile stresses along the tension side of the specimen. These tensile stresses caused pre-cracking that promoted ASR/DEF expansion. The tensile pre-strains along the direction of the longitudinal reinforcement were considered in the model. However, the tie-bar force did not cause any stresses in the transverse (out-of-plane) direction of the specimen and hence the tensile prestrains were not considered in modeling the strains along the direction of the transverse reinforcement.

The computed expansion strains from the model were compared to the strains from the DEMEC points, which measured surface strains. Chapter 4 demonstrated that similar strains were recorded between the DEMEC points that measured external expansion strains and the internal strain gages that measured the internal strains. However, when very large surface strains were measured on the specimens, the DEMEC readings did not compare well with the internal strains because of the limitations on the range of strains that could be measured by the internal gages, and the influence of localized effects on the internal strain measurements. Additionally, it is possible to install DEMEC points on existing structures and monitor them over time, to get an estimate of the parameters that are required to drive the model. As demonstrated in the chapter, it is extremely important to compute the relevant reinforcement ratio, as it affects the extent of expansion that can be caused by ASR/DEF.

Due to the orientation of the specimen during its field conditioning, different parts of the specimen were subjected to various amounts of moisture and hence different degrees of saturation. To account for this, the degree of saturation for the horizontal exposure faces and for strains caused by vertical cracks on the vertical exposure faces was assumed to be greater than the degree of

saturation for the strains caused by horizontal cracks in the vertical exposure face. This assumption was also backed by the field expansion data. In an actual structure, many of these parameters cannot be determined realistically, and therefore it is important to assume relevant values based on sound reasoning.

The results of this investigation show that if appropriate values are assigned to the limited input parameters required for the model, the proposed minimalist semi-empirical model can be effectively used to model the ASR/DEF induced expansion in reinforced concrete members that are exposed to field conditions.

5.5 CLOSURE AND KEY FINDINGS

By taking into account the appropriate input parameters for the proposed expansion model, the expansion strains caused by ASR/DEF in reinforced concrete specimen can be estimated within reasonable bounds as demonstrated in this chapter. Considering the wide scatter in the field measured strains, the model predicts the general expansion behavior reasonably well. The key observations and findings from this chapter are summarized below:

- Depending on the region of the specimen that is being considered, the moisture content and hence the degree of saturation can be different. Especially, on the horizontal exposure faces, water tends to pool/stand for longer when compared to the vertical exposure face, where the water runs off almost immediately.

- The orientation of the cracks can also lead to differences in the expansion strain behavior. On vertical exposure faces, vertical cracks that cause horizontal expansion strains allow for more rapid water ingress into the specimen through the cracks, when compared to horizontal cracks, which results in vertical strains.

- The expansion data obtained from the field vary widely. Much of the scatter can be explained based on the influence of the neighboring reinforcement, the location of strain (DEMEC) measurements, and the orientation of the exposure face.

- The proposed model takes into account the tensile prestrains caused by the tie-bar force (which simulates gravity loads) in the direction of the longitudinal reinforcement.

- Considering the complex nature of the C-Beam specimen and ASR/DEF induced expansion strains, the proposed model captures the expansion strains caused by ASR/DEF quite well.

6 EXPERIMENTAL INVESTIGATION OF LARGE-SCALE SPECIMENS WITH HEAVY ASR/DEF DETERIORATION

6.1 INTRODUCTION

To study the effects of ASR/DEF deterioration on reinforced concrete specimens a total of four specimens were designed, constructed, subjected to outdoor weather conditioning, and finally tested in the laboratory to identify the ultimate load carrying capacity. Of the four specimens, Specimen 1 was the control specimen and was stored indoors under climate controlled conditions, without exposure to moisture. Specimens 2, 3, and 4 were placed outdoors and weathered for varying durations up to five years. To accelerate the possibility of deterioration from the effects of ASR/DEF a supplemental water sprinkler system was used to increase the number of wetting and drying cycles experienced. Specimens 2 and 4, respectively, were conditioned for a period of nine months and two years and were classified to have *slight* and *moderate* deterioration due to ASR/DEF effects. The control Specimen 1 and the deteriorated Specimens 2 and 4 were tested in the laboratory and their results presented in the Phase 1 report of this investigation (Mander et al., 2012). From the results reported in Mander et al. (2012), it was evident that Specimens 2 and 4 with slight and moderate amounts of ASR/DEF deterioration had greater stiffness and strength, and slightly greater ductility when compared to the control Specimen 1. The mode of failure in all the three specimens was observed to be the same, which was a brittle joint shear failure within the beam-column joint. It was concluded that the slightly higher strength was due to the beneficial effect of the prestress induced by the ASR- or DEF-induced swelling strains in the concrete.

Specimen 3, which is the specific subject of this experimental investigation, was subjected to the deterioration program for a total exposure period of five years. From the field observations, Specimen 3 can be classified as having *heavy* deterioration due to ASR/DEF effects. It is considered important to compare the performance of Specimen 3 with the control Specimen 1, and the deteriorated Specimens 2 and 4 to evaluate the significance of *heavy* deterioration due to ASR/DEF effects.

This chapter presents the experimental procedures along with the overall force-deformation behavior of Specimen 3. The experimental test results are compared with the other three specimens

previously tested. Conclusions are thus drawn on how heavy ASR/DEF deterioration affects the structural performance of reinforced concrete bridge piers.

6.2 EXPERIMENTAL INVESTIGATION

6.2.1 Concrete Compressive Strength

During the construction of each specimen, standard 4 in. by 8 in. concrete cylinders were cast according to ASTM Standard C31 (ASTM-C31, 2008) so that concrete compression strength data of cylinder tests in accordance with ASTM C39 (ASTM-C39, 2008) could be determined by accepted practices. One-half of these cylinders were stored in a curing/wet room at 100 percent humidity and 73.4°F, while the other half were stored at the same location and conditions as their companion specimens. Figure 6-1a and b, respectively, show the physical state of the concrete cylinders that were conditioned in the wet room under 100 percent humidity and in the field adjacent to Specimen 3. Compared to the cylinders cured in the wet room, it is evident that the concrete cylinders that were conditioned outdoors and subjected to alternate wetting and drying cycles were more heavily damaged from the adverse swelling strain effects of ASR/DEF.

Table 6-1 presents the measured compressive strength of standard 4 in. by 8 in. concrete cylinders at the time of testing for Specimens 3. Owing to the severely cracked nature of the field-cured cylinders, they consistently show much lower compressive strength compared to the wet-room cured specimen.

6.2.2 Experimental Test Setup

The experimental setup that was used by Mander et al. (2012) to test Specimen 4 was used for testing Specimen 3 with slight modifications. Figure 6-2a and b, respectively, show the three-dimensional view and the actual experimental test setup. Figure 6-3 shows the plan and front elevation view of the experimental test setup. One 220 kip MTS (model 244.51S) actuator in displacement control was used in this setup. As in the earlier tests of C-Beam specimen by Mander et al. (2012), the specimen was oriented such that the column was placed on two hinge supports, and the beams were oriented vertically. The actuator was placed on one side of the specimen at a distance of 22 in. from the surface of the specimen to the centerline of the actuator. On the other

(a) Wet-Room Cured Cylinder *(b) Field-Cured Cylinder*

Figure 6-1: Comparison of Cured and Field Cylinders.

Table 6-1: Concrete Material Properties of C-Beam Specimen 3.

Concrete Properties	**28 days**		**Time of Testing 1977 days**	
	Wet-Room Cured	Field-Cured	Wet-Room Cured	Field-Cured
$f_c^{'}(ksi)$	5.14 5.31; 4.97	5.19 5.25; 5.14	5.93 5.46; 6.11; 6.10; 6.06	1.86 1.58; 1.85; 1.70; 2.30
$E_c(ksi) = 1800\sqrt{f_c^{'}(ksi)}$	4080	4100	4380	2454

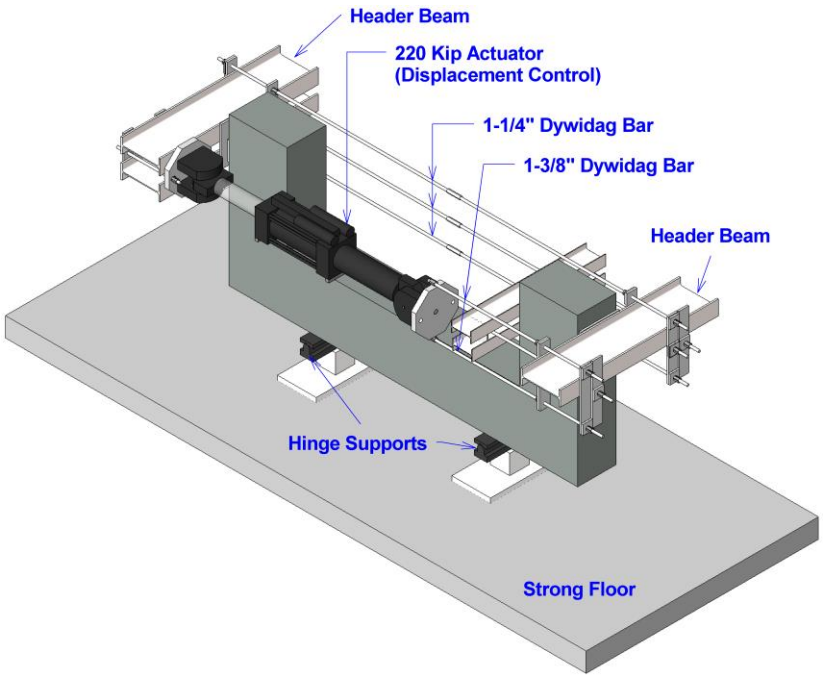

(a) 3-D View of the Experimental Setup

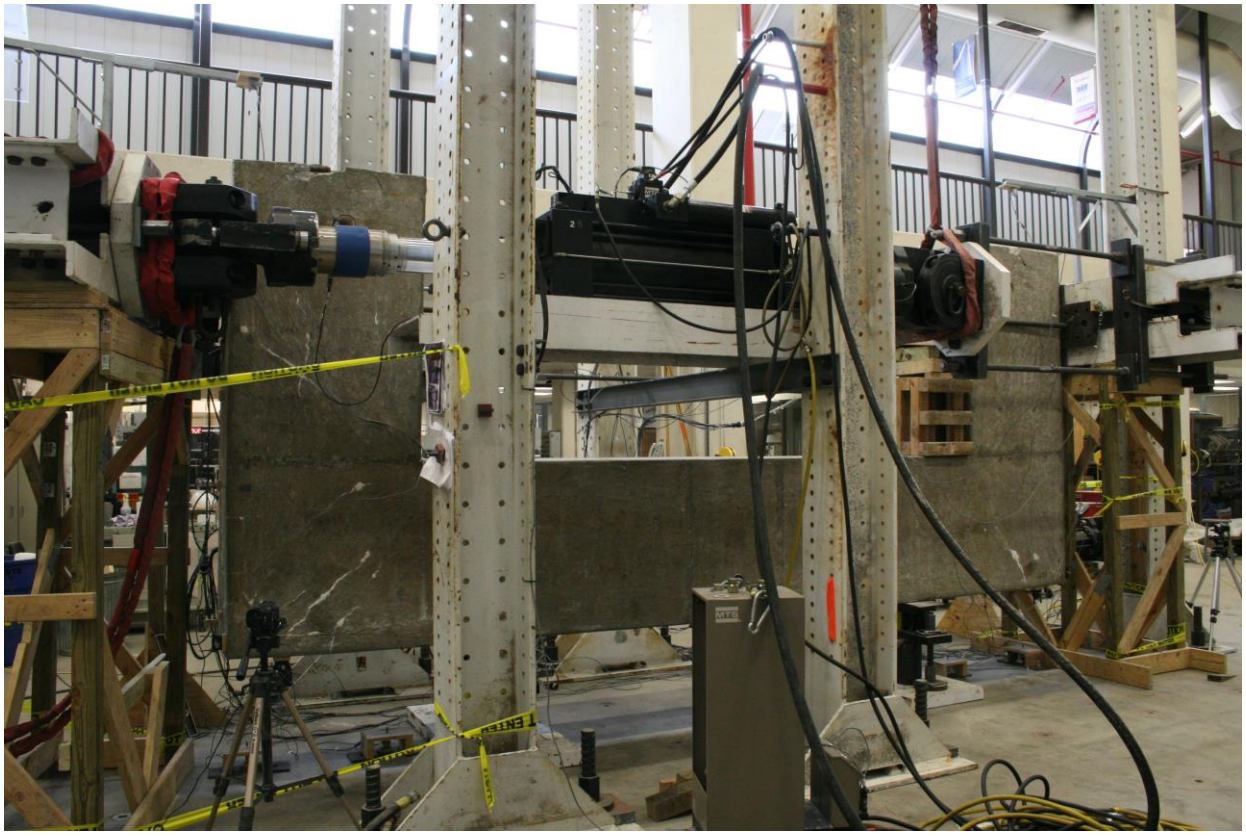

(b) Experimental Setup at High-Bay Laboratory, Texas A&M University, College Station

Figure 6-2: Experimental Test Setup for C-Beam Specimen 3.

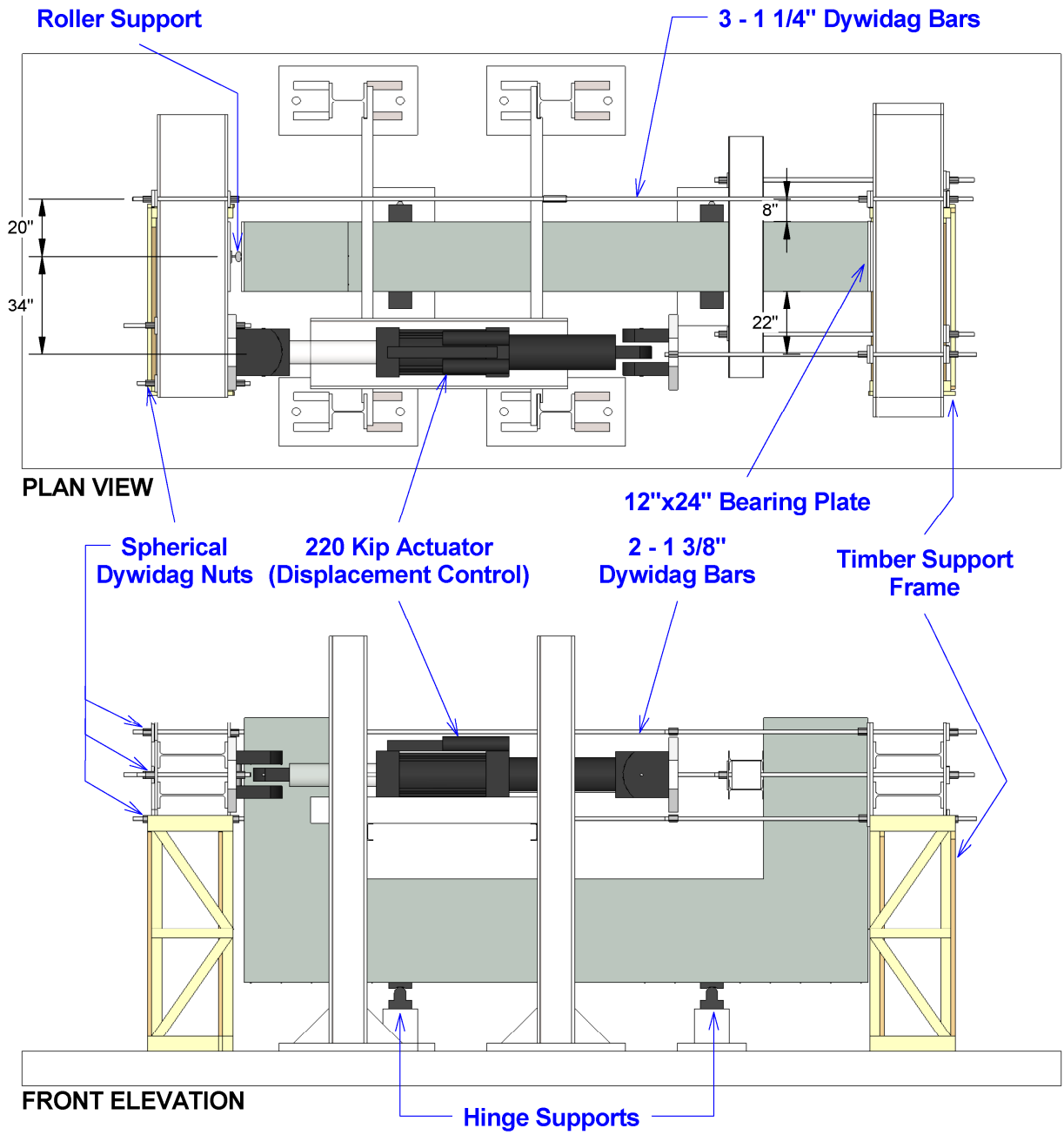

Figure 6-3: Plan and Front Elevation View of Experimental Setup for Specimen 3.

side of the specimen three 1.25 in. diameter high strength DYWIDAG threadbars were aligned vertically at a distance of 8 in. from the surface of the specimen to the center of the bars. A leverage mechanism was created between the actuator and the DYWIDAG threadbars using a roller support on one side of the specimen. With this setup a 2.7:1 mechanical lever arm was created using a single actuator to create a total loading capacity of 594 kip. As it was unclear how ASR/DEF deterioration affected Specimen 3, a single test was performed to determine the ultimate strength capacity and the behavior of Specimen 3, without any prejudice toward the singly or the doubly reinforced beams.

6.2.3 Instrumentation

Figure 6-4 shows the external and internal instrumentation layout used to obtain experimental results to determine the overall force-deformation results and to understand the internal behavior and failure mechanism of the specimen. Experimental data obtained from the instrumentation were also used to compare the analytical modeling results that are presented in the next chapter. The specimen was externally instrumented using linear variable differential transformers (LVDTs) and string-potentiometers (SP), and was internally instrumented using strain gages attached to steel and embedded concrete gages.

The global displacements at the applied loading points on the specimen were obtained by taking an average of the measured displacements above and below the header beam. The drift of the beam relative to the column was measured using two LVDTs mounted to a rigid structure that was fixed to the column surface of the specimen. The overall deflected shape of the specimen was obtained from the externally mounted string pots secured to the external structure or mounted on the strong floor of the laboratory.

Figure 6-4b shows the experimental deformations associated with the SAT and truss modeling were measured using LVDTs mounted to aluminum truss members that were rigidly connected to the specimen between selected nodal points. Each node point had an embedded DEMEC connector securely attached into the specimen. Aluminum members with pin-slotted end connections were attached to two DEMEC connectors of interest, and the LVDTs were attached to measure the relative deformations between the node points. The two beams of the specimen each had six members with six node points (Figure 6-4b). Crack widths or inferred principal tensile

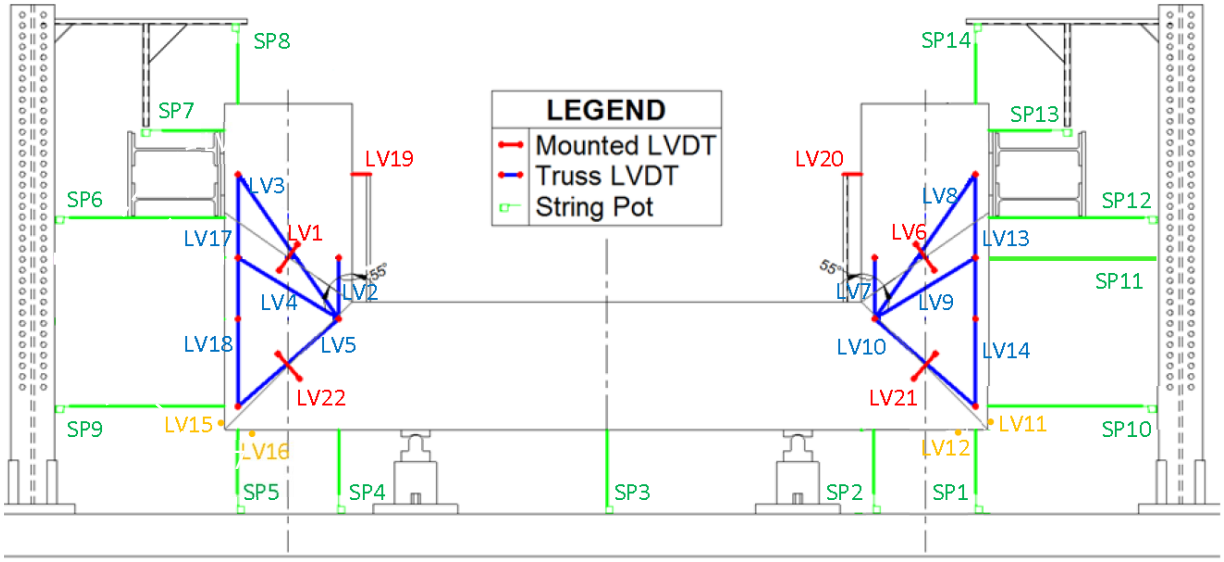

(a) External Instrumentation Layout

(b) LVDT Truss Setup

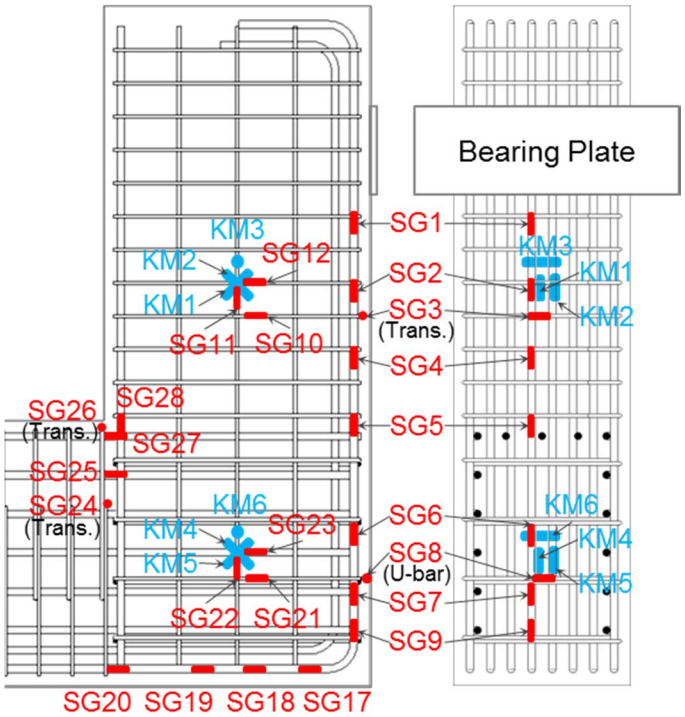

(c) Internal Instrumentation Layout

Figure 6-4: External and Internal Instrumentation Layout.

strains perpendicular to the corner-to-corner arch struts in the beams, and joints were measured with four LVDTs mounted perpendicular to the anticipated crack angles (55° and 45° in the beam and joint, respectively).

In order to provide insight into the internal deformation strains, an assortment of strain gages were affixed to the reinforcing steel at locations shown in Figure 6-4c. To measure the strain in the corner-to-corner concrete struts of the beam and joint regions, embedded concrete gages were secured to the center of the cross-section and oriented in the three principal directions relative to the arch strut as shown in Figure 6-4c. The concrete strains in the direction of the diagonal struts were denoted as gages KM1 and KM4; the concrete strains perpendicular to these struts were denoted as gages KM2 and KM5; and the concrete strains in the out-of-plane transverse direction were denoted as gages KM3 and KM6 (Figure 6-4c).

6.2.4 Experimental Testing Procedure and Loading History

At the end of the deterioration phase, Specimen 3 was transported back to the laboratory for experimental testing. The tie-bar force on the specimen was released before setting up the C-Beam specimen for the load test. Strain gages were attached to each of the two DYWIDAG bars during the removal of the tie-bars to measure the residual tie-bar force left. From the data the average residual strain in the tie-bars was recorded as 0.00173, which corresponds to a total residual tie-bar force of 159 kip (cross-section area of 1 3/8 in. DYWIDAG bars = 1.58 in^2), amounting to 21 percent in time-dependent prestress loss over the five-year conditioning period. The release of the tie-bar forces mimicking the gravity loads had minimal effect, if any, on the cracks that were caused by ASR/DEF expansion indicating the permanent damage that was caused on the specimen.

The effects of ASR/DEF on the structural performance of Specimen 3 were not known before the structural testing. Therefore, to obtain unbiased results from the structural testing, a single test was performed without protecting either of the two beams as was done with the control specimen. As mentioned earlier, the test was performed using a single actuator and a leverage mechanism.

Initially the specimen was loaded to 200 kip as a trial run to ensure that the experimental setup and the mounted instrumentation were performing as expected and then the specimen was

fully unloaded. Later the specimen was loaded continuously until failure without any pauses. The specimen reached its ultimate load capacity of 498 kip before failing in a sudden brittle manner.

6.2.5 Experimental Performance

Figure 6-5 shows the physical condition of the singly reinforced side of C-Beam Specimen 3 at various loads during the test. It is evident that there are no visible changes in the physical appearance of the specimen at the knee-joint when the load is increased from 0 kip (Figure 6-5a) to 200 kip (Figure 6-5b). Similarly, there are no visually identifiable new cracks or difference in the crack width when the load is increased from 200 kip (Figure 6-5b) to 498 kip (Figure 6-5c) just before the failure of the specimen. However, Figure 6-5d shows that just after failure a large portion of the cover concrete in the beam-column region spalled off.

Similarly, Figure 6-6 shows the physical condition of the double reinforced side of C-Beam Specimen 3 before the load testing began and just after the failure of the specimen. As evident in Figure 6-6, no visible changes in the crack size were observed at the knee-joint of the doubly reinforced side of Specimen 3.

6.2.6 Force-Displacement Behavior

Figure 6-7 presents the observed experimental force-displacement behavior of C-Beam Specimen 3. The tip displacement is plotted as the average displacements measured by the string pots that were placed just above and below the header beams, while the total tip displacement is the sum of the tip displacements of the singly and doubly reinforced beams.

Figure 6-7a and b, respectively, show the force-deformation response of the doubly reinforced and the singly reinforced beam. The response of the doubly reinforced beam was found to be stiffer than the singly reinforced beam. The tip displacement observed on the doubly reinforced beam is about half of what was observed in the singly reinforced beam.

Figure 6-7c shows the force versus total tip-displacement of the C-Beam specimen. The ultimate load capacity of Specimen 3 was 498 kip. It is evident from Figure 6-7c that as soon as the ultimate load carrying capacity was achieved, the specimen suddenly failed in a brittle fashion.

(a) At 0 kip

(b) At 200 kip

(c) At 498 kip (Just before Failure)

(d) Just after Failure

Figure 6-5: Physical Condition of Specimen 3 at Various Loads: Singly Reinforced Beam

(a) At 0 kip

(b) At 498 kip

Figure 6-6: Physical Condition of Specimen 3 at Various Loads: Doubly Reinforced Beam.

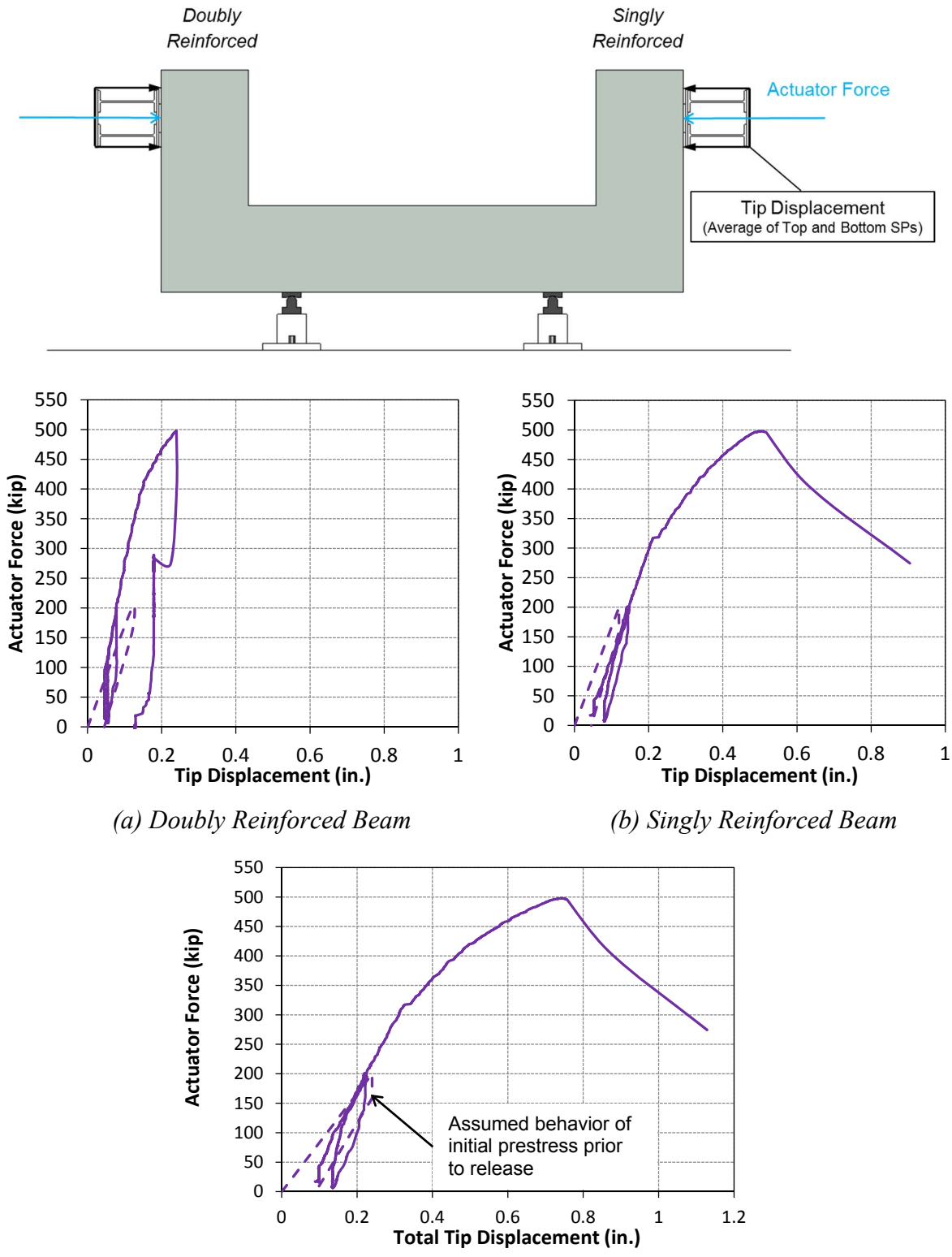

(a) Doubly Reinforced Beam

(b) Singly Reinforced Beam

(c) Total Tip Displacement

Figure 6-7: Force-Displacement Behavior of C-Beam Specimen 3.

6.2.7 Failure Assessment

As in the case with the control Specimen 1, and *slightly* and *moderately* deteriorated Specimens 2 and 4, the failure in *heavily* deteriorated Specimen 3 was a brittle joint shear failure through the beam-column joint region. The failure was triggered by concrete softening of the joint corner-to-corner diagonal strut. Figure 6-8b shows the strains that were recorded in the internal concrete gages KM4–KM6 located in the beam-column joint as shown in Figure 6-8a. The initial offset that is observed in the concrete gages is due to the expansion strains that were recorded during the deterioration phase of Specimen 3. As noted in the earlier chapter, the tensile strains measured in KM4 along the corner-to-corner diagonal strut is likely due to the localized formation of ASR gel around the concrete gage. However, it is to be noted that high tensile strains were recorded in concrete gages KM5 and KM6 that were perpendicular to the compressive diagonal strut. Though much variation in the strains is not observed during the experimental loading phase of Specimen 3, it is evident from Figure 6-8b that the tensile strains transverse to the diagonal strut caused significant softening of the corner-to-corner arch strut of the C-Beam specimen. The transverse reinforcement in the joint region did not have sufficient capacity to take the force redistributed immediately following the initial failure mode. The insufficient anchorage of the transverse U-bars in the joint region and the lack of transverse reinforcement along the back face of the column resulted in a brittle failure of the C-Beam specimen. This in turn resulted in the sudden bursting of cover concrete in the knee-joint of the specimen.

The displacements that were measured by the truss LVDTs shown in Figure 6-8c were used to infer the strains parallel and perpendicular to the diagonal struts. Figure 6-8d and e, respectively, show the strains parallel and perpendicular to the diagonal strut in the beam and the joint of the singly reinforced side of C-Beam Specimen 3. The initial offset shown in Figure 6-8d and e are the expansion strains that were recorded during the deterioration phase. Strains both parallel and perpendicular to the struts did not alter much until the specimen reached close to its ultimate load capacity. As shown in Figure 6-8e, the strain perpendicular to the corner-to-corner diagonal strut in the beam-column region increased rapidly just before the specimen reached its ultimate load capacity. It is evident that the strain perpendicular to the diagonal strut causes rapid softening of the diagonal compression member leading to the sudden ductile failure of the C-Beam specimen. The failure mechanism of Specimen 3 is similar to that of the other C-Beam specimens presented

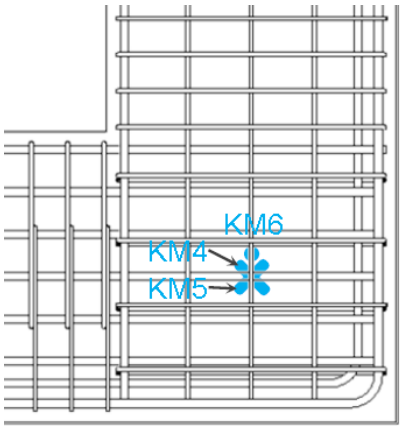

(a) Location of KM Gages at the Failure Joint

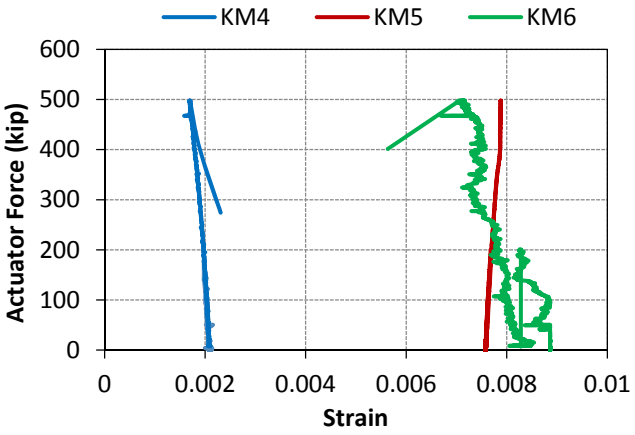

(b) Internal Concrete Strain Recorded in the KM Gages (Initial Offset due to Strains Recorded during Deterioration Phase)

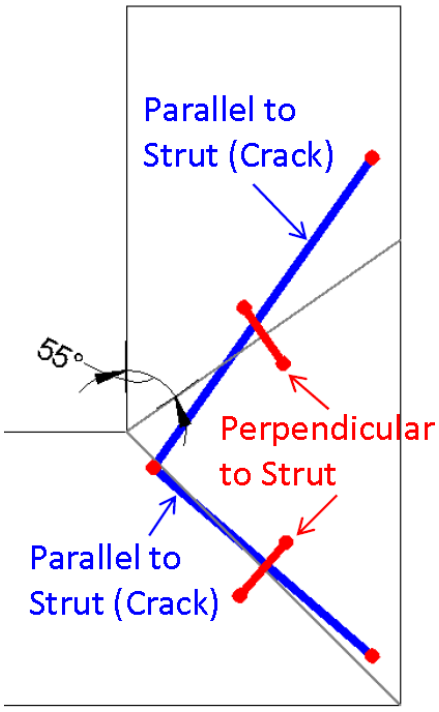

(c) Truss LVDTs Located Parallel and Perpendicular to Diagonal Struts

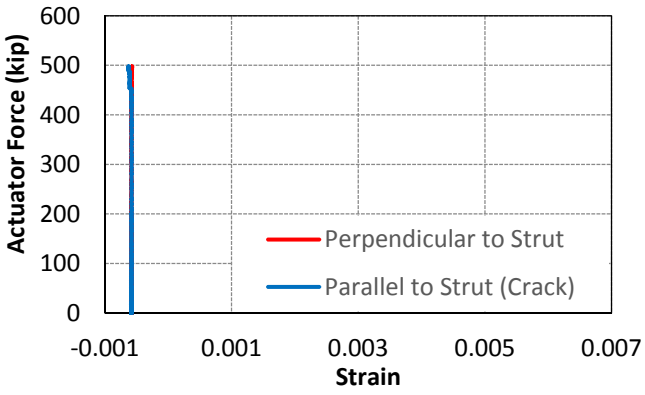

(d) Inferred LVDT Strains in the Specimen Beam

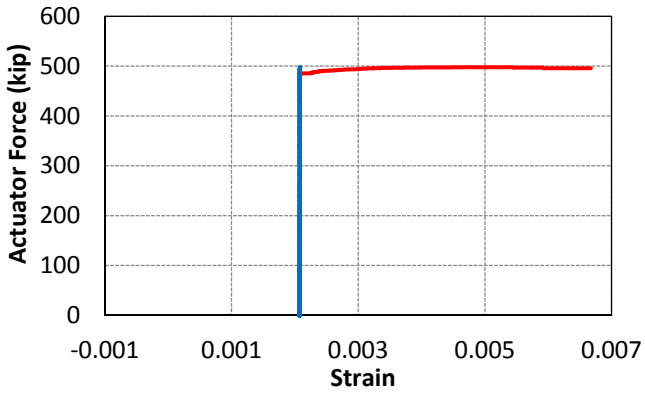

(e) Inferred LVDT Strains in the Specimen Joint

Figure 6-8: Internal and External Strains at Critical Regions of C-Beam Specimen 3.

in Phase 1 of this study by Mander et al. (2012). However, it is noted that the growth of strains perpendicular to the struts in the Specimens 1, 2, and 4 are much more gradual, leading to a more overall ductile force-deformation behavior of the C-Beam specimens.

Figure 6-9 shows the physical state of the failure end of C-Beam Specimen 3. Figure 6-9a clearly shows a significant crack along the diagonal compression strut in the beam-column joint of the C-Beam specimen. As shown in Figure 6-8d, the tensile strain transverse to the diagonal strut causes the formation of the crack along the diagonal strut. Figure 6-9a also shows spalling of the cover concrete in the exterior knee-joint of the specimen. Figure 6-9b and c show the opposite faces of the exterior knee-joint after all the loose concrete was removed. It is evident that diagonal cracks were observed on both faces of the specimen. Also, seen in Figure 6-9c is the crushing of cover concrete in the interior corner, which initiated before the specimen reached its ultimate load carrying capacity. Figure 6-9d shows the physical condition of the specimen at the exterior joint along the cap face of the specimen beam-column joint after all the loose concrete was removed. It is evident from Figure 6-9d that there was debonding and pullout of the U-bars, which resulted in the transverse U-bars bulging out of the specimen. Also evident in Figure 6-9d is the bulging of the external longitudinal reinforcement. Figure 6-9e shows the bottom side (column face) of the beam-column joint where the specimen failed. As shown in the photograph, a large portion of cover concrete spalled from this region. Clearly, the absence of transverse reinforcement in the column face of the beam-column joint resulted in the bulging of the specimen in the lateral direction, resulting in the spalling of cover concrete. Figure 6-9f shows a close-up view of the corrosion observed in the longitudinal reinforcement. Corrosion of longitudinal and transverse reinforcement is also evident in Figure 6-9b–f.

The out-of-plane behavior at the column and cap-face of the beam-column joint is shown in Figure 6-10. The strains in the out-of-plane direction in the beam column-joint were monitored using LVDT 11 and 12, which were, respectively, mounted on the cap and column face of the joint. The strains were deduced from displacements recorded by the LVDTs over their gage length. As shown in Figure 6-10c, the out-of-plane strains in the column face were slightly greater than the strains recorded in the beam-face. It is seen that the out-of-plane strains in the column face of the specimen suddenly increased immediately after the specimen reached its ultimate load, supporting the sudden bursting behavior of the specimen. This is evidently due to the lack of transverse reinforcement in the column face of the beam-column joint.

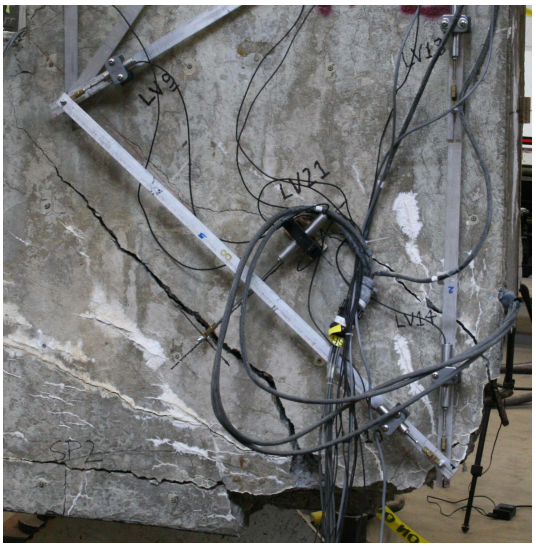

(a) Failure of Diagonal Strut and Bursting of Concrete at Exterior Corner

(b) Exterior Corner after Removal of Spalled Concrete (Opposite Face Shown in c)

(c) Interior and Exterior Corner after Removal of Spalled Concrete (Opposite Face Shown in b)

(d) Anchorage Debonding of U-Bars, and Lateral Displacement of Longitudinal Steel, in the External Beam-Column Joint

(e) Under Side of Exterior Corner Joint after Removal of Spalled Concrete

(f) Corrosion of Longitudinal Steel at the Exterior Knee-Joint

Figure 6-9: Physical State of the Failed End after Load Testing of Specimen 3.

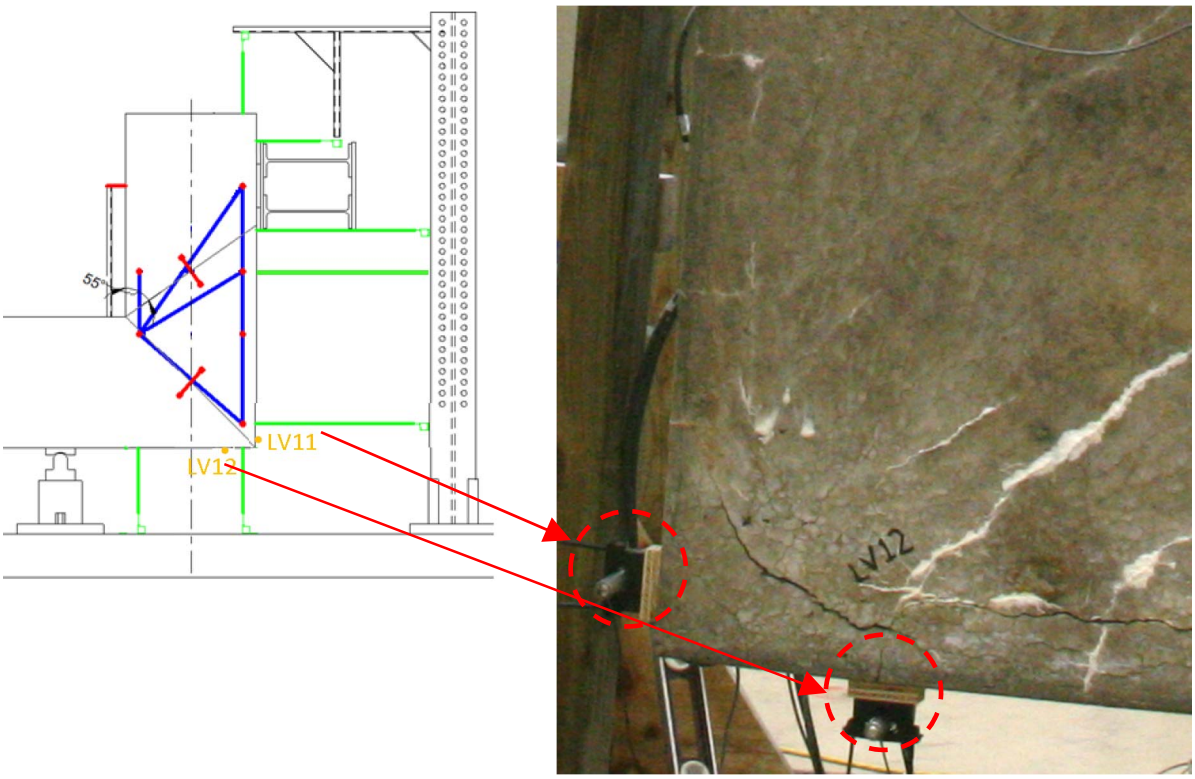

(a) Layout of LVDTs to Compute Out-of-Plane Strains

(b) LVDTs Attached to the Specimen to Measure Out-of-Plane Strains

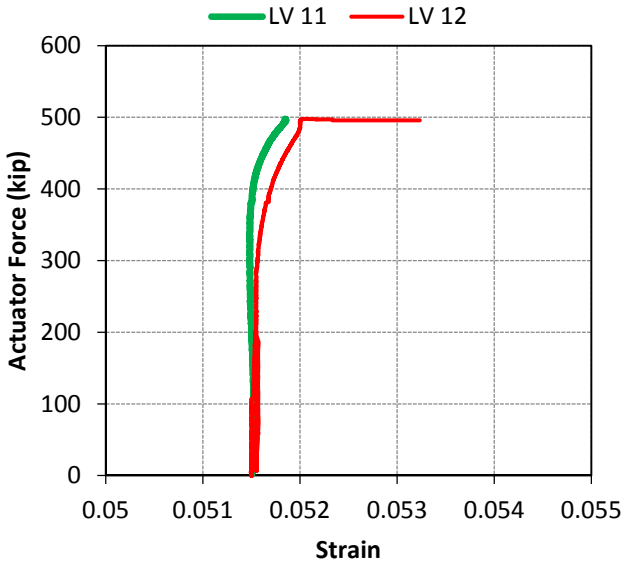

(c) Strains in the Out-of-Plane Direction in the Cap and Column Face

Figure 6-10: Observed Out-of-Plane Strains in the Beam-Column Joint of C-Beam Specimen 3.

6.3 DISCUSSION AND COMPARISON WITH PREVIOUS TESTS

Figure 6-11 presents a comparison of the force-deformation behavior of all four C-Beam Specimens. It is to be noted here that Specimen 1 was the control specimen and was not subjected to ASR/DEF deterioration. Specimens 2 and 4 showed *slight* and *moderate* amounts of deterioration due to ASR/DEF expansion, and Specimen 3 was subjected to *heavy* damage due to ASR/DEF related expansion. Also presented in Figure 6-11 are the joint shear capacity, the nominal load capacity, and the yield load of the C-Beam specimens, which were computed in accordance with the procedure detailed in Phase I of this report (Mander et al., 2012).

In contrast with the control (*undamaged* by ASR/DEF) Specimen 1, which had a load capacity of 474 kip, the ultimate load capacity of Specimen 3 was 498 kip. This result for Specimen 3 is close to the ultimate load capacity of Specimens 2 and 4, which were recorded at 500 kip and 503 kip, respectively. The increasing levels of stiffness observed from the control Specimen 1, to the deteriorated Specimens 2, 4, and 3 in that order, is attributed to the beneficial prestressing effects on concrete from the longitudinal and transverse reinforcement arising from the ASR/DEF induced concrete expansion. Although higher ductility was observed in Specimens 2 and 4 compared to the control Specimen 1, Specimen 3 with *heavy* ASR/DEF deterioration showed somewhat less ductility. However, the extent of damage caused by ASR/DEF deterioration in Specimen 3 did not result in a reduced load carrying capacity.

Figure 6-12 shows a comparison of the post-failure condition of each knee-joint for the four C-Beam specimens. It is evident from Figure 6-12a and b that Specimens 1 and 2 which were *undamaged* and *slightly* damaged, respectively, showed no signs of corrosion in the longitudinal or transverse reinforcement. In addition, the lapped U-bars in Specimens 1 and 2 remain tied together and are intact. Figure 6-12c (*i* and *ii*) shows the post peak-load condition of the *moderately* damaged Specimen 4. The onset of corrosion in the longitudinal and transverse reinforcement is evident in the photographs. Also note that bulging of the lapped U-bars close to the bottom edge of the knee-joint, indicating the onset of loss of confinement restraint in the softened concrete. Figure 6-12d (*i* and *ii*) shows the post-failure physical condition of *heavily* damaged Specimen 3, where a significant degree of corrosion may be observed in the longitudinal and transverse reinforcement. From Figure 6-12d it is evident that there is significant bulging and complete

(a) Specimen 1: Undamaged

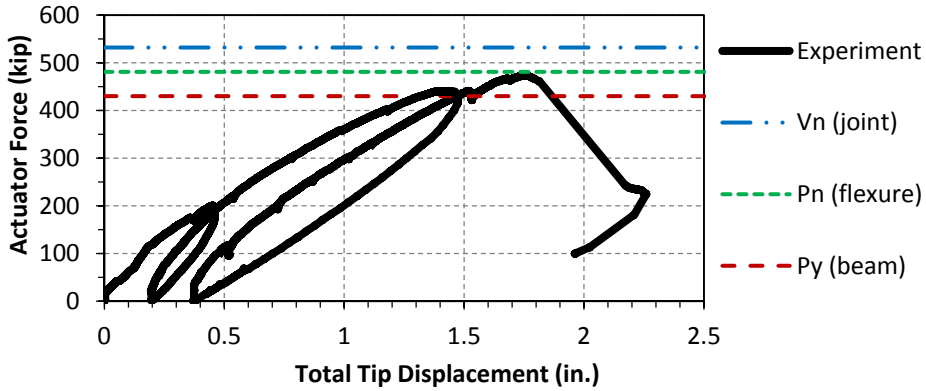

(b) Specimen 2: Slight Damage

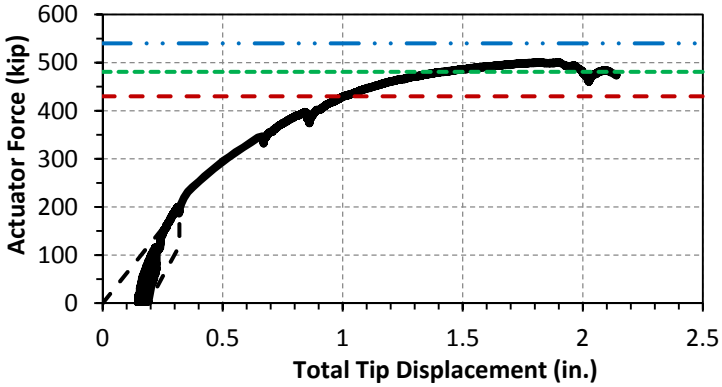

(c) Specimen 4: Moderate Damage

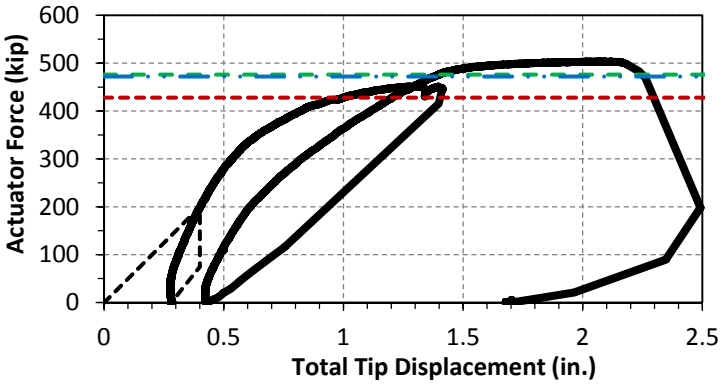

(d) Specimen 3: Heavy Damage

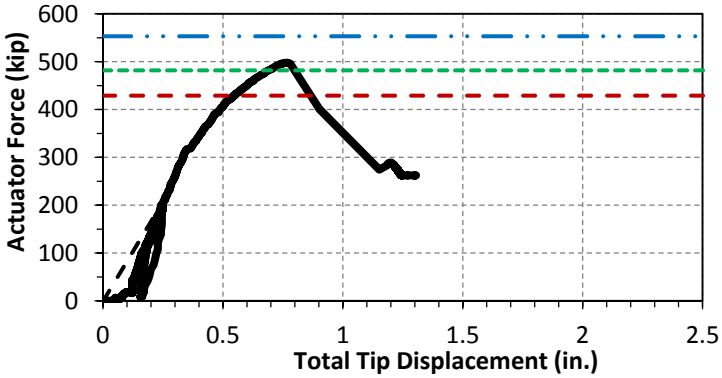

Figure 6-11: Comparison of Force-Deformation Behavior of C-Beam Specimens Subjected to ASR/DEF Deterioration.

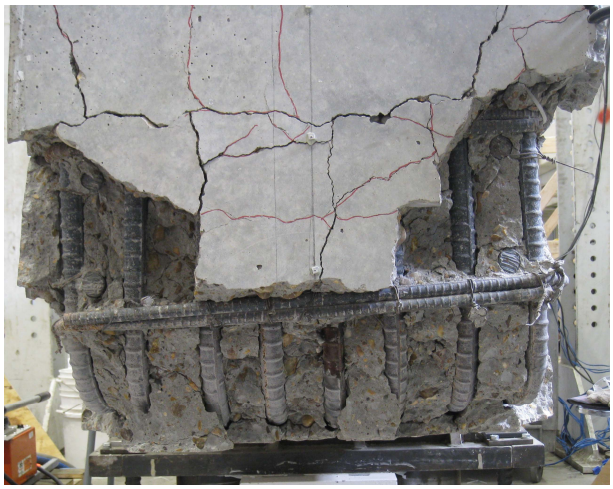

(a) Specimen 1 (Undamaged)

(b) Specimen 2 (Slight Damage)

(i) Front View

(ii) View from Bottom

(c) Specimen 4 (Moderate Damage)

(i) Front View

(ii) View from Bottom

(d) Specimen 3 (Heavy Damage)

Figure 6-12: Corrosion and Post-Peak Load Damage at Failure: A Comparison of the Four Specimens at the Knee-Joint.

de-bonding of the lapped U-bars close to the bottom edge of the Specimen 3 knee-joint. The lapped U-bars further away from the edge of the knee-joint also show signs of significant bulging. It is evident that the loss of anchorage and bulging of the U-bars in Specimen 3 caused considerable loss in confinement of the softened concrete, resulting in an embrittled performance and sudden early loss of load in the *heavily* damaged C-Beam Specimen 3.

6.4 KEY FINDINGS FROM THE EXPERIMENTAL TESTING PROGRAM

C-Beam Specimen 3, which was the subject of this experimental study, was allowed to deteriorate over a period of five years and was categorized to be subjected to *heavy* deterioration due to ASR/DEF expansion. Based on the experimental load testing of Specimen 3 to failure, the following key findings are summarized:

- In spite of the large number of cracks and heavy damage observed on the C-Beam specimen during the deterioration phase, the experimental program showed that the load carrying capacity of the heavily deteriorated specimen was similar to the slightly and moderately damaged C-Beam specimens. All the deteriorated specimens had higher load carrying capacity compared to the undeteriorated control specimen.

- The force-deformation response of the heavily damaged C-Beam specimen was observed to be much stiffer than all the other C-Beam specimens owing to the higher prestress effects due to ASR/DEF expansion. However, the overall ductility of the specimen was much less compared to the other specimens.

- The failure mechanism of Specimen 3 was observed to be the same as the other three C-Beam specimens, in spite of its *heavily* deteriorated state. As in the earlier case the failure mechanism was classified to be brittle joint shear failure in the beam-column joint. This mechanism resulted mainly because of insufficient anchorage of the transverse U-bars in the joint region and also due to the lack of out-of-plane reinforcement along the column face in the joint region.

- A significant amount of corrosion was observed in the longitudinal and transverse reinforcement in the beam-column joint. However, the corrosion of reinforcement did not seem to affect the load carrying capacity of the C-Beam specimen. It is not clear if more

severe exposure conditions like higher humidity or exposure to salt water could lead to more rapid and severe corrosion, and how that would affect the load carrying capacity of the C-Beam specimen.

7 FORCE DEFORMATION MODELING OF EXPERIMENTAL RESULTS

7.1 INTRODUCTION

One of the primary goals of this research was to propose modifications to the SAT modeling approach to account for ASR/DEF induced deterioration in D-regions. However, as demonstrated in Phase I of this research (Mander et al., 2012), it was shown that SAT is a lower bound plastic truss model that does not provide a unique solution, nor does the SAT method give any sense of the related deformations in the structure. It was also shown that the SAT methods may provide unduly conservative predictions of the ultimate load and did not predict the mode of failure correctly. This resulted in the development of an analysis technique called the Compatibility Strut-and-Tie Method that incorporates deformation compatibility into the analysis and considers the contribution of the truss and the arch mechanism toward shear and flexure resistance. C-STM provides a holistic view of the structural behavior and a complete force-deformation pathway to failure. The formulation and validation of the C-STM are presented in Phase I of this research report.

The application of C-STM to the C-Beam specimens was presented in Mander et al. (2012) with good agreement demonstrated between the model simulation and experimental force-deformation observations. The C-STM model was capable of simulating well the internal strain-based behavior of the C-Beam specimen to provide an insight into the behavior and failure mechanism of each specimen. The general overall and specific internal behavior of the control Specimen 1 and field conditioned Specimens 2 and 4 with respective *slight* and *moderate* amounts of deterioration were also presented in the Phase I report (Mander et al., 2012). The C-STM modeling of Specimen 3, which was exposed to the elements outdoors for five years and resulted in *heavy* damage by ASR/DEF deterioration, is presented in this chapter. The overall force-deformation results and the internal behavior of Specimen 3 are compared with the experimental observations for that specimen and are also compared with the companion Specimens 1, 2, and 4 of the Phase I study.

Based on field observations and understanding of how ASR/DEF related expansion affected the structure at the time of reporting (Mander et al., 2012), certain material property

modification factors were proposed and incorporated into the C-STM modeling technique. One of the recommendations made was for the prestressing stresses (f_{ps}) in the longitudinal and transverse reinforcement caused by ASR/DEF related expansion. Different multipliers to determine the prestressing stresses were proposed for slight, moderate, and heavy damage caused by ASR/DEF deterioration on the structure. Although, these factors were based on well-reasoned arguments supported by rational engineering judgment, they could not be definitively quantified. However, due to the development of the new model proposed for ASR/DEF related expansion presented in Chapter 3 the state of strains in each structural member due to ASR/DEF swelling can be assessed for a specified age of the structure. Thus, the prestressing stresses to be applied on the C-STM model can be obtained from the proposed model for ASR/DEF expansion strains. In this chapter, the results from the C-STM modeling for the C-Beam specimens, incorporating the ASR/DEF related expansion prestrains obtained from the proposed expansion model are presented.

7.2 OVERVIEW OF C-STM

The formulation and other important aspects of the C-STM such as the combined modeling of the truss and arch action, C-STM geometry and axial rigidity, and constitutive element material relations are presented in detail in Phase I of this report (Mander et al., 2012). A few of the aspects of modeling that have been improved hence are presented herein.

7.2.1 The Softening of Diagonal Concrete Struts

The compressive strength of diagonal concrete struts is reduced by the tensile strains acting orthogonal to the compression strain, and this is widely known as concrete softening. As presented in Mander et al. (2012), the softening coefficient can be computed as:

$$\zeta = \frac{1}{1+\left\langle \frac{\varepsilon_1 - 0.0012}{3\varepsilon_{co}} \right\rangle} \tag{7-1}$$

where ε_{co} = the strain corresponding to the concrete compressive strength; ε_1 = strain transverse to the diagonal compressive strut, and $\langle \bullet \rangle$ are Macaulay brackets where if $\varepsilon_1 < 0.0012$, then the term in $\langle \bullet \rangle$ is set to zero.

Vecchio and Collins (1993) and Belarbi and Hsu (1995) conducted extensive experimental studies to investigate the behavior of softened concrete. Based on the compression softening data obtained from panel test results presented in Figure 7-1a (Vecchio, 2000) the softening coefficient can be represented by:

$$\zeta = \frac{1}{1 - 0.25\left(\varepsilon_1 / \varepsilon_2\right)} \tag{7-2}$$

where $\varepsilon_2 =$ the compression strain (negative) in the diagonal member. The strains ε_1 and ε_2 can be obtained from the C-STM analysis.

In comparing the experimental force-deformation results of C-Beam Specimen 3 with 4, it is evident that there needs to be a simple method to discriminate between softened confined and unconfined concrete. Unconfined softened concrete occurs where there is an absence of completely enclosed or hooked hoops around badly damaged concrete section that results in large transverse strains. It is proposed to distinguish between the confined and unconfined softened concrete by the two different softened concrete models shown in Figure 7-1b.

7.2.2 The Assessment of Deteriorated Cover Concrete Properties

The assigned concrete strength within each concrete truss member needs to be appropriately factored to account for the damage caused by ASR/DEF expansion in cover concrete. The modified concrete strength is defined as:

$$f'_{cASR} = \lambda f'_c \tag{7-3}$$

where $\lambda =$ the strength reduction factor that is based on the extent of damage observed. The right column of Figure 7-2 shows the average of the modeled transverse tensile expansion strains (ε_1) in the beam and column of the deteriorated C-Beam specimens. The horizontal bands indicate the range of transverse strains for *undamaged* ($0 < \varepsilon_1 < 0.0012$), *slight* ($0.0012 < \varepsilon_1 < 0.006$), *moderate* ($0.006 < \varepsilon_1 < 0.016$), and *heavy* ($\varepsilon_1 > 0.016$) damage. Substituting the range of ε_1 values into (7-1) results in the following range of strength reduction factors; default values of λ are also recommended if precise values of ε_1 are unknown but the visually observed degree of damage is as indicated by Figure 7-2:

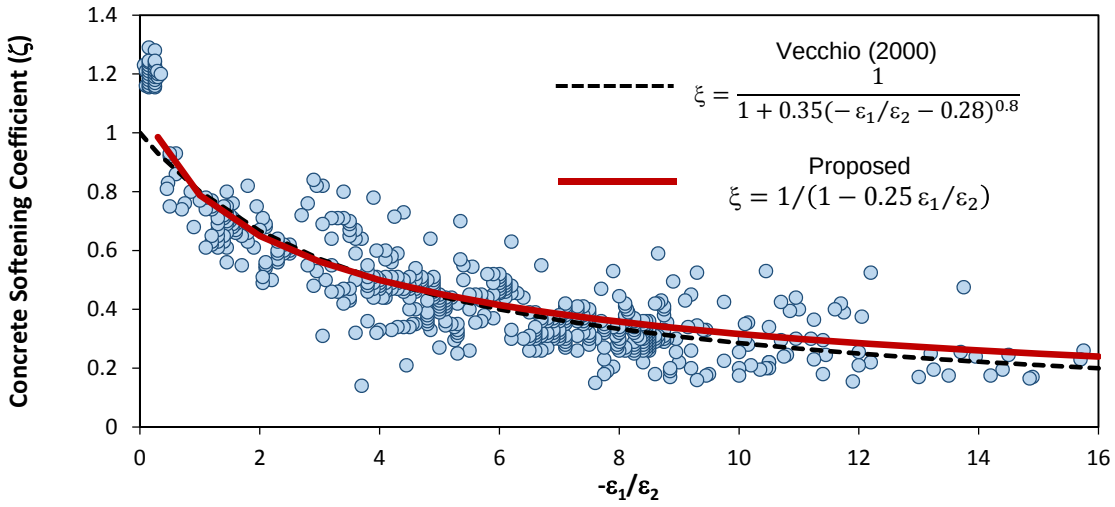

(a) Compression Softening Data Obtained from Panel Tests (Vecchio, 2000)

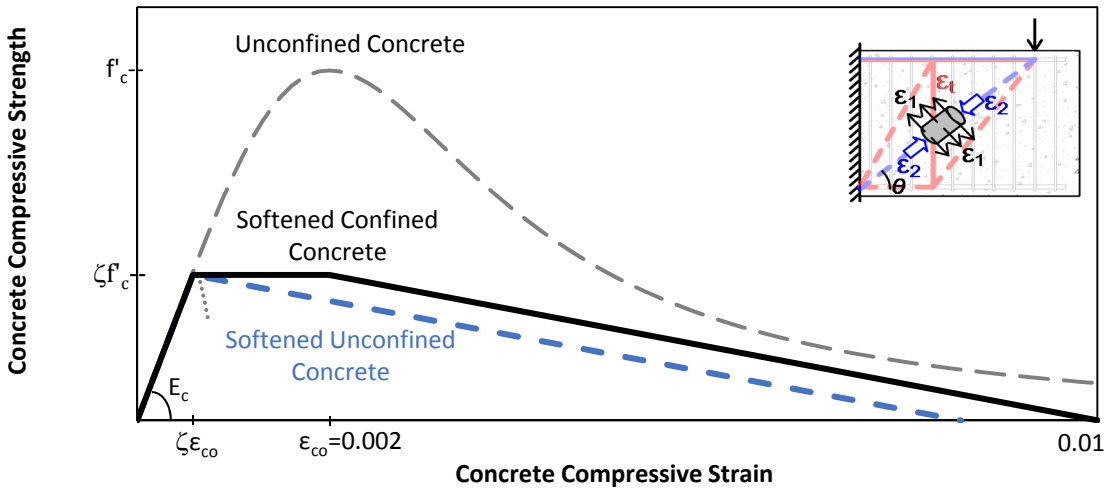

(b) Compression Softened Concrete Model

Figure 7-1: Diagonal Concrete Elements.

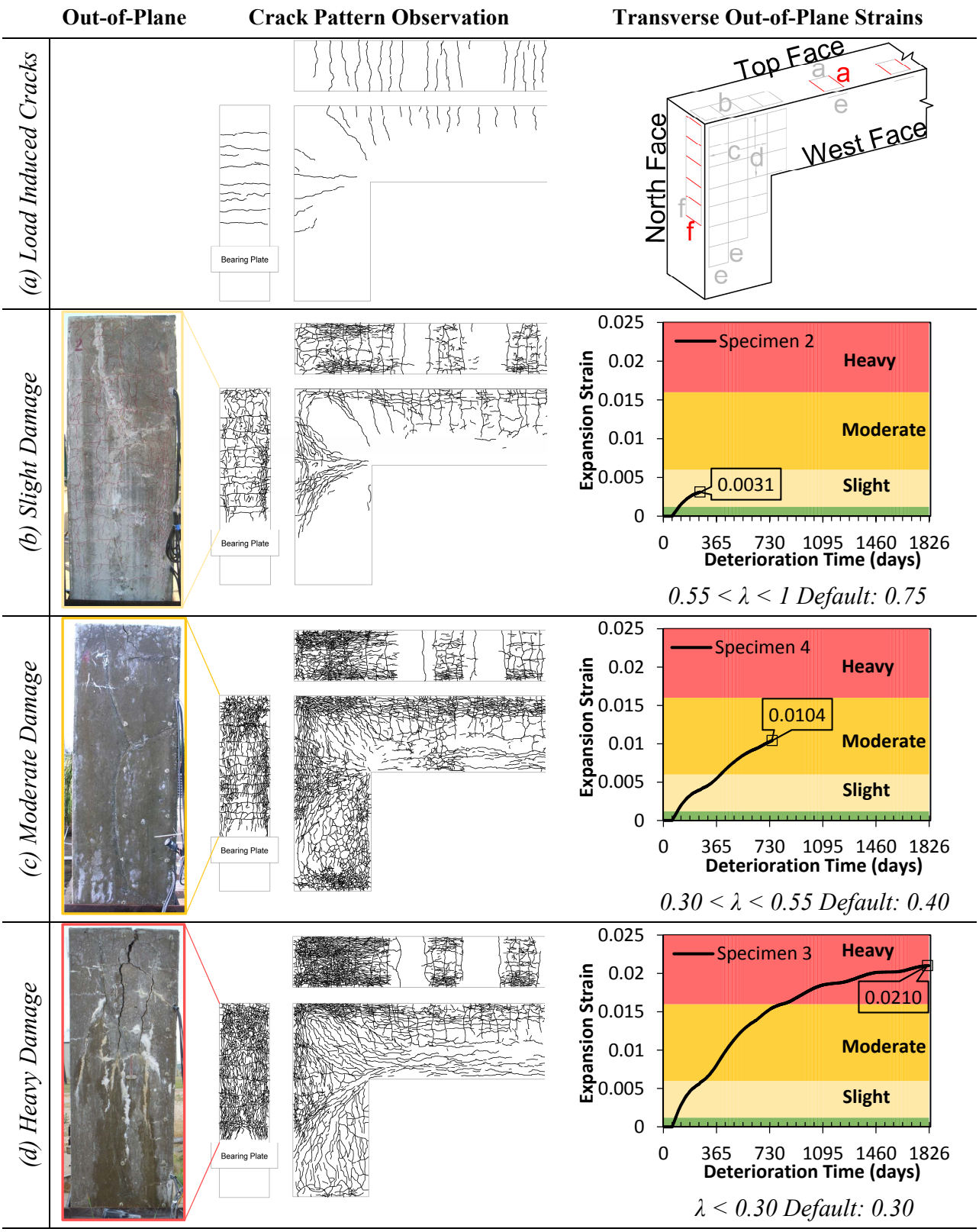

Figure 7-2: Deteriorated Specimen Appearance, and the Modeled Transverse Strains in the C-Beam Out-of-Plane Direction.

- *Undamaged* concrete $\lambda = 1$ Default $\lambda = 1$.
- *Slight* damage $0.55 < \lambda < 1$ Default $\lambda = 0.75$.
- *Moderate* damage $0.30 < \lambda < 0.55$ Default $\lambda = 0.40$.
- *Heavy* damage $\lambda < 0.30$ Default $\lambda = 0.30$.

The out-of-plane photographs and the crack pattern observations presented in Figure 7-2 show the physical state of the C-Beam specimens that fall into the category of *undamaged*, *slight*, *moderate*, and *heavy* damage. Note that the crack pattern on *moderately* damaged Specimen 4 looks similar to the crack pattern on the *heavily* damaged Specimen 3. However, the cracks in the out-of-plane direction of Specimen 3 were wider compared to Specimen 4 as shown in the photographs in Figure 7-2. Additionally, the crack width strains (sum of crack widths/overall width) in the beam and column out-of-plane region were about one-half that of the surface strains that were measured from the DEMEC points from the same region. Thus, it is possible to relate the crack width strains with the actual expansion strains and thereby determine the extent of damage caused by ASR/DEF expansion on the structure from Figure 7-2.

7.2.3 The Prestressing Effect in Reinforcement Caused by Concrete Swelling

The constraint offered by longitudinal reinforcement and transverse hoops to the swelling of core concrete puts tensile strains on the reinforcing steel, which in turn puts the concrete into a state of prestress. The prestressing forces can be evaluated based upon the expansion strains in the specimen, at the end of its exposure period. For this, the expansion model that was presented earlier in Chapter 3 and later applied to the C-Beam specimens in Chapter 5 can be used to determine the expansion strains and hence compute the corresponding prestressing force. In lieu of the above exhaustive expansion strain analysis, the following updated recommended values can be used.

Depending on the extent of damage (*slight, moderate,* or *heavy*) due to ASR/DEF effects the following recommendations are made for prestressing stresses (f_{ps}) in longitudinal reinforcement:

- *Undamaged* concrete $f_{ps} = 0$.
- *Slight* damage $f_{ps} = 0.3 f_y$.
- *Moderate* damage $f_{ps} = 0.5 f_y$.
- *Heavy* damage $f_{ps} = 1.1 f_y$.

in which f_y = yield stress of longitudinal reinforcement.

Similarly the recommendations for prestressing stresses in hoops are:

- *Undamaged* concrete $f_{ps} = 0$.
- *Slight* damage $f_{ps} = 0.5 f_{yh}$.
- *Moderate* damage $f_{ps} = 1.0 f_{yh}$.
- *Heavy* damage $f_{ps} = 1.25 f_{yh}$.

in which f_{yh} = yield stress of transverse hoops.

Appropriate modifications to the stress-strain behavior of the reinforcing steel, as explained in Mander et al. (2012) and shown later in section 7.5.1, are made to account for the prestressing effects.

7.3 THE STRUCTURE

Figure 7-3 presents the prototype structure, reinforcing layout, and cross-section of the C-Beam specimen. The experimental specimen was designed as a "C" shape sub-assemblage such that two large-scale bridge bent components were placed back-to-back, so that they could be tested as a self-reacting system. The C-Beam specimen had a constant cross-section of 3 ft deep and 2 ft wide that was symmetrical with the exception of the beam compression steel. The physical model scale factors representing the doubly reinforced straddle bent (Figure 7-3a) and the singly reinforced cantilevered bent (Figure 7-3b) were approximately 0.75 and 0.5, respectively.

The longitudinal reinforcement consisted of 10 No. 8 bars running continuously around the outside and hooked at the end of each beam. The singly reinforced beam had two No. 8 straight compression bars for construction purposes. The doubly reinforced beam had symmetrical compression and tension reinforcement.

(a) Straddle Bent

(b) Cantilever Bent

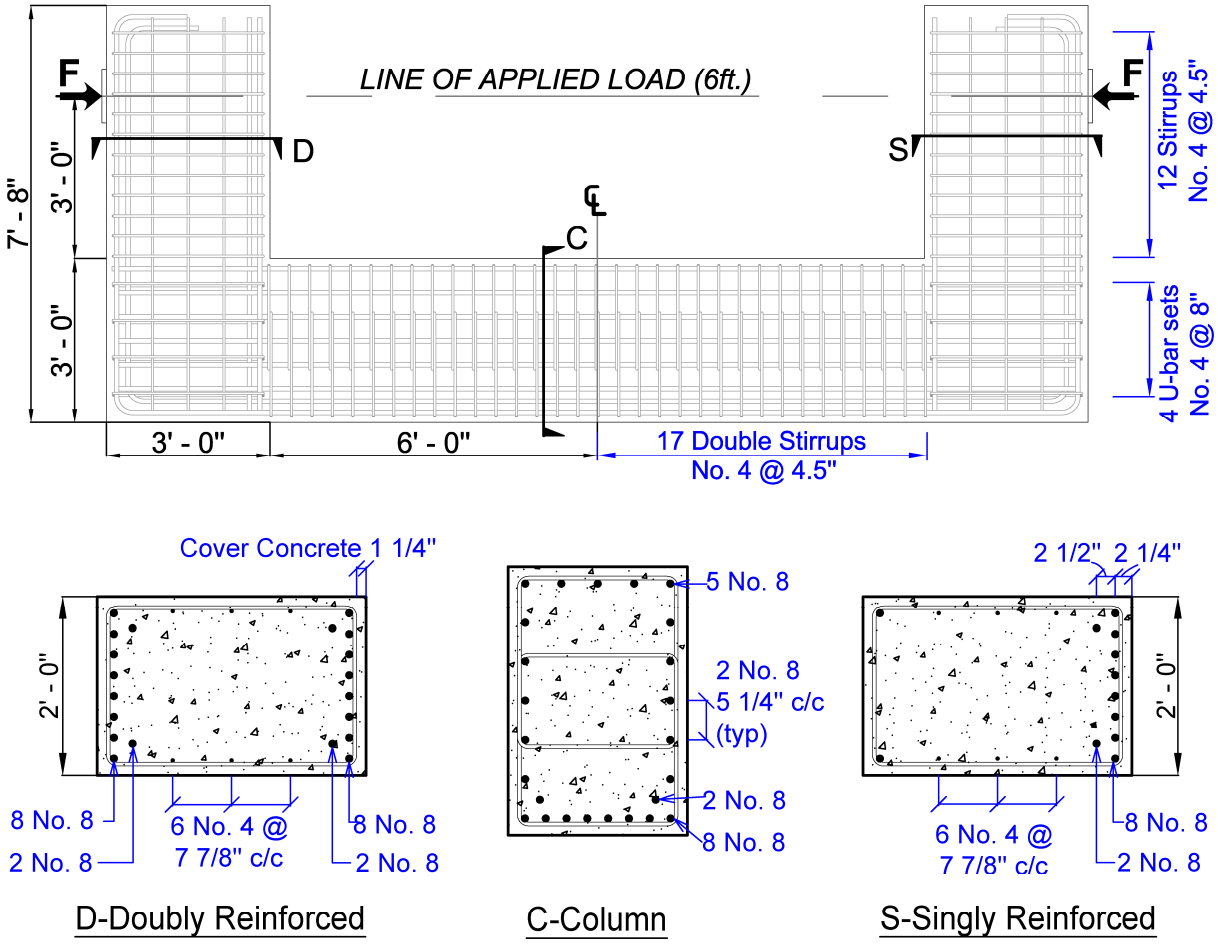

(c) Reinforcement Details

Figure 7-3: Representative Structures, and Elevation and Cross-Section of the C-Beam Specimens.

The longitudinal beam distribution steel (distributed along the beam web) consisted of three sets of No. 4 straight bars equally spaced. Transverse beam reinforcement consisted of closed stirrups with a center-to-center spacing of 4.5 in. starting at the column face. The longitudinal column distribution steel consisted of five sets of No. 8 bars equally spaced. Transverse column reinforcement had overlapping No. 4 stirrups spaced at 4.5 in. centers. The beam-column joint was reinforced with four No. 4 U-bars at 8 in. centers continuing from the transverse beam reinforcement.

Table 7-1 presents the reported material strength data on the test day and experimental test results for Specimen 3, which was conditioned outdoors for a period of five years and showed *heavy* damage due to ASR/DEF deterioration.

7.4 PRESENT CODE-BASED STRENGTH PREDICTIONS

The code based design approaches that were discussed in detail in Phase I of this report are used to predict the response of the Specimen 3 C-Beam. The results from the analysis are presented in Table 7-1 and are discussed briefly below.

Stage 1: Nominal beam theory

The various aspects of Stage 1 analysis are discussed below.

- The yield moment (M_y^b) and the externally applied load causing first yield (P_y^b) were calculated based on standard beam theory. The analysis resulted in a yield moment of $M_y^b = 1291$ kip-ft and a yield force of $P_y^b = 430$ kip for the doubly reinforced beam.

- The nominal flexural moment (M_n^f) was calculated by normal practice as per the AASHTO LRFD *Bridge Design Specifications* (2010). Based on the nominal flexural moment M_n^f, and knowing the shear span to the face of the column $L_b = 36$ in., the externally applied load causing flexure on the bent cap was found to be $P_n^f = 482$ kip for the doubly reinforced beam of Specimen 3.

Table 7-1: Material Properties, Stage 1 and 2 Analyses, and Experimental Results.

		Specimen 3		Comments
Material Properties	$f_c^{'}$ *(ksi)*	5.93		
	E_c *(ksi)*	4390		
	Age at testing (years)	5.4		
Stage 1 Analyses (Sectional)	**Beam reinforcement**	**Double**	**Single**	
	M_y^b *(kip.ft)*	1291	1279	
	$\boldsymbol{P_y^b}$ **(kip)**	**430**	**426**	
	M_n^f *(kip.ft)*	1445	1425	
	$\boldsymbol{P_n^f}$ **(kip)**	**482**	**475**	
	$\phi_f P_n^f$ *(kip)*	434	428	$\phi_f = 0.9$
	$\boldsymbol{V_n^s\,(kip)}$	**286**	**291**	
	$\boldsymbol{V_n^j\,(kip)}$	**553**	**560**	
Stage 2 Analyses (SAT)	$\boldsymbol{P_y^{SAT}}$ **(kip)**	429		Based on longitudinal steel yield.
	$\phi_v P_y^{SAT}$ *(kip)*	300		
	$\boldsymbol{P_n^{SAT}}$ **(kip)**	**349***		Based on node capacity.
	$\phi_v P_n^{SAT}$ *(kip)*	244		
Experimental Results	P_{Yield}^{Expt} *(kip)*	--		
	$\boldsymbol{P_{Failure}^{Expt}}$ **(kip)**	**498**		
	Δ_{Yield}^{Expt} *(in.)*	--		
	$\Delta_{Failure}^{Expt}$ *(in.)*	0.77		
	μ	--		
Theory /Expt.	$P_n^{SAT} / P_{Failure}^{Expt}$	0.70		

*Expected Critical failure mode capacity.
Subscript: *b*=beam; *s*=shear; *j*=joint;
SAT=strut-and-tie; *Expt*=Experiment.

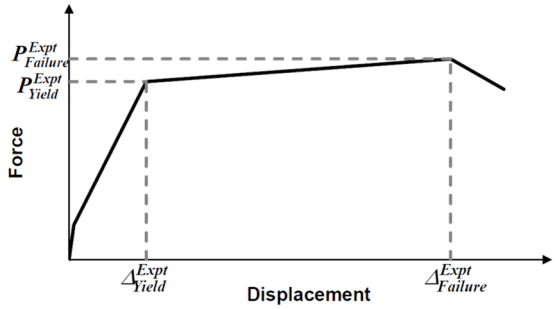

Notation for experimental results:

- In the computation of shear capacity (V_n^s), due to the absence of prestressing tendons, the component of shear carried by tendons $V_p = 0$. The parameters β and θ were calculated based on Method 1 specified in the AASHTO LRFD *Bridge Design Specifications* (2010). For Specimen 3, the shear capacity for the doubly reinforced beam was found to be $V_n^s = 286$ kip and for the joint was found to be $V_n^j = 553$ kip.

- The strength reduction factor for shear and flexure are $\phi_v = 0.90$ and $\phi_f = 0.90$, respectively. For the doubly reinforced beam of Specimen 3, $\phi_v V_n^s = 0.90 \times 286 = 257$ kip is less than $\phi_f P_n^f = 0.90 \times 482 = 434$ kip. This implies that the factored shear capacity for the beam is insufficient, which can lead to a potentially brittle shear failure in the beam.

- It is important to investigate the shear in the beam-column joint, as this can be a critical section. Shear in the beam-column joint can be found from the shear force diagram of the equivalent beam model of the C-Beam specimen (as shown in Phase I report). The vertical joint shear for Specimen 1 was found to be $V_{jv} = 560$ kip. Considering the contribution of the hoops/ties within the joint (V_{truss}) and the corner-to-corner joint arch (V_{arch}), the joint shear capacity of the joint was found to be $V_n^j = 553$ kip for the doubly reinforced side of Specimen 3. Thus for Specimen 3, for the joint $\phi_v V_n^j = 0.90 \times 553 = 498$ kip is less than $\phi_f V_{jv} = 0.90 \times 560 = 504$ kip.

From the Stage 1 analysis of C-Beam Specimen 3, it can be concluded that the factored shear capacities for both the beam and the joint are insufficient. Given that beam-column joints are strictly D-regions where beam theory is not sufficient to explain the performance, this warrants further investigation and a SAT analysis is performed.

Stage 2: SAT analysis

The various aspects of Stage 2 analysis are discussed below.

- The procedure for building the SAT model for the C-Beam specimen is discussed in detail in Phase I of this report. As in the case with the other three C-Beam specimens, based on

the node geometries, the CTT node for Specimen 3 was found to be the most critical node, with an allowable stress factor $f_{cu} = 0.65 f_c^{'}$. The node strength of the CTT node based on the concrete strength $(f_c^{'})$ of Specimen 3 at the time of testing was found to be $F_{cu} = 588$ kip.

- The external load required to cause failure based on the node capacity of the CTT node for Specimen 3 was back calculated and found to be $P_n^{SAT} = 349$ kip. It is noted that $P_n^{SAT} < P_n^f$ and also $\phi_v P_n^{SAT} < \phi_f P_n^f$. Therefore, as in the case of Specimens 1, 2, and 4, the joint capacity for Specimen 3 is technically undependable. The results from the SAT analysis are summarized in Table 7-1.

It can be seen from the results presented in Table 7-1 that the load at failure for Specimen 3 was $P_{Failure}^{Expt} = 498$ kip. However, the capacity of Specimen 3 obtained from flexure and SAT analysis are $P_n^f = 482$ kip and $P_n^{SAT} = 349$ kip, respectively. Both methods (beam flexure and SAT) completely miss the actual failure mode (joint shear failure).

Figure 7-4 shows the experimental force-deformation curves of C-Beam Specimen 3. Also plotted on the graph are the strength capacities obtained from the code-based analyses. The experimental results are shown with an initial offset to mimic the gravity loads that were applied to the specimen while being conditioned in the field. The dashed lines show the computed (assumed) behavior of this initial prestress effect prior to release of the prestress. As shown in Figure 7-4, the analysis results do not give any indication of the overall behavior of the structure, and hence the strength-only predictions are represented as horizontal lines.

Due to *heavy* ASR/DEF induced expansion damage in the concrete, the longitudinal and the transverse reinforcement in C-Beam Specimen 3 yielded during the deterioration phase. Therefore, as shown by the experimental results in Figure 7-4, there is no definite yield point observed for C-Beam Specimen 3.

P_y^b = External load causing flexural yield

P_n^f = External load causing beam flexure

$V_n^s = V_s + V_c$ = Nominal beam shear

$V_n^j = V_{truss} + V_{arch}$ = Joint shear

P_y^{SAT} = External load based on longitudinal steel yield from SAT

P_n^{SAT} = External load based on node capacity from SAT

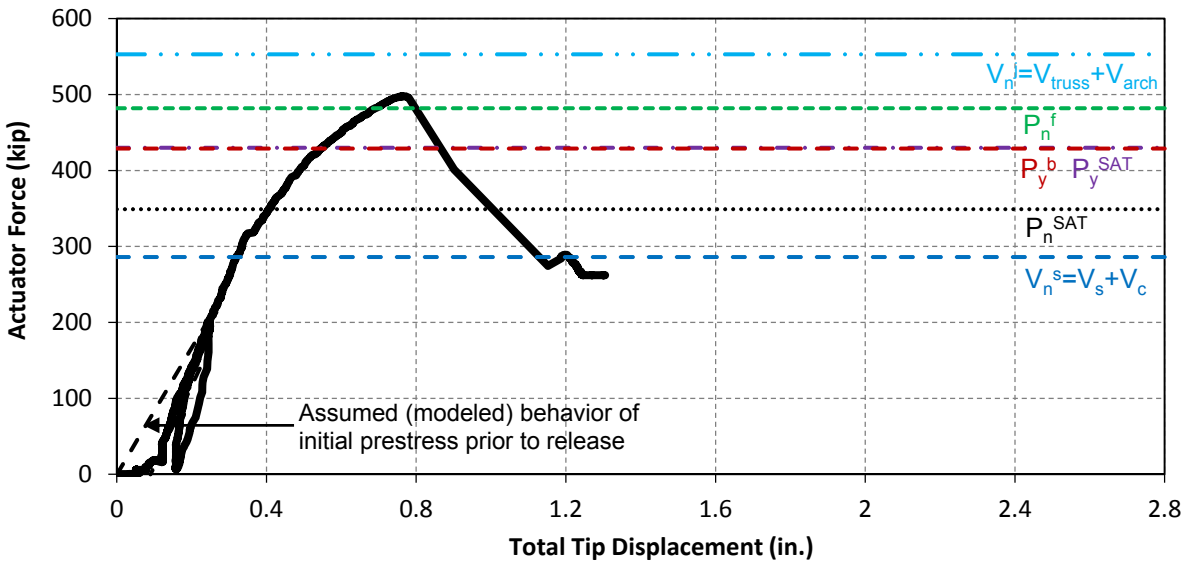

Figure 7-4: Experimental, Stage 1 and Stage 2 Results for C-Beam Specimen 3.

It can be concluded from the analysis results that it is somewhat inconclusive as to what will be the failure mode of the specimen, as it is observed that the joint capacity is (theoretically) undependable. Additionally, the SAT analysis does not take into account the effects of ASR/DEF damage. To better understand the behavior of the structure and its final mode of failure, the C-STM analysis is applied in what follows.

7.5 Strength and Deformation Capacity Using C-STM

7.5.1 The C-STM Model

Even though the C-STM is a minimalist model, the C-STM analysis is able to provide a good insight into the overall force-deformation behavior and to understand the non-linear mechanics within the C-Beam specimens that lead to different modes of behavior and eventual failure. The development of the displacement-controlled C-STM has been extensively discussed in Mander et al. (2012) and its force-controlled predecessor in Scott et al. (2012a, b). Therefore, only a brief description of the model is presented herein.

Figure 7-5 shows the C-STM topologies for the C-Beam specimens (a) without and (b) with ASR/DEF induced damage. Figure 7-5a shows the C-STM model that was developed for Specimen 1, which was the control specimen and had no ASR/DEF induced damage. Initial post-tension loads (shown as PT in Figure 7-5a) were applied to the tension chord of the protected beam in order to replicate post-tensioning effects in accordance with Phase I and Phase II of testing. This model essentially represents the C-STM analysis *without* any ASR/DEF effects.

Specimens 2, 4, and 3 showed *slight, moderate,* and *heavy* damage due to the effects of ASR/DEF. Figure 7-5b shows the C-STM model for C-Beam Specimens 2, 3, and 4. Prestressing forces were applied on the longitudinal and transverse members in the beam and column in order to replicate the prestress effects that arise as a consequence of the swelling within the core concrete due to ASR/DEF effects. Depending on the extent of ASR/DEF deterioration, the strength reduction factor for cover concrete recommended in Section 7.2 was adopted. The confinement ratio (Mander et al., 1988) was calculated to be $K_{cc} = f_{cc}^{'} / f_{co}^{'} = 1.20$ for the beam and $K_{cc} = 1.28$ for the column for Specimen 2. For Specimen 4, the confinement ratio was calculated to be

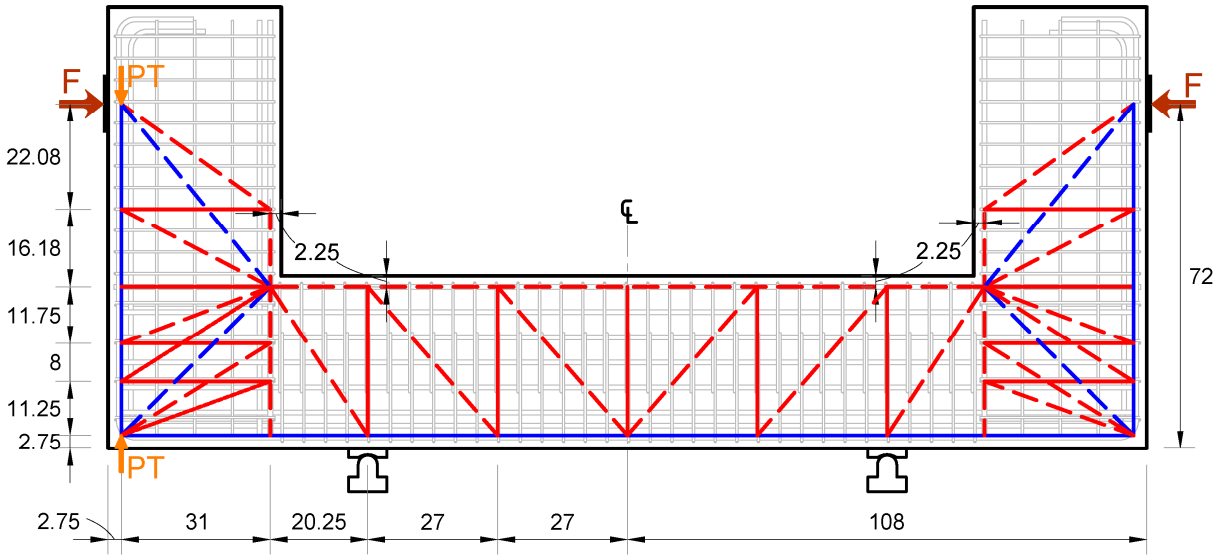

(a) Specimen 1: Without ASR/DEF Damage

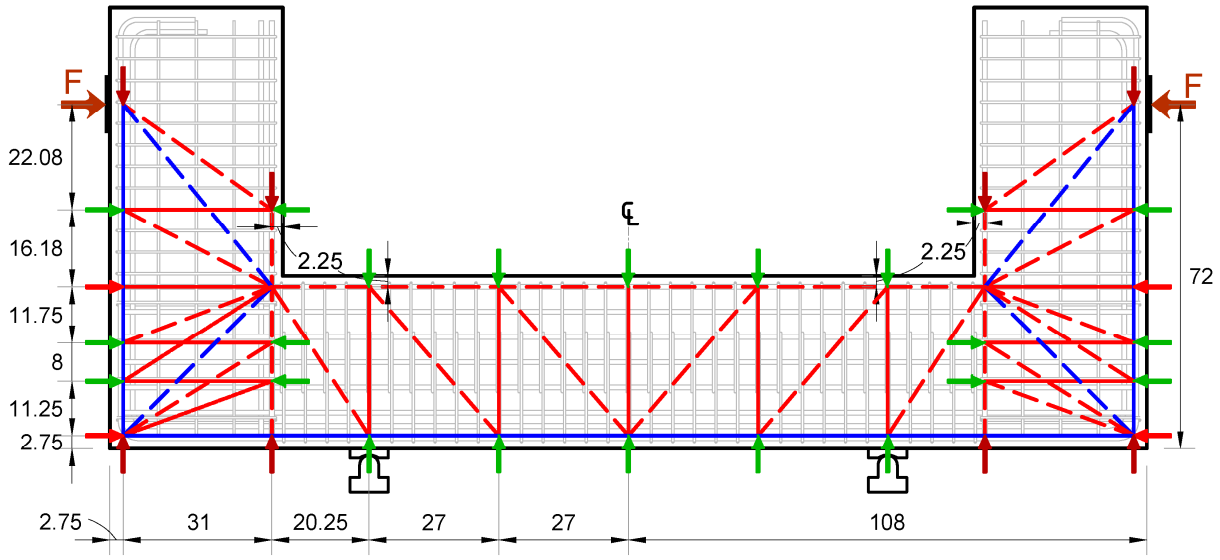

(b) Specimen 2,3, and 4: With ASR/DEF Damage

Primary tension reinforcement
Ties representing bundles of hoops
Concrete struts for the truss
Central concrete arch
Initial confinement effect in hoops and longitudinal steel due to concrete swelling, modeled as a set of externally applied nodal forces

Figure 7-5: Modeling the C-Beam Specimens without and with ASR/DEF Damage.
Note: The additional forces in (b) represent the prestress effect actively induced in the reinforcing steel caused by ASR/DEF induced concrete swelling.

$K_{cc} = 1.28$ for the beam and $K_{cc} = 1.35$ for the column. Similarly for Specimen 3 the confinement ratio was calculated as $K_{cc} = 1.21$ for the beam and $K_{cc} = 1.31$ for the column. As both the cover and core concrete areas contribute to the area of the strut in the C-STM model, a weighted average value of concrete compressive strength is used in the C-STM model. The computation of the effective concrete compressive strength for Specimen 3 is presented in detail in Appendix II.

The prestress in the longitudinal and transverse reinforcement was deduced from the ASR/DEF expansion model presented in Chapter 3, unlike the earlier work (Mander et al., 2012) where recommendations were made for the prestrains based on the level of damage. Table 7-2 presents the prestrains for the different longitudinal and transverse members of the C-STM for Specimens 2, 3, and 4. Detailed computations for the prestrains are presented in Appendix II. Based on the prestrains and the area of the steel member, the prestress force on the C-STM members was back calculated. The stress-strain relation of the reinforcement are also modified accordingly as presented in Figure 7-6 and explained in detail in Mander et al. (2012).

7.5.2 Results of C-STM Analysis

Figure 7-7 presents the overall force-deformation results obtained from the C-STM analysis for the four C-Beam specimens, along with a comparison of the results with the experimental behavior. The simulation results of Specimen 1, which was the control specimen, is the same as that presented in Mander et al. (2012) and is repeated here for completeness. As noted earlier Specimens 2, 4, and 3, respectively, showed *slight*, *moderate*, and *heavy* damages due to ASR/DEF expansion. The C-STM simulates the overall behavior of each specimen quite well. In the case of Specimen 1, the initial tension-stiffening effect was captured well by the C-STM. In the case of the deteriorated specimens, ASR/DEF expansion strains caused by the swelling of concrete put the reinforcing steel into a state of tension, which in turn prestressed the concrete. When this prestress effect was modeled accordingly by applying external loads and modifying the steel stress-strain relations (Figure 7-6), the behavior of the C-Beam specimens affected by ASR/DEF expansion was accurately captured. It is to be noted that the confined softened concrete model presented in Section 7.2 was used in modeling the softened concrete behavior of the diagonal concrete struts. While this resulted in good simulation results for Specimens 1, 2, and 4, it is evident from Figure 7-7d that using confined softened model led to an over-estimation of the ductility of the

Table 7-2: Prestrains in C-STM Members for C-Beam Specimens.

Member	Specimen 2	Specimen 4	Specimen 3
S1	0.0018	0.0044	0.0079
S2	0.0016	0.0036	0.0065
S3	0.0017	0.0038	0.0076
S4	0.0020	0.0046	0.0104
S5	0.0028	0.0068	0.0181
S6	0.0010	0.0027	0.0042
S7	0.0008	0.0021	0.0031
S8	0.0010	0.0027	0.0043
S9	0.0016	0.0043	0.0088
S14/S15	0.0032	0.0075	0.0217
S16/S22	0.0018	0.0044	0.0057
S17/S19	0.0014	0.0028	0.0034
S18/S20	0.0014	0.0025	0.0034
S21	0.0030	0.0133	0.0204

Note: Detailed computation of prestrains for Specimen 3 presented in Appendix II.

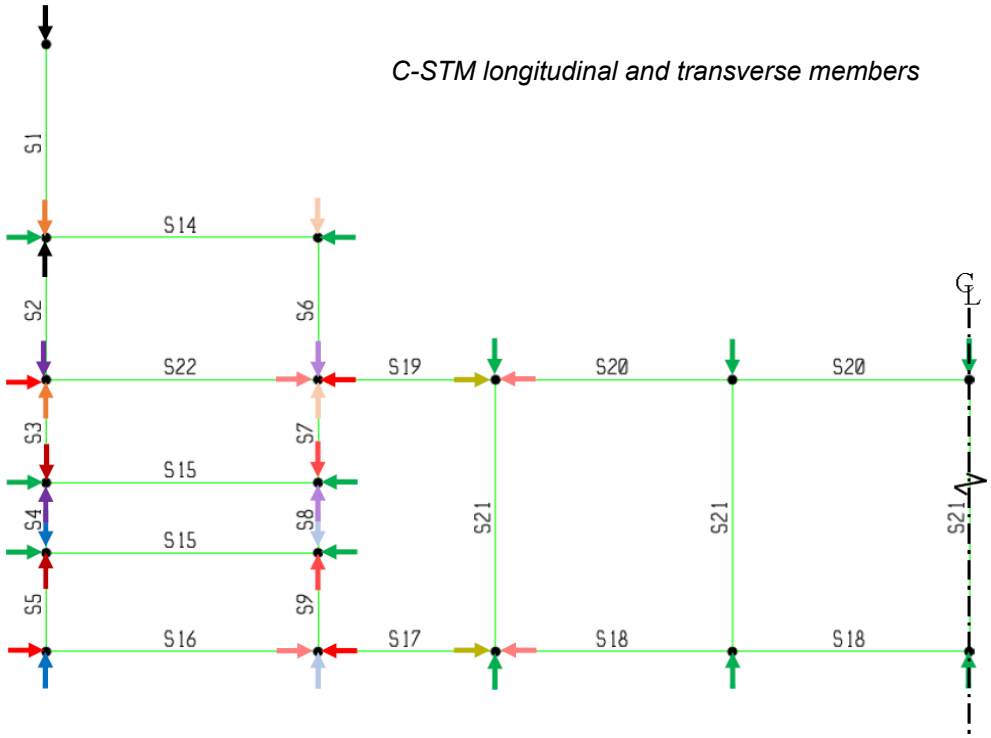

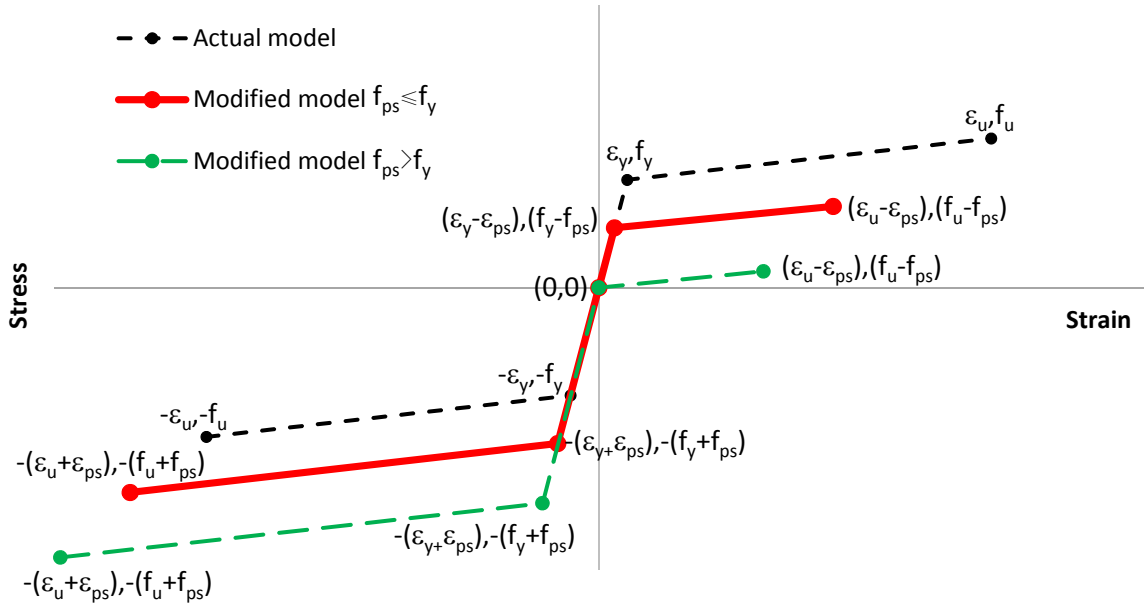

Figure 7-6: Modified Stress-Strain Model for Steel to Account for Prestressing Effects due to ASR/DEF.

(a) Specimen 1: Undamaged

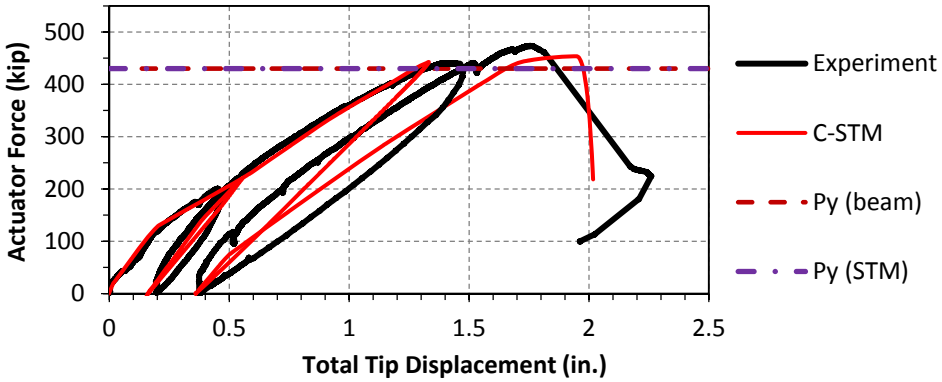

(b) Specimen 2: Slight Damage

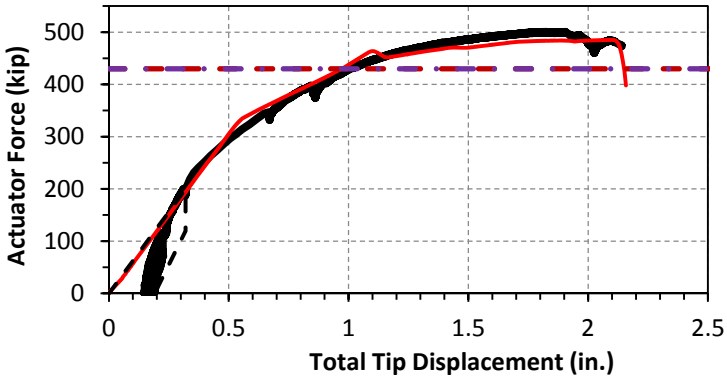

(c) Specimen 4: Moderate Damage

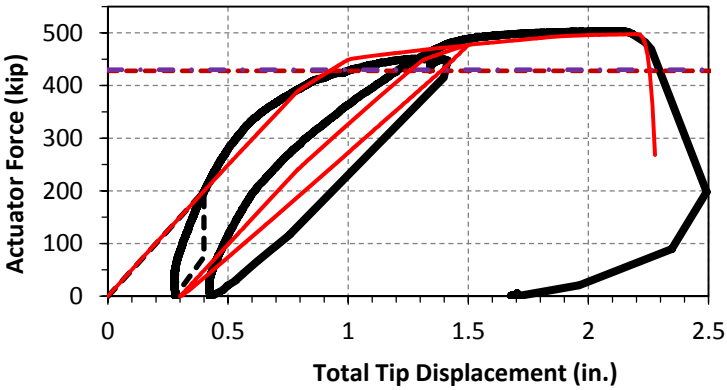

(d)Specimen 3: Heavy Damage

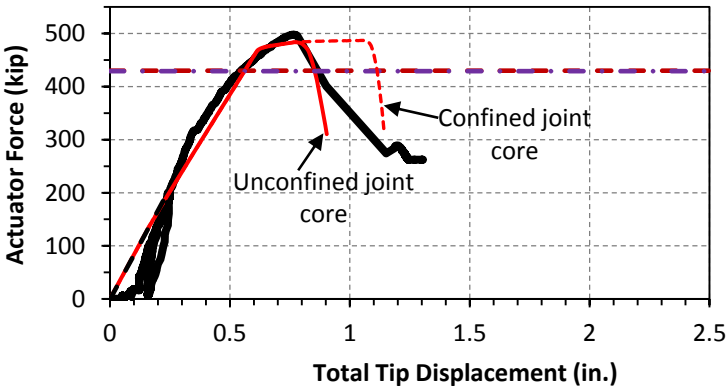

Figure 7-7: Comparison of Experimental and C-STM Results for C-Beam Specimens Subjected to ASR/DEF Deterioration.

structure. However, the unconfined softened model results in good agreement between the experimental observations and the C-STM modeled results. Due to the presence of large tensile strains in the badly damaged joint region that had poor reinforcement detailing, the use of the unconfined softened model is justified for Specimen 3.

The main difference between the simulated results presented here and those presented earlier in Phase I of this study (Mander et al., 2012) is the manner in which the prestressing forces applied to the C-STM were computed. As mentioned earlier, instead of using the modification factors that were recommended in Mander et al. (2012), the prestrains were obtained from the ASR/DEF model that was developed earlier in Chapter 3 and applied to the C-Beam specimens in Chapter 5.

The difference observed between the modeled and the observed behavior during the unloading and reloading is attributed to the partial opening/closing of cracks in the presence of shear deformations. This leads to a greater hysteresis in the experimental results than obtained through the C-STM modeled results, where concrete opening/closing is crisp and tight.

7.5.3 Interrogation of Internal Strains from C-STM and Comparison with Experimental Results

Phase I of this report demonstrated that the internal behavior obtained from C-STM compared well with the member behavior obtained from the internal strain gages and KM gages and the externally mounted LVDTs. Due to the severe nature of deterioration is Specimen 3, most of the internal sensors had failed (assumed to be due to rebar corrosion). Therefore only limited internal strain data were gathered during the test.

Figure 7-8 shows a comparison of internal strains obtained from C-STM with the experimental strains obtained from the limited number of embedded strain gages and concrete gages and the surface mounted LVDTs. The initial offset in the strain data is due to the strains caused by expansion of concrete during the deterioration phase. It is evident that the increase in strain with the applied load was almost linear until the ultimate load was achieved. This was owing to the high amounts of prestress that the structure was subjected to due to the expansion caused by ASR/DEF. Even though the strains obtained from the C-STM do not precisely agree with experimental data, the trends shown by the model are quite similar to the experimental data.

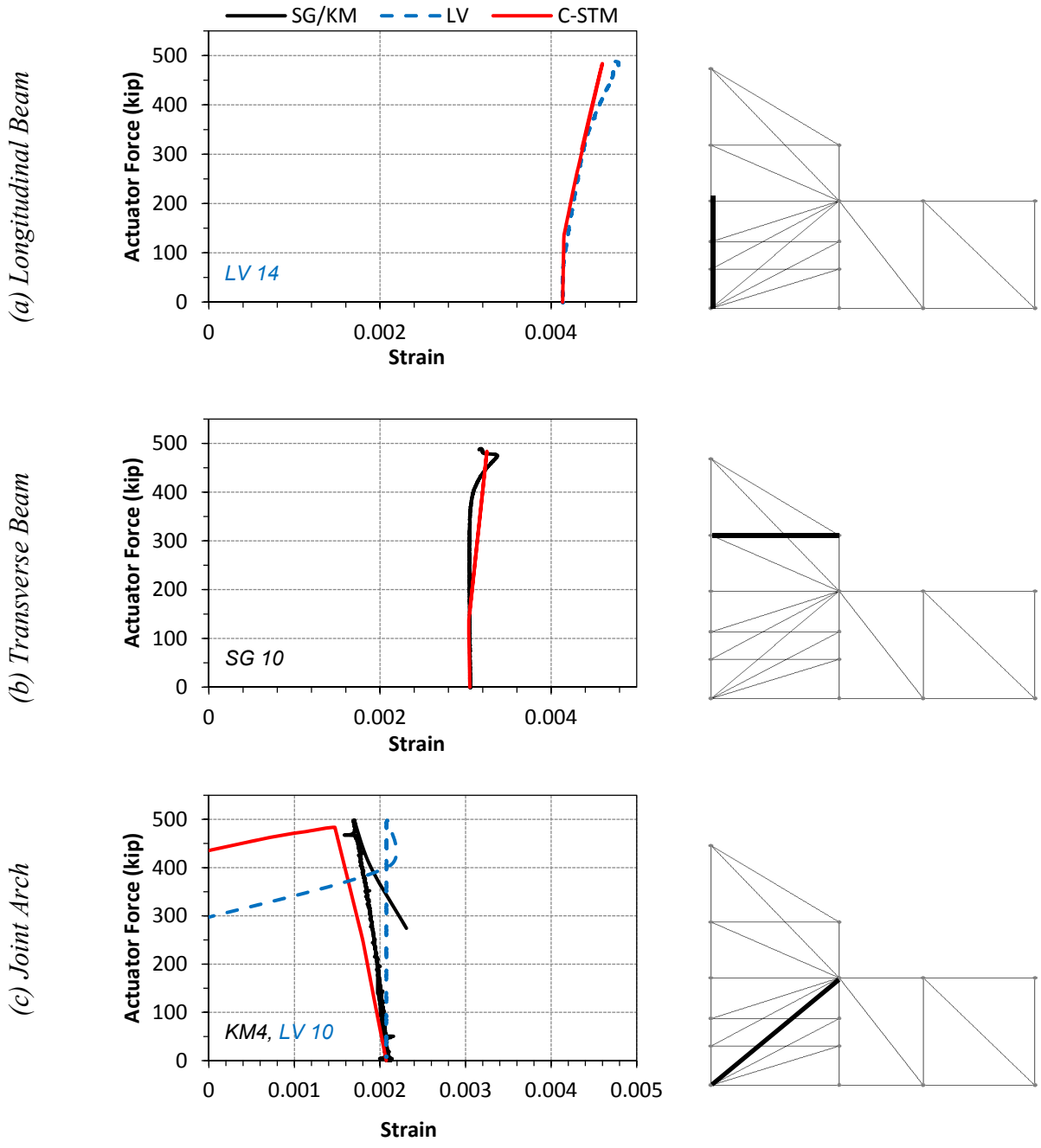

Figure 7-8: Experimental vs. C-STM Comparison of Nonlinear Concrete and Steel Response: Specimen 3.

7.6 FAILURE ANALYSIS

All the nonlinear mechanisms that developed progressively in the various constituent members of the C-STM are presented in this sub-section. Figure 7-9a–d show the development of nonlinear hinges formed during the C-STM analysis (left column of Figure 7-9) of the four specimens. When this information is combined with the overall force-deformation behavior of the specimens (the graphs in Figure 7-9), some insight into the progression of nonlinear hinge formation with respect to the global force-deformation behavior of the structure is obtained. These modeled outcomes shown in Figure 7-9 agree well with the visual observations made during each experiment.

It should be noted that Specimens 3 and 4 were heavily cracked due to the effects of ASR/DEF related expansion. Therefore, for Specimens 3 and 4 the concrete tensile strength was neglected in the C-STM analysis. As noted earlier, prestress forces were applied to the C-STM model to simulate the effects of expansion caused by ASR/DEF on the structure. Concrete decompression in Figure 7-9 refers to the stage when the effects of the applied prestress are overcome by the applied loading and the concrete strains become tensile (positive).

Based on field observed strain gage data in Specimens 2, 3, and 4, it is evident that the reinforcement yielded prior to testing. Similar observations are made in the C-STM analysis. For Specimen 2 a major change in stiffness in the force-deformation behavior occurred when the longitudinal steel in the beam-column region yielded (events 19–20 in Figure 7-9b). However, in Specimen 4 the major change in stiffness of the force-deformation behavior occurred when decompression occurred in the longitudinal concrete member in the beam and the beam-column region of the specimen (events 7–8 in Figure 7-9c). Similar observations were also made for Specimen 3 where the major change in stiffness occurred during the decompression of longitudinal concrete members in the beam and beam-column region (events 4–5 in Figure 7-9d) just before the failure of the specimen.

From Figure 7-9 it is evident that by overlaying the commencement of formation of non-linear hinges in the different members of the C-STM on the overall force-deformation behavior of the specimen, a deep insight into the internal mechanism of the specimen behavior can be obtained.

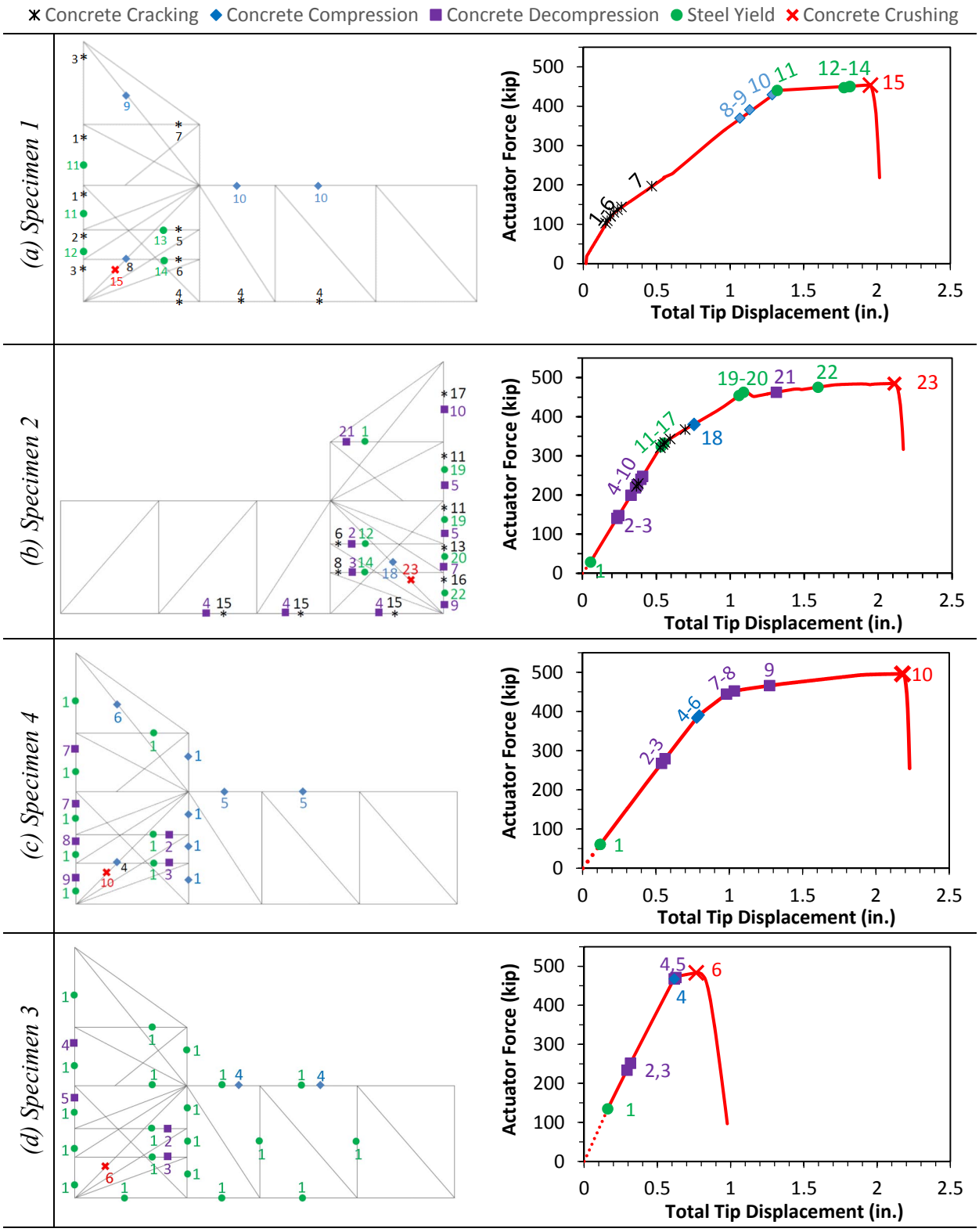

Figure 7-9: Computed Sequence of Non-Linear Behavior Events.
(Note: Specimens 1, 2, 4, and 3 respectively, had no, minor, moderate, and heavy ASR/DEF damage).

Also it is clear that the final event that resulted in the collapse of the C-Beam specimens with and without ASR/DEF damage was the compression softening of the corner-to-corner (arch) strut in the beam-column joint and the CTT node failure was an outcome of that failure mechanism.

7.7 DISCUSSION

Figure 7-10a shows overall force-deformation behavior of all the four C-Beam specimens obtained from the C-STM model. The stiffness change in the control Specimen 1 at about 130 kip was due to the first cracking of concrete. For Specimens 2, 4, and 3, the major stiffness changes were at 335 kip, 450 kip, and 465 kip, respectively. This change in stiffness occurred when the decompression of the prestress effect occurred at the critical cross-sections.

Figure 7-10b presents the experimental performance of the C-Beam specimens. The behavior of the specimens during the initial prestress process was not captured accurately. Therefore, the initial displacement of the experimental results is offset based on the C-STM observations.

It is evident from Figure 7-10 that the computationally modeled C-STM results are in good agreement with the experimental observations from the C-Beam specimens. A comparison between the C-STM and experimental ultimate load capacity for the four C-Beam specimens is presented in Table 7-3. The ultimate load computed from the C-STM is within 5 percent from the experimental results.

The various levels of deterioration caused by ASR/DEF expansion on the concrete structure were also successfully modeled into the C-STM, and the results are in good agreement with the experimental observations. The C-STM also overcomes the difficulties associated with identifying the cause of failure and the failure mechanism associated with the C-Beams. Additionally, they also provide an insight into the sequence of behavior modes that led to the failure of the structure and if the structural response was ductile or brittle.

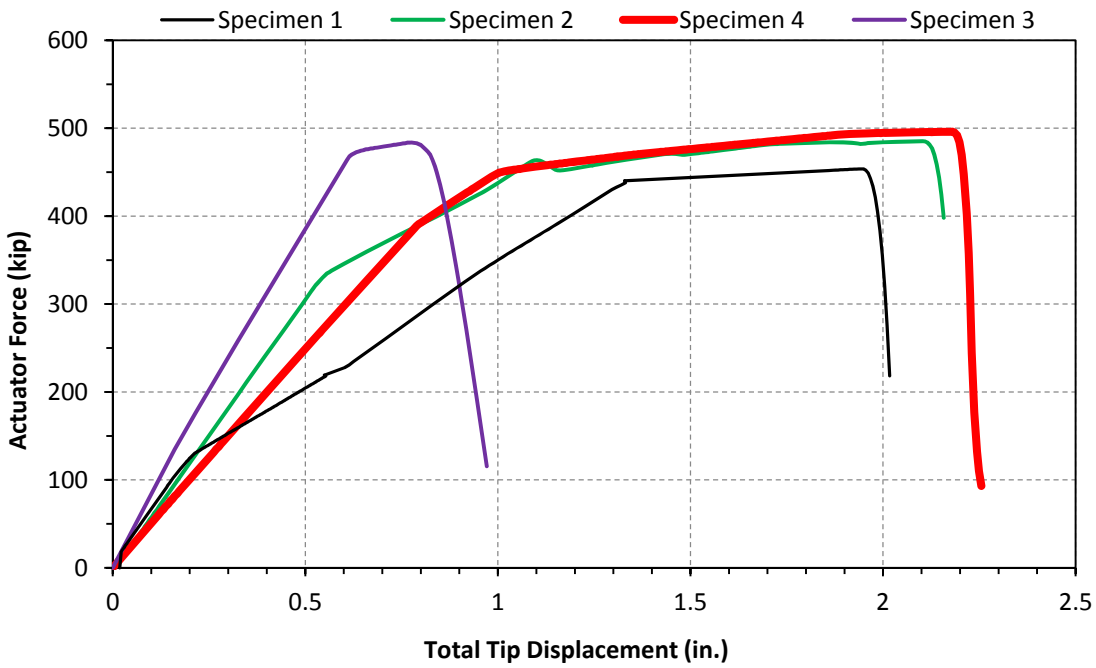

(a) C-STM Results

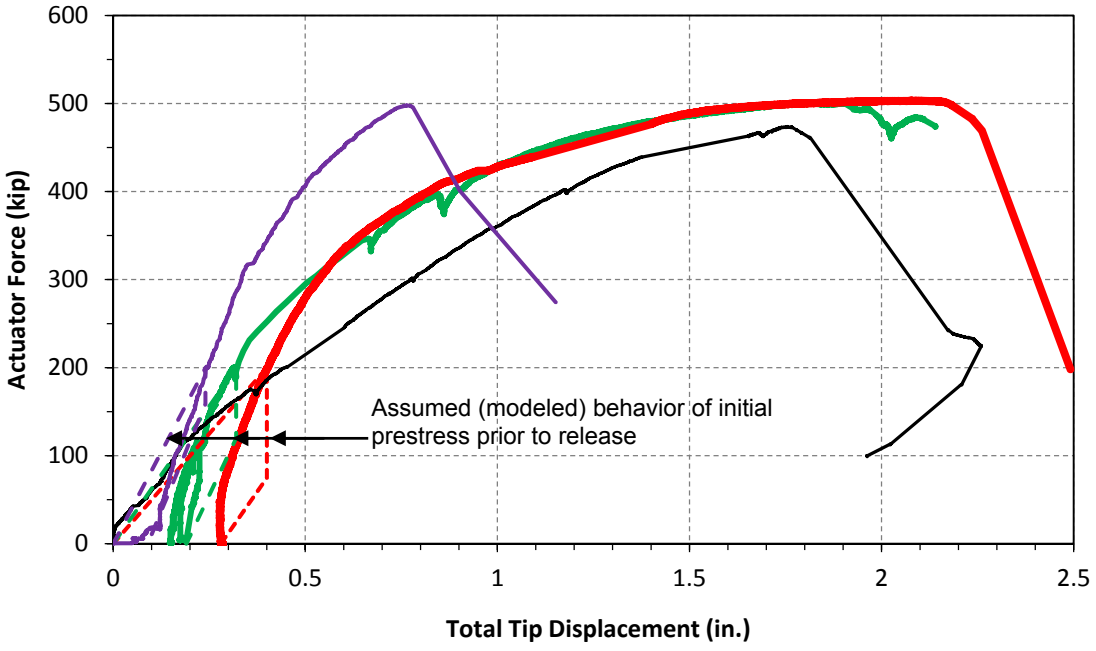

(b) Experimental Performance

Figure 7-10: Force-Deformation Results for C-Beam Specimens.

Table 7-3: Ultimate Load Capacity of C-Beam Specimens.

	C-STM	Experiment
Specimen 1 (Control Specimen)	454	474
Specimen 2 (*Slight* ASR/DEF deterioration)	485	500
Specimen 4 (*Moderate* ASR/DEF deterioration)	496	503
Specimen 3 (*Heavy* ASR/DEF deterioration)	484	498

7.8 KEY FINDINGS FROM C-STM MODELING

As demonstrated in this chapter the C-STM analysis technique has definite advantages as summarized below:

- The C-STM is capable of modeling the overall performance and the internal behavior of the structure, and the results compare well with the experimental observations.

- By taking into account the appropriate material properties and the prestressing effects caused by ASR/DEF expansion, *slight*, *moderate*, and *heavy* levels of deterioration caused by ASR/DEF expansion can be directly modeled in the C-STM analysis.

- From a failure analysis based on the results obtained from the C-STM, the trigger mechanism and the final cause of failure of the structure can be accurately captured, which at times is elusive during experimental investigations.

8 SUMMARY, CONCLUSIONS, AND RECOMMENDATIONS

8.1 SUMMARY

A large number of bridge piers in Texas exhibit premature concrete deterioration in the D-regions, owing to the detrimental effects of ASR and DEF related expansion. The nature of cracking caused by ASR and DEF reactions in concrete has been a major concern for TxDOT engineers as it creates an uncertainty about the strength and safety of each bridge structure.

The current report in conjunction with the earlier companion study conducted by Mander et al. (2012), as part of TxDOT funded project 0-5997, investigated the effects of premature concrete deterioration caused by ASR and DEF in D-regions by means of an experimental and analytical program. The following are the main tasks that are addressed in this second and final report:

- Monitor the deterioration phase of Specimen 3, which was exposed to the environmental conditions for a total period of five years, through visual observations and mechanical measurements.
- Perform the destructive testing of deteriorated Specimen 3 and compare its performance with previously tested deteriorated C-Beam specimens.
- Determine the cause of failure of the C-Beam specimen based on visual observations and the measurements made during the destructive testing of Specimen 3.
- Develop and validate a minimalist analytical model to simulate the strain expansion induced by ASR and DEF in reinforced concrete structures.
- Apply the ASR/DEF induced strain expansion model to the C-Beam specimens to model the expansion observed over time.
- Devise a method to incorporate the effects of ASR/DEF into the C-STM technique.
- Apply the C-STM technique to the experimentally tested C-Beam specimens.

A brief summary of the experimental and analytical program follows:

Deterioration program

- Specimen 3 was constructed as part of the total four C-Beam specimens that were designed and constructed to be representative of two typical bridge bents in Texas: (i) the cantilever bent and (ii) straddle bent.
- Of the four specimens, the control Specimen 1, and two deteriorated Specimens 2 and 4 that, respectively, showed *slight* and *moderate* ASR/DEF damage were tested and reported in Phase 1 of this report (Mander et al., 2012).
- Specimen 3 was field conditioned for a total of five years, and based on the visual observations and strain measurements, Specimen 3 was classified as showing *heavy* deterioration due to ASR/DEF effects.

Destructive load testing

- At the end of the deterioration phase, Specimen 3 was transported back to the laboratory to determine the effects *heavy* ASR/DEF deterioration had on the load carrying capacity of the C-Beam specimen.
- Similar to the other deteriorated C-Beam specimens, the singly reinforced side of Specimen 3 failed. The failure mechanism, which was a brittle joint shear failure along the diagonal corner-to-corner concrete arch in the beam-column joint, was observed to be the same in all the four C-Beam specimens. However, Specimen 3 showed a considerably stiffer response and reduced ductility when compared to the other C-Beam specimens.
- It was concluded that the more brittle nature of failure was due to the lack of reinforcement in one side of the joint region, while the other side possessed lapped hoops, which evidently became ineffective at high levels of ASR/DEF expansion.
- In spite of the *heavy* damaged nature of cracking arising from concrete swelling caused by ASR/DEF deterioration, Specimen 3 had similar ultimate load capacity as the other two deteriorated specimens and all the three deteriorated specimens had higher load capacity than the *undamaged* control specimen.

- After five years of outdoor conditioning, Specimen 3 exhibited a considerable degree of corrosion damage in the reinforcing steel. However, the extent of corrosion observed in Specimen 3 did not have any adverse effect on its load carrying capacity. Nevertheless, due to corrosion, the lapped hoops in the beam-column joint zone were ineffectual in confining the joint core concrete. Consequently, due to the ill-confined concrete, any ductility capability the C-Beam specimens previously exhibited (in Specimens 1, 2, and 4) was lost and the failure mode of Specimen 3 was sudden and brittle.

Analytical modeling: ASR/DEF expansion

- A minimalist model was developed and validated to simulate the expansion observed in reinforced concrete specimens subjected to ASR/DEF expansion. This model has few input parameters and is capable of taking into account the daily variations in temperature and degree of moisture saturation of concrete structures.
- It was demonstrated that if the correct reinforcement ratios were computed, the model could simulate the expansion strains over time quite well. The developed model was used to simulate the expansion strains that were observed in the C-Beam specimens, and generally good agreement between the model and observed data was observed.

Analytical modeling: C-STM

- The robustness of the C-STM analysis technique was demonstrated in Phase I of this report (Mander et al., 2012). By appropriately modifying the material properties, and taking into account the prestressing effects caused by ASR/DEF expansion, the effects of ASR/DEF on the structure can be implemented in the C-STM technique.
- To capture the more serious level of *heavy* damage caused by ASR/DEF expansion, it is necessary to discriminate between softened confined and unconfined concrete. This was introduced into the C-STM analysis by slightly reducing the post-peak softened strain of the diagonal compression strut concrete.
- Based on ASR/DEF volume expansion modeling, a direct method is now available to compute the amount of prestress to be applied on the structure to mimic the effects caused

by swelling of concrete. The C-STM was able to capture well the overall and the internal behavior of the structure without and with ASR/DEF deterioration quite well.

8.2 CONCLUSIONS

The following key conclusions can be drawn from the experimental and analytical study:

Concrete deterioration due to ASR/DEF

- ASR/DEF expansion in concrete can cause severe cracking in reinforced concrete specimens. The largest crack that was observed on C-Beam Specimen 3 that was exposed to the environmental conditions and supplemental water supply for five years was found to be approximately 1.2 in. wide.
- The strains in the longitudinal and transverse reinforcement exceeded the yield strain over the course of the deterioration phase of Specimen 3 at one year and six months of exposure, respectively.
- The cracks act as a pathway for moisture ingress into the core of the specimen. In turn this moisture promotes a considerable amount of corrosion of the exposed reinforcing bars.
- Corrosion of reinforcement within the specimen was not self-evident during field inspections. There was none of the common rust stains that one would expect to observe when significant corrosion is present. Thus the true condition of Specimen 3, while badly cracked from ongoing ASR/DEF damage, was quite *deceptive*.

Observations from destructive testing

- The cause of failure of Specimen 3 during its destructive load testing was observed to be a brittle shear failure through the corner-to-corner arch in the beam-column joint. This failure mode was the same as that observed in the previous C-Beam specimens without and with varying levels of ASR/DEF induced deterioration.
- The trigger of the failure mechanism was the decompression of concrete that was prestressed due to the restraint offered by reinforcement to ASR/DEF induced concrete

expansion. Once concrete decompression occurred, a redistribution of joint forces through the transverse reinforcement in the joint was necessary.

- Since the joint transverse reinforcement had limited capacity and as that had already yielded during the deterioration/expansion phase, there was a sudden drop in resistance and the failure was brittle. As in the case of the other three C-Beam specimens, the lack of proper detailing in the beam-column joint led to this failure mechanism.
- However, the ultimate load capacity of the *heavily* deteriorated Specimen 3 was found on par with the *slightly* and *moderately* deteriorated specimens, and remained above the ultimate load capacity of the control Specimen 1.
- The stiffness of Specimen 3 was notably higher than the other C-Beam specimens. This is attributed to the higher level of concrete swelling observed in Specimen 3, which in turn put the concrete into a greater level of prestress and thereby more effectively confined the core concrete.
- Although no sign of corrosion was observed during the deterioration phase, through spalling of cover concrete or rust stains on the concrete specimen, considerable amounts of corrosion in the reinforcement was observed after removal of the cover concrete after the experimental test. The deterioration period of five years was evidently not sufficient for the adverse effects of corrosion to reduce rebar area to affect the results. Nevertheless, this outcome cannot be assumed to apply to longer term field exposure.

Observations from analytical modeling of ASR/DEF expansion

- The proposed minimalist model needs limited input parameters, which can be deduced from expansion observations and material properties.
- The model can simulate the expansion caused by ASR and/or DEF in laboratory specimens cured under standard conditions to accelerate ASR/DEF expansion.
- In addition to the effects of varying temperature and moisture on ASR/DEF induced expansion, the effects of compressive and tensile stresses were also included in the formulation.

- By taking into account the appropriate reinforcement ratios, the model was able to simulate the expansion strains in the longitudinal and transverse directions. Considering the complex nature of the ASR/DEF expansion mechanism, and the wide scatter of field recorded data, the model was able to simulate the expansion strains quite well.

Observations from C-STM modeling

- The C-STM technique was employed to model the experimental C-Beam specimen in this study and was able to simulate quite well the overall force-deformation behavior and the internal behavior of the *heavily* deteriorated Specimen 3.
- The C-STM was also able to identify the progression of non-linear mechanisms and the final mode of failure of the C-Beam specimen.
- It was demonstrated that by carefully considering the effects of ASR/DEF on the structure, necessary modifications could be made to the C-STM to model structures affected by ASR/DEF expansion.

8.3 RECOMMENDATIONS

8.3.1 Present Practice

The swelling model that was developed in this study can be used to predict the expansion strains that are caused by ASR/DEF related expansion in reinforced concrete structures. With this model it is possible to obtain the progression of expansion strains over time, and the maximum expansion strains that can be expected in the various regions of the structure. Based on the expansion strains obtained, it is possible to compute the prestressing forces that need to be applied to the C-STM analysis to efficiently model the effects of ASR/DEF within the structure. Using the C-STM analysis it is possible to estimate the behavior, in terms of stiffness, strength and the post-peak failure mode of the structure under varying levels of ASR/DEF deterioration.

8.3.2 Future Work

The minimalist semi-empirical modeling technique that was developed and validated in this study shows much promise as an efficient way to model ASR/DEF related expansion in reinforced concrete structures. However, due to the lack of sufficient information, the values of the moisture

content for the vertical and horizontal exposure phases, which is an input parameter, had to be estimated based on rational arguments, observations, and judgment. The actual measured moisture content in the specimen can aid in further refining the expansion model.

Although the specimens in this study were subjected to accelerated deterioration conditions to promote ASR and DEF in a short time, it is not unlikely that a structure under service will show such damage. Structures that are close to the coastline that are constantly sprayed with salt water could become a very aggressive environment for ASR/DEF induced deterioration. It would be interesting to investigate how such severe exposure conditions could accelerate the expansion caused by ASR/DEF mechanisms, especially if there was a possibility of concurrent corrosion deterioration.

Although corrosion of steel had commenced during the deterioration phase in the present study, it did not adversely affect the overall load carrying capacity of the specimens. When structures prone to ASR/DEF expansion are exposed to more aggressive environments, such as coastal bridges, corrosion of steel will inevitably be accelerated. It would be of interest to investigate how rebar steel corrosion in conjunction with ASR/DEF deterioration affects the long-term behavior of the structure.

REFERENCES

AASHTO. (2007). "LRFD Bridge Design Specification." *American Associate of State Highway and Transportation Officials*, Washington, DC.

AASHTO. (2010). "LRFD Bridge Design Specification." *American Associate of State Highway and Transportation Officials*, Washington, DC.

Ahmed, T., Burley, E., and Rigden, S. (1998). "The Static and Fatigue Strength of Reinforced Concrete Beams Affected by Alkali-Silica Reaction." *ACI Materials Journal*, 95, 376–388.

ASTM-C31. (2008). "Standard Practice for Making and Curing Concrete Test Specimens in the Field." *American Society for Testing and Materials*, West Conshohocken, PA.

ASTM-C39. (2008). "Standard Test Method for Compressive Strength of Cylindrical Concrete Specimens." *American Society for Testing and Materials*, West Conshohocken, PA.

Baldwin, N.J.R. and Knights, J. (2010). "Thermal Analysis of Pre-cast Concrete Blocks Exhibiting Delayed Ettringite Formation (DEF)." *Proceedings of Structural Faults & Repair Conference*, Edinburgh, UK, CD Rom.

Barbarulo, R., Peycelon, H., Prené, S., and Marchand, J. (2005). "Delayed Ettringite Formation Symptoms on Mortars Induced by High Temperature Due to Cement Heat of Hydration or Late Thermal Cycle." *Cement and Concrete Research,* 35(1), 125–131.

Bažant, Z.P. and Steffens, A. (2000). "Mathematical Model for Kinetics of Alkali–Silica Reaction in Concrete." *Cement and Concrete Research*, 30, 419–428.

Belarbi, A. and Hsu, T.T.C. (1995). "Constitutive laws of Softened Concrete in Biaxial Tension-Compression." *ACI Structural Journal*, 92(5), 562–573.

Bouzabata, H., Multon, S., Sellier, A., and Houari, H. (2012). "Effects of Restraint on Expansion due to Delayed Ettringite Formation." *Cement and Concrete Research*, 42(7), 1024–1031.

Bracci, J.M., Gardoni, P., Eck, M.K., and Trejo, D. (2012). "Performance of Lap Splices in Large-Scale Column Specimens Affected by ASR and/or DEF." *Rep. No. FHWA/TX-12/0-5722-1,* Texas A&M Transportation Institute, The Texas A&M University System.

Brunetaud, X., Divet, L., and Damidot, D. (2008). "Impact of Unrestrained Delayed Ettringite Formation-Induced Expansion on Concrete Mechanical Properties." *Cement and Concrete Research*, 38, 1343–1348.

Capra, B. and Sellier A. (2003). "Orthotropic Modelling of Alkali-Aggregate Reaction in Concrete Structures: Numerical Simulations." *Mechanics of Materials*, 35(8), 817–830.

Charlwood, R.G., Solymar, S.V., and Curtis, D.D. (1992). "A Review of Alkali Aggregate Reactions in Hydroelectric Plants and Dams." *Proceedings of International Conference of Alkali-Aggregate Reactions in Hydroelectric Plants and Dams*, Fredericton, Canada, 129.

Clark, L.A. (1991). "Modeling the Structural Effects of Alkali-Aggregate Reactions on Reinforced Concrete." *ACI Materials Journal*, 88(3), 271–277.

Collepardi, M. (1999). "Damaged by Delayed Ettringite Formation." *Concrete International*, 21(1), 69–74.

Collepardi, M. (2003). "A State-of-the-Art Review on Delayed Ettringite Attack on Concrete." *Cement and Concrete Composites*, 25, 401–407.

Deschenes, D.J., Bayrak, O., and Folliard, K.J. (2009) "ASR/DEF-Damaged Bent Caps: Shear Tests and Field Implications." *Technical Report No 12–8XXIA006*, Texas Department of Transportation.

Diamond, S. (1996). "Delayed Ettringite Formation-Process and Problems." *Cement and Concrete Composites*, 18, 205–215.

Ekolu, S.O., Thomas, M.D.A., and Hooton, R.D. (2007). "Implications of Pre-Formed Microcracking in Relation to the Theories of DEF Mechanism." *Cement and Concrete Research*, 37, 161–165.

Eriksen, K., Edvardsen, C., and Jakobsen, U.H. (2006). "Delayed Ettringite Formation and Expansive Cracking in Unreinforced Concrete." *Proceedings of 8th International Concrete Conference and Exhibition, Concrete in Hot and Aggressive Environments*, Al Manamah, Bahrain, CD Rom.

Fan, S. and Hanson, J.M. (1998). "Effect of Alkali Silica Reaction Expansion and Cracking on Structural Behavior of Reinforced Concrete Beams," *ACI Structural Journal*, 95(5), 498–505.

Farage, M., Alves, J.L.D., and Fairbairn, E.M.R. (2004). "Macroscopic Model of Concrete Subjected to Alkali–Aggregate Reaction." *Cement and Concrete Research*, 34(3), 495–505.

Fairbairn E.M.R., Ribeiro F.L.B., Lopes L.E., Toledo-Filho R.D., and Silvoso, M.M. (2005). "Modelling the Structural Behavior of a Dam Affected by Alkali-Silica Reaction." *Communications in Numerical Methods in Engineering*, 22(1), 1–12.

Folliard, K.J., Barborak, R., Drimalas, T., Du, L., Garber, S., Ideker, J., Ley, T., Williams, T., Juenger, M., Fournier, B., and Thomas, M.D.A. (2006). "Preventing ASR/DEF in New Concrete: Final Report." *Report No. FHWA/TX-06/0-4085-5*, Center for Transportation Research Report.

Fozein Kwanke, N.J.C., Koenders, E.A.B., Bouwmeester, W.J., and Walraven, J.C. (2009). "Concrete Armor Units for Breakwaters." *Concrete International*, 34–40.

Fu, Y. (1996). "Delayed Ettringite Formation in Portland Cement Products." Dissertation, University of Ottawa, Ontario.

Furusawa, Y., Ohga, H., and Uomoto, T. (1994). "An Analytical Study Concerning Prediction of Concrete Expansion due to Alkali-Silica Reaction." *Third International Conference on Durability of Concrete*, Nice, France, 757–780.

Giannini, E., Folliard, K., Zhu, J., Bayrak, O., Kreitman, K., Webb, Z., and Hanson, B. (2013). "Non-Destructive Evaluation of In-Service Concrete Structures Affected by Alkali-Silica Reaction (ASR) or Delayed Ettringite Formation (DEF)–Part 1." *Rep. No.* FHWA/TX-13/0-6491-1*,* Center of Transportation Research, The University of Texas at Austin.

Glasser, D. and Kataoka, N. (1981). "The Chemistry of Alkali-Aggregate Reaction." *Cement and Concrete Research*, 11, 1–9.

Gravel, C., Ballivy, G., Khayat, K., Quirion, M., and Lachemi, M. (2000). "Expansion of AAR Concrete Under Triaxial Stresses: Simulation with Instrumented Concrete Block." *Proceedings of 11th Int. Conf. on AAR*, Centre de Recherche Interuniversitaire sur le Béton, Québec, Canada, 949–958.

Groves, G.W. and Zhang, X. (1990). "A Dilatation Model for the Expansion of Silica Glass/OPC Mortars." *Cement and Concrete Research*, 20, 453–460.

Heinz, D. and Ludwig, U. (1987). "Mechanism of Secondary Ettringite Formation in Motars and Concretes Subjected to Heat Treatment." *ACI Spec. Publ. (Concrete Durability),* 100(105), 2059–2071.

Hobbs, D.W. (1981). "The Alkali-Silica Reaction–A Model for Predicting Expansion in Mortar." *Magazine of Concrete Research*, 33(117), 208–220.

Hobbs, D.W. (1988). *Alkali-Silica Reaction in Concrete*. London: Thomas Telford.

Hobbs, D.W. (1999). "Expansion and Cracking in Concrete Associated with Delayed Ettringite Formation." *American Concrete Institute,* SP-177, 159–181.

Huang, M. and Pietruszczak, S. (1996). "Numerical Analysis of Concrete Structures Subjected to Alkali-Aggregate Reaction." *Mechanics of Cohesive-Frictional Materials*, 1(4), 305–319.

Huang, M. and Pietruszczak, S. (1999). "Modeling of Thermomechanical Effects of Alkali-Silica Reaction." *Journal of Engineering Mechanics,* 125(4), 476–485.

Jones, T.N. and Poole, A.B. (1986). "Alkali Silica Reactions in Several UK Concretes: The Effect of Temperature and Humidity on Expansion and the Significance of Ettringite Development." *Proceedings of 7th International Conference on Alkali Aggregate Reactions*, Ottawa, Ed Grattan, P. Bellew. Noyes Publications, Park Ridge, NJ, 446–450.

Jones, A.E.K. and Clark, L.A. (1996). "The Effects of Restraint on ASR Expansion of Reinforced Concrete." *Magazine of Concrete Research*, 48(174), 1–13.

Ingham, J. (2012). "Briefing: Delayed Ettringite Formation in Concrete Structures." *Proceedings of Institution of Civil Engineers Forensic Engineering*, 2, 59–62.

Ingham, J. and McKibbins, L. (2013). "Briefing: Concrete Structures Affected by Cracking." *Proceedings of Institution of Civil Engineers Forensic Engineering*, 166, 3–8.

Karthik, M.M, and Mander, J.B. (2011). “Stress-Block Parameters for Unconfined and Confined Concrete Based on a Unified Stress-Strain Model.” *Journal of Structural Engineering*, 137(2), 270–273.

Kelham, S. (1996). “The Effect of Cement Composition and Fineness on Expansion Associated with Delayed Ettringite Formation.” *Cement and Concrete Composites*, 18, 171–179.

Kurtis, K.E. (2003). “Chemical Additives to Control Expansion of Alkali–Silica Reaction Gel: Proposed Mechanisms of Control.” *Journal of Material Science*, 38, 2027–2036.

Larive, C. and Louarn, N. (1992). “Diagnosis of Alkali Aggregate Reaction and Sulphate Reaction in French Structures.” *Proceedings of 9th International Conference on Alkali Aggregate Reactions*, London, Concrete Society, 587–598.

Larive, C., Laplaud, A., and Joly, M. (1996). “Behavior of AAR-Affected Concrete: Experimental Data.” *Proceedings of 10th Int. Conf. on AAR*, A. Shayan, ed., Melbourne, Australia, 670–677.

Larive, C. (1998). “Apports combinés de l’expérimentation et de la modélisation à la compréhension de l’alcali-réaction et de ses effets mécaniques.” *Rep. OA 28, ERLPC Collection*, Laboratoire Central des Ponts et Chaussées, Paris.

Larive, C., Joly, M., and Coussy, O. (2000). “Heterogeneity and Anisotropy in ASR-Affected Concrete: Consequences for Structural Assessment.” *Proceedings of 11th International Conference on AAR*, Centre de Recherche Interuniversitaire sur le Béton, Québec, Canada, 969–978.

Lawrence, B.L., Myers, J.J., and Carrasquillo, R.L. (1999). “Premature Concrete Deterioration in Texas Department of Transportation Precast Elements.” *American Concrete Institute,* SP-177, 141–158.

Léger, P., Côté, P., and Tinawi, R. (1996). “Finite Element Analysis of Concrete Swelling due to Alkali-Aggregate Reactions in Dams.” *Computers and Structures*, 60(4), 601–611.

Li, K. and Coussy, O. (2002). “Concrete ASR Degradation: from Material Modeling to Structure Assessment.” *Concrete Science and Engineering,* 4, 35–46.

Liu, S.H. (2012). "Structural Assessment of D-regions Affected by Alkali Silica Reaction/Delayed Ettringite Formation." Ph.D. Dissertation, Texas A&M University, College Station, Texas.

Mander, J.B., Priestley, M.J.N., and Park, R. (1988). "Theoretical Stress-Strain Model for Confined Concrete." *ASCE Journal of Structural Engineering*, 114(8), 1804–1826.

Mander, J. B., Bracci, J. M., Hurlebaus, S., Grasley, Z., Karthik, M. M., Liu, S.-H., and Scott, R. M. (2012). "Structural Assessment of "D" Region Affected by Premature Concrete Deterioration: Technical Report." *Rep. No. FHWA/TX-12/0-5997-1,* Texas A&M Transportation Institute, The Texas A&M University System.

Mander, T.J., Mander, J.B., and Head, H. (2011). "Modified Yield Line Theory for Full-Depth Precast Concrete Bridge Deck Overhang Panels." *Journal of Bridge Engineering,* 16(1), 12–20.

Martin, R.P., Renaud, J.C., and Toutlemonde, F. (2010) "Experimental Investigations Concerning Combined DEF and AAR." *Proceedings of 6th International Conference on Concrete under Severe Conditions*, Merida, Mexico, 287–295.

Martin, R.P., Metalssi, O.O., and Toutlemonde, F. (2013) "Importance of Considering the Coupling Between Transfer Properties, Alkali Leaching and Expansion in the Modeling of Concrete Beams Affected by Internal Swelling Reactions." *Construction and Building Materials*, 49, 23–30.

Mielenz, R.C., Marusin, S.L., Hime, W.G., and Jugovic, Z.T. (1995). "Investigation of Prestressed Concrete Railway Tie Distress." *Concrete International*, 17(12), 62–68.

Mohammed, T.U., Hamada, H., and Yamaji, T. (2003). "Alkali-Silica Reaction-Induced Strains over Concrete Surface and Steel Bars in Concrete." *ACI Materials Journal*, 100, 133–142.

Monette, L.J., Gardner, N.J., and Grattan-Bellew, P.E. (2002). "Residual Strength of Reinforced Concrete Beams Damaged by Alkali-Silica Reaction—Examination of Damage Rating Index Method." *ACI Materials Journal*, 99, 42–50.

Multon, S. (2004). "Evaluation Expérimentale et Théorique des Effets de l'alcali-réaction sur des Structures Modèles." *Rep. OA 46, ERLPC Collection*, Laboratoire Central des Ponts et Chaussées, Paris.

Multon, S., Leclainche, G., Bourdarot, E., and Toutlemonde, F. (2004). "Alkali-Silica Reaction in Specimens Under Multi-Axial Mechanical Stresses." *Proceedings of CONSEC'04*, B. H. Oh, et al., eds., Seoul National Univ., Seoul, Korea, 2004–2011.

Multon, S., Seignol, J.F., and Toutlemonde, F. (2005). "Structural Behavior of Concrete Beams Affected by Alkali-Silica Reaction. *ACI Materials Journal*, 102, 67–76.

Multon, S., Seignol, J.F., and Toutlemonde, F. (2006). "Chemomechanical Assessment of Beams Damaged by Alkali-Silica Reaction." *Journal of Materials in Civil Engineering*, 18(4), 500–509.

Multon, S. (2013). Personal e-mail communication received September 20.

Olafsson, H. (1986). "The Effect of Relative Humidity and Temperature on Alkali Expansion of Mortar Bars." *Proceedings of 7th Int. Conf. on AAR*, Noyes, Park Ridge, NJ, 461–465.

Odler, I. (1980). "Interaction Between Gypsum and C-S-H Phase Formed in C_3S Hydration." *7th International Congress on the Chemistry of Cement*, Paris, 493–495.

Pavoine, A., Brunetaud, X., and Divet, L. (2012). "The Impact of Cement Parameters on Delayed Ettringite Formation." *Cement and Concrete Composites*, 34, 521–528.

Pesavento, F., Gawin, D., Wyrzykowski, M., Schrefler, B.A., and Simoni, L. (2012). "Modeling Alkali–Silica Reaction in Non-Isothermal, Partially Saturated Cement Based Materials." *Computational Methods in Applied Mechanics and Engineering*, 225(228), 95–115.

Pettifer, K. and Nixon, P.J. (1980). "Alkali Metal Sulfate – A Factor Common to both Alkali Aggregate Reaction and Sulfate Attack on Concrete." *Cement and Concrete Research*, 10, 173–181.

Pietruszczak, S. (1996). "On the Mechanical Behavior of Concrete Subjected to Alkali-Aggregate Reaction." *Computer and Structures*, 58(6), 1093–1097.

Pietruszczak, S. and Winnicki, A. (2003). "Constitutive Model for Concrete with Embedded Sets of Reinforcement." *Journal of Engineering Mechanics*, 129(7), 725–738.

Poole, A.B. (1992). "Alkali-Silica Reactivity Mechanisms of Gel Formation and Expansion." *Proceedings of 9th International Conference on Alkali-Aggregate Reaction*, London (England). 104, 782–789.

Riding, K.A., Poole, J.L., Folliard, K.J., Juenger, M.C.G., and Schindler, A.K. (2012). "Modeling Hydration of Cementations Systems." *ACI Materials Journal*, 109(2), 225–234.

Salgues, M., Sellier, A., Multon, S., Bourdarot, E., and Grimal, E. (2014). "DEF Modelling Based on Thermodynamic Equilibria and Ionic Transfers for Structural Analysis." *European Journal of Environmental and Civil Engineering*, 18(4), 377–402.

Saouma, V. and Perotti, L. (2006). "Constitutive Model for Alkali-Aggregate Reactions." *ACI Materials Journal*, 103, 194–202.

Scott, R.M., Mander, J.B., and Bracci, J.M. (2012a). "Compatibility Strut-and-Tie Modeling: Part I—Formulation." *ACI Structural Journal*, 109(5), 635-644.

Scott, R.M., Mander, J.B., and Bracci, J.M. (2012b). "Compatibility Strut-and-Tie Modeling: Part II —Implementation." *ACI Structural Journal*, 109(5), 645-653.

Scrivener, K.L. and Taylor, H.F.W. (1993). "Delayed Ettringite Formation: A Microstructural and Microanalytical Study." *Advances in Cement Research,* 5(20), 139–146.

Scrivener, K.L., Damidot, D., and Famy, C. (1999). "Possible Mechanisms of Expansion of Concrete Exposed to Elevated Temperatures During Curing (Also Known as DEF) and Implications for Avoidance of Field Problems." *American Society for Testing and Materials*, 93–101.

Seignol, J.F., Baghdadi, N., and Toutlemonde, F. (2009). "A Macroscopic Chemo-Mechanical Model Aimed at Re-Assessment of DEF Affected Concrete Structures." *Proceedings of 1st International Conference on Computational Technologies in Concrete Structures*, Jeju, Korea, 422–440.

Stanton, T.E. (1940). "Expansion of Concrete through Reaction between Cement and Aggregate." *Proceeding of American Society of Civil Engineers*, 66, 1781–1811.

Swamy, R.N., and Al-Asali, M.M. (1988). "Engineering Properties of Concrete Affected by Alkali-Silica Reaction." *ACI Materials Journal*, 85, 367–374.

Swamy, R.N., and Al-Asali, M.M. (1989). "Effect of Alkali-Silica Reaction on the Structural Behavior of Reinforced Concrete Beams." *ACI Materials Journal*, 86, 451–459.

Taylor, H.F.W., Famy, C., and Scrivener, K.L. (2001). "Delayed Ettringite Formation." *Cement and Concrete Research*, 31, 683–693.

Ulm, F.J., Coussy, O., Kefei, L., and Larive, C. (2000). "Thermo-Chemo-Mechanics of ASR Expansion in Concrete Structures." *Journal of Engineering Mechanics*, 126(3), 233–242

Vecchio, F.J. and Collins, M.P. (1993). "Compression Response of Cracked Reinforced Concrete." *Journal of Structural Engineering*, 119(12), 3590–3610.

Vecchio, F.J. (2000). "Analysis of Shear-Critical Reinforced Concrete Beams." *ACI Structural Journal*, 97(1), 102–110.

Wimpenny, D.E., White, P.S., and Eden, M.A. (2007). "Two Case Studies of the Management of Bridges Diagnosed with Delayed Ettringite Formation." *Proceedings of 5th Institution of Civil Engineers International Bridge Design, Construction and Maintenance Conference*, Beijing, China. Thomas Telford, London, UK, 448–457.

Winnicki, A. and Pietruszczak, S. (2008). "On Mechanical Degradation of Reinforced Concrete Affected by Alkali-Silica Reaction." *Journal of Engineering Mechanics*, 134(8), 611–627.

APPENDIX I: CALCULATIONS FOR CHAPTER 5

The computation of reinforcement ratio and the maximum expansion strain to simulate the ASR/DEF induced expansion in C-Beam Specimen 3 is presented in this appendix.

	COMPUTATION OF REINFORCEMENT RATIO (ρ) AND MAXIMUM EXPANSION STRAIN $\left(\varepsilon_{\rho}^{max}\right)$ FOR C-BEAM SPECIMEN 3	1/8

GENERAL NOTES

General Parameters Used

$f_c^{'} = 5.93$ ksi $\quad E_c^{actual} = 4390$ ksi $\quad f_t^{'} = 0.580$ ksi $\quad \varepsilon_t = 0.000132$

$f_y = 65$ ksi $\quad E_s = 29000$ ksi $\quad \varepsilon_y = 0.00224$

$t_r(\theta_o) = 120$ days $\quad \varepsilon_{pc}^{ASR} = 0.05$ $\quad n = \dfrac{E_s}{E_c/3} = 19.82$

Maximum Expansion Strain

The C-Beam specimens were subjected to tie-bar force to simulate gravity loads on the structure. This resulted in the specimen being precracked, which further accelerated the expansion process as these cracks provided a pathway for moisture ingress. To take into account the precracked nature of the specimen, Eq. 3-16a (which is repeated below for convenience) was used in the computation of the expansion strains $\left(\varepsilon_{\rho}^{max}\right)$.

$$\varepsilon_{\rho}^{max} = \frac{\varepsilon_o^{max}\varepsilon_t + \rho n\left(\varepsilon_y^2 - \varepsilon_{ps}^2\right) + \varepsilon_t\varepsilon_{pc} - \left(\frac{\varepsilon_t}{2}\right)^2}{2\left(\frac{\varepsilon_t}{2} + \rho n\left(\varepsilon_y - \varepsilon_{ps}\right) - \frac{\sigma_{const}}{E_c}\right)} \qquad 3\text{-}16a$$

Development Length (ACI Equations)

Mander et al. (2011) established that to develop the full yield strength of the reinforcement, the reinforcing bars transverse to the member edge should be longer than the bar development length (l_d).

#8 bars: $\left(l_d\right) = \left(\dfrac{f_y\psi_t\psi_e}{20\lambda\sqrt{f_c^{'}}}\right)d_b = \left(\dfrac{65000(1)(1)}{20(1)\sqrt{f_c^{'}}}\right)d_b = 3250\dfrac{d_b}{\sqrt{f_c^{'}}} = 42.20''$

#4 bars: $\left(l_d\right) = \left(\dfrac{f_y\psi_t\psi_e}{25\lambda\sqrt{f_c^{'}}}\right)d_b = \left(\dfrac{65000(1)(1)}{25(1)\sqrt{f_c^{'}}}\right)d_b = 2600\dfrac{d_b}{\sqrt{f_c^{'}}} = 16.88''$

CASE 1	COMPUTATION OF REINFORCEMENT RATIO (ρ) AND MAXIMUM EXPANSION STRAIN (ε_ρ^{max}) FOR C-BEAM SPECIMEN 3	2 / 8

COLUMN TOP FACE MEMBER REGION

Section depth (d) = overall depth (D) - depth to neutral axis (kd_{col}) = 36-13.98 = 22.02"

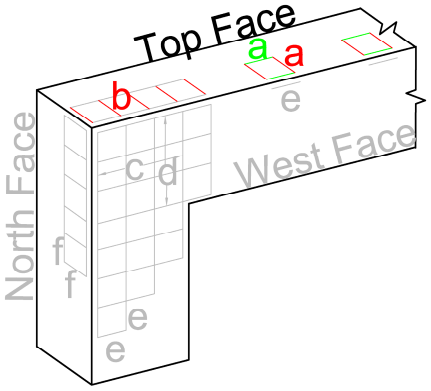

Direction: Transverse (a)

Reinforcement type: #4 bars with c/s area A_s = 0.19635 in^2 @ 4.5" c/c spacing

Reinforcement ratio $\rho = A_s/(sd) = 0.00198$

Additionally, as there are no tensile prestrains in the transverse direction, $\varepsilon_{pc} = \varepsilon_{ps} = 0$.

Maximum expansion strain $\varepsilon_\rho^{max} = = 0.02202$

Direction: Longitudinal (a)

DEMEC measurements are made along two lines, one close to the edge of the column, and the other closer to the middle of the column cross-section. As the DEMEC readings are limited to the two lines, the strains measured could be more localized. Therefore narrow strips under the DEMEC points are considered to compute the reinforcement ratio. Because of their localized effects the average reinforcement ratio is considered.

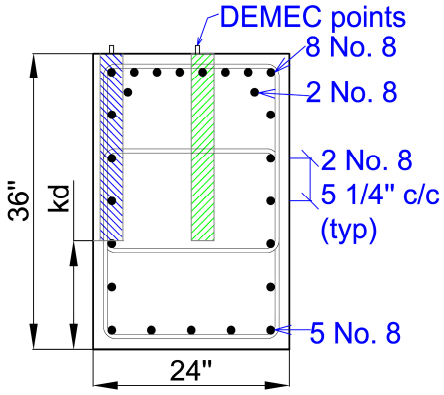

Width of strip (b) = 2.785" (shaded blue and green)

c/s area of concrete A_c = (22.02) (2.785) = 61.33 in^2

DEMEC points location	Close to column edge (shaded blue)	Close to column center (shaded green)
A_s (in^2)	3.1416 (4-#8 bars)	0.7854 (1-#8 bar)
$\rho = A_s/(bd)$	0.05122	0.01281
Average ρ	0.03202	

$\varepsilon_{pc} = \varepsilon_{ps} = 0.00067$ obtained from C-STM model.

$\varepsilon_\rho^{max} = = 0.0045$

Figure 5-4a shows the expansion results obtained in the transverse and longitudinal direction on the member region of the column top face of the C-Beam specimen.

CASE II	COMPUTATION OF REINFORCEMENT RATIO (ρ) AND MAXIMUM EXPANSION STRAIN (ε_{ρ}^{max}) FOR C-BEAM SPECIMEN 3	3/8

COLUMN TOP FACE JOINT REGION

Direction: Transverse (b)

There are no transverse hoops on the column top face in the joint region. Therefore, $\rho = 0$ is considered for the region close to the edge. However, in the region away from the edge and close to the column member region, the influence of transverse reinforcement in the column member region is considered. A $\rho = 0.00198/2 = 0.00099$ is assumed.

Since there are no tensile prestrains in the transverse direction, $\varepsilon_{pc} = \varepsilon_{ps} = 0$.

$\varepsilon_{\rho}^{max} = = 0.0304$

Figure 5-4b shows the transverse expansion strains in the joint region of the C-Beam specimen top face.

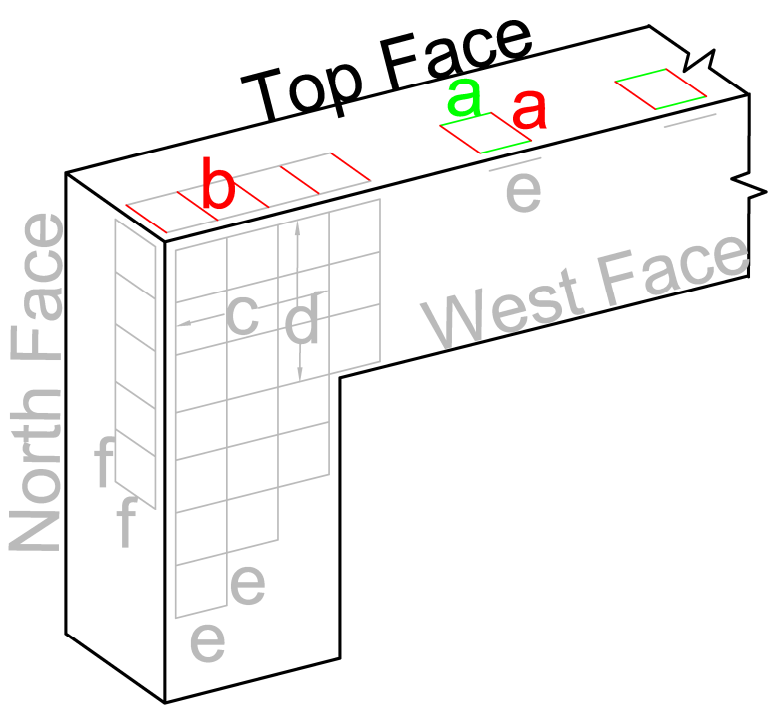

CASE III	COMPUTATION OF REINFORCEMENT RATIO (ρ) AND MAXIMUM EXPANSION STRAIN (ε_ρ^{max}) FOR C-BEAM SPECIMEN 3	4 / 8

BEAM COLUMN JOINT REGION

Concrete and steel volume in half the section-depth ($d = 12''$) is considered for calculating the reinforcement ratio.

Direction: Vertical DEMEC Points along Beam Longitudinal Steel

Depending on the location of the DEMEC points on the face of the beam cross-section, two separate reinforcement ratios are computed.

DEMEC location	Close to member edges (shaded blue)	For interior DEMEC points (shaded green)
Area of steel, A_s	3.9270 in^2 (5-#8 bars)	0.5890 in^2 (3-#4 bars)
Area of concrete, A_c	(12)(6.1875) = 74.25 in^2	(12)(23.625) = 283.5 in^2
ρ	0.0529	0.00208

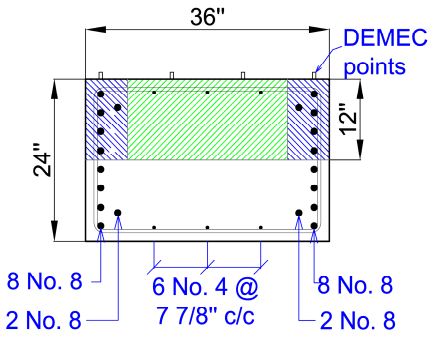

The reinforcement ratio is scaled down for the DEMEC points close to the C-Beam specimen edges.

Scaled reinforcement ratio for:	DEMEC 145 and 146 close to specimen top edge	DEMEC 139-142, still within the development length
l	5.25''	15.75''
$\rho_{reduced} = \rho(l/l_d)$	0.00208(5.25/16.88) = 0.000647	0.0529(15.75/42.20) = 0.01974
With ($\varepsilon_{pc} = \varepsilon_{ps} = 0$), ε_ρ^{max} =	0.03514	0.00453

Figure 5-4c shows two curves for the expansion results from the model. Curve A corresponds to the case where the expansion strains are computed closer to the top edge of the specimen (within development length zone close to top edge) and Curve B for expansion strains computed away from the top edge (within development length zone away from top edge).

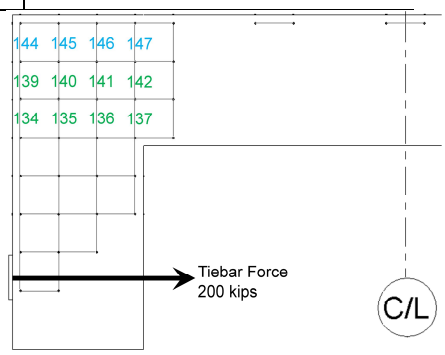

CASE IV	COMPUTATION OF REINFORCEMENT RATIO (ρ) AND MAXIMUM EXPANSION STRAIN (ε_{ρ}^{max}) FOR C-BEAM SPECIMEN 3	5/8

BEAM COLUMN JOINT REGION

Concrete and steel volume in half the section-depth ($d = 12''$) is considered for calculating the reinforcement ratio.

Direction: Horizontal DEMEC Points along Column Longitudinal Steel

Depending on the location of the DEMEC points on the face of the beam cross-section, two separate reinforcement ratios are computed.

For DEMEC within the development length zone and close to the specimen edges (first layer of DEMEC points 158, 162, 166, and 170) the portion shaded in green is used to compute the reinforcement ratio as the influence of the reinforcement at the extremes (shaded blue) is unlikely to influence the expansion close to the specimen edge.

DEMEC location	Close to member edges (entire shaded region)	For interior DEMEC points (shaded green)
Area of steel, A_s	10.21 in^2 (12-#8 and 4-#4 u-bars, not shown)	4.7124 in^2 (5-#8 and 4-#4 u-bars, not shown)
Area of concrete, A_c	(12)(36) = 432 in^2	(12)(26.25) = 315 in^2
ρ	0.0236	0.01496

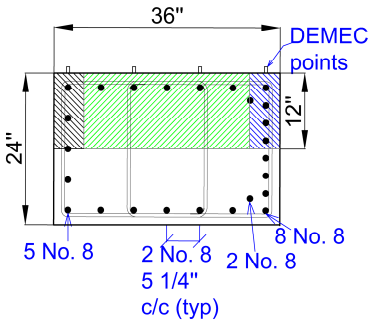

The reinforcement ratio is scaled down for DEMEC points close to C-Beam specimen edges.

Scaled reinforcement ratio for:	DEMEC 159, 163, 167, and 171 still within the development length	DEMEC 158, 162, 166, and 170 close to specimen edge
l	15.75"	5.25"
$\rho_{reduced} = \rho(l/l_d)$	0.0236(15.75/42.20) = 0.00881	0.01496(5.25/42.20) = 0.001861
With ($\varepsilon_{pc} = \varepsilon_{ps} = 0$), ε_{ρ}^{max} =	0.00816	0.02278

Figure 5-4d shows the expansion strains, close and away from the specimen edge, obtained from the model.

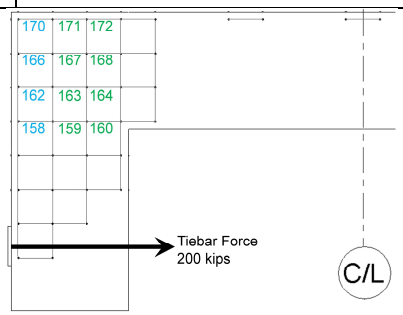

CASE V	COMPUTATION OF REINFORCEMENT RATIO (ρ) AND MAXIMUM EXPANSION STRAIN (ε_ρ^{max}) FOR C-BEAM SPECIMEN 3	6 / 8

BEAM WEST FACE

Concrete and steel volume in half the section-depth ($d = 12''$) is considered for calculating the reinforcement ratio.

Direction: Longitudinal

As the DEMEC points are considerably away from the specimen edge, the reinforcement in the entire half-depth of the cross-section ($d = 12''$) is considered as localized effects near the edges are eliminated.

Area of steel, A_s	8.44 in² (10-#8 and 3-#4 bars)
Area of concrete, A_c	(12) (36) = 432 in²
ρ	0.01954
With ($\varepsilon_{pc} = \varepsilon_{ps} = 0$), ε_ρ^{max} =	0.00456

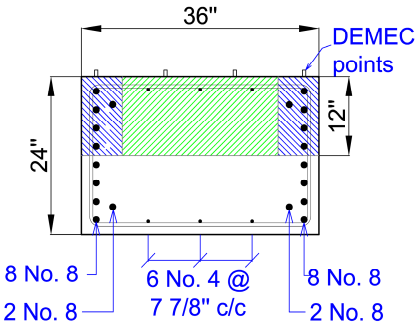

The reinforcement ratio is scaled down for the DEMEC points within the development length zone.

Scaled reinforcement ratio for:	DEMEC 123-125 within the development length zone
l	35.15"
$\rho_{reduced} = \rho(l/l_d)$	0.01954 (31.75/42.20) = 0.01470
With ($\varepsilon_{pc} = \varepsilon_{ps} = 0$), ε_ρ^{max} =	0.00559

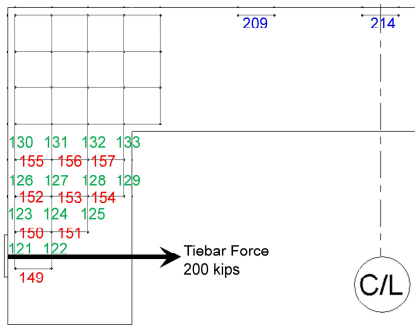

Direction: Transverse

Reinforcement type: #4 bars with c/s area 0.19635 in² @ 4.5" c/c spacing.

Reinforcement ratio $\rho = A_s/(sd) = 0.00364$.

As there are no tensile prestrains in the transverse direction, $\varepsilon_{pc} = \varepsilon_{ps} = 0$.

Maximum expansion strain $\varepsilon_\rho^{max} = = 0.01526$.

Figure 5-4e shows the expansion strain s in the longitudinal and transverse direction on the beam west face.

CASE VI	COMPUTATION OF REINFORCEMENT RATIO (ρ) AND MAXIMUM EXPANSION STRAIN (ε_{ρ}^{max}) FOR C-BEAM SPECIMEN 3	7/8

COLUMN WEST FACE

Direction: Longitudinal

The DEMEC points in the column of the specimen west face were located close to the specimen top edge; therefore the reinforcement ratio is calculated considering the area shaded in blue.

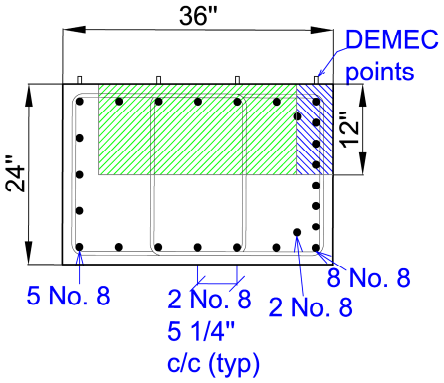

Area of steel, A_s	3.927 in² (5-#8 bars)
Area of concrete, A_c	(12) (4.875) = 58.5 in²
ρ	0.0671

$\varepsilon_{pc} = \varepsilon_{ps} = 0.00067$ obtained from C-STM model. $\varepsilon_{\rho}^{max} = 0.00296$

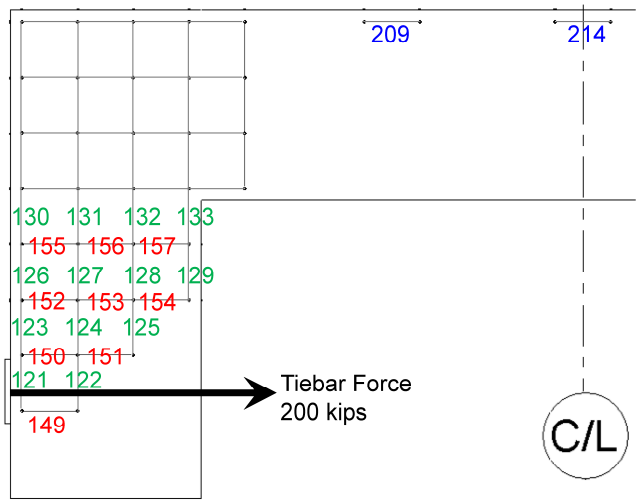

Figure 5-4e shows the expansion strains in the longitudinal direction on the column west face.

CASE VII	COMPUTATION OF REINFORCEMENT RATIO (ρ) AND MAXIMUM EXPANSION STRAIN (ε_{ρ}^{max}) FOR C-BEAM SPECIMEN 3	8 / 8

BEAM NORTH FACE

Section depth (d) = overall depth (D) - depth to neutral axis (kd_{beam}) = 36-11.31 = 24.69"

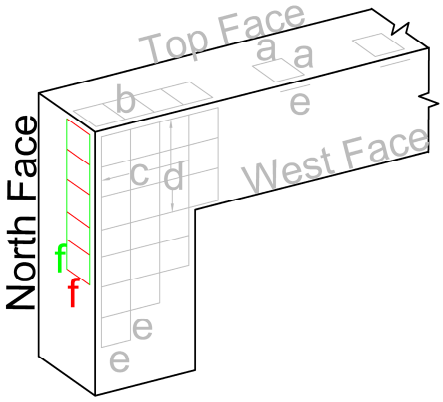

Direction: Transverse (f)

Reinforcement type: #4 bars with c/s area A_s = 0.19635 in² @ 4.5" c/c spacing

Reinforcement ratio $\rho = A_s/(sd) = 0.00177$

As there are no tensile prestrains in the transverse direction, $\varepsilon_{pc} = \varepsilon_{ps} = 0$.

Maximum expansion strain $\varepsilon_{\rho}^{max} = = 0.0234$

Direction: Longitudinal (f)

DEMEC measurements are made along two lines, one close to the edge of the beam, and the other closer to the middle of the beam cross-section. As the DEMEC readings are limited to the two lines, the strains measured could be more localized. Therefore narrow strips under the DEMEC points are considered to compute the reinforcement ratio. Because of their localized effects the average reinforcement ratio is considered.

Width of strip (b) = 2.785" (shaded blue and green)

c/s area of concrete $A_c = (24.69)(2.785) = 68.76$ in²

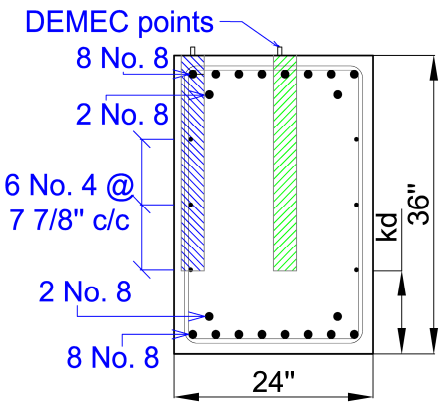

DEMEC points location	Close to beam edge (shaded blue)	Close to beam center (shaded green)
A_s (in²)	1.1781 in² (1-#8 and 2-#4 bars)	0.7854 in² (1-#8 bar)
$\rho = A_s/(bd)$	0.01713	0.01142
Average ρ	0.01428	

$\varepsilon_{pc} = \varepsilon_{ps} = 0.00084$ obtained from C-STM model.

Maximum expansion strain $\varepsilon_{\rho}^{max} = 0.00855$

Figure 5-4f shows the expansion strain results on the north face of the C-Beam specimen.

APPENDIX II: CALCULATIONS FOR CHAPTER 7

In this appendix, the computation of concrete material properties to be used in the C-STM for CBeam Specimen 3 is presented first. This is followed by the computation of prestrains to be applied to the C-STM model for Specimen 3 to simulate the effects of ASR/DEF into the analysis.

	COMPUTATION OF MATERIAL PROPERTIES TO PERFORM THE C-STM ANALYSIS FOR C-BEAM SPECIMEN 3	1 / 2

1. Computation of Confinement Ratio for Beam and Column

Concrete compressive strength obtained experimentally from cylinder tests, $f_c^{'}$ =5.93 ksi. As the strains in the steel were much higher than the yield strain, f_y =75 ksi is considered for the following computations.

Computation of concrete confinement ratio: beam

kd (in.)	11.31
A_{cc} (in^2) $=(c_c+d_s/2)\times b_c$	206
A_e (in^2) $=(c_c+d_s/2)\times b_c -$ area of shaded region	124.58
$k_e = A_e / A_{cc}$	0.605
f_{lx} (ksi) $= k_e \dfrac{A_{str} f_y}{(c_c+d_{str})s}$	0.201
f_{ly}(ksi) $= k_e \dfrac{2A_{str} f_y}{b_c s}$	0.188
Smallest confining stress ratio $f_{ly}/f_c^{'}$	0.032
Largest confining stress ratio $f_{lx}/f_c^{'}$	0.034
K (from chart)	1.21

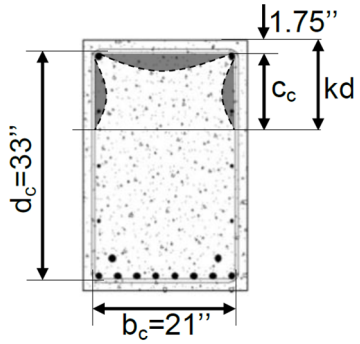

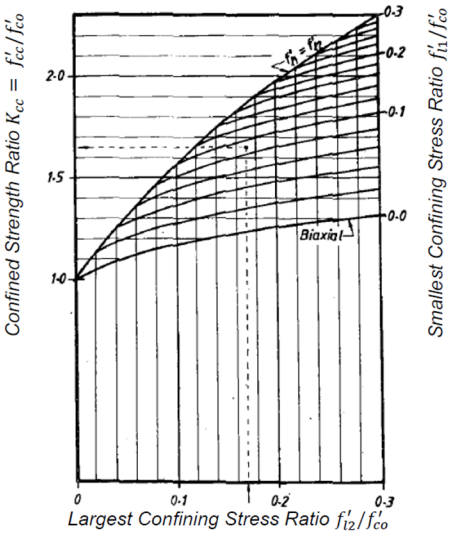

Computation of concrete confinement ratio: column

kd (in.)	13.98
A_{cc} (in^2) $=(c_c+d_s/2)\times b_c$	693
A_e (in^2) $=(c_c+d_s/2)\times b_c -$ area of shaded region	560.85
$k_e = A_e / A_{cc}$	0.81
f_{lx} (ksi) $= k_e \dfrac{(A_{str})_x f_y}{sd_c}$	0.321
f_{ly}(ksi) $= k_e \dfrac{(A_{str})_y f_y}{sb_c}$	0.252
Smallest confining stress ratio $f_{ly}/f_c^{'}$	0.042
Largest confining stress ratio $f_{lx}/f_c^{'}$	0.054
K (from chart)	1.31

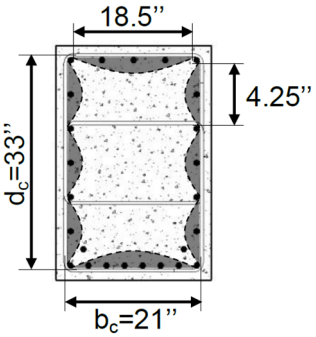

2. Computation of effective concrete strength

kd = depth from the compression face to the neutral axis

Total area of concrete assigned to the chord members = breadth x depth to neutral axis from compression face, $A_{total} = b \times kd = 24 \times kd$

	Beam	Column
kd (in.)	11.31	13.98
Area of cover concrete (in^2) $A_{cover} = 2(1.5) \times kd + [b - 2(1.5)]1.5$	65.43	73.44
Area of core concrete (in^2) $A_{core} = [24 - (2 \times 1.5)](kd - 1.5)$	206	262.1
Contribution of cover concrete to the total area = A_{cover} / A_{total}	0.241	0.219
Contribution of core concrete to the total area = A_{core} / A_{total}	0.759	0.781
Effective f_c' from graph (ksi)	5.46	6.07

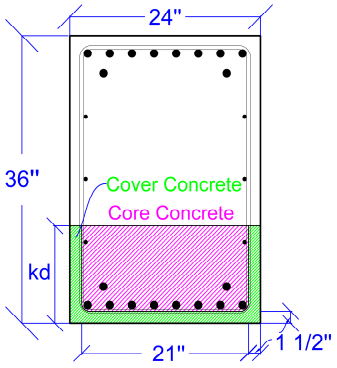

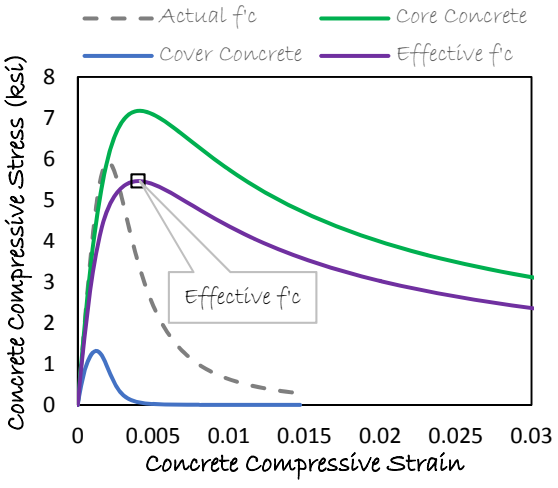

Concrete Stress-Strain Relation for Beam

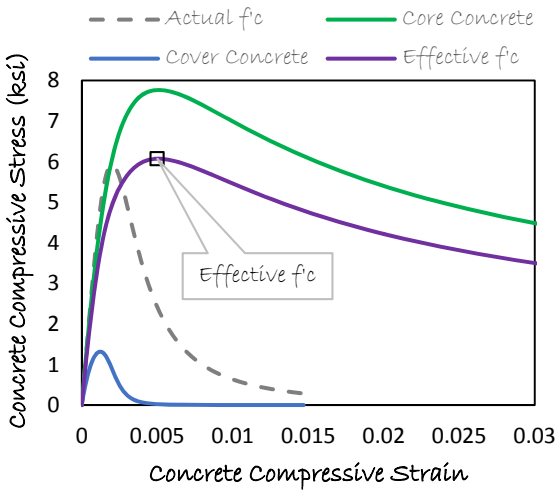

Concrete Stress-Strain Relation for Concrete

	COMPUTATION OF PRESTRAINS IN THE VARIOUS MEMBERS OF THE C-STM MODEL FOR SPECIMEN 3	1 / 5

General notes

Development length for Specimen 3 #8 bars (DL) = 42.20"

Distance to center of C-STM members (l)

Member	from beam short face (in.)	from column face (in.)
S1	31.04	58.22
S2/S6	50.17	39.09
S3/S7	64.135	25.125
S4/S8	74.01	15.25
S5/S9	83.635	5.625
	from beam long face (in.)	
S16	15.5	
S17/S19	41.125	

Note: values in blue are less than the development length.

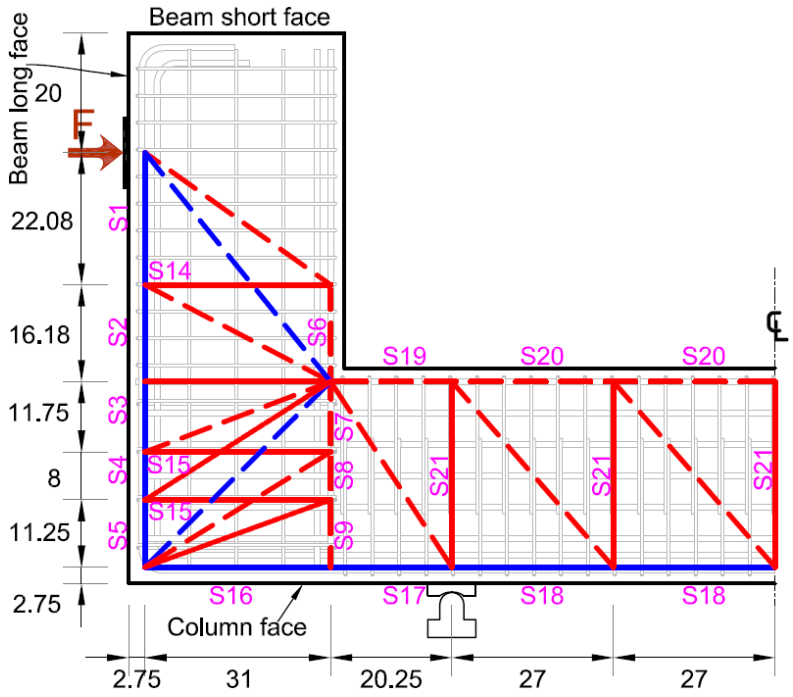

	COMPUTATION OF PRESTRAINS IN THE VARIOUS MEMBERS OF THE C-STM MODEL FOR SPECIMEN 3	2/5

Longitudinal beam members (S1-S5)

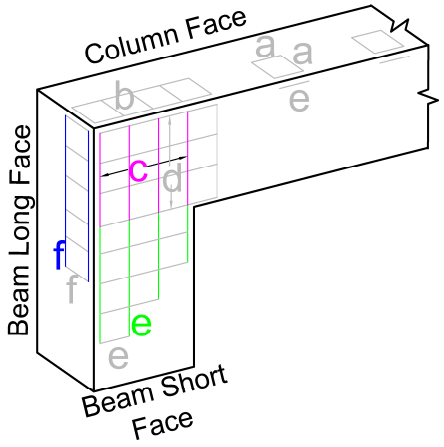

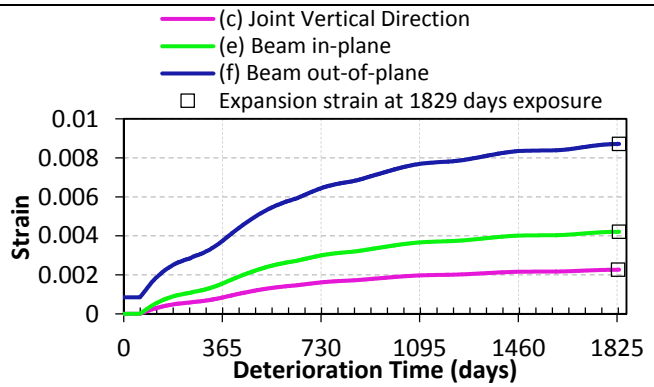

Modeled Expansion Strains Outside Development Length Zone

The prestrains in the longitudinal beam members (S1-S5) are computed considering the average of modeled expansion strains at the end of the exposure period (1829 days) in the joint vertical direction (c presented as Case III in Appendix I) or longitudinal beam in-plane direction (e presented as Case V in Appendix I) and longitudinal beam out-of-plane direction (f presented as Case VII in Appendix I).

Note: $\rho_{eff} = (l / DL)\rho$ and $\varepsilon^{1829}_{\rho(eff)}$ = expansion strain at 1829 days of exposure.

		Joint vertical direction c (Case III, Appendix I)		Longitudinal beam out-of-plane direction f (Case VII, Appendix I)		Average prestrain
Outside DL		$\rho = 0.0529$ $\varepsilon^{1829}_{\rho} = 0.00226$		$\rho = 0.01428$ $\varepsilon^{1829}_{\rho} = 0.00871$		
C-STM Member	l from column face (in.)	ρ_{eff}	$\varepsilon^{1829}_{\rho(eff)}$	ρ_{eff}	$\varepsilon^{1829}_{\rho(eff)}$	
S5	5.625	0.00705	0.00884	0.0019	0.0274	0.01812
S4	15.25	0.01912	0.00427	0.00516	0.01652	0.01040
S3	25.125	0.0315	0.00305	0.00850	0.01214	0.00759
S2	39.09	0.0490	0.00235	0.01323	0.00914	0.00575
	l from beam short face	Longitudinal beam in-plane e (Case V, Appendix I)		Longitudinal beam out-of-plane direction f (Case VII, Appendix I)		Average prestrain
S2	Outside DL	$\rho = 0.01954$ $\varepsilon^{1829}_{\rho} = 0.0042$		$\rho = 0.01428$ $\varepsilon^{1829}_{\rho} = 0.00871$		0.00646
S1	31.04"	$\rho_{eff} =$ 0.01437	$\varepsilon^{1829}_{\rho(eff)} =$ 0.00523	$\rho_{eff} =$ 0.01050	$\varepsilon^{1829}_{\rho(eff)} =$ 0.01060	0.00792

Note: Prestrain values presented in blue are adopted for the corresponding C-STM member.

	COMPUTATION OF PRESTRAINS IN THE VARIOUS MEMBERS OF THE C-STM MODEL FOR SPECIMEN 3	3 / 5

Longitudinal Beam Members (S6-S9)

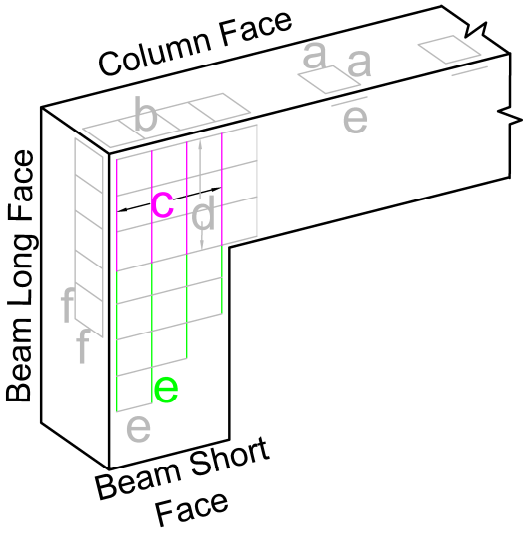

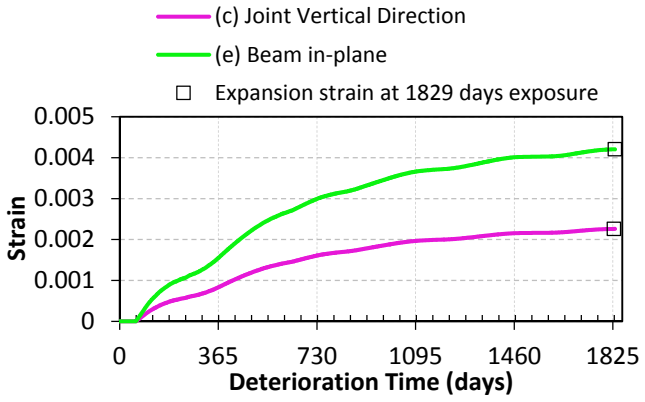

Modeled Expansion Strains Outside Development Length Zone

The prestrains in the longitudinal beam members (S6-S9) are computed considering the modeled expansion strains at the end of the exposure period in the joint vertical direction (c presented as Case III in Appendix I) or longitudinal beam in-plane direction (e presented as Case V in Appendix I).

		Joint vertical direction c (Case III, Appendix I)	
Outside DL		$\rho = 0.0529$ $\varepsilon_{\rho}^{1829} = 0.00226$	
C-STM Member	l measured from column face (in.)	ρ_{eff}	$\varepsilon_{\rho(eff)}^{1829}$
S9	5.625	0.00705	0.00884
S8	15.25	0.01912	0.00427
S7	25.125	0.0315	0.00305
S6	39.09	0.0490	0.00235
	l measured from beam short face	Longitudinal beam in-plane e (Case V, Appendix I)	
S6	Outside DL	$\rho = 0.01954$ $\varepsilon_{\rho}^{1829} = 0.0042$	

Note: Prestrain values presented in blue are adopted for the corresponding C-STM member.

	COMPUTATION OF PRESTRAINS IN THE VARIOUS MEMBERS OF THE C-STM MODEL FOR SPECIMEN 3	4 / 5

Longitudinal column members (S16-S20)

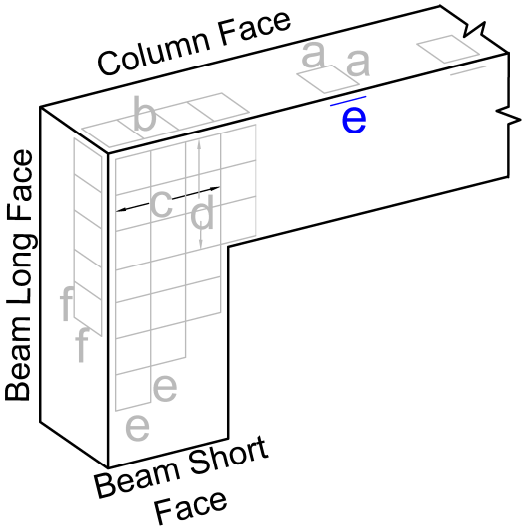

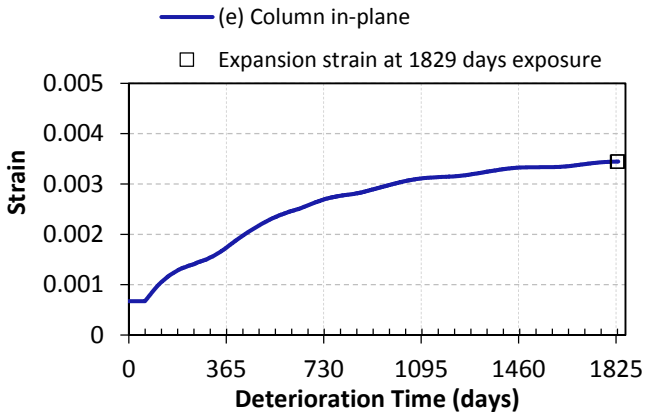

Modeled Expansion Strains Outside Development Length Zone

The prestrains in the longitudinal column members (S16-S20) are computed considering the modeled expansion strains at the end of the exposure period (1829 days) in the column longitudinal face (e presented as Case VI in Appendix I).

Note: $\rho_{eff} = (l / DL)\rho$ and $\varepsilon^{1829}_{\rho(eff)}$ = expansion strain at 1829 days of exposure.

C-STM Member	l measured from beam long face (in.)	Column longitudinal direction e (Case VI, Appendix I)	
S18/S20	Outside DL	$\rho = 0.0671\ \varepsilon^{1829}_{\rho} = 0.0034$	
		ρ_{eff}	$\varepsilon^{1829}_{\rho(eff)}$
S17/S19	41.125	0.06539	0.0034
S16	15.5	0.02465	0.00565

Note: Prestrain values presented in blue are adopted for the corresponding C-STM member.

	COMPUTATION OF PRESTRAINS IN THE VARIOUS MEMBERS OF THE C-STM MODEL FOR SPECIMEN 3	5 / 5

Transverse members (S14, S15, S21)

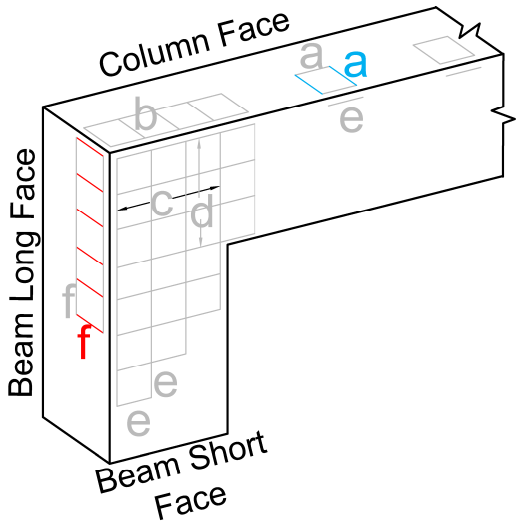

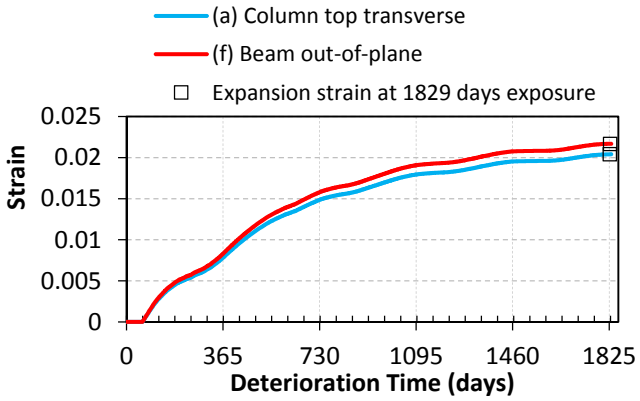

Modeled Expansion Strains Outside Development Length Zone

The prestrains in the transverse members in the beam (S14) and the beam-column joint (S15) are computed considering the modeled expansion strains at the end of the exposure period (1829 days) in the beam out-of-plane region (f presented as Case I in Appendix I). Similarly, the prestrains in the column transverse members (S21) are computed from the modeled expansion strains in the column top transverse region (a presented as Case II in Appendix I).

Note: $\rho_{eff} = (l / DL)\rho$ and $\varepsilon^{1829}_{\rho(eff)}$ = expansion strain at 1829 days of exposure.

C-STM Member	ρ	$\varepsilon^{1829}_{\rho} =$
S14/S15	0.00177	0.02166
S21	0.00198	0.02038

Note: Prestrain values presented in blue are adopted for the corresponding C-STM member.